Metal foam-salt hydrate composites for thermochemical energy storage

Yutong Liu

▶ **To cite this version:**

Yutong Liu. Metal foam-salt hydrate composites for thermochemical energy storage. Solid mechanics [physics.class-ph]. Institut Polytechnique de Paris, 2023. English. NNT : 2023IPPAX066 . tel-04532215

HAL Id: tel-04532215
https://theses.hal.science/tel-04532215

Submitted on 4 Apr 2024

HAL is a multi-disciplinary open access archive for the deposit and dissemination of scientific research documents, whether they are published or not. The documents may come from teaching and research institutions in France or abroad, or from public or private research centers.

L'archive ouverte pluridisciplinaire **HAL**, est destinée au dépôt et à la diffusion de documents scientifiques de niveau recherche, publiés ou non, émanant des établissements d'enseignement et de recherche français ou étrangers, des laboratoires publics ou privés.

INSTITUT POLYTECHNIQUE DE PARIS

NNT : 2023IPPAX066

Thèse de doctorat

Metal foam-salt hydrate composites for thermochemical energy storage

Thèse de doctorat de l'Institut Polytechnique de Paris
préparée à l'École polytechnique

École doctorale n°626 Ecole doctorale de l'Institut Polytechnique de Paris (ED IP Paris)
Spécialité de doctorat: Mécanique des fluides et des solides, acoustique

Thèse présentée et soutenue à Palaiseau, le 25/09/2023, par

Yutong LIU

Composition du Jury :

Laurence FOURNAISON Directrice de recherche, INRAE	Présidente
Véronique AUBIN Professeure, CentraleSupélec	Rapporteure
Loïc FAVERGEON Maître de recherche, École des Mines de Saint-Étienne	Rapporteur
Laurence BODELOT Maîtresse de conférences, École polytechnique	Examinatrice
Marc TUPIN Directeur de Recherche, CEA	Examinateur
Olivier CASTELNAU Directeur de Recherche, École nationale supérieure d'Arts et Métiers	Examinateur
Alexandre Dimanov Directeur de recherche, École polytechnique	Directeur de thèse
Didier DALMAZZONE Professeur, ENSTA Paris	Co-Directeur de thèse

路漫漫其修远兮，吾将上下而求索。

---- 屈原《离骚》

REMERCIEMENT

Trois années d'études à l'étranger touchent à leur fin, marquées par la pandémie, les changements majeurs dans la géopolitique mondiale et la naissance de notre premier enfant, une joie inattendue au milieu de tout. Je suis reconnaissante pour cette période, reconnaissante envers toutes les personnes rencontrées et tous les événements vécus ici au cours de ces trois années, qui m'ont permis de grandir.

Tout d'abord, je tiens à remercier mon directeur de thèse, Alexandre Dimanov, pour avoir proposé un sujet de recherche aussi intéressant. Cela m'a permis de ressentir la joie et le sentiment d'accomplissement de la recherche scientifique pendant ces trois années de doctorat. Merci à lui pour son soutien lorsque j'ai rencontré des difficultés dans mes recherches sur la partie mécanique et quand la direction de recherche n'était pas claire. Merci également à Didier Dalmazzone, co-directeur de thèse, pour son aide cruciale dans la partie thermochimique de ma recherche. J'ai beaucoup apprécié travailler avec vous sur la conception des expériences, résoudre les problèmes et analyser les résultats ensemble. Merci à mes deux directeurs pour leur soutien et leur compréhension au cours de ces trois années. Je vous souhaite une excellente santé et beaucoup de succès dans vos carrières.

Un grand merci à mon collègue, Simon Hallais, pour sa disponibilité et ses conseils en nombreux essais mécaniques réalisés. Je suis reconnaissante pour la patience dont tu as fait preuve en partageant avec moi de nombreuses connaissances sur les techniques de préparation d'échantillons, l'utilisation du MEB, la connaissance de l'EBSD, les méthodes de lithographie, et bien d'autres encore. Merci d'avoir toujours été là pour m'aider à résoudre les divers problèmes expérimentaux et pour partager des moments agréables autour des essais, de vacances, de discussions sur la musique, les différences culturelles franco-chinoises et même des questions mondiales d'actualité et politiques. J'espère sincèrement que nous aurons l'occasion de nous revoir en France ou en Chine.

Je tiens à exprimer ma gratitude envers mes collègues, Zahra, Nina et Xinjie. Merci de devenir des bonnes amies pendant ma thèse, partageant les joies de la vie et surmontant les difficultés de la recherche ensemble. Merci à Michel Bornert pour son orientation sur la technologie DIC, merci à vous pour la fourniture des ressources pour la micro-tomographie, et merci pour l'opportunité de participer aux expériences au Centre de Rayonnement Synchrotron. Un merci spécial à Alexandre Tanguy pour son aide en cas de difficultés expérimentales, à Patrick Aimedieu pour son assistance dans l'utilisation de la micro-tomographie pour caractériser les échantillons, et à

Hakim Gharbi pour son encadrement dans la DVC. Merci à Halim Abdelfattah pour son aide avec les problèmes informatiques et à Alexandra Joly pour son soutien administratif. Je vous souhaite à tous une excellente santé, une vie quotidienne heureuse et la réalisation de tous vos souhaits !

Un grand merci au Laboratoire de Mécanique des Solides (LMS) de l'École Polytechnique et à l'Unité de Chimie et Procédés (UCP) de l'ENSTA pour les conditions et l'environnement de recherche fournis. Je remercie mes collègues du LMS pour leur chaleur et leur attention habituelles, ainsi que pour les cadeaux d'adieu que j'ai beaucoup appréciés. Mes remerciements vont également au Centre Interdisciplinaire Energy4Climate (E4C) et à Total Energy pour leur soutien financier.

Je souhaite exprimer ma gratitude envers les membres du jury pour leur évaluation rigoureuse et pour leurs remarques judicieuses qui m'ont permis de voir plus loin.

Un immense merci à ma famille, à mon conjoint Dr. Yujiong Chen, qui a partagé avec moi le voyage en France pour poursuivre un doctorat et qui a simultanément obtenu son diplôme. Merci pour ton soutien constant, en particulier autour de la naissance de notre bébé. Tu es mon meilleur ami, mon amour éternel ! Merci à mes parents, Lixin et Dongmei, pour leur soutien pendant nos études de doctorat, et spécialement pour être venus en France pendant le mois le plus occupé de notre préparation de thèse pour prendre soin de notre bébé. Merci à notre chouchou, Zhilin, merci d'être arrivé dans la dernière année de la thèse, merci d'avoir enrichi notre vie de parents en France. Merci pour ta santé, ta bonne humeur, ton appétit insatiable et ton amour du sommeil. Tu es la plus grande surprise de notre période de doctorat en France !

感谢我的母校上海交通大学和恩师们对我的栽培，感谢母校对校友一直的关心和牵挂，祝愿母校桃李满天下！

博士学习的结束也标志着我 22 年的学生生涯的结束，现在终于轮到我来回报祖国和社会，争取早日在日后的工作中实现自身的价值。愿我们能早日在自己擅长且感兴趣的领域一展身手，愿我们日后能有足够的实力安心享受人生，愿我们能找到一种最好的方式来回报一路上所有帮助过我们的人们。

最后祝愿祖国强大。

RESUME

L'expansion rapide de la capacité de production d'énergie solaire entraîne le développement prompt de systèmes de stockage de l'énergie thermique (TES) fiables et peu coûteux pour faire face au décalage entre la demande et l'offre d'énergie, compensant ainsi la nature intermittente de l'énergie renouvelable et fournissant de l'énergie à la demande. Grâce à ses avantages tels qu'une densité énergétique élevée, de faibles pertes de chaleur, une flexibilité de stockage de chaleur quotidienne et saisonnière et une réduction significative des coûts, le stockage thermochimique de la chaleur (THS) a gagné en popularité au cours des dernières décennies parmi les technologies TES existantes. Les systèmes THS basés sur les réactions de sorption/désorption de vapeur d'eau des sels hygroscopiques sont les plus simples et les moins coûteux, et ils ont un impact environnemental minimal. De plus, ils sont plus adaptés aux applications à basse température, comme le chauffage domestique, en raison de leurs faibles énergies d'activation. Cependant, les sels hygroscopiques présentent des inconvénients importants tels que le gonflement excessif et l'agglomération des particules de sel cristallin pendant les cycles d'hydratation/déshydratation, ce qui dégrade progressivement l'efficacité du transfert de chaleur et de masse, d'où une performance et une stabilité cycliques médiocres.

Pour atténuer les limitations mentionnées ci-dessus, nous proposons un composite basé sur une mousse métallique à cellules ouvertes en tant que matrice hôte, contenant du chlorure de calcium comme sel hygroscopique dispersé dans les pores. La résistance mécanique et la densité relativement faible de la mousse métallique en tant que matrice hôte garantissent la possibilité de fabriquer des composants légers et durables, adaptés aux opérations de manipulation, d'empilement et de montage, nécessaires pour le dimensionnement et la fabrication adéquats des réacteurs thermochimiques flexibles et polyvalents pour les futures applications industrielles et commerciales de matériaux thermochimiques (TCM). De plus, avec une microstructure adaptée évitant l'agglomération et le gonflement des cristallites de sel, ce matériau composite faciliterait les transferts de vapeur d'eau et de chaleur, améliorant ainsi les performances du système de stockage de chaleur thermochimique.

Ce travail se concentre d'abord sur les propriétés mécaniques des mousses métalliques. Le comportement de déformation multi-échelle de différents mousses métalliques a été étudié par des essais de compression réalisés in situ avec

observation par microscopie optique avec caméra à haute résolution et microscopie électronique à balayage (MEB). La technique de microtomographie à rayons X a aussi été appliquée. Les images ont été analysées par corrélation d'images numériques 2D et 3D (CIN) pour le calcul des champs de déplacement et de déformation. Les résultats montrent que pour l'intégrité mécanique, la microstructure de la mousse métallique est plus importante que le métal lui-même. La localisation des déformations est limitée dans les mousses métalliques avec microstructure plus homogène, ce qui empêche l'effondrement complet des pores et préserve ainsi les propriétés de transfert. En revanche, une microstructure de mousse métallique hétérogène entraîne la formation de bandes de localisation importantes, qui peuvent entraver le transfert de vapeur d'eau, ce qui affecte les performances du composite.

Les propriétés thermochimiques des composites mousse métallique-sel sont étudiées par calorimétrie différentielle à balayage (DSC) et par calorimétrie à l'état isotherme. En particulier, les propriétés thermochimiques des composites pendant les cycles d'hydratation/déshydratation sont comparées à celles de poudres de sel. L'évolution des propriétés thermochimiques est analysée par l'observation in situ de l'évolution microstructurale au cours des cycles d'hydratation/déshydratation dans un microscope électronique à balayage environnemental (MEBE). Il est montré que les composites présentent une amélioration significative en termes de stabilité cyclique et de quantité d'énergie libérée/stockée, par rapport à la poudre de sel en vrac. Les observations in situ MEBE montrent que le gonflement et la déliquescence induisent une redistribution modérée des hydrates de sel dans la mousse métallique. Cependant, la porosité ouverte du composite est préservée. La mousse métallique empêche efficacement l'agglomération des sels et la perte de surface de réaction spécifique, ce qui explique l'amélioration substantielle des propriétés thermochimiques du composite et de sa stabilité cyclique.

En conclusion, le composite mousse métallique-hydrate de sel développé dans notre travail est adapté pour le stockage de l'énergie thermochimique, offrant à la fois des avantages mécaniques et thermochimiques. D'une part, la mousse métallique assure l'intégrité structurelle permettant une manipulation industrielle flexible des unités de stockage thermochimique. D'autre part, la mousse métallique assure la stabilité microstructurale du matériau réactif, préservant une durée de vie économiquement durable. Enfin, les composites ont une faible empreinte environnementale et permettent un recyclage total.

CONTENTS

1. Introduction

1.1. Research background

The global energy crisis has been exacerbated by a combination of factors such as the rapid economic rebound after the Covid-19 pandemic, extreme weather events, disrupted conventional energy supplies and geopolitical reasons, triggering an unprecedented momentum in the development of renewable energy. The soaring prices of conventional fossil energy sources have increased the competitive price benefit of renewable energy, while raising awareness of the energy security advantages offered by domestically produced renewable energy worldwide.

According to the International Energy Agency 2022 report on renewable energies, driven by existing and new policies and new ones introduced in China (the 14th Five-Year Plan), the European Union (the REPowerEU plan), the United States (the US Inflation Reduction Act), renewable energy capacity is expected to grow by 2400 GW which accounts for more than 90% of the expansion of global electricity capacity over 2022-2027 (see Fig. 1.1) [1].

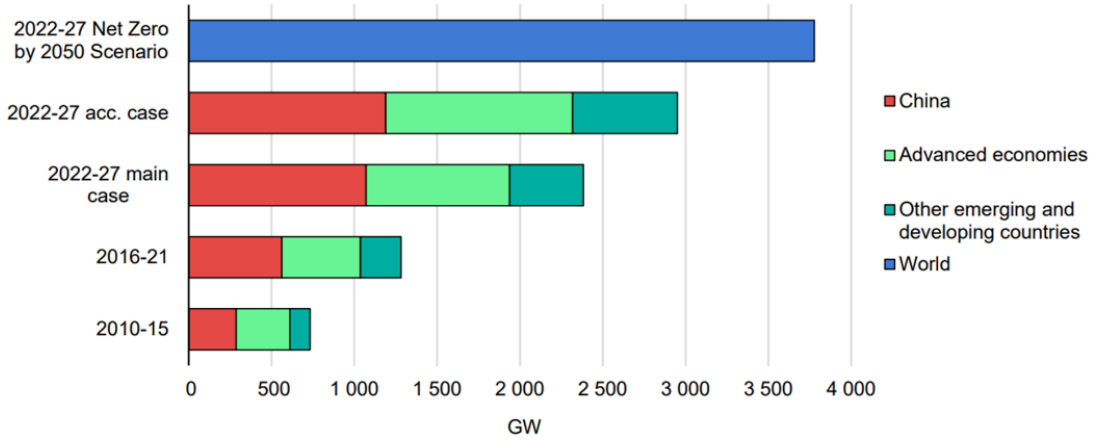

Fig. 1.1 Global renewable capacity expansion in 2010-2027 [1].

With the forecast of the rapid growth in the implementation of renewable energies, based on the data provided and analyzed by International Energy Agency, it is also anticipated that renewable energy overtakes coal as the world's largest source of electricity generation by early 2025 [1, 2]. In Fig. 1.2a, the percentage of global electricity generation produced by different technologies in 2015, 2021 and 2027 is shown. The forecast shown in Fig. 1.2a expects the renewables' share of the electricity mix would increase by 10% within five years to reach 38% in 2027, replacing the shares of coal, natural gas as well as nuclear. This great change in the electricity mix has mainly been driven by the rapid expansion of solar photovoltaics (PV) capacity in the next 5 years. As illustrated in Fig. 1.2b, by the year 2027, cumulative solar PV capacity is expected to reach 2350 GW and claims the global largest installed electricity capacity, even exceeding coal and natural gas. It is also

worth noting that the global wind capacity almost doubles by the end of the 2022-27 period, becoming the second largest installed renewable electricity capacity (Fig. 1.2b).

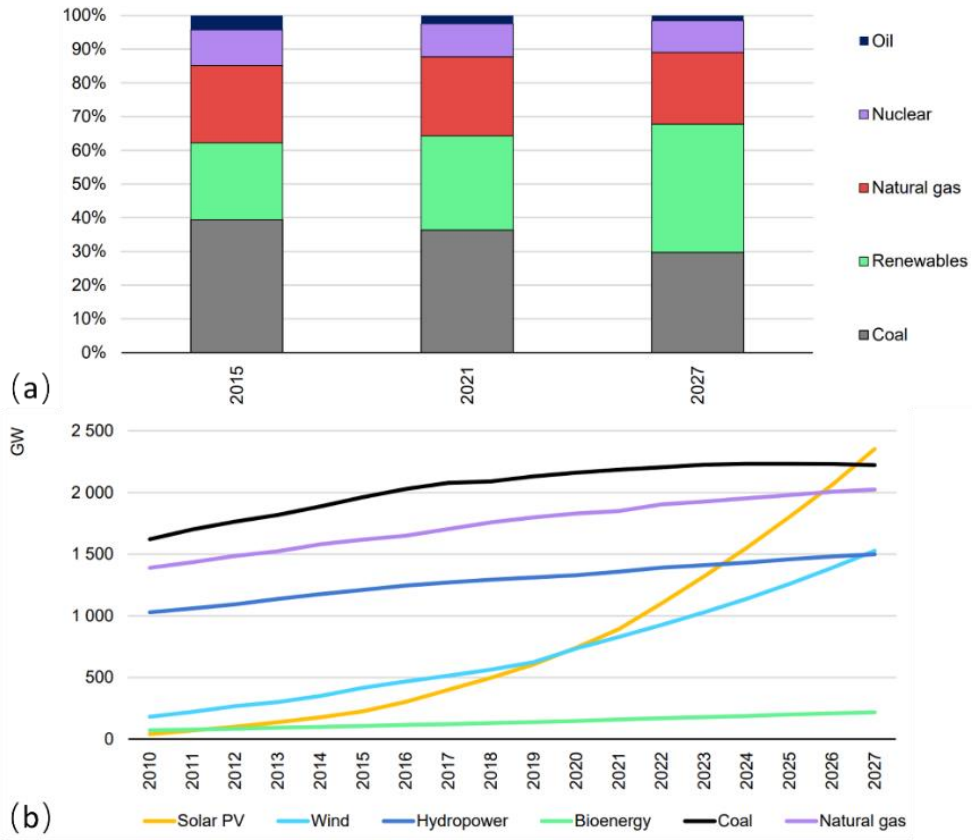

Fig. 1.2 (a) Global electricity generation by different technologies of year 2015, 2021 and 2027, and (b) Cumulative power capacity of different technologies for year 2010-2027 [1, 2].

The main problem with renewable energies such as solar and wind energy is that they are essentially intermittent, which need additional techniques for coping with the mismatch between energy demand and supply. Besides solar PV which converts directly solar to electricity, concentrating solar power (CSP) can also be used to generate electricity by transforming solar energy to mechanical energy and then to electricity [3]. The major advantage of CSP compared to solar PV is that this kind of system allows for storing thermal energy in the CSP plants and converting it to mechanical energy and electricity on demand [4]. Although electrochemical storage for solar PV can be applied to overcome the problem relating to the intermittency of solar energy, electrochemical storage for photovoltaics is still high in cost compared to direct thermal storage systems in CSP plants [5].

The largest amount of energy in the world is used in the form of heating, which accounts for almost half of the world's final energy consumption [1]. In fact, 44% of the final energy consumed for heat is used in buildings for space heating and water heating [1]. In addition to generating electricity by solar energy, the thermal energy produced by solar irradiation can be applied directly in domestic applications.

Thermal energy converted from solar energy and then used in applications such as heating household and domestic hot water (DHW) systems can greatly decrease heat-related CO_2 emission [1, 6].

In all these application scenarios of solar energy mentioned above, the thermal energy storage (TES) system is essential for eliminating the discrepancy between energy supply and demand. It also helps to enhance the efficiency of solar energy systems. The development of effective energy storage technologies and the improvement of the performance of energy harvesting technologies are therefore becoming one of the main research topics for scientists [7]. In the next section, we will present the existing TES systems based on different technologies.

1.2. Thermal energy storage

As introduced above, the usage of solar energy is a current common trend worldwide for generating electricity via photovoltaics (PV) or by concentrating solar power (CSP) as well as for thermal applications related to space heating in domestic sectors [8, 9]. For both CSP plants and thermal applications such as heating buildings using solar energy, it is essential to be equipped with low-cost and reliable thermal energy storage (TES) system to cope with the mismatch between energy demand and supply, thereby increasing the dispatchability of this intermittent renewable energy and providing energy on-demand [5].

For example, the relation between the average daily electricity consumption for a typical household in Melbourne Australia and the solar power production of a 3-kW solar PV during one day is illustrated in Fig. 1.3 [10]. It can be seen that the highest energy demand of a typical household appears at around 7 pm, while solar PV stops producing electricity from around half past 6 in the evening. It is clear that the maximum solar power generation appears at noon and the energy surpassing the low demand quantity of energy during day time will be wasted without an appropriate energy storage system.

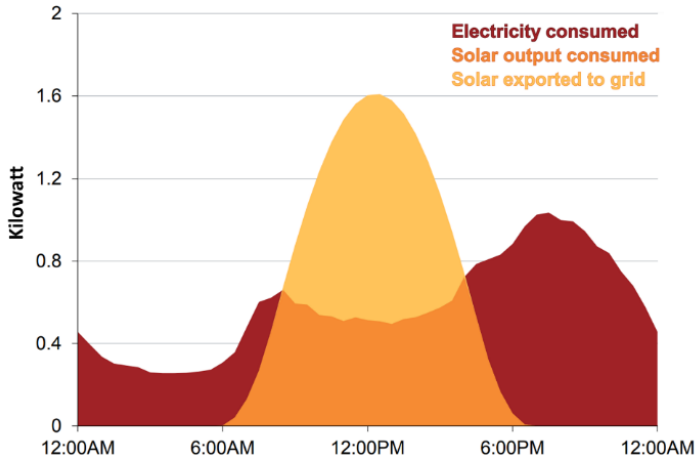

Fig. 1.3 Average power consumption in kW for a typical Melbourne (Australia) household during one day and 3-kilowatt solar PV output [10].

Another mismatch between energy demand and supply arises from the seasonal discrepancy. For instance, Canada is considered to be one of the countries that benefit from a substantial amount of solar radiation. However, given the geographic location and climatic conditions, most Canadian cities receive over 90% of the solar radiation between April and September. While during the winter season, when there is a heightened demand for space heating and domestic hot water supply, the use of solar energy is yet extremely limited [11].

In this context, the purpose of the TES system is to collect and to store the excess solar energy during daytime or during summer time in the form of heat and then be released for different kinds of usage when needed at night or in winter. The energy stored can then be converted into electricity or can be used in its original form of thermal energy to heat the household for instance [12].

There are mainly three existing TES technologies depending on the relevant physico-chemical mechanisms, which are sensible heat storage (SHS) [13, 14], latent heat storage (LHS) [15, 16] and thermochemical heat storage (THS) [17, 18]. The principles of these TES technologies are presented in Fig. 1.4 [19]. These three technologies for thermal energy storge will then be introduced respectively.

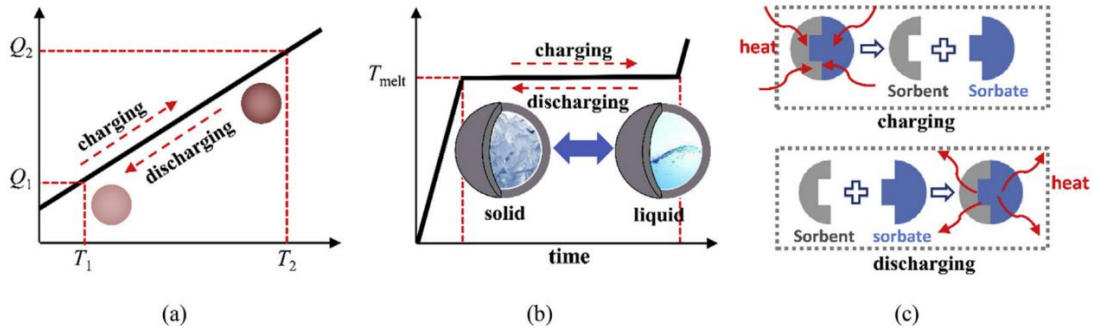

Fig. 1.4 Working mechanism of (a) the sensible heat storage (SHS) system, (b) the latent hear storage (LHS) system and (c) the thermochemical heat storage (THS) system [19].

1.2.1. Sensible heat storage

Sensible heat storage (SHS) system stores thermal energy in form of sensible heat. It is considered to be the simplest method for thermal energy storage by heating or cooling a media material, which could be liquid as water, or solid as rocks, concretes and so on [20]. The use of these non-toxic materials as the storage medium is one of the advantages of SHS systems [21]. As shown in Fig. 1.4a, the amount of sensible heat depends on the difference in temperature of the media material during charging and discharging processes. The stored sensible heat Q_s can be expressed as follows,

$$Q_s = mC_p\Delta T \tag{1}$$

where m is the mass, C_p is the specific heat capacity and ΔT is the variation of

temperature of the media material [14]. Note that during charging and discharging process, there is no phase change in the material.

Sensible heat storage materials have excellent thermal stability especially at high temperatures, due to this reason, they are more often used for high temperature (several hundreds of degrees) applications. It is considered to be a proven technology for installation in commercial CSP plants. The main drawbacks of sensible heat storage materials include relatively low energy storage density (about 150 kJ/kg per 100 ℃) and possible heat loss at any temperatures in long term [3, 7]. Therefore, SHS systems often require containers with large volumes to store an adequate amount of SHS materials, along with sufficient insulation, which would result in the increase of cost and maintenance difficulties.

1.2.2. Latent heat storage

Latent heat storage (LHS) systems store and release the thermal energy during phase change processes of the media material at a constant temperature (Fig. 1.4b). The storage capacity can be expressed as follows,

$$Q_l = m\Delta h_m \tag{2}$$

where m is the mass of media material and Δh_m is the latent heat during phase changing process (charging during melting).

The media materials used for latent heat storage are named phase change materials (PCM). The first classification of PCMs was given by Abhat in 1983 [22]. PCMs can be divided into 3 categories based on their phase change state, which are solid-solid PCMs, liquid-liquid PCMs and solid-liquid PCMs. Among them, the solid-liquid PCMs are most commonly used for LHS systems. It can be categorized into three groups as organic compounds, inorganic compounds and eutectics. A classification of PCM is shown Fig. 1.5 [23].

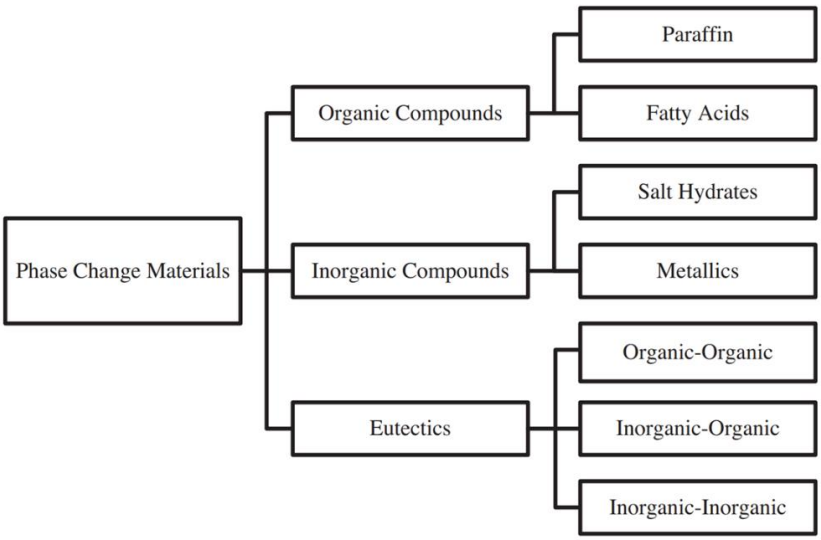

Fig. 1.5 Classification of solid-liquid phase change materials [23].

Desired properties of PCMs include the thermodynamic criteria regarding the appropriate melting point, limited change in volume during the phase change process, the kinetic criteria in terms of the degree of supercooling during crystallization, the chemical criteria such as chemical stability and non-toxic, and finally the economic criteria where the PCM should be available in large quantities and should be easy to get with a reasonable price [22]. The information on the thermal properties of different PCMs used in LHS systems can be found presented in detail in the literature [22-26].

Comparing to SHS, thanks to the higher energy density of LHS systems, they are capable of producing the same amount of energy but with lower volume [3].

SHS and LHS are considered as relatively mature technologies that have been developed and reached commercial implementation, yet, thanks to the high energy density, small heat losses, seasonal heat storage adaptability and significant cost reduction of thermochemical heat storage (THS) systems, this technology has attracted more attention and experienced a prompt development in the past decades [14, 27-29].

1.2.3. Thermochemical heat storage

In general, unlike SHS and LHS systems where heat is stored directly in sensible or latent heat, thermochemical heat storage (THS) stores heat indirectly through physico-chemical process that consumes thermal energy in the charging process and releases thermal energy in the discharging process [30]. Thermochemical heat storage systems are normally divided into chemical reactions (without sorption) and sorption [8, 30, 31]. THS systems based on sorption mechanisms have advantages as the energy required to activate the reaction is lower, which makes it more suitable for low temperature applications [8].

As shown in Fig. 1.4c, the sorption thermal energy storage systems enable charging and discharging processes through reversible reactions between a sorbent and a sorbate. For a better understanding of the classification the thermochemical energy storage based on sorption, the terminological framework needs to be defined and explained. In publications of the Solar Heating & Cooling Programme (SHC) of the International Energy Agency (IEA), two main concepts related to thermochemical storage are defined: adsorption and absorption. Adsorption is defined as the bonding of two phases on the surface of the adsorbent, leaving the original structure unchanged [30-32]. While in the absorption process, a new compound besides the absorbent and the absorbate is formed. This bonding occurs at the molecular scale, thus inducing the change in composition and morphological structure of the sorbent [30-32].

The term “sorption” is first used by MaBain in 1909 to refer to both absorption and adsorption [33]. In the domain of thermochemical energy storage, different

expressions, such as “chemical”, “thermochemical”, “thermochemical sorption” as well as “sorption” have all been applied by different authors in related papers on sorption thermal energy storage [34-37]. Efforts have been undertaken in existing literature to clarify the definitions of these terms and to classify thermochemical heat storage systems based on different mechanisms. For N’Tsoukpoe et al. [38], thermochemical storage was considered to be a part of chemical energy storage, along with electrochemical and electromagnetic energy storage methods. As shown in Fig. 1.6 [38], the author further classified thermochemical storage into three categories: chemical adsorption, chemical absorption, and thermochemical without sorption. However, the definition of “thermochemical without sorption” was not given or explained. The authors then suggested that the sorption thermal storage be divided into four categories, which are liquid absorption, solid adsorption, chemical reaction, and composite materials.

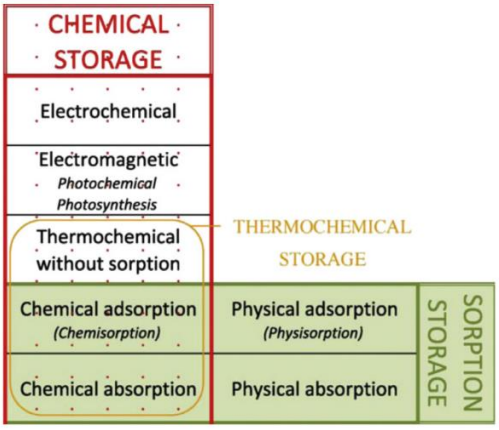

Fig. 1.6 Classification of chemical storage and sorption storage [38].

Based on this classification, Yu et al. proposed definitions of the terminology and the classification of sorption thermal energy storage in 2013 [31] in a review of THS related to the sorption principle. This terminology and classification of thermochemical heat storage have been widely adopted in different reviews since then [8, 32, 37, 39].

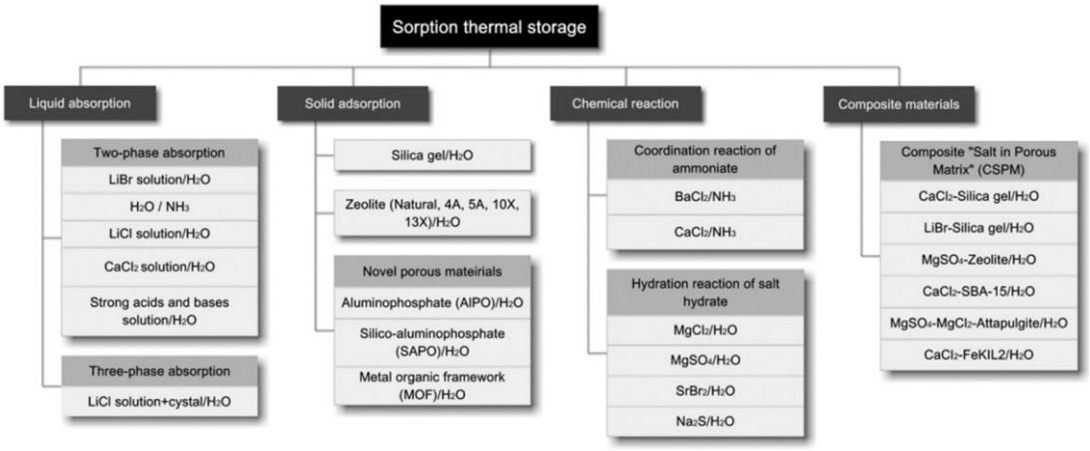

Fig. 1.7 Classification of sorption thermal storage [31].

As proposed by Yu et al. in [31], according to the thermal energy storage mechanism, sorption thermal storage can be further categorized into 4 groups, as shown in Fig. 1.7. Note that the author also clarified in this review [31] that the line between "chemical reaction with sorption" and "chemical reaction without sorption" cannot be clearly defined. In accordance with the conventions used in past research, solid/gas coordination reactions are commonly considered as sorption, including the coordination reaction of ammoniate with ammonia and the hydration reaction of salt hydrate with water [36, 38, 40]. Both of these two reactions can be regarded as coordination reactions, where molecules of ammonia or water vapor are attracted by metal ions to form coordinate bonds. More specifically, a coordination bond forms when a lone electron pair provided by a ligand, such as NH_3 and H_2O, occupies an available hybrid orbit of a central atom, typically a metal ion [31]. While for composite materials, due to their complex composition, it is difficult to clearly distinguish their storage mechanism. Typically, it involves a combination of chemical reactions and other mechanisms, warranting its classification into a separate category. Similar classifications for composite materials can be seen in other literature due to their combined energy storage mechanism [32]. It should be noted that the classification of thermal energy storage

Technically, the characterizations of sorption THS systems can be concluded as follows:

- In summer or during the daytime, solar energy can be used to charge the system by expelling the sorbate (e.g. water vapor) from the sorbent (i.e. silica gel) through the desorption process. Then in winter or at night, the thermal energy stored can be released to meet the demand through the sorption/discharging process by contacting the sorbate with the sorbent.
- The amount of heat required in the charging process for separating the sorbate and sorbent process is higher than that required for phase change of the sorbate, thanks to the elevated bonding force between the sorbent and the sorbate, which brings high storage density with a little volume (Fig. 1.8).
- Thermal energy can only be released once the sorbate and sorbent come into contact with each other, which means that the process is irrelevant to the time span between the charging and discharging process. This facilitates its application for seasonal heat storage.

The typical energy density range of different thermal energy storage systems is presented on the right of Fig. 1.8 and the theoretical volume required for storing 10 GJ of thermal energy of different technologies is presented on the left [8, 30]. It can be seen that compared to SHS and THS systems, thermochemical heat storage offers an outstanding advantage in terms of storage density, for both chemical reactions and sorption-based reactions. What's more, thermal energy loss can also be eliminated by separating the sorbent from the sorbate, enabling the thermal

energy to be stored in a long-term system. For all these reasons mentioned above, the sorption thermochemical heat storage system is currently experiencing prompt development.

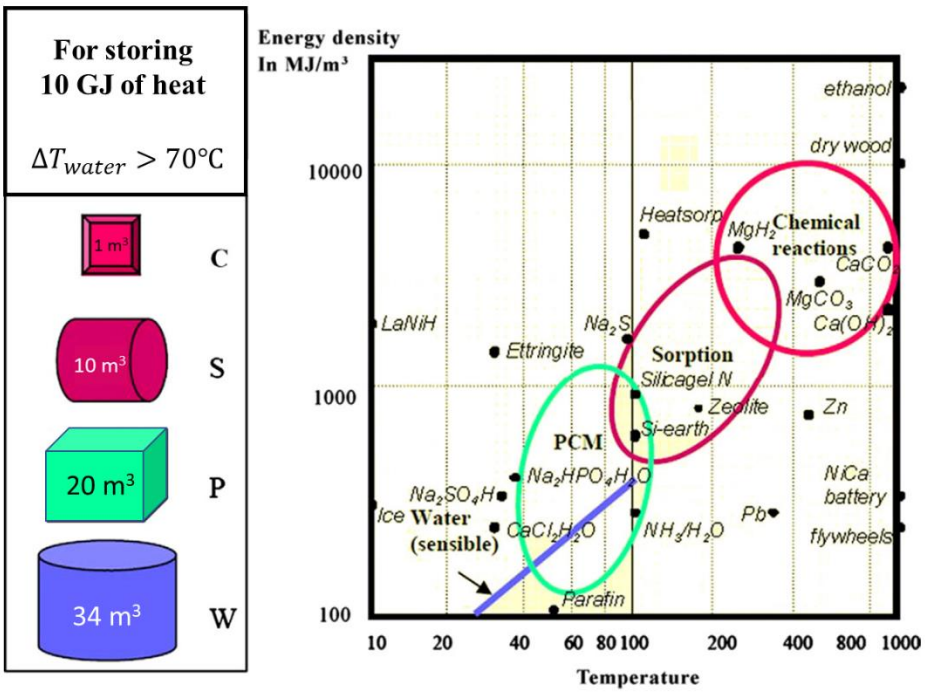

Fig. 1.8 Theoretical volume required for storing 10 GJ thermal energy (considering 25% loss in heat) and the typical energy density of different TES systems [8, 30].

1.3. Sorption thermochemical heat storage system

The sorption THS system can be applied either in open or closed systems [41]. For open systems, as the name implies, the reactant gas needs not to be stored but comes from and released directly to the surrounding environment during the discharging and charging process respectively. The working principle of an open sorption THS system is shown in Fig. 1.9a [39]. In open sorption systems, not only heat and entropy are exchanged with the environment, but also mass exchange occurs with the sorbate as a medium. In the charging process, ambient air is dried and heated (by solar energy for instance), then enters a reactor filled with sorbents to expel the sorbate (e.g. water vapor) from it. This process increases the humidity of the air and decreases its temperature. Then in the discharging process, cool air with humidity (serving as sorbate) enters the same reactor and contact with the sorbent. The heat released during this process will increase the temperature of the air and this hot air will then be used to heat households or water.

Note that the cooling load of air conditioning consists of two parts, which are latent cooling and sensible cooling [30]. The former can be achieved by dehumidification of the supply air of the building, while the latter can be realized by lowering the air temperature in the room. Open sorption systems can be applied to provide

dehumidification through the discharging process and can also be used for sensible cooling by adiabatic humidification through the charging process with the humidified cooler outlet air [30, 42, 43].

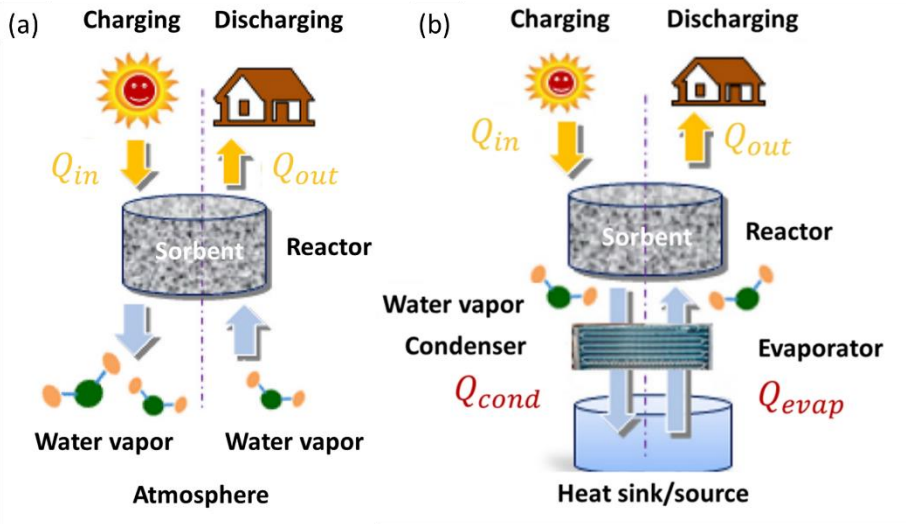

Fig. 1.9 Schematic of the operation principle of (a) the open system and (b) the closed system of the sorption THS system. Based on the schematic presented in [39].

In contrast to open systems, closed systems are isolated from the environment. No mass is exchanged with the environment, but only the entropy [30, 31]. The working principle of closed sorption THS systems is illustrated in Fig. 1.9b. In the charging process, the sorbent and sorbate in the reactor are heated up by the heat source (e.g. solar energy), resulting in the escape of the sorbate (water vapor for example) from the sorbent. The sorbate then passes through a condenser and transforms from gas to liquid at a low temperature. The phase change thermal energy related to condensation is then stored in the heat sink. While for the discharging process, in reverse to the charging process, it consists of a step of evaporation of the sorbate and another sorption reaction between the sorbate and the sorbent in the reactor.

Research has been carried out based on an energy and exergy analysis for comparing the open and closed THS systems [44]. It is reported that the energy and exergy efficiencies of open systems are 69% and 23%, higher than those of closed systems, which are 50% and 9%, respectively. Comparing the open system to the closed system, it is clear that the open systems have advantages such as simplicity of the system and capability of operating at ambient pressure, which leads to a lower cost of implementation. While for closed systems, vacuum conditions are always required to ensure a maximum mass transport of sorbate into the reactor [45]. In addition, the necessary components like condenser, evaporator, and sorbate reservoir add to the complexity of closed systems, not only raising the cost but also making maintenance relatively difficult. However, the exchange of mass of open systems with the environment means that sorbate should be chosen carefully for safety reasons [31, 32]. In conclusion, it is hard to decide on a better system

between the open one and the closed one. The specific choice should be made based on the actual needs and the ambient temperature and humidity of local climate conditions.

1.4. Salt hydrate as thermochemical material

As introduced in the previous part, the open THS systems have been widely studied due to the advantages of low cost and simplicity of the systems, partially thanks to the use of water vapor in ambient air as sorbate [34, 46-49]. In addition, THS systems based on water vapor also provide advantages as stable, safe, and environmentally friendly in terms of reducing CO_2 emission [50]. The open sorption THS system based on the reversible gas-solid reaction between thermochemical materials (TCM) and water vapor can be described as follows:

$$TCM \cdot nH_2O_{(s)} + \Delta H_r \rightleftharpoons TCM \cdot mH_2O_{(s)} + (n-m)H_2O_{(g)} \quad (3)$$

where ΔH_r is the molar reaction enthalpy.

The optimal operation of TES depends to a large extent on the selection of a suitable TCM. An appropriate TCM should meet certain requirements [3, 8, 14, 31], such as

- High energy storage density (>1 GJ/m^3), as high as possible to reduce the volume and material required for storing a certain amount of energy.
- Elevated cycling stability, to postpone the replacement of its system components, thus reducing the maintenance costs.
- Suitable operating temperature, which adapts to the climate conditions of the installation site while meeting the requirements of the application.
- Sufficient thermal conductivity and vapor diffusion channels to ensure appropriate heat and mass transfer properties.
- Stable mechanical properties, which should be sufficient to guarantee the long-term physical integrity of the system.
- Low or non-toxicity, so that it can be applied in households with safety and can be handled easily during and after use.
- Economic viability, which means the material used should be inexpensive, abundant and readily available to ensure a steady supply.
- Low or no active reaction energy required, for a rapid adsorption speed.

As promising TCMs, salt hydrates have been widely studied in the recent decade [51-56]. Research mainly focused on THS systems based on reversible hydration reactions of hygroscopic salts. The property of being fully or largely dehydrated under a temperature of 150 ℃ ensured the ability of salt hydrates and water vapor systems to operate at a relatively low temperature, which suits well for applications such as seasonal and other long-term energy storage [39, 57]. In addition, it is an important driving factor in the utilization of low-level industrial waste heat and solar

energy [58]. As illustrated in Fig. 1.10, during the charging process (Fig. 1.10a), the salt hydrates with more water molecules are dehydrated into that with fewer water molecules or into anhydrous salt by heat generated from low-grade thermal energy, such as solar energy and industrial waste heat, or by surplus electricity, so that the thermal energy is stored in this salt hydrate-based THS system. When needed, water vapor is then sent into the reaction bed for hydrating the hygroscopic salts (discharging) to release the thermal energy stored for space heating or domestic hot water (DHW) supply (Fig. 1.10b).

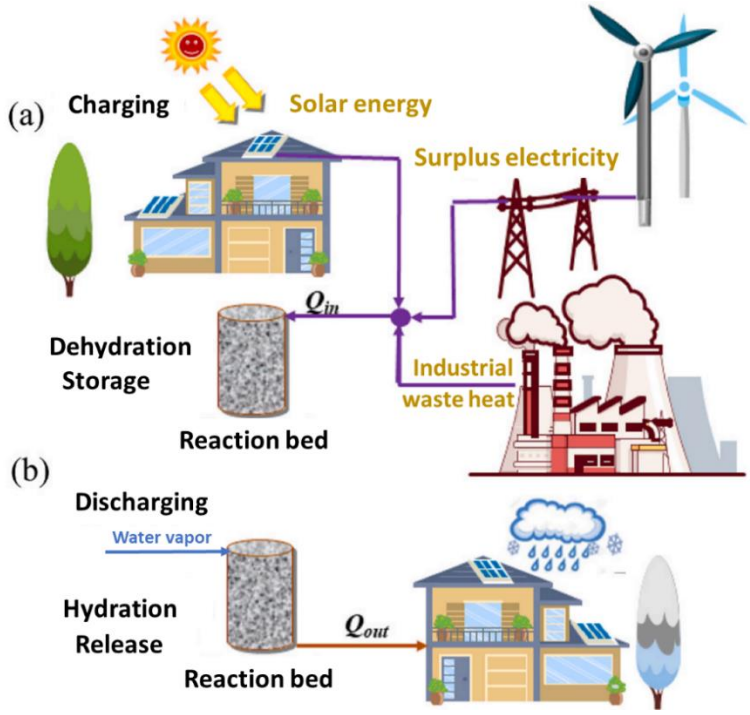

Fig. 1.10 Schematic of hygroscopic salt-based sorption THS system during (a) the charging process through dehydration of the salts and (b) the discharging process through hydration of the salts [39].

The most studied hygroscopic salts include calcium chloride ($CaCl_2$), magnesium chloride ($MgCl_2$), magnesium sulfate ($MgSO_4$), sodium sulfide (Na_2S), and strontium bromide ($SrBr_2$) [54, 59-62]. These salts have multiple hydrated forms with a general formula of $M{\cdot}nH_2O$, which can be considered to be solid solutions of inorganic salts (M) and water molecules (H_2O) [63]. During hydration processes, the salts are assumed to attract more water molecules to transform into hydrates of higher hydration levels. However, when the relative humidity reaches a specific threshold value depending on the temperature and the property of the salt, a saturated solution of the salt forms. This solid-to-liquid transition is called deliquescence, and the relative humidity at which deliquescence starts is defined as the deliquescence relative humidity (DRH) [64]. It is also called the equilibrium relative humidity for the deliquescent process [65]. It is important to note that in the usual cases where no pre-processing is done, the deliquescence of salt will induce mass transfer problems and corrosion problems [31].

In conclusion, despite the generally high energy density offered by pure or mixed salt hydrates, problems related to high costs, restrictive operating conditions and/or the toxicity of the materials prevent their large-scale deployment without special treatments [66-68]. Additionally, hygroscopic salts present non-negligible drawbacks related to the volume change of the salt particles, such as excessive swelling and agglomeration during hydration/dehydration cycles [69-71], as well as the potential deliquescence phenomenon if the relative humidity exceeds the deliquescence relative humidity (DRH), which progressively degrade heat and mass transfer efficiency and lead to poor cyclic stability [39, 72, 73]. Efforts should be made to overcome these drawbacks mentioned above so that hygroscopic salts for sorption thermochemical heat storage systems can be used more efficiently.

1.5. Selective water sorbent (SWS)

To alleviate the limitations mentioned above and to better exploit the potential of the high energy density of hygroscopic salts, a family of composite sorbents named Selective Water Sorbents (SWS) has been proposed and designed by Aristov et al. [74, 75]. The concept is to impregnate hygroscopic salts in a porous host matrix with open pores, thus this two-phase sorbent is also called composite "salt in porous matrix" (CSPM) or "salt in matrix" (SIM) [8, 39, 76, 77]. This combined structure will limit excessive volume changes due to swelling and agglomeration by confining the salt crystals to the open pores, hence preventing loss of the specific reaction surface. The presence of pores also provides more efficient pathways for mass and heat transfer, which would both promote the kinetics of hydration/dehydration reaction [78]. The schema of water vapor interactions with the selective water sorbent (SWS) during hydration and dehydration processes is illustrated in Fig. 1.11 [79]. It can be seen that the thermal energy storage process of SWSs mainly consists of two mechanisms, which are the chemical reaction between the salt and water vapor (about 10%-15% of total sorption), and the liquid absorption (about 80%) [79, 80]. Note that the adsorption on the host matrix is 3% to 5% of the total sorption which is negligible in the first approximation [79]. It is also reported in the research of Aristov et al. [79] that the porous matrix structure has a great impact on the properties of the embedded hygroscopic salt, thus the sorption capacity of an SWS is not a linear superposition of the capacities of the salt and the matrix, but rather a result of their mutual influence.

The most commonly investigated composites concerned $CaCl_2$, LiCl, $MgSO_4$, $MgCl_2$, $SrBr_2$ salts, and nanoporous (several nm to tens of nm) host matrices such as zeolites, silica gels, carbon-based materials, alumina, vermiculites and metal-organic frameworks (MOF) [81-90]. The most common synthesis method used for the impregnation of salt into the open pore host matrix is by incipient wetness technique under atmospheric or vacuum conditions [19, 77, 91]. Note that there should be a trade-off between the mass concentration of the loading salt and the

free porosity of the host matrix after the impregnation of salt. Insufficient mass concentration of salt will certainly decrease the energy storage capacity, but inadequate free porosity of the host matrix will impede the heat and mass transfer, so an appropriate ratio between the two must be adapted to achieve a better performance of the SWS-based sorption THS system.

In spite of the promising possibilities offered by these different composite systems of SWSs (porous host matrices and hygroscopic salts) to be applied to different applications according to different operation conditions, these works were still not considered for commercial deployment because of problems related to inappropriate charging temperature, low thermal conductivity and possible leakage of the salt solution after deliquescence [39, 71, 76].

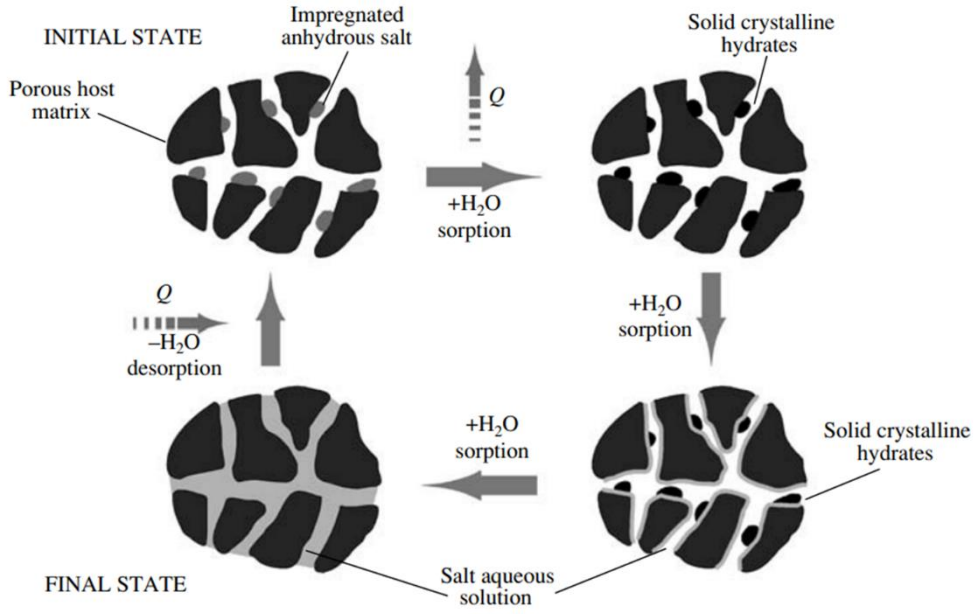

Fig. 1.11 Schematic of interactions between water vapor and selective water sorbent (SWS) [79].

1.6. Research objectives of this work

In our work, we present an original composite “salt in porous matrix” (CSPM) type SWS, specifically designed for thermochemical energy storage. The composite consists of open-cell metal foam (pore size about 350 µm) as host matrix and calcium chloride as hygroscopic salt dispersed and confined in the pores.

1.6.1. Hygroscopic salt: calcium chloride

Calcium chloride ($CaCl_2$) is widely used in energy-efficient thermal engineering. It is an affordable industrial by-product offering many advantages such as its hygroscopic property, high energy storage density, low cost, easy availability, non-toxicity, and suitability for low-temperature operation conditions [92-97]. For example, calcium chloride is used as phase change material for latent heat storage

[98], in desiccant cooling and dehumidification processes [99, 100], as a chemical adsorbent in refrigeration and heat pump machines [101], and as thermochemical material in sorption THS systems [94, 102, 103].

Calcium chloride is highly hygroscopic and there exist 5 known states of calcium chloride with generic formula $CaCl_2 \cdot nH_2O$, where n = 0, 1, 2, 4, 6, naming anhydrate, monohydrate, dihydrate, tetrahydrate, and hexahydrate, respectively. The phase diagram of the $CaCl_2$-H_2O system is shown in Fig. 1.12 [104]. The bold solid line represents the point at which a certain solution reaches saturation concerning a solid phase (ice or $CaCl_2$ hydrates). Besides, the phase diagram clearly indicates the melting point of $CaCl_2$ hydrates. For example, the tetrahydrate $CaCl_2 \cdot 4H_2O$ will begin to melt at a peritectic temperature of around 45.3 ℃ to the crystal of dihydrate $CaCl_2 \cdot 2H_2O$ and solution (incongruent melting).

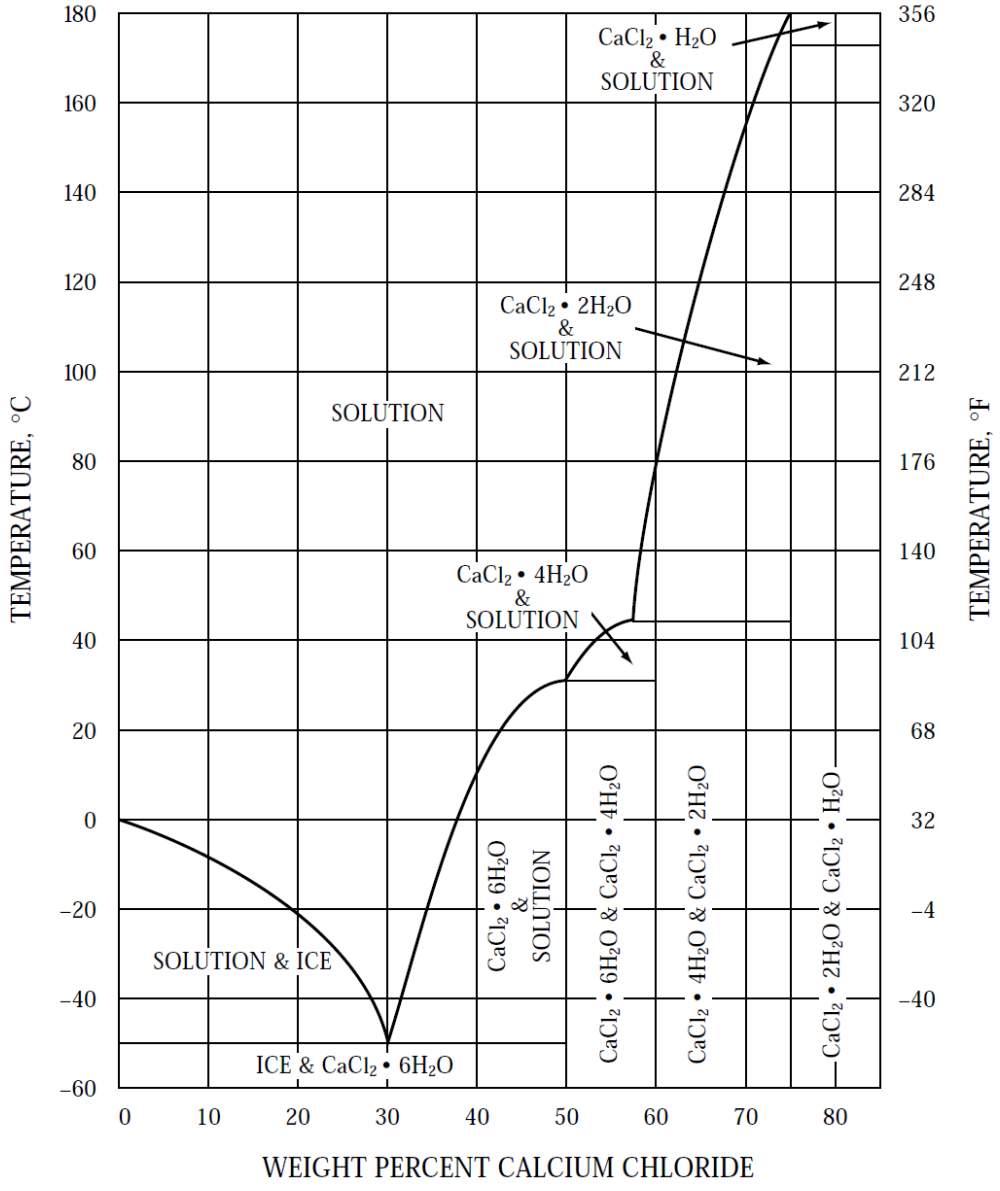

Fig. 1.12 Phase diagram for $CaCl_2$-H_2O system under pressure of 1 atm [104].

The vapor pressure of $CaCl_2$ solutions and the dissociation pressures of the $CaCl_2$ hydrates in terms of temperature are shown in Fig. 1.13 [104]. The air relative humidity in equilibrium with $CaCl_2$ solution can be obtained. Firstly, the vapor pressure of pure water at a certain temperature can be read from the line where the weight percent of calcium chloride is 0. For example, the corresponding value for a temperature of 25 ℃ is 24 mm Hg, while the vapor pressure of 30% $CaCl_2$ solution is 15 mm Hg. The equilibrium relative humidity is then the ratio 15/24, which is 63%. The bold solid black line, which represents the saturated solution curve, provides the minimum water vapor pressure needed for the deliquescence of solid calcium chloride hydrates to occur. For example, from Fig. 1.13, we can see that the water pressure for calcium chloride to deliquescent at 30 ℃ is 7 mm Hg, which is a relative humidity of around 22%.

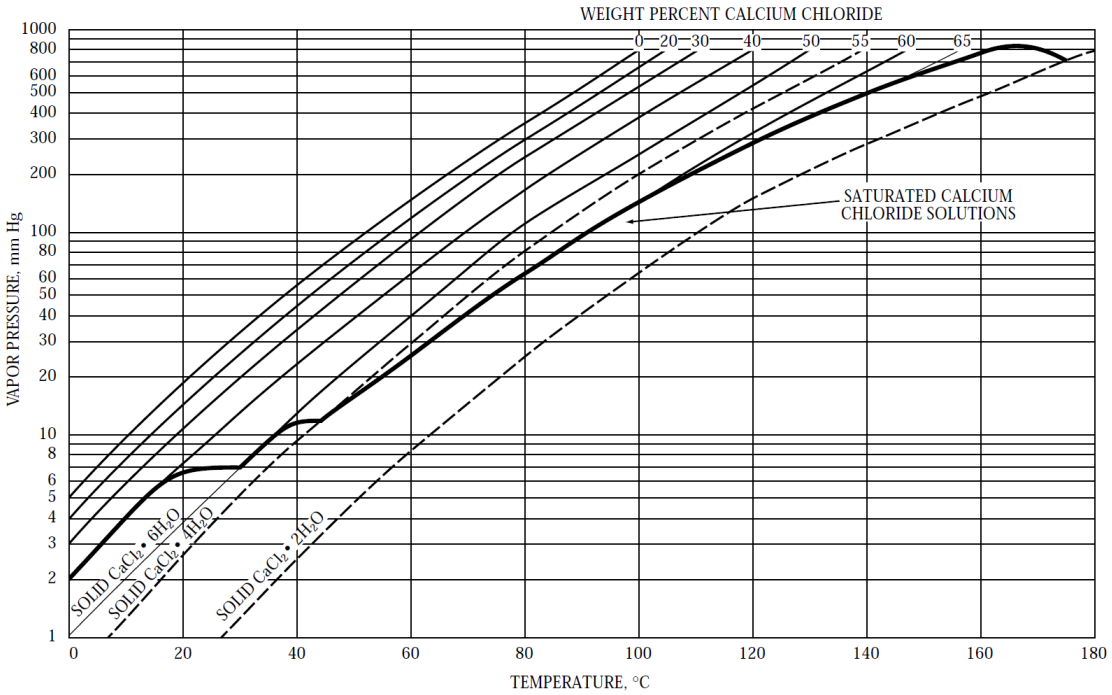

Fig. 1.13 Vapor pressure vs. temperature of $CaCl_2$ hydrates and solutions [104].

Solid-gas reactions between calcium chloride and water vapor have been widely studied for domestic applications since the sorbate water vapor is much preferred over other sorbates. In Table 1.1, we present the enthalpies of hydration reactions between different calcium chloride hydrates, calculated with data provided by the National Bureau of Standards table [105]. The enthalpies reported in the literature were compatible with the theoretical values. For example, the $\Delta H_{reaction}$ of reaction No.3 was tested to be 118 kJ/mol^{salt} [106] and 368 kJ/mol^{salt} of reaction No.5 [107]. Levitskij et al. reported that the $\Delta H_{reaction}$ of reaction No.1 to be 15.0 kJ/mol^{salt}, 8.4 kJ/mol^{salt} for reaction No.2 and 98.6 kJ/mol^{salt} for reaction No.5 with the H_2O molecules existing in form of liquid [108].

Table 1.1 Enthalpies of hydration reactions between different calcium chloride hydrates.

No.	Hydration reactions	$\Delta H_{reaction}\ (kJ/mol^{salt})$
1	$CaCl_{2(s)} + H_2O_{(g)} \rightarrow CaCl_2 \cdot H_2O_{(s)}$	71.6
2	$CaCl_2 \cdot H_2O_{(s)} + H_2O_{(g)} \rightarrow CaCl_2 \cdot 2H_2O_{(s)}$	51.9
3	$CaCl_2 \cdot 2H_2O_{(s)} + 2H_2O_{(g)} \rightarrow CaCl_2 \cdot 4H_2O_{(s)}$	117.1
4	$CaCl_2 \cdot 4H_2O_{(s)} + 2H_2O_{(g)} \rightarrow CaCl_2 \cdot 6H_2O_{(s)}$	120.7
5	$CaCl_{2(s)} + 6H_2O_{(g)} \rightarrow CaCl_2 \cdot 6H_2O_{(s)}$	361.3

Calcium chloride is proposed as a promising TCM, both as pure salt hydrate and as impregnated salt in composite form, for the following advantages and features:

- High hygroscopic sorption capacity in both solid and liquid form [109]. The theoretical enthalpy for anhydrate of calcium chloride being hydrated to hexahydrate is 361.3 kJ/mol^{salt} and the anhydrous $CaCl_2$ is capable of adsorbing water vapor equivalent to 90% of its own weight under ambient temperature and pressure [110].
- Simple accessibility and low cost. Calcium chloride is produced in large quantities as a by-product of industrial processes (such as the Solvay soda-ash process) [111]. It can also be produced by limestone reaction with hydrochloric acid (HCl), or in the United States, by purifying natural brines from salt lakes [111]. Because of the easy availability, large quantity produced and no rare metal involved, calcium chloride is considered to be one of the cheapest hygroscopic salt hydrates [9]. This facilitates the use of calcium chloride in the sorption THS system because it usually requires a large quantity of salt for thermal energy storage.

Combined with other advantages such as less corrosiveness [96, 112] and low-temperature operating range [113] compared to other salt hydrates, calcium chloride is considered to be an appropriate choice for sorption THS systems, especially for common building applications. However, certain drawbacks related to the formation of liquid after the deliquescence of salt [73], the swelling/expansion and agglomeration during hydration/dehydration cycles [69-71, 114], which leads to poor cyclic stability. As Jabbari-Hichri et al. reported [107], after the first complete dehydration of the hexahydrate of calcium chloride, it can regain only 2.6 H_2O molecules in the second cycle, indicating a 37% loss in potential energy storage capacity compared to the first cycle.

Therefore, to make better use of the high theoretical energy storage capacity of calcium chloride, we choose to confine calcium chloride in a porous host matrix to form an SWS material. To date, there have been various studies on the encapsulation of $CaCl_2$ in different porous materials such as SWS materials.

For silica serving as the host matrix, Courbon et al. [115] proposed an original

synthesis method based on repeating impregnation and drying of the composite until reaching the desired salt content. An SWS containing 43 wt% of $CaCl_2$ and using silica gel as the host matrix was obtained through this method. Its energy storage capacity was 1080 kJ/kg, with an energy storage density of 211 kWh/m^3 (=0.76 GJ/m^3) considering the packing density. Barsk et al. [103] developed a modified dry water-style synthesis method for microencapsulation of calcium chloride with hydrophobic fumed silica nanoparticles. Results showed that with temperature increased to 30 ℃, the volumetric energy storage capacity of this SWS can reach 1.4 GJ/m^3, corresponding to a gravimetric energy storage density of around 2400 kJ/kg. It is also reported that samples containing 98 wt% dry $CaCl_2$ (about 5 mg) did not degrade in terms of sorption performance during hydration/dehydration cycles. However, deliquescence occurred before the appearance of tetrahydrate and hexahydrate.

For carbon-based material serving as host matrix, Wei et al. [102] used inexpensive coal tar as a carbon precursor and applied a scalable one-pot pyrolysis strategy to synthesize the pomegranate-type SWS of $CaCl_2$ and carbon shell. Interestingly, they performed a light-to-heat conversion experiment to simulate sunlight of 1000 W/m^2. Under the irradiation of light, the surface temperature of the sample with 65 wt% $CaCl_2$ (Ca/CT200-700) reached 75 ℃. It reached a volumetric energy storage density of 254 kWh/m^3 (=0.91 GJ/m^3) and a gravimetric energy storage density of 922 kJ/kg after 230 min of irradiation. Zhang et al. [116] developed a composite consisting of $CaCl_2$ and carbon nanotube. It is found that the thermochemical performance of the composite can be influenced by the hydrophilic/hydrophobic properties of the carbon nanotube matrix. A hydrophilic matrix can improve water retention and maintain the material's porous structure stable.

Another type of matrix is called metal-organic framework (MOF). They are crystalline inorganic-organic hybrid porous materials, composed of organic ligands linking the inorganic metal ions or metal clusters through coordinate bonds. Their modular nature enables extensive synthetic tunability, allowing for precise chemical and structural control [117]. Touloumet et al. [118] realized an SWS by aluminum fumarate (AF) MOF and $CaCl_2$, with a salt content of 25-60 wt%. The energy storage density of this composite was 1840 kJ/kg, which was found to increase with the added amount of salt to the MOF matrix. It is also reported that the energy storage capacity is higher for the composite than the added contributions of salt and the AF matrix. Shi et al. [119] characterized a series of MOFs/$CaCl_2$ composite. The experimental results showed that the composites based on hydrophilic MOFs had higher energy storage density, which was 1274 kJ/kg. In terms of cyclic ability, the investigated MOFs/$CaCl_2$ composites presented a performance degradation of 6.8%-7.9% after 17 cycles of hydration/dehydration.

Other less commonly studied host matrices for confining $CaCl_2$ include vermiculite

(mainly consists of aluminum, iron and magnesium silicates minerals, ~1.2 GJ/m^3 of volumetric energy storage density and ~2000 kJ/kg of gravimetric energy storage density [83, 120]), ethyl cellulose (~0.4 GJ/m^3 of volumetric energy storage density and ~2100 kJ/kg of gravimetric energy storage density [120]), MCM-41 (a mesoporous material of the family of silicate and aluminosilicate solids, ~2100 kJ/kg [94]), bentonite (~719 kJ/kg [121])and alumina (~576 kJ/kg [121]).

It is worth noting that the performance of composite materials using calcium chloride and the same host matrix may exhibit significant differences reported in various literature. For example, the SWS reported in [115] composed of $CaCl_2$ and silica gel as host matrix had an energy storage capacity of 1080 kJ/kg, while the same kind of composite reported in [121] only had an energy storage capacity of 746 kJ/kg. In fact, the performance may be greatly affected by the synthesizing method, the salt mass concentration, the operation condition, and other related factors [31]. Therefore, it is difficult to conclude which host matrix yields the optimal performance, and is also challenging to compare the performance of composite materials containing calcium chloride synthesized with different host matrices according to the existing literature. For more information on the comparison of energy storage density of different sorption materials synthesized with calcium chloride, the reader is addressed to [31, 103, 122]. A summary of the energy storage density of different TCMs reported in various research is presented in Fig. 3.20 at the end of section 3.4.2, with the experimental result obtained from our work marked in the figure along with the overall summary.

1.6.2. Host matrix: open-cell metal foam

According to the definition given by the International Union of Pure and Applied Chemistry [123], in the context of sorption, the pores are classified according to their sizes. Pore widths that are larger than 50 nm are defined as macropores, that between 2 nm and 50 nm are defined as mesopores, and that smaller than 2 nm are defined as micropores. Currently, the host matrices that have been extensively investigated are almost all microporous or mesoporous materials, which can hardly provide mechanical strength directly to the composite or the system. In our work, we propose to use open-cell metal foam as the host matrix of SWS composite for thermochemical heat storage.

Metal foam has gained special attention and has become one of the most promising structural materials in industrial applications and for scientific research in recent decades [124]. In addition, metal foams have been commercialized thanks to advanced manufacturing processes developed, which also allowed to reduce the cost of this material [125-127]. The mean applications of metal foam can be divided into two groups, depending on the structural or functional properties of the material [125]. Structural applications make use of the light-weight and specific mechanical properties of metal foams. For example, metal foams can be used as

support frames for solar panels and in applications related to the automotive and aerospace industries, where lightweight components are required and their energy absorption capacity can be utilized in case of crashes [127]. As for functional applications, metal foams are applied for sound absorption, for serving as gas diffusion layer, electrode or flow fields in fuel cells, and in certain solar energy harvesting systems as heat transfer media, thanks to the large open area resulting from the porous structure combining with the excellent thermal and electrical conductivity [126, 127]. Another important advantage of metal foam is that by varying the design of metal foam, such as the porosity, pore size and density, thickness of struts, etc., we can easily alter the mechanical properties of the metal foam and its interactions with the fluid that passes through the metal foam based on our needs [125, 128, 129].

Metal foams are usually grouped into open-cell metal foam and closed-cell metal foam. The most significant difference between these two kinds of metal foams is whether the pores are connected to each other [130]. Open-cell metal foams are composed of interconnected pores that form a network in the structure. They are constituted of three-dimensional unit polyhedral cells, formed by solid struts running along cell nodes and interconnecting at higher degree cell nodes, hence building a reticular tri-dimensional network [131]. The typical pore microstructure of closed-cell metal foam and open-cell metal foam is shown in Fig. 1.14a and b, respectively.

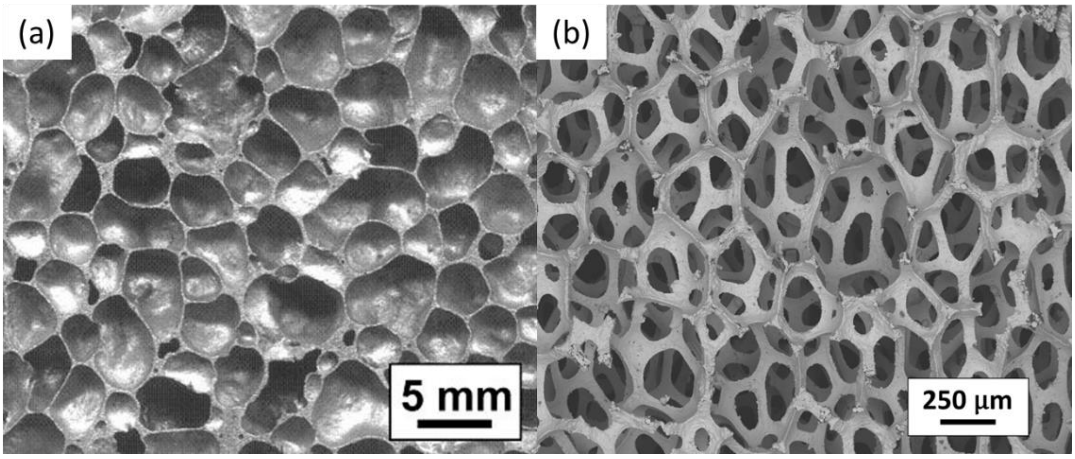

Fig. 1.14 Typical microstructure of (a) closed-cell metal foam (aluminum) [132] and (b) open-cell metal foam (nickel).

For SWS material applied in sorption thermochemical heat storage systems, an open-cell metal foam matrix offers additional advantages related to their elevated mechanical strength and high thermal conductivity, which would ensure mechanical resistance, but also improved heat transfer kinetics [128]. The mechanical strength and relatively low density of metal foam serving as host matrix ensure the possibility of manufacturing lightweight and durable components, adapted to handling, stacking and mounting operations, which are necessary for adequate dimensioning

and fabrication of flexible and polyvalent thermochemical reactors for future industrial and commercial TCM applications [129]. Besides, the reticulation of large open porosity, with several hundred-micrometer pore sizes, provides large open volumes allowing for swelling of salt hydrates without occluding pore spaces, and hence preserving the mass transfer kinetics. Therefore, metal foam-salt hydrate composites meet all requirements for heat and mass transfer process, which are essential for the performances of thermochemical composite [133]. Additionally, metal foams can be produced using recycled metal materials, which also offers certain environmental advantages [134].

As the designed SWS-type metal foam-hygroscopic salts composite in this work is to be used as a thermochemical heat storage material, it is beneficial to understand the application of metal foams in other energy storage systems, in order to select the most suitable metal foam as the host matrix for our application scenario in terms of porosity, pore size, material, etc. In fact, in thermal energy storage applications, the open-cell metal foam has already been used as one of the porous support materials of phase change materials (PCM) in latent heat storage systems in order to ameliorate the heat transfer rate due to the low thermal conductivity of PCMs (about 0.1 W/m·K) [135]. Due to the high thermal conductivity of around 400 W/m·K, the most investigated metal foam as support for PCMs is copper foam, followed by aluminum foam (around 220 W/m·K) and nickel foam (around 90 W/m·K) [126, 136].

There are mainly two methods for synthesizing the metal foam/PCM composite. The first method consists of pouring hot liquid PCM into a container and mix with the metal foam support [137, 138]. The second method involves infiltrating the liquid PCM into metal foam support under vacuum condition [139]. Both approaches are enlightening, but not applicable for our research purposes. Since for latent heat storage, the energy storage capacity is proportional to the amount of PCM impregnated in the metal foam support, we would like to infiltrate as much PCM material in the metal foam as possible. However, in order to use metal foam as host matrix in SWS composites, it is essential to ensure that a sufficient portion of pores remain empty and free of salt so that the heat and mass (water vapor) transfer properties can be guaranteed. Therefore, we need to develop a synthetic method suitable for the purpose of this study, while paying attention to the balance of salt mass concentration and void porosity after the impregnation of salt.

In all the existing studies, metal foams as the support material for PCMs have been proven to improve the overall effective thermal conductivities exponentially compared to pure PCMs [126, 135, 136, 139-143]. However, in some research, properties besides thermal conductivity were investigated, which can help us gain insight into how different metal foams may influence the properties of the composite material. Xiao et al. [139, 140] compared the heat storage capacity of

paraffin embedded in copper foam and nickel foam with identical porosity and pore size. It is reported that copper foam had slightly higher specific heat compared to nickel foam as support of PCM, while nickel foam had better performance in terms of heat storage capacity due to its higher heat capacity compared to copper. They also noted that nickel foam had better corrosion resistance compared to copper foam and aluminum foam. Similar results were reported in the work of Huang et al. [142] and Ferfera et al. [141], proving nickel foam/PCM composite had higher heat storage capacity compared to copper foam/PCM composite.

It is also worth noting that the most popular PCM embedded in the metal foam in experiments so far is paraffin, instead of hygroscopic salts. On one hand, this is resulting from the low-cost, easy availability and chemical stability of paraffin [141]. On the other hand, hygroscopic salts have the problem of leakage when they are melted during latent heat storage [144]. According to the summary made by Zhang et al. [126] on the metal foams used in metal foam/PCM composites, most of the pore size was between 0.6 to 5 mm. Therefore, during the hydration/dehydration cycling tests with the metal foam-salt composite we designed, attention must be paid to whether the leakage occurs when hygroscopic salt deliquesces into a liquid state. Possibly the use of metal foams with smaller pore sizes would avoid leakage problems to some extent.

In general, experimental studies on the comparison of the metal foam/PCM composites are limited. However, according to the available experimental results, among the three mainly employed metal foams (copper, aluminum, and nickel), copper foams offer a higher effective thermal conductivity and a more homogeneous internal temperature distribution of the composite, which resulted from the higher thermal conductivity of copper compared to the other two materials. On the other hand, thanks to the higher heat capacity, nickel foam/PCM composites offer a higher thermal storage capacity compared to copper foam/PCM composites. In addition, as the properties of aluminum foam include high stiffness, low density, inexpensive, easily accessible and can be produced from recycled aluminum materials [145, 146], there is also a strong interest in studying the possibilities and advantages and disadvantages of using it as the host matrix.

In conclusion, in this work, we present a composite “salt in porous matrix” (CSPM) type SWS, specifically designed for thermochemical energy storage. The composite consists of open-cell metal foam as host matrix and hygroscopic salt dispersed and confined in the pores. With an adapted microstructure avoiding agglomeration during swelling and shrinking of the salt crystallites related to hydration and dehydration respectively, this composite material is expected to facilitate the transfers of water vapor and heat and prevent loss of specific reaction surface, thus improving the performance of the thermochemical heat storage system. Based on the results of the literature research, the SWS-type metal foam-salt composites with

copper foam, nickel foam and aluminum foam with pore size of about 350 μm as host matrix, combing calcium chloride as hygroscopic salt will be synthesized and studied.

1.7. Plan of the thesis

As presented in the previous section, the research objective of this thesis is to synthesize an SWS-type composite based on open-cell metal foam as host matrix, containing calcium chloride as hygroscopic salt dispersed in the pores for sorption thermochemical heat storage systems, to alleviate the limitation related to drawbacks of hygroscopic salts such as swelling and agglomeration of the crystalline salt particles during hydration/dehydration cycles, which progressively leads to decreasing specific reaction surface, and kinetics of heat and mass transfer, thus resulting in efficiency degradation due to poor cyclic performance and stability.

As this composite TCM would be stacked in applications, it is essential to make sure that the whole system maintains structurally reliable under the condition of use. For instance, the porous system should not collapse under its own weight. Therefore, the mechanical behavior of the metal foam and metal foam-salt composite needs to be studied.

Since it is the metal foam serving as host matrix that provides major mechanical strength to the composite, this thesis work focuses on the mechanical properties of metal foam in the first part. The multiscale deformation behavior of different types of metal foams was studied by compression tests realized in situ with observation by optical microscopy with high-resolution camera (pixel size of 2.75 μm) and scanning electron microscopy (SEM). Laboratory X-ray microtomography technique was also applied before and after the compression tests. The images were analyzed by 2D and 3D Digital Image Correlation (DIC) for the computation of 2D and 3D full displacement fields and the corresponding strain fields. Additionally, the microscopic deformation behavior of a massive aluminum sample was analyzed by 2D DIC, with a special focus on investigating the grain boundary behavior at 150 °C. The experimental approaches of the above-mentioned experiments and techniques applied for analyzing the results will be presented in section 2.2 and section 2.3. All the results regarding the mechanical properties of different types of metal foams will be presented in section 2.4. The results related to the mechanical properties of the metal foams will then be summarized and discussed in section 2.5.

In the second part, the thermochemical properties of the metal foam-salt composites are investigated. The synthesis method of the composite will first be presented in section 3.2. We studied by isothermal reaction calorimetry the thermochemical properties of the composites during hydration/dehydration cycles and they are compared with those of salt hydrate powders of calcium chloride. The evolution of the thermochemical properties is further analyzed, based on in situ

observation of the microstructural and morphological evolution during hydration/dehydration cycling in an environmental scanning electron microscope (ESEM). The experimental procedures of these mentioned experiments will be introduced in section 3.3. The results concerning the thermochemical properties of the metal foam-salt composites and that of bulk calcium chloride powder will be demonstrated and compared in section 3.4, along with the analysis of the evolution of the thermochemical properties based on in situ ESEM observations. The conclusion regarding the thermochemical properties of metal foam-salt composites with different metal foams serving as host matrix will be summarized in section 3.5.

Finally, the overall conclusion and perspectives regarding the work of this thesis on metal foam-salt hydrate composites for sorption thermochemical heat storage will be drawn in the last part.

2. Mechanical properties of metal foam-salt composite

2.1. Introduction

2.1.1. Description of problematic

As presented in the previous part, the use of metal foam as the host matrix provides mechanical strength and ensures that lightweight and durable components can be manufactured, offering natural stacking and mounting conditions for future industrial and commercial applications of thermal chemical materials. As this TCM would be stacked for use (as illustrated in Fig. 2.1), it is essential to make sure that the whole system maintains structural reliability under the condition of use. For instance, the porous system should not collapse under its own weight.

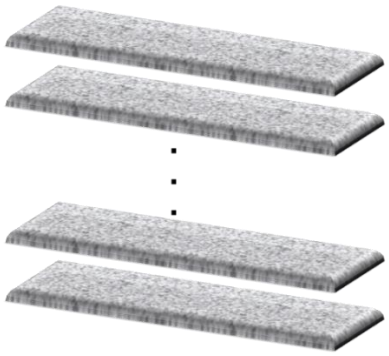

Fig. 2.1 Schematic of stacking metal foam-salt hydrate composites as thermochemical material for future industrial applications.

In fact, space heating accounted for more than 60% of the energy consumption in the building sector, and the energy consumption of space heating in France in 2021 was about 110 kWh/m^2 [147]. While the theoretical volume required for storing 1 GJ (~278 kWh) of thermal energy by sorption THS system is 1 m^3 [8, 30]. To estimate the potential load on the metal foam in real applications, we consider a room surface of s m^2, with the corresponding energy demand for heating this room being about 110 s kWh. This implies that approximately 0.4 s m^3 of sorption thermochemical material is needed, considering the correponsding theoretical energy storage density. Under ideal conditions, if the metal foam panels (along with the salt contained within it) can be installed beneath the room's entire surface area s, the required total thickness of the metal foam panels will then be $0.4s/s$=0.4 m.

The load on the bottommost layer of metal foam is determined by the total weight of the upper layers of metal foam and salt, and it is inseparably linked to factors such as the thickness of a single layer of metal foam, salt mass concentration, the metal foam density, and so on.

For example, if we consider the copper foam and aluminum foam used in our study, the thickness of one panel was 4 mm. Based on the previous calculation, 10 layers of copper foam would be stacked together to provide the energy demand. The

pressure on the bottommost layer applied by the upper layers would be the weight of 9 layers of copper foam and the salt contained in them. By using the metal foam properties listed in Table 2.1, we have the density of the copper foam and aluminum foam to be 347.95 kg/m^3 and 739.36 kg/m^3, respectively. The salt mass content we could achieve was about 50% for copper foam-based composite and 20% for aluminum foam-based composite. So the total mass of the upper 9 layers (metal foam+salt) would induce a pressure on the bottommost layer to be around 2.7 kPa for copper foam and about 3.6 kPa for aluminum foam.

Here, we must emphasize that the pressure calculated above for the bottommost layer of metal foam represents the minimum load it may experience in practical use. In other words, the lower metal foam layer will be subjected to, at least, the pressure calculated above, induced by the weight of the upper layers and the containing salt. This is because our estimation was based on ideal conditions. Specifically, we used the theoretically achievable energy storage density of the sorption thermochemical materials for estimation; however, the actual energy density will significantly impact the volume of energy storage material required. Additionally, we assumed that the material could be uniformly installed across the entire house area, which is challenging to achieve in practice due to constraints imposed by house construction or cost limitations. Meanwhile, we have not yet considered the supplementary equipment or components required for the actual use of this energy storage system. Due to the limitations of house size, these devices may need to be stacked together with the TCMs, potentially exerting additional pressure on the lower part of the stack.

Furthermore, we have only considered the energy demand for the residential space heating sector. In reality, thermal energy stored in TCM can also be used to heat water for domestic use or even for cooking. An increase in thermal energy demand will undoubtedly escalate the required volume of energy storage materials and the system, imposing additional load on the bottommost layer. Moreover, if this energy storage system is applied to meet the thermal storage needs of large-scale industrial production, it may necessitate even larger volumes of metal foam for stacking. This would pose a more severe challenge to the mechanical performance of the lower layers of the metal foams.

For the above reasons, it is essential to explore the complete mechanical behavior of the metal foam under compression to address various application scenarios that may arise in real engineering applications when serving as the host matrix of the hygroscopic salt for thermochemical heat storage.

2.1.2. State of the art of metal foam mechanical properties

As introduced in section 1.6.2, metal foams are artificial materials designed to replicate natural structures like bones, wood, or honeycomb, displaying intriguing

physical and mechanical properties that find a broad range of applications in various industries [124]. Concentrating on applications of metal foams that demand consistent mechanical properties, it is crucial to study and understand the deformation mechanism of the metal foams not only to enhance the commercial acceptance of the related applications but also to fulfill the quality control purpose. Additionally, the study on the deformation mechanism of metal foam plays a vital role in improving the design of materials and their relative applications.

Gibson and Ashby [131] studied and reported the deformation mechanism of cellular materials in 1997 which revealed their distinctively different mechanical behavior compared to the bulk material of which the foams are made. Foams typically experience compressive loading in most of their applications, so the compression test is most commonly applied for studying the mechanical properties of foams [131]. A schematic stress-strain curve of metal foam for compression is shown in Fig. 2.2, featuring three distinct regions, which are the linear elastic region, the plateau region, and the densification region. The elastic region is governed by the bending of cell walls, which presents the initial slope of the stress-strain curve as Young's modulus, E. The plateau following the elastic region occurs due to the formation of plastic hinges in the metal foam that yields. As the metal foam pores approach complete collapse, the opposing cell walls come into contact, leading to additional strain that compresses the solid material itself. This results in a final phase characterized by a rapid increase in stress, which is the densification region [130, 131].

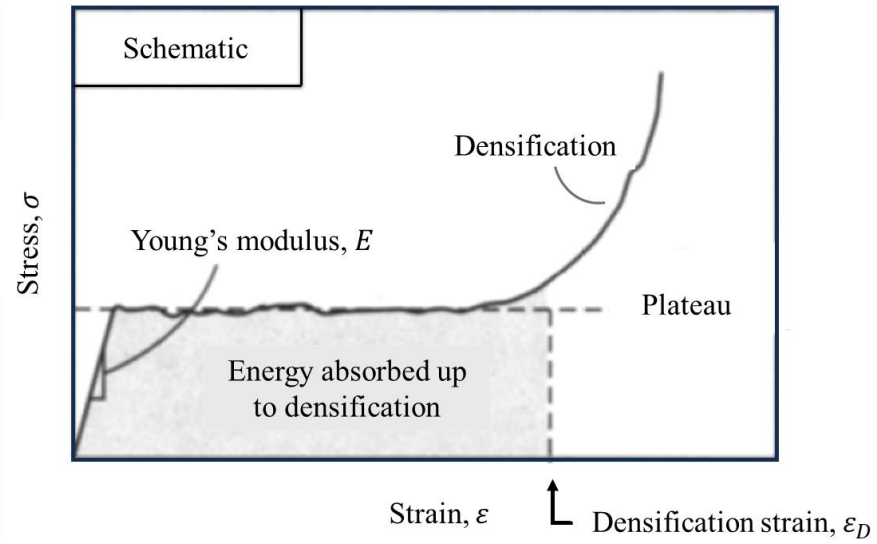

Fig. 2.2 Schematic stress-strain curve of metal foam in compression [130].

The relation between Young's modulus and the relative density of the foam is given by the scaling relation shown as follows [130, 131]. It is based on modeling, as detailed in the book of Gibson and Ashby [131], with extensive testing primarily conducted on polymeric foams, and is also derived from empirical fits to experimental data [130].

$$\frac{E}{E_s} = \alpha \left(\frac{\rho}{\rho_s}\right)^2 \quad (4)$$

where E_s is the Young's modulus and ρ_s the density of the material from which the foam is made, while E and ρ, the Young's modulus and density of the metal foam, respectively. α is a constant that represents all of the geometric constants of proportionality, and empirical results show that α is between the range of 0.1~4 [130]. Note that the Young's modulus here is expressed in GPa.

Efforts were made to study the possible influential factors on the compressive deformation mechanism of metal foams. These studies have consistently shown that the mechanical properties of metal foams are strongly influenced by their microstructural characteristics. Factors such as the type of metal used, cell topology (open-cell or closed-cell), relative density ρ/ρ_s (the foam density, ρ, divided by that of the solid metal from which the foam is made, ρ_s), porosity, pore size and shape, as well as anisotropy, all play significant roles in determining the mechanical response of metal foams [148-150].

Papadopoulos et al. [151] fabricated pure closed-cell aluminum foams (pore size range from 0.7 to 1.8 mm) and studied their mechanical properties by in situ SEM compression test. The experimental results were compared to the theoretical value using the scaling relation for mechanical properties reported in [130, 131, 152] and it exhibited a good agreement with the theoretical values. Bart-Smith et al. [153] investigated the mechanisms of compressive deformation on commercial open-cell aluminum alloy foam with a relative density ρ of 0.08. They observed that the pores located in the localization bands were mainly elliptical, leading them to conclude that the shape of the pores has a greater impact on the yielding behavior compared to the pore size. Deshpande et al. [154] studied the strain rate sensitivity of compressive behavior with commercial open-cell aluminum alloy foams with a relative density ρ of 0.07 and an average pore size of 1.2 mm and with commercial close-cell aluminum alloy foam with a relative density ρ between 0.16 ~ 0.4 and an average pore size of 1 mm. They found that the deformation localized in weak bands in the close-cell foam, while it deformed uniformly for the open-cell foam over the strain rate of 10^{-3} s^{-1} to 5000 s^{-1}. They also demonstrated that over this range of strain rate, the plateau stress and the densification strain were insensitive to the strain rate, but were dependent on the relative density of the foam. Park et al. [155] conducted compression tests on closed-cell steel foam (relative density of 0.53-0.54) and reported that the measurements of cell wall curvature revealed that an elevated mean curvature was associated with a decrease in yield strength, and the strengths of the foam typically deviated from the predictions of the Gibson–Ashby theory [130, 131] by one order of magnitude. This difference is considered to be derived from the morphological defects of the cell wall, creating strain localization and stress concentrations that would degrade the yield strength, which

is contingent upon the strength of the most vulnerable cross-section within the foam. Kaya et al. [150] presented the deformation and pore collapse behavior of 316L open-cell stainless steel foams with two porosities, which are 30 ppi (pores per inch, average pore size of 1.78 mm) and 45 ppi (average pore size of 1.07 mm). They observed from the experiment that the deformation behavior of the metal foams is highly influenced by microstructure, namely the closed pores and their distribution in the foam structure. They also concluded that the mechanical properties of both foams were influenced by the inhomogeneity in their microstructures rather than by differences in cell size at the same relative density. Hong et al. [156] presented two methods, which are freeze-casting (FC) and space-holder (SH) for fabricating the open-cell copper foam with porosity of about 63-78% and compared their compressive deformation behavior. The process FC produced copper foam with a lamellar pore structure with pore size about 13 μm, while the copper foam produced through SH process presented a polygonal pore structure with pore size around 84 μm. The FC-Cu foam showed nearly 30 times higher compressive yield strength compared to that of the SH-Cu foam. The authors explained that this originated from the morphological difference in the microstructure of the foams resulting from the different starting powder types and the heat-treatment conditions. They also observed that the deformation in the case of SH-Cu foam was much more homogeneous, dominated by the deformation mechanism of strut bending and buckling, compared to the FC-Cu foam, which predominantly deformed from the fracture of the struts during the plateau regime.

Besides the relative density, porosity, pore shape and size, strain rate, inhomogeneity in microstructure, and the fabrication method of the metal foam, the temperature also has a non-negligible effect on the mechanical properties of metal foams. Especially for thermal storage applications, it is important to test and understand the compressive behavior of metal foams at high temperatures. Aly [157] studied the compressive behavior of commercial closed-cell aluminum foam ALPORAS (average pore size of 4.5 mm [145]). It is reported that the compressive strength of the foam continued to decrease with the increase of the temperature from 25 ℃ up to 620 ℃. The author explained that the softening effect of the aluminum foam with the increase in temperature is related to the grain boundary sliding of the foam. Mansoor et al. [158] conducted compression tests on commercial open-cell aluminum foam with a relative density of 0.07 and a pore size of 40 ppi (about 2 mm). Results demonstrated that the foam presented a 95% decrease in tensile strength and a continuous decrease in Young's modulus (from 1.5 GPa to 70 MPa) with the increase in temperature from 25 ℃ to 450 ℃. Xiao et al. [159] investigated the temperature influence on the compression properties of open-cell Ni-20Cr foam (pore size from 500 to 1700 μm) under the temperature range of ambient temperature and 550 ℃. They reported that the yield strength was significantly dependent on temperatures. It decreased parabolically following

the Gibson-Ashby model and Kock's kinetic model [131, 160]. Tavares et al. [161] conducted compression tests on aluminum (AlMgSi0.5) open-cell foam with pore size of around 2.7 mm and a porosity of 71.4%-81.8%. They observed that the aluminum foam begins degrading at the temperature of only 150 ℃. More precisely, the foam retained only about 45% of its yield strength at 150 ℃ compared to that measured under ambient temperature, and had only 4.4% remaining at 500 ℃.

According to the research findings on the mechanical properties of metal foams in the literature, we understand that, in addition to relative density, various microscopic structural features of metal foams (such as porosity, pore size and shape, structural inhomogeneity) and compression conditions (such as temperature, strain rate) can influence their performance.

The metal foams used in this study are commercial ones in copper, aluminum, and nickel. In Table 2.1, we present the various characteristic values of the metal foams used. The pore sizes of the metal foams studied in the literature are mostly in the millimeter range, while the pore size of the metal foams we used is only about 350 μm. Besides, considering the application of the metal foam in our study, 150 ℃ is considered the upper limit of temperature that the metal foam-salt composite may reach in actual use for domestic heat applications [39]. As the temperature may have a non-negligible impact on the mechanical properties of metal foam, it is thus necessary to investigate the mechanical behavior of metal foam at the ambient temperature as well as at 150 ℃.

Visualizing local strain fields is crucial for comprehending micro- or meso-mechanical deformation in foams, especially in the dependable design of foam-based components. Digital image correlation (DIC) stands out as a powerful technique in materials science, enabling the visualization of full-field displacements and strain maps with sub-pixel accuracy, which is particularly valuable for investigating failures on the sample surface [162]. The principle of DIC and a detailed introduction of this technique is presented in section 2.2.3. Bart-Smith et al. [153] were the first to apply DIC on metal foam sample surface for computing the strain map. They visualized the localization bands on both closed-cell and open-cell Al alloy foam surface and observed a more homogeneous deformation for the open-cell foam than for the closed-cell foam. The authors noted that the pores located on the strain localization bands were primarily elliptical, from which they deduced that the pore shape may have great impact on the deformation behavior of metal foams. Zhou et al. [163] applied DIC technique for study the compressive behavior of open-cell aluminum foams (pores size around 2.5 mm) up to a macroscopic strain of 28%. Bending of the struts was identified as the primary mode of deformation under compression, given that a majority of the foam struts were inclined concerning the loading axis.

Based on 2D images, DIC provides us with in-plane information and helps to

visualize the localization bands forming during the entire compression process. However, digital volume correlation (DVC) is required for obtaining spatial deformation information. The image acquisition process involves the use of X-ray microtomography technique, which will be presented in detail in section 2.2.4. To date, there exists very limited literature about applying the DVC technique for capturing the 3D strain field and visualizing the 3D strain localization bands inside the metal foam. Thanks to the home-developed software CMV (developed by M. Bornert), we are capable of studying the deformation mechanism of metal foam in three dimensions, including the computation of three-dimensional strain fields and the visualization of the localization bands inside and on the surface of the metal foam samples. This provides valuable and meaningful information for studying and understanding the compressive deformation mechanism of metal foams.

2.1.3. Research plan

As explained in the previous parts, it is essential to explore the complete mechanical behavior of the metal foam under compression to address various application scenarios that may arise in real engineering applications to ensure reliable and high quality when serving as the host matrix of the hygroscopic salt for thermochemical heat storage.

As indicated by the literature, in addition to relative density, various microscopic structural features of metal foams (such as porosity, pore size and shape, structural inhomogeneity) and compression conditions (such as temperature, strain rate) can influence their performance. This section aims to examine the mechanical properties of the selected metal foams under compression and identify suitable foam structures that can serve as optimal host matrices for thermochemical materials at ambient temperature and at 150 ℃.

Our primary criteria for selecting metal foams were small cell sizes and their commercial availability at affordable prices. During the microstructural characterization of the various metal foams used in this study, we observed significant differences in microstructure and composition among the different foam types. These microstructural variations necessitated a comprehensive investigation of the multiscale mechanical behavior of the metal foams. Understanding the microstructural evolution during deformation and its influence on the macroscopic deformation behavior of the metal foam is of paramount importance considering the application purpose. Additionally, we identified the presence of numerous interfaces within the cross-sections of the metal foam struts, prompting us to conduct micromechanical tests on bulk aluminum samples, with a special focus on exploring phenomena related to grain boundary localization.

The multiscale mechanical behavior of different types of metal foams was investigated using displacement-controlled compression tests. In situ observations

were performed using scanning electron microscopy (SEM) and optical microscopy equipped with a high-resolution camera (pixel size of 2.75 µm). Compression tests monitored with optical microscopy were continuous, while SEM observations were conducted stepwise, with the displacement temporarily blocked during image acquisition. Additionally, laboratory X-ray microtomography was employed before and after the compression test. The acquired images were analyzed using 2D and 3D Digital Image Correlation (DIC) techniques to compute full displacement fields and corresponding strain fields. These analyses provided valuable insights into the type of deformation (diffuse or localized) and facilitated the identification of local deformation mechanisms. The microscopic deformation behavior of the solid aluminum sample was analyzed using 2D DIC, with a particular focus on the behavior of grain boundaries at a moderately high temperature of 150 °C.

In this chapter, the experimental approach of compression tests on metal foams is presented in section 2.2, including the description of sample preparation and characterization techniques used. In section 2.3, the experimental approach of compression test on a massive aluminum sample for studying the grain boundaries behavior is introduced, with a highlight on the electron beam lithography technique for patterning features on the sample surface in order to perform digital image correlation. In section 2.4, the multiscale mechanical behavior of different metal foams and massive aluminum in uniaxial compression tests are presented and analyzed. Finally, in section 2.5, discussions of the experimental results and the corresponding conclusions are drawn regarding the mechanical characteristics of metal foam, which provides mechanical strength to the metal foam-salt hydrate composites as a thermochemical material.

2.2. Experimental approach of compression test on metal foam

In this section, the metal foam used for in situ uniaxial compression test and sample preparation method are presented. The observation techniques such as scanning electron microscopy (SEM) and X-ray microtomography are described. The analytical techniques of 2D and 3D Digital Image Correlation (DIC) are introduced. The experimental setup and procedure of in situ uniaxial compression test with SEM and optical microscopy are described in detail.

2.2.1. Material and sample preparation

The mechanical strength of metal foam-salt hydrate composite is provided by the host matrix, which means its mechanical properties depend primarily on the mechanical properties of the metal foam.

Commercial nickel foam (Recemat BV, Ni>99.5%), copper foam (Recemat BV, Cu>99.8%) and aluminum foam (American Elements, Al≈86%) were chosen for serving as the host matrix of the composite according to their appropriate pore size. The properties of these metal foams are presented in Table 2.1. The relative density

of a metal foam is defined as the foam density, ρ, divided by that of the material from which the foam is made, ρ_s. The metal foam density ρ was measured in lab by weighing a certain metal foam sample of known volume.

Table 2.1 Properties of the commercial metal foam chosen as host matrix of the composite.

Foam type	Structure	Density ρ (kg/m^3)	Relative density ρ/ρ_s	Average pore size (μm)	Porosity
Ni foam	Open cell	320.59	0.04	350	96.0%
Cu foam	Open cell	347.95	0.04	400	93.5%
Al foam	Open cell	739.36	0.27	400	40.0%

All these metal foams were delivered in the form of sheets, with various dimensions. To neglect the boundary effects during the uniaxial compression test, it is recommended that the sample size exceeds the mean cell size by a factor of 7 and the ratio of sample length to diameter (or thickness) must be greater than 1.5 [130]. In this context, we prepared parallelepiped-shaped samples with dimensions of 4.5 mm x 4.5 mm x 7.0 mm, which were cut from the metal foam sheets by rotary tools and an automatic cut-off machine (Accutom-100, STRUERS). The cut-off wheel type is 10S15 with a rotation speed of 3000 t/min and a feed rate of 0.1 mm/s. Yet, due to the limitation of the thickness of the nickel foam sheet purchased (1.4 mm), the uniaxial compression test was performed only on copper foam and aluminum foam. Thereafter, the samples were processed in different ways to meet different experimental requirements which will be presented in detail in the subsequent sections.

2.2.2. SEM characterization of metal foam

The structural and microstructural morphology characterization of the metal foam was studied using scanning electron microscopy (SEM). SEM is a versatile tool that allows observations to be made over a wide range of scales, typically ranging from mm to μm. It uses a focused high-energy electron beam (primary electron beam) to scan the sample surface with spot size in nanoscale. Through the interaction between the beam and the matter of the sample surface, various physical information is collected, amplified and then reimaged to characterize the surficial microscopic morphology of the sample, along with its crystallographic and chemical structure. These different physical characteristics are obtained based on different types of interactions between the particle (electron beam) and the matter (sample surface). The secondary electrons (SE) mode is based on inelastic interactions between the primary electron beam and the sample surface. Resulting secondary electrons are ejected from the scanned surface, then accelerated and collected by the SE-detector placed aside the electron column (see Fig. 2.3) for amplification and imaging. The SE mode essentially allows visualizing topographic features, because the technique has a large depth of focus. The backscattered electrons (BSE) mode

corresponds to the elastic interaction (rebound) between the primary electrons and the constitutive atoms near the surface of the sample. The rebounding primary electrons are collected by the BSE detector facing the scanned sample surface (see Fig. 2.3). The energy of the backscattered electrons depends on the sample density and most importantly on the atomic number of the targeted constitutive atoms, which allows imaging based on contrasts between different phases. In turn, the BSE mode also provides crystallographic contrasts for single-phase polycrystals, owing to the crystallographic disorientation between neighboring grains. Further precise information on local crystallographic orientations may be obtained by analysis of electron backscatter diffraction (EBSD) patterns. Scanning the sample surface in EBSD (Electron Backscatter Diffraction) mode provides crystallographic orientation maps, enabling discrimination among different phases as well as different grains within the same phase. Additionally, EBSD allows for the characterization of local intracrystalline disorientations associated with locally heterogeneous crystal plasticity and dynamic recrystallization (polygonization). At last, the energy dispersive spectroscopy (EDS) technique integrated into SEM enables surface mapping of chemical composition. The principle relies on inelastic interactions between the primary electrons and the electronic structure of the targeted material. Once excited, the constitutive electrons emit X-rays upon relaxation, and the energy depends essentially on the structure of the constituent electrons, which is representative of different chemical elements. To find more details on SEM principles the reader is addressed to the book *A beginners' guide to scanning electron microscopy* [164]. The primary components of the SEM are shown in Fig. 2.3. The SE and BSE imaging modes were both used in this study for characterizing the metal foam sample. EBSD and EDS techniques were also applied for analyzing the crystallographic structure and chemical composition of the metal foams studied.

Our apparatus (FEI QUANTA 650 FEG-ESEM) has the particularity to use a field emission gun (FEG) based electron column, which provides substantially better spatial resolution than the traditional technology based on electron emitting tungsten filament (see [164]). It is capable of operating in environmental mode, which allows for the presence of residual water vapor in a degraded vacuum condition. This feature is extremely important for the microscopic characterization of the swelling and deliquescent behavior of the salt-hydrates confined in the metal foam designed for thermochemical heat storage in the present work.

In addition, the SEM in our lab has a special feature adapted to the implementation of miniaturized deformation machines. It is therefore possible to follow the evolution of samples during deformation from a macroscopic scale to a microscopic scale by performing in situ compression tests.

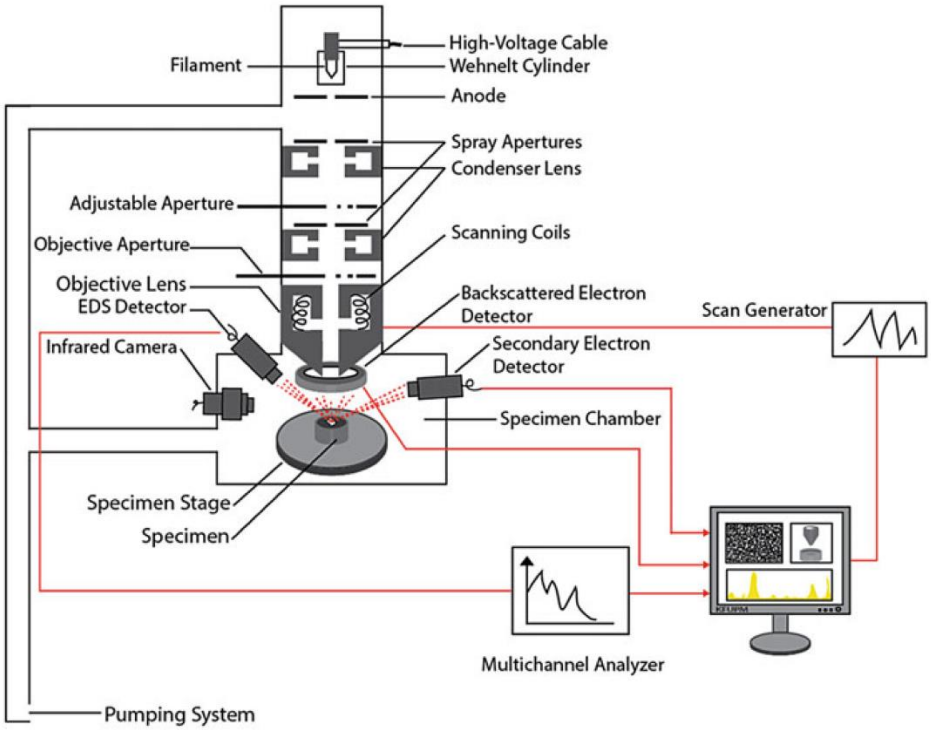

Fig. 2.3 Schematic of the SEM components [164].

Sample preparation

For observation of the bulk metal foam structure, the samples were thoroughly rinsed with ethanol and deionized water and then dried with compressed air before observation via SEM. The accelerating voltage was set at 15 kV for imaging.

For observation of the metal foam microstructure, the samples were saw-cut and appropriately polished. For copper foam, cross-section ion polishing was performed. For aluminum foam, the samples were first polished with SiC grinding papers until grit sizes reached 5 µm (P 4000), then polished by diamond paste with grit sizes of 3 µm and 1 µm, followed by planar ion polishing (by machine PECS™ II GATAN). Imaging conditions were adapted to characterize the polycrystalline nature of the metal foams and to highlight the phases and grains composing the metal foam struts, therefore the accelerating voltage was set at 8 kV for imaging.

2.2.3. Digital image correlation

Nowadays, digital image correlation (DIC) has been a technique widely used in experimental mechanics. The development of 2D field measurements by DIC began in the early 1980s in the field of solid and fluid mechanics [165, 166]. It allows for obtaining the strain field over the entire surface of a sample from two images taken of the same zone at different mechanical state. Derived from the same principle, new technique has developed and improved enormously, such as 3D image correlation with field measurements in volume. Today, both 2D and 3D DIC are commonly used in experimental mechanics for multiscale studies. These techniques

help to achieve the purpose of understanding the macroscopic properties of materials by studying their microstructural properties. Both of these techniques are based on the same principle of displacement field measurements and require powerful image acquisition means according to the scale of observations. For example, 2D DIC requires CCD cameras with macroscopic and microscopic optics or SEM, while 3D DIC requires images taken by X-ray, either under a synchrotron beam or in laboratory microtomography.

In our study, both the 2D and 3D DIC techniques were used for calculating the complete strain field of the loaded metal foam. 2D DIC technique was additionally used for investigating the grain boundary and interfaces behavior after deformation of the massive metal. Both of them were achieved by using the software CorrelManuV (CMV) developed in Laboratoire de Mécanique des Solides by M. Bornert. In the following part, we first present the general principles of the DIC method by restricting it to the 2D case. Based on the same principles, the 3D DIC is a volumetric extension of the 2D DIC and will be briefly presented at the end of the section.

Principle of DIC

In general, the principle of digital image correlation consists of 3 steps:

1) Acquirement of a series of images of the same area in different mechanical states.
2) Associate homologous points based on the "similarity" of their neighborhood.
3) Deduce the displacement field, then by discrete derivation, the deformation field.

2D Digital Image Correlation

As mentioned above, DIC is performed on a set of images taken of the same region of interest (ROI) throughout the entire deformation process of the material. In 2D cases, the images are composed of pixels, which are defined by their coordinates and grayscale. Usually, the image taken before loading is defined as the reference and others taken during the deformation are compared to it while calculating the displacement field.

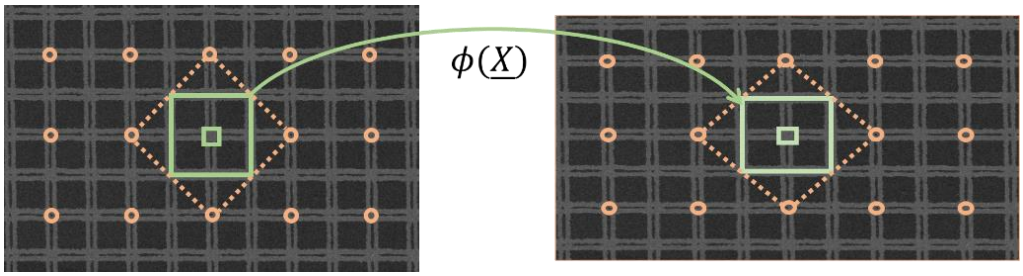

Fig. 2.4 Schematic of the Digital Image Correlation principle, with the reference image on the left and the deformed image on the right.

First of all, a matrix of points is defined on the reference image. A correlation domain is then defined around each point. The correlation domain is usually

defined in the form of a square with a distribution of the grayscale. The local contrast (distribution of grayscale) is considered unchanged during deformation. By finding the same distribution of the grayscale, one point is then identified in the deformed image.

As shown in Fig. 2.4, the green correlation domain of point $\underline{X}$ is transformed by ϕ from the reference image to the deformed image. The area of the integration domain is indicated in orange in the figure. The grayscale of the reference image is noted f and that of the deformed image is noted g. By the assumption of the conservation of the grayscale distribution, one gets

$$g\left(\phi(\underline{X})\right) = f(\underline{X}) \tag{5}$$

By taking into account the image noise g', a possible change in contrast c, and the possible change in brightness b, one gets

$$g\left(\phi(\underline{X})\right) = c \cdot f(\underline{X}) + b + g' \tag{6}$$

To find the point with coordinates $\underline{X}$ in the deformed image, a correlation coefficient $C(\phi_0)$ is defined as follows. The DIC algorithm seeks to find the apparent local deformation ϕ_0 that is closest to the real deformation ϕ and minimizes the coefficient $C(\phi_0)$.

$$C(\phi_0) = 1 - \frac{\sum_{i\in D}\left[g\left(\phi_0(X_i)\right) - \langle g\rangle_D\right] \cdot \left[f(X_i) - \langle f\rangle_D\right]}{\sqrt{\sum_{i\in D}[g(\phi_0(X_i)) - \langle g\rangle_D]^2} \cdot \sqrt{\sum_{i\in D}[f(X_i) - \langle f\rangle_D]^2}} \tag{7}$$

where $\langle g\rangle_D$ is the average of the grayscales in the correlation domain D of $g(\phi_0(X_i))$ and $\langle f\rangle_D$ the average of $f(X_i)$ in domain D. The coefficient $C(\phi_0)$ is defined based on the Zero mean Normalized Cross-Correlation (ZNCC), which is able to eliminate the influence of local variations in contrast and brightness.

The value of $C(\phi_0)$ is from 0 to 2. The lower its value, the better the correspondence between the domains in two images, and the better the quality of the correlation.

To calculate the deformation field from the displacement field obtained by DIC, the transformation gradient $\underline{\underline{F}}$ is given by

$$\underline{\underline{F}} = \frac{\partial \underline{x}}{\partial \underline{X}} \tag{8}$$

with $\underline{X}$ the position of a mass point in the reference image and $\underline{x}$ its position in the deformed image. By definition, one gets

$$\underline{x} = \phi(\underline{X}) \tag{9}$$

So, the corresponding displacement of $\underline{X}$ between these two images can be expressed as

$$\underline{u} = \underline{x} - \underline{X} \tag{10}$$

Combining equations (8)-(10), one gets

$$\underline{\underline{F}} = \frac{\partial \phi}{\partial \underline{X}}(\underline{X}) = \frac{\partial \underline{u}}{\partial \underline{X}}(\underline{X}) + \underline{\underline{1}} \tag{11}$$

with $\underline{\underline{1}}$ the identity tensor of the second order.

The Green-Lagrange strain tensor $\underline{\underline{E}}$ is defined as

$$\underline{\underline{E}} = \frac{1}{2}[\underline{\underline{F}}^T \cdot \underline{\underline{F}} - \underline{\underline{1}}] \tag{12}$$

For infinitesimal strains, one gets

$$\underline{\underline{\varepsilon}} = \frac{1}{2}[\underline{\underline{F}}^T + \underline{\underline{F}}] - \underline{\underline{1}} \tag{13}$$

where $\underline{\underline{\varepsilon}}$ is the infinitesimal strain tensor.

For a given domain from the reference image Ω and its edge $\partial\Omega$, the average transformation gradient over this domain can be expressed as

$$\langle \underline{\underline{F}} \rangle_\Omega = \frac{1}{V_\Omega} \int_\Omega \underline{\underline{F}}\, d\omega \tag{14}$$

with V_Ω the volume of the domain Ω.

According to Green's Theorem, the above equation can be transformed to

$$\langle \underline{\underline{F}} \rangle_\Omega = \frac{1}{V_\Omega} \int_{\partial\Omega} \underline{x} \otimes \underline{v}\, da \tag{15}$$

with $\underline{v}$ the outer normal vector.

Thus, the global Green-Lagrange strain tensor for domain Ω can be written as

$$\underline{\underline{E}}_\Omega = \frac{1}{2}\left[\langle \underline{\underline{F}} \rangle_\Omega^T \cdot \langle \underline{\underline{F}} \rangle_\Omega - \underline{\underline{1}}\right] \tag{16}$$

and the infinitesimal strain tensor as

$$\underline{\underline{\varepsilon}}_\Omega = \frac{1}{2}\left[\langle \underline{\underline{F}} \rangle_\Omega^T + \langle \underline{\underline{F}} \rangle_\Omega\right] - \underline{\underline{1}} \tag{17}$$

Note that for experimental procedures, the magnification of the SEM should be kept the same for one series of images, the distortions of images are minimized and neglected. Also, note that only the component on the XY plan of the transformation

gradient $\underline{\underline{F}}$ can be measured. Information on the Z coordinate is not available.

So, according to equation (15), the 2-D in-plane components of the local transformation gradient for a given dot p can be expressed as

$$\underline{\underline{F}}^p = \frac{1}{S_{\Sigma^p}} \int_{\partial\Sigma^p} \underline{x} \otimes \underline{v}\, dl \tag{18}$$

where Σ^p is the domain chosen around the given dot p whose coordinates on the reference image are (X, Y) and the coordinates on the deformed image are (x, y). S_{Σ^p} is the area of the domain Σ^p and $\partial\Sigma^p$ is its boundary (as shown in Fig. 2.5). It is clear that the outer normal vector $\underline{v}$ and $\underline{v}dl$ are both constant on one segment of the domain boundary $\partial\Sigma^p$.

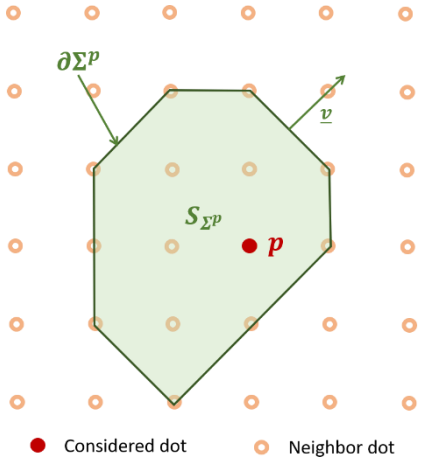

Fig. 2.5 Schematic of the integral domain for calculating the local transformation gradient at a given point.

The number of grid dots on the boundary $\partial\Sigma^p$ is considered to be N and the coordinates of the n^{th} dots on the boundary to be $\underline{x}^n$. By assuming that the variation of $\underline{x}$ between two extremal points of the segment is linear, one gets

$$\underline{\underline{F}}^p = \frac{1}{2S_{\Sigma^p}} \sum_{n=1}^{N} [\underline{x}^n + \underline{x}^{n+1}] \otimes \underline{v}^n\, dl^n \tag{19}$$

with $\underline{v}^n$ the outer normal vector of the segment between the two dots n and $n+1$ and dl^n the length of this segment. Note that by numbering the dots of the boundary $\partial\Sigma^p$ counterclockwise, the following expression can be derived

$$[\underline{v}^n dl^n] = \begin{bmatrix} Y^{n+1} - Y^n \\ -X^{n+1} + X^n \\ 0 \end{bmatrix} \tag{20}$$

By substituting equation (20) into equation (19), one gets

$$\underline{\underline{F}}^p = \frac{1}{2S_{\Sigma^p}} \sum_{n=1}^{N} \begin{bmatrix} (x^n + x^{n+1})(Y^{n+1} - Y^n) & (y^n + y^{n+1})(Y^{n+1} - Y^n) \\ (x^n + x^{n+1})(-X^{n+1} + X^n) & (y^n + y^{n+1})(-X^{n+1} + X^n) \end{bmatrix} \tag{21}$$

while S_{Σ^p} the area of Σ^p is computed as

$$S_{\Sigma^p} = \frac{1}{2}\sum_{n=1}^{N} \begin{vmatrix} X^n & X^{n+1} \\ Y^n & Y^{n+1} \end{vmatrix} \tag{22}$$

Note that superscript $N+1$ is the same as superscript 1.

In the software CorrelManuV (CMV), there exist 4 types of the domain around the considered dot that can be chosen as Σ^p.

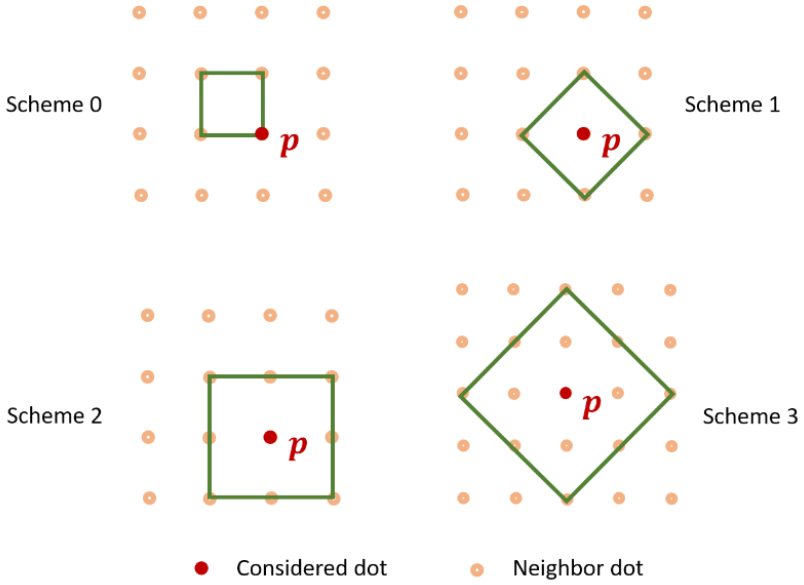

Fig. 2.6 Different schemas of possible integration domain for local gradient calculation.

As shown in Fig. 2.6, Scheme 0 has the smallest domain area and provides the most localized information on the considered grid dot, yet the considered dot is not centered and its result is very sensitive to the image noise. While Scheme 3 has the largest averaging surface that may provide the best precision, it may also smooth local strain heterogeneities and may also lose information on grain boundaries. Therefore, Scheme 1 and Scheme 2 are usually chosen when we want to have relatively good precision and obtain enough local information at the same time.

By using equation (17), we can write ε_{XX}, ε_{XY}, ε_{YY} in terms of F_{XX}^p, F_{XY}^p and F_{YY}^p:

$$\varepsilon_{XX} = F_{XX}^p - 1 \tag{23}$$

$$\varepsilon_{XY} = \frac{1}{2}(F_{XY}^p + F_{YX}^p) \tag{24}$$

$$\varepsilon_{YY} = F_{YY}^p - 1 \tag{25}$$

However, we need the out-of-plane displacement ε_{ZZ} to deduce the three remaining components. We make therefore 2 hypotheses:

1. The axis normal to the observation plane is the main axis of the deformation

and there is no out-of-plane rotation, entailing $F_{XZ} = F_{YZ}$.

2. An additional hypothesis allowing to evaluate ε_{ZZ}. Three choices are offered in CMV:
   a) Plane deformation: $\varepsilon_{ZZ} = 0$
   b) Isochoric deformation: $Tr(\underline{\underline{\varepsilon}}) = 0 \Rightarrow \varepsilon_{ZZ} = -(\varepsilon_{XX} + \varepsilon_{YY})$
   c) Axisymmetric deformation: let ε_i denote the principal strains with $i \in [1,2,3]$, $\varepsilon_{ZZ} = \varepsilon_1$ if $|\varepsilon_1| < |\varepsilon_2|$ and $\varepsilon_{ZZ} = \varepsilon_2$ otherwise.

To highlight localized deformations, the von Mises equivalent deformation ε_{eq} can be used, which can highlight local distortions better than the components of $\underline{\underline{\varepsilon}}$. It's a scalar practical for analyzing the intensity of the 'average' deformation at each point, especially when we want to highlight slip bands and grain boundary sliding.

By assuming the axisymmetric deformation hypothesis, the equivalent von Mises strain ε_{eq} can be written as a function of the deviatoric deformation $\underline{\underline{\varepsilon}}^{dev}$:

$$\varepsilon_{eq} = \sqrt{\frac{2}{3}\left(\underline{\underline{\varepsilon}}^{dev} : \underline{\underline{\varepsilon}}^{dev}\right)} \tag{26}$$

or

$$\varepsilon_{eq} = \frac{2}{3}|\varepsilon_1 - \varepsilon_2| \tag{27}$$

This value will be represented on the strain maps presented in the following sections. The ε_{eq} value calculated at a point is assigned to the coordinates of that point in the reference image. Note that this calculation of equivalent strain is similar to a quantification of the strain deviatoric plane, independently of any hypothesis about the ε_{ZZ} component. It is therefore also a measure of the strain distortion in the observation plane, which may be relevant for measuring localized slipping, as opposed to its isotropic part $(\varepsilon_1 + \varepsilon_2)/2$, which measures the variation in surface area (zero in the case of pure slipping).

3D Digital Image Correlation

The 3D DIC method is a volume extension of the 2D DIC method presented above. They share the same general principle. For measuring the displacement field, a virtual three-dimensional grid on the reference volume is created (see Fig. 2.7). These cubes represent the correlation domain that we defined. This correlation domain consists of a set of voxels (volumetric extension of the pixel). The recognition of the correlation domain from reference to deformed domains is accomplished by minimizing the correlation criterion defined in (7). An optimization by trilinear interpolation of grayscales can be used to evaluate the variations of grayscales between two adjacent voxels, thus obtaining a "sub-voxel" accuracy.

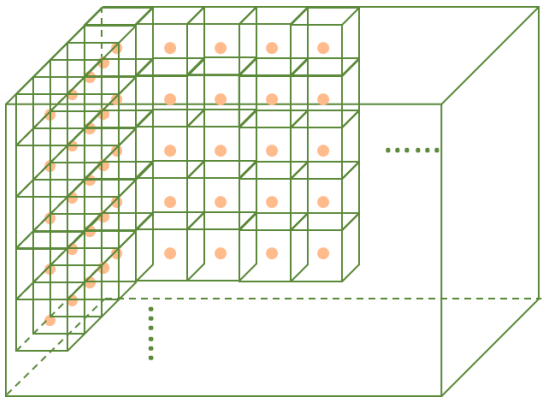

Fig. 2.7 Virtual 3D grid created in the ROI of the reference volume.

The correlation domain is modified by the deformation presented in Fig. 2.8. Finally, the calculation of the deformations requires knowing the values of the displacement of each point. Since the displacement measurements are discrete, interpolation is needed to calculate the displacement between the measurement points. This interpolation is performed using an eight-node cubic finite element shape function based on a trilinear interpolation of the displacement. The technique is described more precisely in [167, 168].

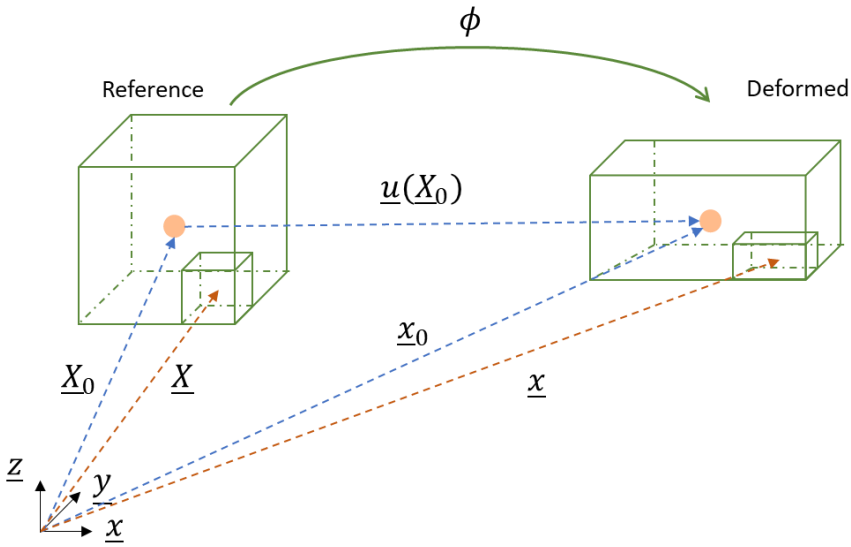

Fig. 2.8 Schema of transformation in volume with the large cube representing the correlation domain and the small cube representing a voxel.

In particular, it is important to note that in order to reduce systematic errors in the results measured by DIC technique and to improve its accuracy, the surface of the sample (2D case) or the sample as a whole (3D case) must have a sufficiently strong contrast. This contrast can be a natural contrast derived from the material itself. In cases where the material itself does not provide sufficient contrast, markers need to be artificially introduced into the material to enable the recognition of grayscales of the correlation domain between the reference and the deformed image. In addition, the scale of the markers varies according to the investigated scale.

For example, for the study of the macroscopic deformation behavior of the metal foam, thanks to its porosity and the appropriate size of the strut, the natural contrast provided by metal foam is already sufficient for X-ray microtomography imaging. For imaging by optical microscopy with high-resolution camera, the lightening system causes reflections on the surface of the metal foam and thus affects the imaging, so additional surface treatment is required. The details of this part will be described in section 2.2.6, and the DIC results will be presented in section 2.4.2.

While for the study of the microscopic deformation behavior at the grain and interface scale, electron beam lithography technology is required to achieve markers in micrometer or even nanometer scales. The details of the use of electron beam lithography for marking patterns on the sample surface will be introduced in section 2.3.2, and the corresponding DIC results will be presented in section 2.4.3.

2.2.4. X-ray microtomography

X-ray tomography is a well-established non-destructive imaging technique initially developed and applied in the field of medical radiography with a resolution of about 2 mm [169]. While the X-ray microtomography (μCT or micro-CT) technique enables imaging with pixel size in μm range. The first X-ray microtomography system was developed and reported by Jim Elliott in 1982 and the first published X-ray microtomographic images had a pixel size of around 50 μm [170]. The technique allows the reconstruction of 3D images of an object from a series of 2D radiographic projections of the object created by X-ray in absorption contrast mode. The main advantage is that the technique is non-destructive. It has been widely used in materials science for decades for the three-dimensional characterization of the microstructure of materials [171-174].

The X-ray microtomography technique consists of two parts, the first is the 2D projection image acquisition and the second is the 3D image reconstruction. For radiography image acquisition, the system is designed with an X-ray tube as the X-ray source, a rotation stage for placing the sample while obtaining radiographic images at various alignment angles, and an X-ray detector. The tube emits a beam of X-ray which passes through the object, interacts with matter (absorption) and gets captured after attenuation by the detector. The relationship between the intensity of the incident and the transmitted beam is given by the Beer-Lambert law,

$$I = I_0 \exp(-\mu L) \tag{28}$$

where I_0 is the incident intensity, I is the X-ray intensity measured after passing through the object, L is the length of the X-ray path through the object, and μ is the linear attenuation coefficient, which depends not only on the chemical nature and the number of atoms constituting the object along the X-ray trajectory but also

on the energy of the X-rays.

Fig. 2.9 shows the X-ray tomography system (Ultratom, RX Solutions) used for this study, which is located in the Navier Laboratory (Champs sur Marne, France). The system was equipped with two sources, one with a maximum of 230 kV and a maximum intensity of 1 mA, the other with a maximum of 160 kV and a maximum intensity of 10 µA. A rotating stage is located in front of the source, allowing the precise rotation of the sample during image acquisition. The X-rays were captured by a plat panel detector (PaxScan 4343DX-I, Varex Imaging), with a total of 3072 × 3072 pixels and a pixel pitch of 139 µm.

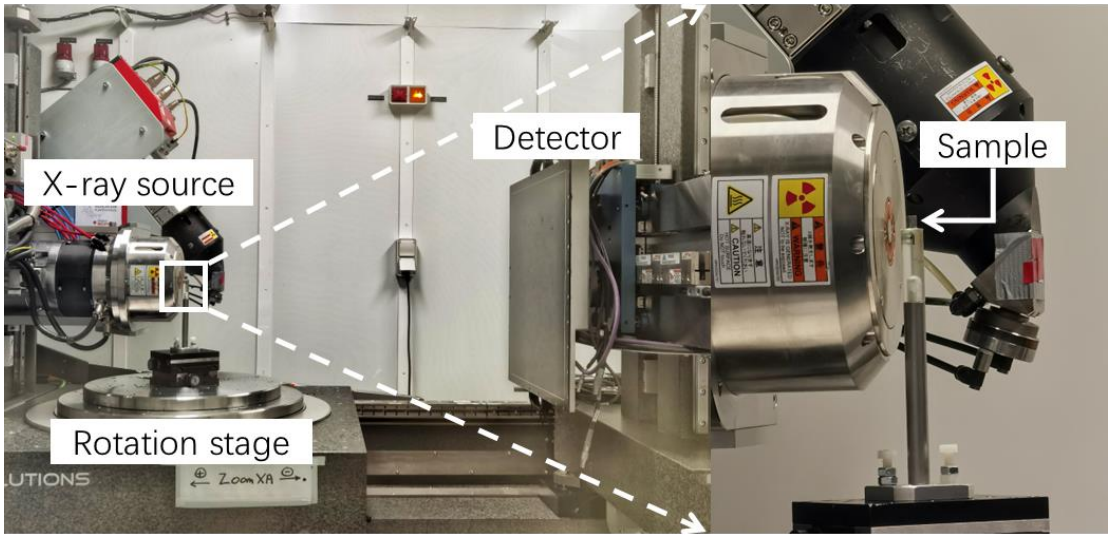

Fig. 2.9 Photo of X-ray microtomography system used for sample 2D projection image acquisition.

Scans were performed before and after the loading of the metal foam. For scanning the initial state of metal foam samples, the scans were realized under 90 kV with an intensity of 90 µA. While the scan after loading was realized under 120 kV with an intensity of 33 µA. All the images were in a format of 16 bits. Other information regarding the scans is shown in Table 2.2. The 2D projection images were then reconstructed into a 3D volume using the software X-Act developed by RX-Solutions. Measurement of the deformation was realized by a 3D version of software CMV mentioned in section 2.2.3 [167, 168, 175] and then the deformation field was visualized by the application Paraview.

Table 2.2 Information of X-ray microtomography performed on metal foam samples.

Foam type		Voltage (kV)	Current (µA)	Resolution (nb of voxel)	Voxel size (µm)
Cu foam	Before loading	90	90	2302×2302×4800	2.4
	After loading	120	33	2498×2498×2999	2.4
Al foam	Before loading	90	90	2100×2300×4476	2.4
	After loading	120	33	2100×2400×3400	2.4

2.2.5. In situ SEM uniaxial compression test

In the past, the mechanical compression tests were performed ex situ SEM and the resulting microstructures of the deformed samples were observed by SEM afterward, known as the post-mortem conditions. However, this approach does not allow to follow chronologically the development of the deformation microstructures and to detect the activation of different deformation mechanisms along the loading process. In order to access the chronology of the deformation processes and the active microphysical mechanisms, one needs to perform micro-mechanical deformation tests in situ using the SEM or optical microscopy. However, such an approach necessitates the development of a specific miniaturized deformation machine corresponding to the limited size of the SEM chamber and the necessary test conditions. Since the beginning of the 21st century, our laboratory has been conducting micromechanical testing with in situ observation using optical microscopy and SEM. Micro-mechanical testing allows us to obtain common mechanical properties such as tensile and compressive strength, as well as the Young's modulus. But most importantly, it allows for the direct observation of deformation localization phenomena and retrieval of local strain heterogeneity in relation to the sample's microstructure. The first reported in situ SEM compression test was performed in 1968 by Gane and Bowden [176]. Since then, numerous micro-mechanical testing machines suitable for in situ SEM tests were designed and a large number of studies were accomplished by this characterization method [177-180]. In addition to simple observation, the development of parallel pattern techniques (i.e., deposition of artificial patterns on the sample surface providing local optical contrasts [181]) has allowed for in situ kinematic measurements. This enables the characterization of surface displacement fields and the computation of full mechanical strain fields.

In our study, in situ SEM uniaxial compression test was performed on metal foam samples to investigate their mechanical properties during compression. As described above, the samples were in form of parallelepipeds with the size of 4.5 mm × 4.5 mm × 7.0 mm. The micro machine and the assembly used for this experiment are presented in Fig. 2.10. It was designed and manufactured in our laboratory (Laboratoire de Mécanique des Solides) specifically for in situ SEM traction or compression tests at ambient temperature or high temperature on micrometer-scale samples. The machine was made of stainless steel in the shape of a "U" and the loading axis was parallel to axis x of the SEM. The axial load was applied by a mobile cross-head, driven by a DC motor and is measured by a load cell (LTH300, FUTEK) with a capacity of 100 lb (444.82 N) placed at the fixed cross-head, in alignment with the loading column. The compression tests were performed in controlled displacement. The black part of the motor (marked in Fig. 2.10a) is an optical encoder, ensuring that the command of displacement sent by the control

box can be accurately followed by the motor.

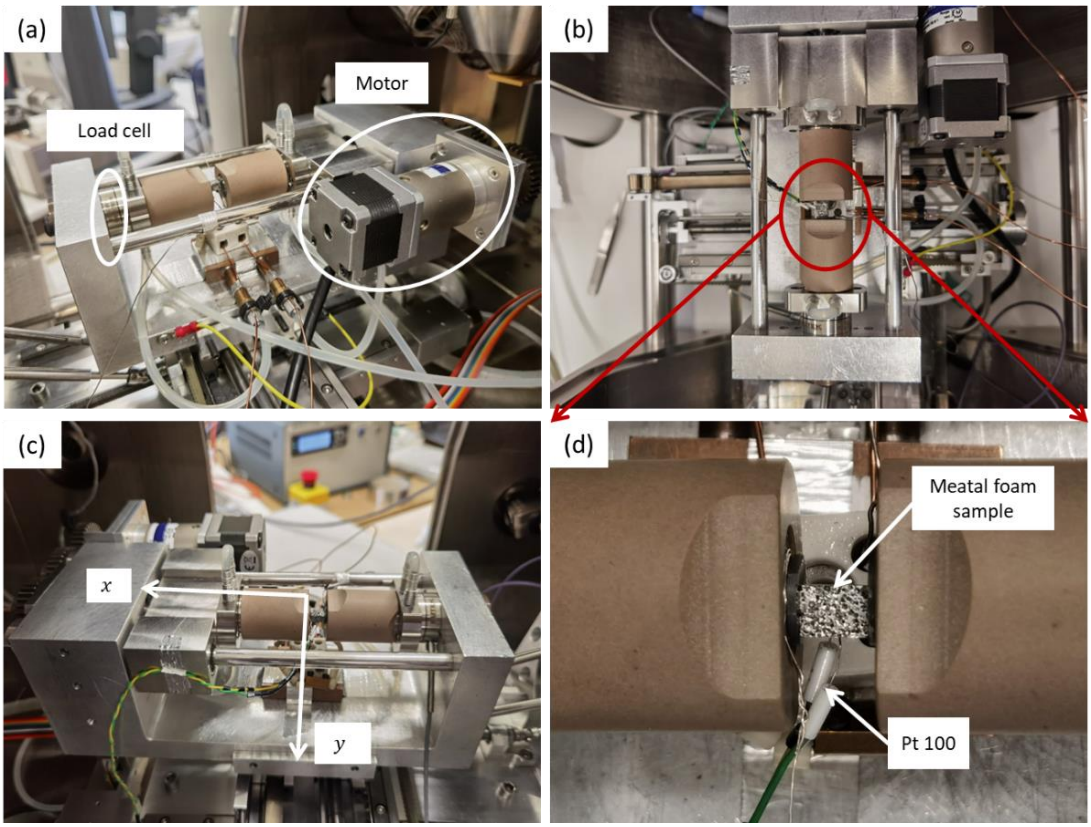

Fig. 2.10 (a) Right view, (b) top view, (c) left view of the custom-built micro compression machine for in situ SEM experiments with (d) zoom on the sample.

The compression tests were performed at a sample temperature of 150 °C to simulate the upper limit of temperature that composite may reach in actual use for domestic heat applications [39] and to investigate its mechanical properties under this extreme condition. The micro machine was designed with components for heating the sample (see Fig. 2.10d and Fig. 2.11). Since vacuum was the SEM imaging condition for this experiment, the heating of the sample could only be accomplished through conduction. Two platinum heating resistance wires, each with a diameter of 0.3 mm and of 1.1 Ω, were wired in series and placed on both sides of the sample to provide symmetrical heating. They were powered by a DC power supply (Model 1687B, BK PRECISION) and were double-wrapped to counteract the magnetic fields that may be generated by the currents in the components, thus avoiding their interference with the electron beam during SEM imaging. SiC was chosen as the material for conducting the thermal energy and heating the sample because of its sufficient thermal conductivity and mechanical resistance. They were made in the form of cylindrical pawns with mirror-polished flat surfaces for good contact with the sample, which ensured a better condition for thermal conduction and less friction between the SiC parts and the sample during compression tests. The SiC pawns and the heating resistance wire were encased in a cylindrical shell made of pyrophyllite ceramics (the brown parts in Fig. 2.10d). This material has

excellent thermal insulation properties that meet the experimental requirements. The shell was heated at 1300°C for about 4 hours, resulting in a yield stress of up to 800 MPa. Water circulation was applied in the system for cooling the stainless-steel machine to make sure that no excessive heat was transmitted to unnecessary parts of the SEM chamber. The cooling circuit was realized by silicone tubes and a chiller centrifugal pump, which delivered a constant temperature of cooling water to the circuit. For the sample temperature at 150 ℃, the cooling water temperature was set at 18 ℃. To monitor the sample temperature and the temperature of heating elements, a Pt100 sensor was glued to the bottom surface of the sample by carbon conductive cement adhesive for measuring the sample temperature, while a thermocouple was inserted into the gap between the SiC pawns and the heating resistance part to measure the oven temperature.

The control and data acquisition of the experiment was done by the home-built software Agnes. A PI (proportional integral)-type controller was used for temperature control. The PI parameters were carefully tuned to avoid any temperature overshoot.

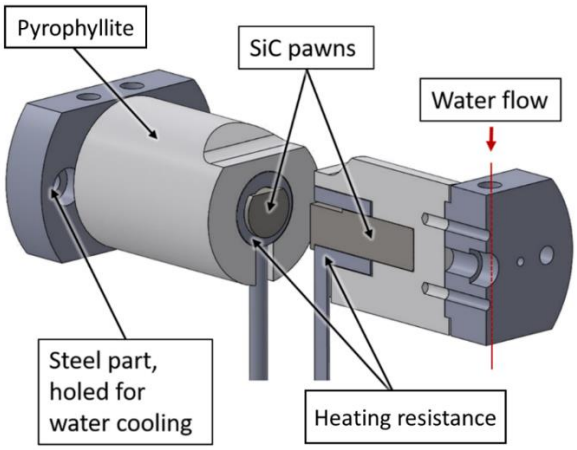

Fig. 2.11 Schematic of the sample heating component of the micro machine [182].

Experimental Protocol

Before the test, the surfaces of the sample in contact with the SiC pawns needed to be carefully polished to make them flat and parallel to ensure continuous contact between the sample and the SiC pawns, which would favor the heat transfer from heated pawns to the sample and to ensure uniform distribution of the applied force during the compression as well. A Pt100 temperature sensor was glued to the bottom face of the metal foam sample by carbon conductive cement adhesive 10-15 min before the test to ensure a secure bond between the sensor and the sample. The water circulation for cooling was set at 18 ℃ and turned on. A preload of 100 N on the force sensor was applied in order to ensure its linear response during the experiment. The sample was then placed between the SiC pawns with the observation surface facing upward. A preload of 2.5 N was added to the sample to

prevent it from dropping. The SEM chamber was closed and pumped to high vacuum. The imaging parameters were selected and verified according to CMV requirements of image grayscale and resolution for performing digital image correlation. In this test, an accelerating voltage of 20 kV and a spot size of 4.5 were chosen as imaging conditions. For heating the sample, the PI parameters were selected to be P = 120 and I = 0.35. During the heating process, the 2.5 N preload applied to the sample would increase due to the thermal expansion of the sample. Therefore, the position of the piston was manually adjusted to maintain the preload at 2.5 N. After the stabilization of the sample temperature at 150 ℃, reference (initial state) images of the chosen ROI were taken before loading. During the compression experiment, the displacement rate was set at 0.002 mm/s. SEM images (with both BSE and SE detectors) were taken after yielding every 100 µm increase in displacement. All the images were in the size of 6144 × 4414 pixels with a pixel size of 1.06 µm. They were compared to the reference image by DIC for measuring the real-time global average axial strain. The load was stopped when the global average axial strain reached the desired value.

2.2.6. In situ uniaxial compression test with optical microscopy

Besides the in situ compression test performed in the SEM, we also performed compression tests with optical microscopy monitoring to enable a multiscale study of the mechanical properties of the metal foams.

The experimental setup is shown in Fig. 2.12. The same micro compression machine as described in 2.2.5 was clamped vertically to an extremely heavy custom-made holder that prevents the machine from parasite movements. The surface of the sample was facing directly to the optical microscope and was frontally enlightened by a ring of blue led directly fixed to the objective. The data during loading was recorded via the home-made software Agnes.

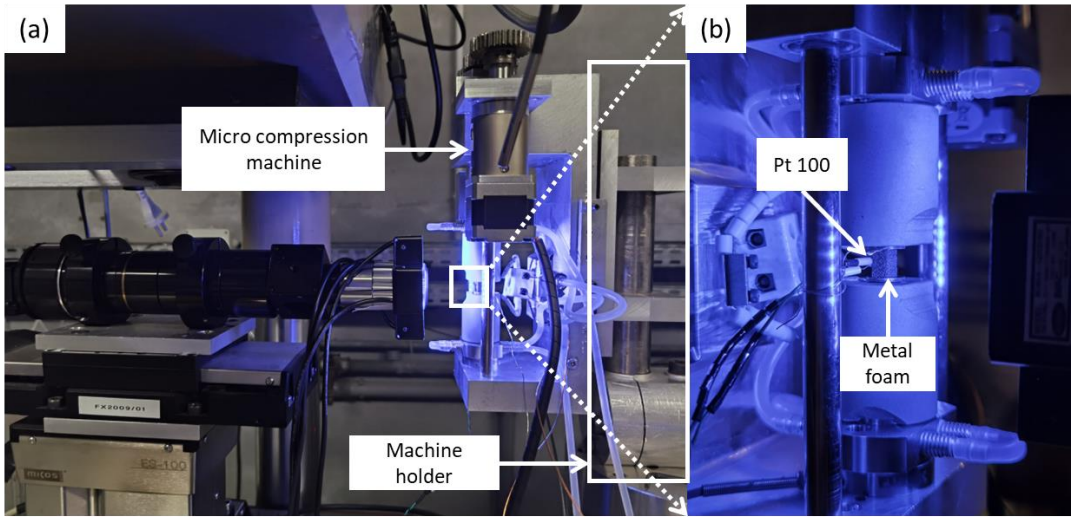

Fig. 2.12 Photo of (a) the global view of the in situ uniaxial compression test setup with an observation by optical microscopy and (b) zoom on the metal foam sample.

The optical microscope system utilized a CCD camera (Prosilica GX 3300, Allied Vision) in conjunction with a x2 objective lens (Mitutoyo) for image acquisition. The resolution of the CCD camera was 3296 × 2472 pixels with a pixel size of 5.5 µm, which indicated that for the optical microscope configuration described above, the recorded image had a pixel size of 2.75 µm, corresponding to a view height of 6.8 mm. The optical microscope was installed on a rotation and three translations motorized micro stages (LS-110 and ES-100, Physik Instrumente). The axis X and Y were parallel to the observation sample surface and the axis Z was the depth normal to the sample surface, with an accuracy of 3 µm and 0.4 µm respectively. The optical system could be moved horizontally along the X-axis and vertically along the Y-axis. While the movement along the Z-axis ensured a proper focus on the observation surface of the sample, with an optimization via an algorithm that maximize the contrast [183]. In addition, the rotation stage allowed the optical system to be properly aligned perpendicular to the sample's surface, preventing translations along X and Y axes from moving the sample surface out of focus. A blue LED light source was selected and mounted around the microscope objective for illuminating the observation surface of the sample at an incident angle of 45°. The small wavelength of blue light (440-490 nm) minimize the systematic error of DIC [184].

The optical microscope image acquisition and control were achieved via a custom-built software Sylvia. It allowed to realize real-time estimation of the plane strain of the observation surface by a simplified DIC procedure, based on a limited amount of measurement points. The principle of DIC used is similar to that introduced in 2.2.3. For applying DIC, measurement points and correlation domains needed to be defined on the reference image. They can be defined automatically as a regular grid covering the whole observation surface, or manually as a limited number of isolated measurement points spread over the region of interest. In our case, 6 to 8 rectangle correlation domains (with side lengths from 15 to 40 pixels) were selected manually with one half on the upper part of the image and the other half on the bottom part. As shown in Fig. 2.13a, 8 correlation domains were selected manually containing necessary contrasts for DIC. The real-time computation of relative displacements at the measurement points enabled us to obtain an initial estimate of the average strain across the observation area. By considering this strain as indicative of the overall sample strain, we were able to adjust the deformation steps to achieve the desired strain values. As presented in Fig. 2.13b, the 8 correlation domains were divided into 4 groups (1-5, 2-6, 3-7, 4-8). As the compression proceeded, the correlation domains relocated to new positions following the deformation of the sample and the mean strain between each group of domains was displayed on the right side of the software interface in real-time. Note that in the case of large deformations, the measurement points and correlation domains may fail to reposition in the deformed image according to the local distribution of grayscale,

such as the domain No.8 shown in Fig. 2.13b. In this case, the measured strain became meaningless with respect to the global deformation of the sample. That's why at least two or three groups of measurement points were used.

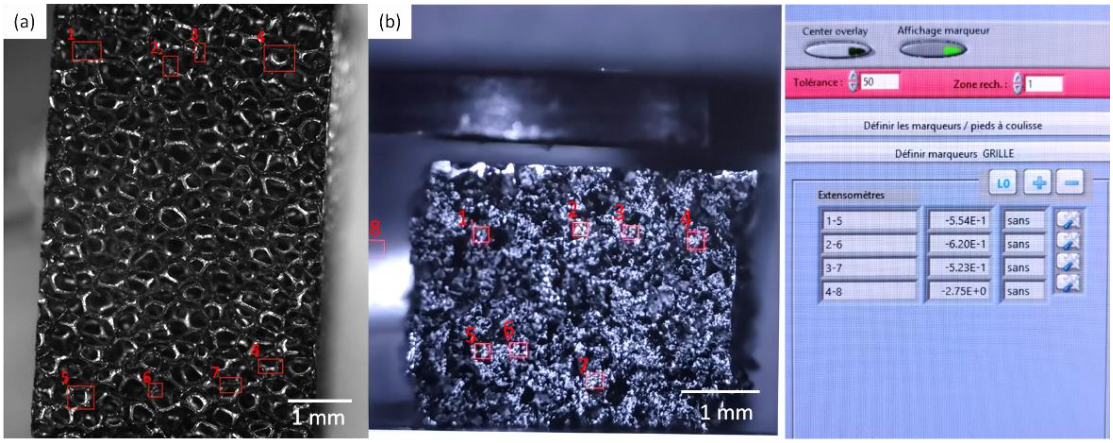

Fig. 2.13 (a) 8 square markers selected on the reference image of a copper foam sample. (b) 8 markers on the deformed image of an aluminum foam sample with mean strain during loading between markers 1-5, 2-6, 3-7 and 4-8 displayed on the right side of the software interface in real-time.

As mentioned above in 2.2.3, sufficiently strong local contrast on the sample surface is required to obtain accurate DIC results. In addition, it is essential that the local contrast (distribution of grayscale) does not excessively change during deformation. In fact, the conservation of the optical flux is the first necessary hypothesis of image correlation. In our case, the metal foam exhibited natural contrasts at both the meso- and macro-scales, thanks to the presence of pores and struts. These contrasts were visible in SEM images as well as in microtomography scans. However, the contrast within the metal foam was insufficient at a smaller local scale. Additionally, when using an optical microscope, the reflective nature of the metal surface led to over-bright areas, causing excessively sharp contrasts and resulting in a loss of local grayscale distribution. Furthermore, during significant deformation of the sample or in cases of intense localization, it was challenging to maintain the conservation of optical flux. This resulted in considerable changes in the local distribution of grayscale throughout the loading process, making it difficult to achieve reliable image correlation.

To solve this problem, artificial markers needed to be introduced to the observation surface of the metal foam sample. These artificial markers make it possible to compare the deformed image with the reference images for calculating the displacement field and strain field by DIC. First, the sample surface was covered entirely with a homogeneous spray of white painting, leaving the surface of the metal foam matt in order to limit the strong reflections of light that may affect the DIC. Airbrush was then used for spraying black paint speckles, serving as markers providing local contrasts for image correlation. The size of the speckles depended on the nozzle diameter of the airbrush and the number of times it is sprayed. In our

experiments, we aimed to keep the size of the speckles within the range of 10 to 50 μm. The photos of metal foam samples after introducing paint speckles as markers are shown in Fig. 2.14. It can be seen that the markers were relatively homogeneously distributed. As shown in Fig. 2.14(e), the size of the black speckles could reach sometimes about one hundred micrometers.

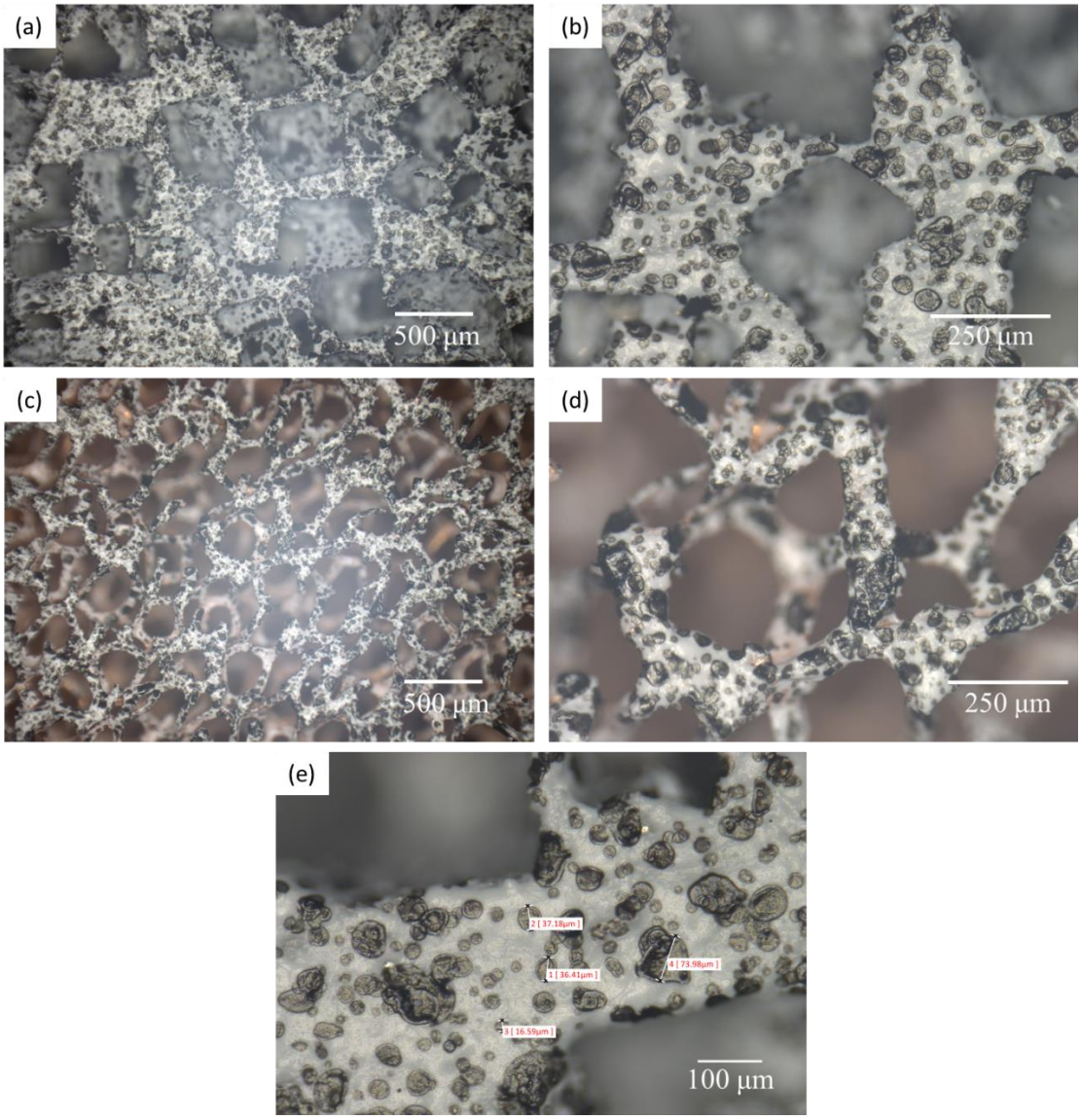

Fig. 2.14 Markers for DIC: paint speckles deposition by airbrush on (a) an aluminum metal foam sample and (c) a copper metal foam sample, with (b) zooming on struts of aluminum metal foam and (d) zooming on struts of copper metal foam. (e) Measurements of the size of black speckles serving as markers for DIC.

Experimental Protocol

First, the micro machine for compression was mounted on the machine holder vertically. Note that before placing the sample, a support was placed between the two SiC pawns to prevent the pyrophyllite shell on top from falling under gravity. A Pt100 temperature sensor was glued to the bottom face of the metal foam sample by carbon conductive cement adhesive 10-15 min before the test to ensure a

secure bond. The water circulation for cooling was set at 18 ℃ and turned on. A preload of 100 N on the force sensor was applied in order to ensure its linear response during the experiment. The sample with the Pt100 sensor glued was then placed between the SiC pawns with the observation surface facing the optical microscope. The focus was adjusted properly and 3 to 4 groups of correlation domains were selected on the reference image via the software Sylvia for tracking the real-time overall strain. After reaching the set temperature of the sample, an image acquisition rate was chosen according to requirements (Table 2.3). The image acquisition was initiated first, followed by the compression at a constant displacement rate. The overall mean strain was calculated via the groups of measurement points and correlation domains chosen, then the load was stopped when the overall strain reached the desired value. The experiment control and data acquisition of the compression test was done by the software Agnes. More experimental details are presented in Table 2.3. The two samples, Cu-to and Al-to, underwent additional X-ray microtomography scans both before and after the compression test. All images recorded during experiments were then analyzed by CMV 2D and 3D for computing the strain maps.

Table 2.3 Sample information and experimental conditions for uniaxial compression tests.

Sample	Size (mm^3)	Marker	T_s (℃)	Load rate (mm/s)	Resolution	Imaging rate
Cu01	6.67×4.49×4.88	Paint speckle	Ambient	0.002	3296×2472	Every 5s
Cu02	7.16×4.47×4.91	Paint speckle	150	0.002	2300×2472	Every 5s
Cu-to	7.18×4.48×4.94	Natural	150	0.002	2055×2472	Every 2s
Al01	6.51×4.60×5.01	Paint speckle	Ambient	0.002	3296×2472	Every 5s
Al02	6.46×4.61×4.98	Paint speckle	150	0.002	2300×2472	Every 3s
Al-to	7.26×4.40×4.82	Natural	150	0.002	2055×2472	Every 2s

* T_s: temperature of sample

2.3. Experimental approach of compression test on massive metal

As mentioned in section 2.1, it was found during SEM observation of metal foams that there were numerous interfaces (secondary phases) and grain boundaries within the cross-sections of the metal foam struts. Previous studies [182, 185] have demonstrated that at 200°C, plastic deformation of polycrystalline aluminum involves strain partitioning within the grains through crystal slip plasticity, as well as along grain boundaries via grain boundary sliding (GBS) mechanisms. In addition, research on high temperature deformation of fine-grained polycrystalline metals, such as magnesium, has shown that GBS may be very pronounced and contribute to grain boundary micro-damage, thus potentially leading to ductile failure [186]. In a previous study [185], GBS was not observed during compression at ambient temperature or 100 °C. The operating temperature of the metal foams used in thermochemical composites is up to 150°C. Therefore, understanding the potential activation of GBS during plastic flow at this temperature is crucial, as it may affect the macroscopic deformation properties of the metal foam. However, studying the

behavior of interfaces and grain boundaries through compression tests on metal foams is challenging due to the size limitations of the metal foam struts. Additionally, estimating the local stress state within the foam structure would be extremely difficult experimentally. To address these limitations, massive aluminum samples were chosen for conducting such experiments.

In this section, the massive aluminum used for in situ SEM uniaxial compression test and sample preparation method are introduced in detail. Electron beam (e-beam) lithography, a technique used to pattern microscopic to mesoscopic features on sample surfaces for performing digital image correlation (DIC) is presented. The experimental setup and procedure of in situ SEM uniaxial compression test on massive metal samples are described in detail.

2.3.1. Material and sample preparation

To perform in situ SEM compression experiments for studying grain boundary behavior during compression at moderate temperature, a low-alloyed aluminum ($AlMn_{0.1}$) containing 0.1% by weight of manganese was chosen as the massive metal sample. It has a relatively low melting point of 667 ℃. The metal foams chosen in this study for serving as host matrix of thermochemical material were in copper, aluminum and nickel. All three of these metals are of the FCC (Face Centered Cubic) crystal structure. Almost pure aluminum, $AlMn_{0.1}$, was chosen as a model massive metal because it was already studied by El Sabbagh [185], who already demonstrated GBS to be active at 200°C. Moreover, the material is also single-phased with relatively low yield stress. From the perspective of estimating the mechanical integrity of a metal foam matrix, such low-strength material allows for exploring the behavior of grain boundaries in the appropriate temperature range (100 – 200°C) at mechanically unfavorable conditions.

The steps of sample preparation are presented as follows:

Sample cutting

The received material was cold-rolled into 1 cm thick plates. Samples were extracted from the core of the plates in the form of a cuboid with a size of 4 mm × 4 mm × 6 mm. The samples were cut with an automatic cut-off machine (Accutom-100, STRUERS) (see Fig. 2.15). The cut-off wheel type was 10S15 with a rotation speed of 3000 t/min and a feed rate of 0.015 mm/s. The size cut should be slightly larger than the target value of the sample so that it could be appropriate after polishing.

Heat treatment

High temperature annealing was needed to recover the lamination texture and to obtain a sufficiently homogeneous microstructure with equiaxed grains and random crystallographic orientations. The heat treatment was carried out in a lab muffle

furnace. The samples were annealed at 500 °C for 20 minutes. The resulting grains presented an average aspect ratio of 1.4, for an average grain size of about 200 µm. The grain size distribution was however quite large, ranging from 50 µm to 300 µm.

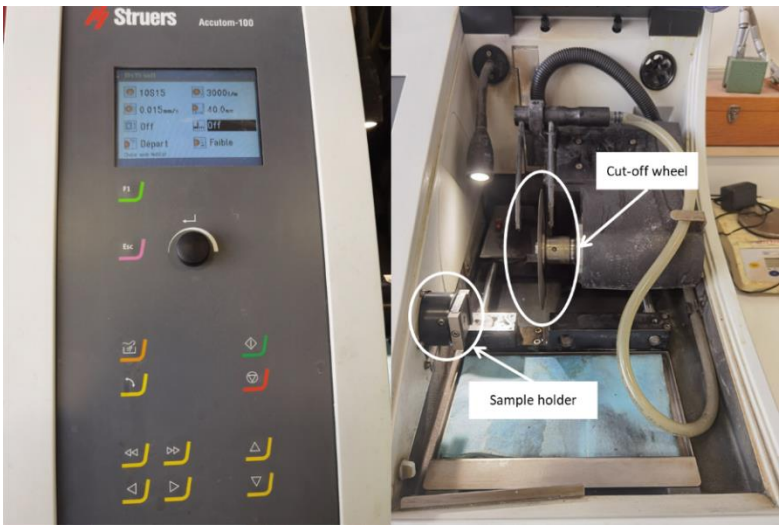

Fig. 2.15 Cut-off machine used for cutting massive aluminum sample in cuboid.

Polishing

For imaging the grain morphology by SEM and for successful e-beam lithography, the observation surface of the sample must be carefully polished. Polishing of the sample consisted of three steps, namely mechanical polishing, electrolytic polishing, and ion polishing. For mechanical polishing, the samples were glued with resin on a custom-built steel polishing base to maintain the parallelism of the surfaces during polishing. As presented in Fig. 2.16, the steel polishing base was heated to the melting point of resin, then the sample was glued.

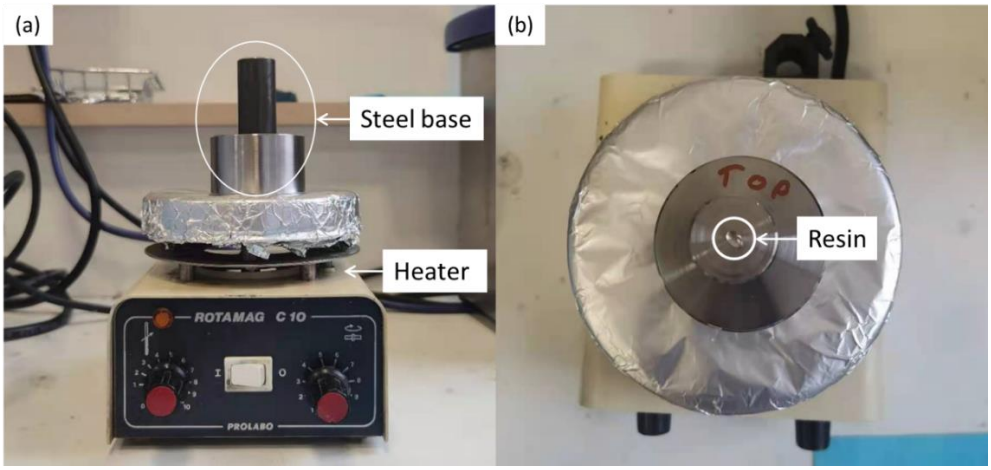

Fig. 2.16 (a) Main view and (b) top view of the steel polishing base heated until the melting of the resin for gluing the sample for mechanical polishing.

Depending on the difference between the actual size of the sample and the target size, the mechanical polishing started with coarse-grained grinding papers, such as P800 or P1200 SiC grinding papers, to flatten all the surfaces so that the sample

became a standard cuboid. Then P2400 and P4000 grinding papers were used for fine polishing. The final step of mechanical polishing was polishing with diamond paste. Diamond paste of 3 µm diameter particles was applied onto the polishing cloth, offering a suspension of diamond particles in alcohol-soluble media. During each step of mechanical polishing, it was important to observe the polished surface under a microscope to ensure that there were no visible scratches. In addition, the polishing cloth for diamond paste should be clean to prevent the introduction of impurities with particles larger than 3 µm, which could leave visible scratches on the polished surface.

Before electrolytic polishing, the samples were rinsed thoroughly in ethanol and dried with compressed air. The electrolyte used was commercial acid STRUERS AII. It should be refrigerated and taken out of the refrigerator shortly before use. The polishing was started at a temperature of about 10 °C. A magnetic stirrer was placed right in the center of the beaker bottom to maintain a continuous vortex during the polishing process. The sample was plunged into the beaker 1 cm below the electrolyte surface, between the center of the vortex and the edge of the beaker, avoiding direct contact between the sample and the beaker. The electrolytic polishing was accomplished at the voltage of 15 V and the current between 1 A and 1.5 A for 20 seconds. The sample was then rinsed in ethanol and then in deionized water for final cleaning.

Usually, the sample surface after mechanical polishing and electrolytic polishing as described above was sufficient for observing the grain morphology. However, in our case, ion polishing was also needed because, after several attempts, it was found that only after ion polishing the surface of the sample was flat enough for e-beam lithography to be completed successfully.

The ion polishing was performed with the machine PECS™ II GATAN under 3 keV for 5 minutes (see Fig. 2.17a and b). In Fig. 2.17c, the sample surface after ion polishing is presented.

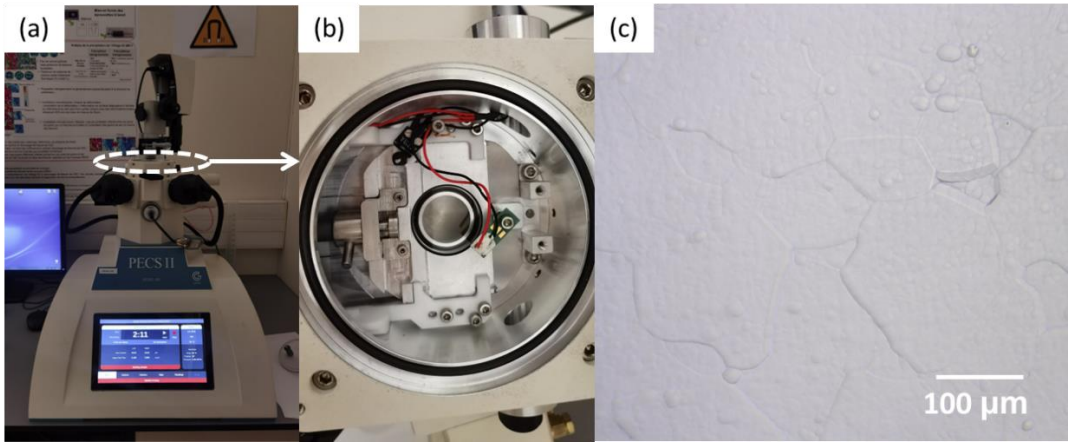

Fig. 2.17 (a) Machine used for ion polishing with (b) a top view of the sample chamber entrance. (c) Optical microscopy image of sample surface after ion polishing.

The obtained sample surface corresponded to both requirements for SEM observation, EBSD (electron backscattered diffraction), and e-beam lithography. Fig. 2.18 shows the grain morphology observed by SEM in Z-contrast mode. It is clearly shown that grain boundaries could be well distinguished after the polishing procedure (Fig. 2.18b). The e-beam lithography technique applied for DIC will be introduced in detail in the next section.

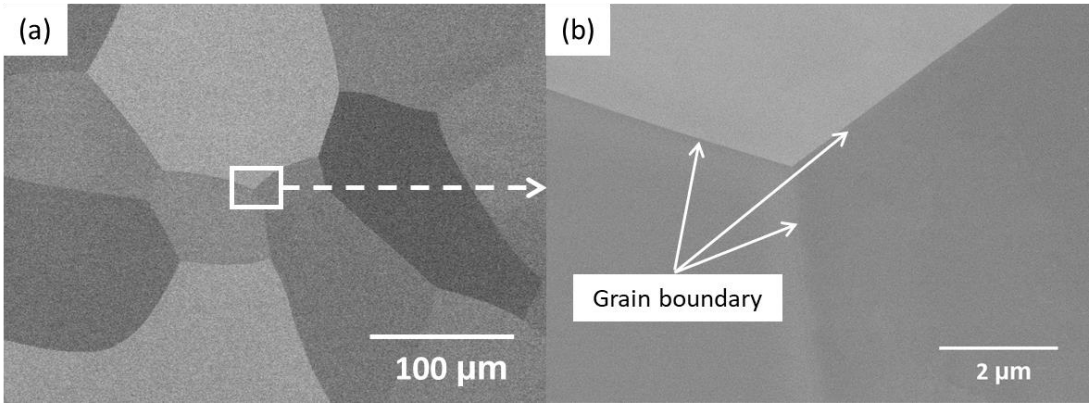

Fig. 2.18 Z-contrast SEM image of (a) (x131 magnification) $AlMn_{0.1}$ sample grain morphology with (b) zoom (x12700 magnification) on grain boundaries between 3 grains.

2.3.2. Electron beam lithography

2D digital image correlation (DIC) technique was used for investigating the plane strain with a special interest in grain boundary behavior during the deformation of the massive aluminum sample via the software CorrelManuV (CMV, introduced in section 2.2.3). As mentioned in section 2.2.3, sufficiently local contrasts on the observation surface are required for applying the DIC technique and for reducing systematic errors. In our case, unlike metal foams, the single-phased massive aluminum sample did not provide natural contrasts. Therefore, the technique of e-beam lithography was applied to realize surface patterns in the selected ROI of the sample surface for obtaining artificial local contrasts.

E-beam lithography (EBL) has been widely applied in micromechanical studies for patterning nanoscale, microscale or mesoscale structures and features on substrates. It uses a focused electron beam in a scanning electron microscope to form patterns on a resist layer. Thanks to the focused electron beam, it possesses advantages such as high spatial resolution, flexibility of the pattern geometry, capability of reproducing the pattern and achieving extreme positioning accuracy [187-190].

This section introduces the e-beam lithography process used in this work, which has been developed at the Laboratoire de Mécanique des Solides over the past two decades. The process was designed for creating custom patterns on sample surfaces with high local contrast, enabling digital image correlation with CorrelManuV (CMV). The e-beam lithography technique has been adapted to the specific scale of interest, taking into account factors such as sample size and its

microstructure. In this work, new patterns were designed and realized. In addition, we improved some steps of the process and determined the appropriate parameters required for the optimization of the patterns obtained by e-beam lithography using SEM.

As shown in Fig. 2.19, the process of e-beam lithography in our study included 5 steps before getting the final-state sample.

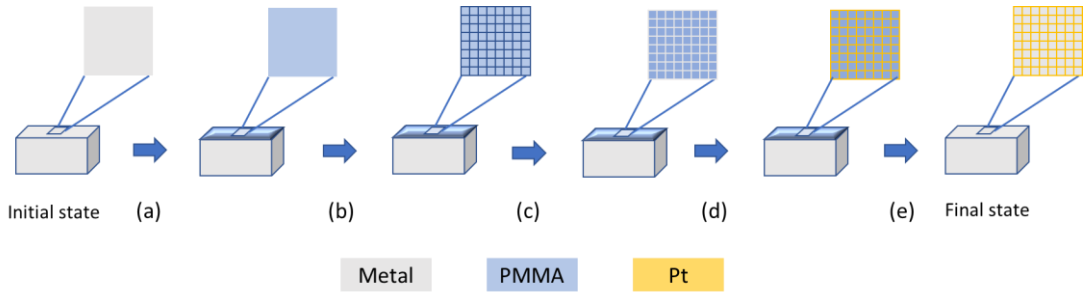

Fig. 2.19 Flow diagram of the e-beam lithography process. (a) Spin-coating of PMMA (b) E-beam exposure (c) Pattern developing (d) Thin-film deposition of Pt (e) Dissolution of PMMA.

(a) Spin-coating of PMMA

The first step of e-beam lithography involves exposing a resist layer to electron irradiation, following a predetermined pattern. A widely used e-beam positive resist is polymethyl methacrylate (PMMA) polymer which changes its solubility upon irradiation of the electron beam. The electron struck upon the resist causes local chain scission, making the area exposed to the electron beam more soluble in the developer [188, 190]. Therefore, our first step of e-beam lithography was the deposition of polymer PMMA on the sample surface. It was important to keep the surface of the sample extremely clean and flat after ion polishing so that the thin layer of PMMA deposited on the surface could be sufficiently uniform. The PMMA used in our case was a commercial solution diluted at 5 g/L. The sample was glued firmly at the center of the spindle plate of the spin coater and 2 or 3 drops of PMMA were loaded to the surface of the sample. The spinning was accelerated until it reached the desired angular speed of 4500 rpm and remained at this rotation speed for 90 seconds. Note that the thickness of the PMMA layer strongly depends on the spinning angular speed and the spinning duration. It is important to control the thickness of the PMMA layer since it may affect the success of the following steps of the e-beam lithography. The PMMA deposited onto the sample surface was then polymerized at 140°C for 40 minutes.

Fig. 2.20 presents the sample surface after PMMA deposition. A distinct iridescence can be observed near the borders of the sample due to the local thickness variation of the PMMA layer. The absence of such features in the central part of the surface can be considered as a criterion for the success of PMMA deposition.

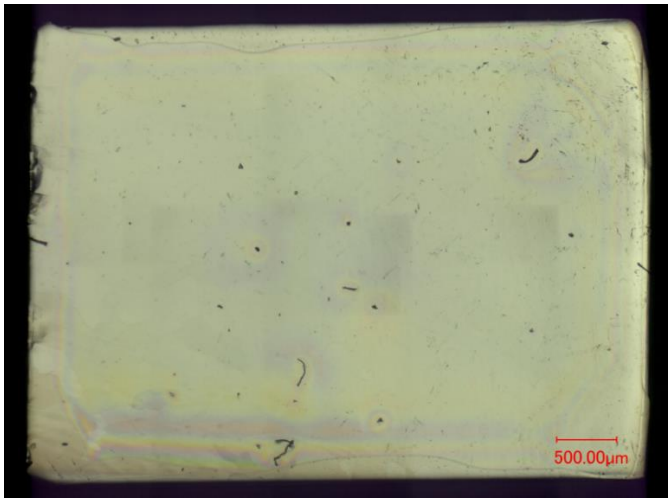

Fig. 2.20 Sample surface after deposition of PMMA under optical microscope.

(b) **E-beam exposure**

The coated sample was then placed in the SEM chamber for electron-beam irradiation. The exposure path of the focused electron beam following a predefined pattern was accomplished with our FEI QUANTA 650 FEG-ESEM, which is equipped with a nanolithography module (ELPHY Quantum, RAITH GmbH). A beam blanker with a switch on/off time in the nanosecond scale was used. The sample was placed on a universal sample holder manufactured by RAITH. It comprised a calibration standard, named Chessy, and an integrated Faraday cup for measuring the total beam current at the sample surface (see Fig. 2.21).

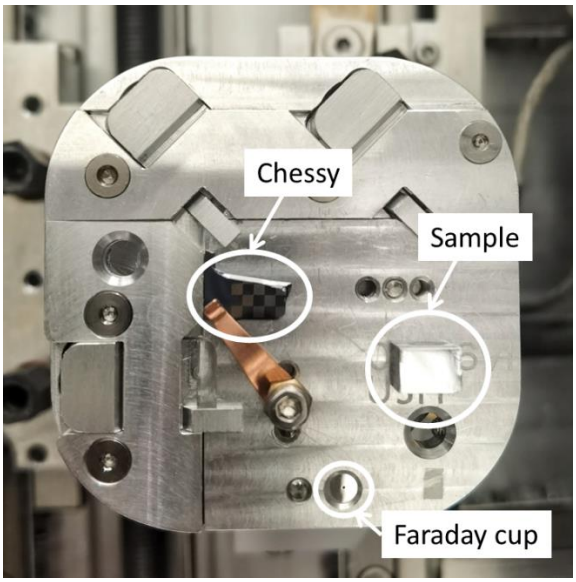

Fig. 2.21 The universal sample holder used for e-beam lithography with SEM, comprising a calibration standard (Chessy) and a Faraday cup.

Different e-beam conditions were applied to find out the most suitable ones for our sample and designed pattern. The conditions of the beam chosen are listed in Table 2.4.

Table 2.4 Electron beam settings for forming patterns on the PMMA

Spot Size	Working Distance (mm)	Accelerating Voltage (kV)
6	8	25

Based on experience gained from previous experiments, the digital image correlation via CMV requires marker patterns to contain at least 6 pixels in the scanning direction of the electron beam. Therefore, the electron dose and pattern step size must be appropriately chosen, otherwise, the number of pixels may not reach the required level, even at the highest imaging resolution, thus affecting the accuracy of the DIC. To obtain a clear pattern with the proper size, different doses and step sizes were tested. The chosen parameters are shown in Table 2.5.

Table 2.5 The selected electron dose parameters for e-beam lithography.

Line			Area		
Step size (μm)	Dose (pC/cm)	Dwell time (ms)	Step size (μm)	Dose (μC/cm^2)	Dwell time (ms)
0.02	8400	0.0091	0.04	165	Every 5s

Fig. 2.22 presents four patterns designed and realized in our work, which were grids, crosses, double-grids and diamonds.

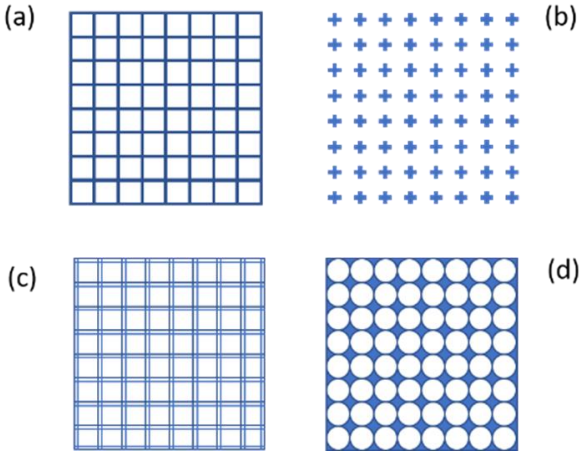

Fig. 2.22 Schematic of various simple patterns designed for e-beam lithography. (a) Grids (b) Crosses (c) Double-Grids and (d) Diamonds.

(c) Pattern developing

After irradiation of the PMMA resist layer with the e-beam following a given pattern, the sample was immersed in the developer solvent. This developer solvent, comprising 35% vol. methyl isobutyl ketone (MIBK) and 65% vol. isopropyl alcohol (IPA), caused the dissolution of the exposed PMMA while leaving the unexposed regions intact. After rinsing the sample with ethanol and drying, the surface was observed by optical microscopy to verify if the patterns were clearly developed. As presented in Fig. 2.23, we tried different types of patterns on the sample surface. After irradiation exposure and developing we could clearly observe the patterns under an optical microscope. If any of the two steps, exposure and developing,

didn't proceed smoothly, there may be consequences such as those shown in Fig. 2.23b and d, in which case we need to remove all PMMA from the sample surface, polish the sample again, and restart the whole e-beam lithography procedure from scratch. It can be seen that the successful patterns should have distinct boundaries and proper right angles as shown in Fig. 2.23a and c. Only in this case, we can move on to the next step.

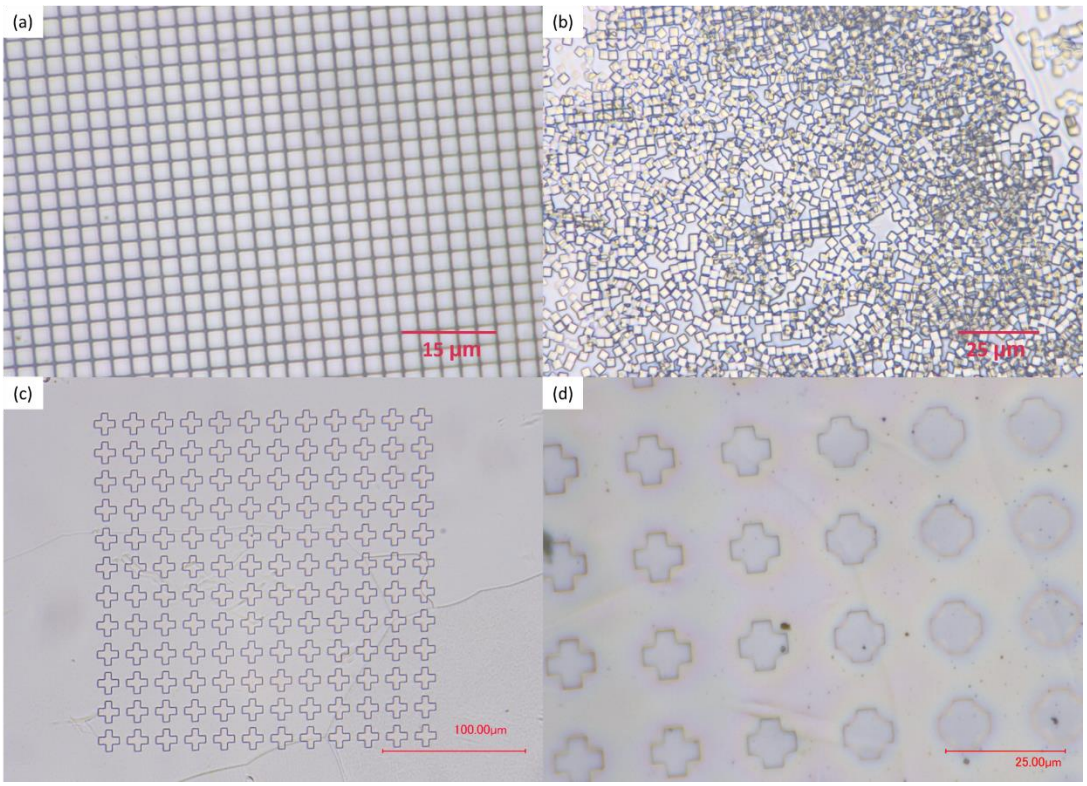

Fig. 2.23 Optical microscope image of successful (a) grids and (c) cross pattern after exposure and developing process, while unsuccessful patterns such as (b) the grids displaced after developing process and (d) the crosses with blurred and rounded boundaries.

(d) Thin-film deposition of Pt

The deposition of platinum thin film onto the previously developed patterns was achieved by sputtering and evaporation of platinum. Plasma sputtering allows for very good initial adhesion of a very thin Pt film, then evaporation ensures homogeneous deposition of a thicker Pt film. Platinum was chosen instead of gold (a commonly used metallization material) due to the risks of alloying the gold and the aluminum substrate. The platinum was deposited in the developed patterns, that is to say in the dissolved spaces of the irradiated polymer PMMA. Therefore, the platinum adhered directly to the sample surface revealed by the developing process, as well as on the rest of the intact PMMA, as illustrated in Fig. 2.24. The sputtering of Pt was performed on a standard SEM metallization coating machine by BIO-RAD and the evaporation of Pt was performed with the Auto 306 thermal evaporator by EDWARDS (see Fig. 2.25). One of the differences between the sputtering coating and evaporation coating was that evaporation was highly

directional, while sputtering was non-directional. Firstly, a platinum layer with a thickness of 1 nm was deposited by sputtering, then the platinum layer with a thickness of 6 nm was deposited by evaporation. With the appropriate dose of e-beam, it formed a trapezoid with a narrow top and a wide bottom in the PMMA layer after being exposed to the e-beam. Therefore, after the two deposition processes described above, there existed a platinum layer with a thickness of only 1 nm on the corners and sidewalls of the PMMA voids, as circled in red in Fig. 2.24. This very thin lateral Pt film ensured the penetration of the second dissolving solution, aiming at removing the rest of the intact part of the PMMA in the next and final step.

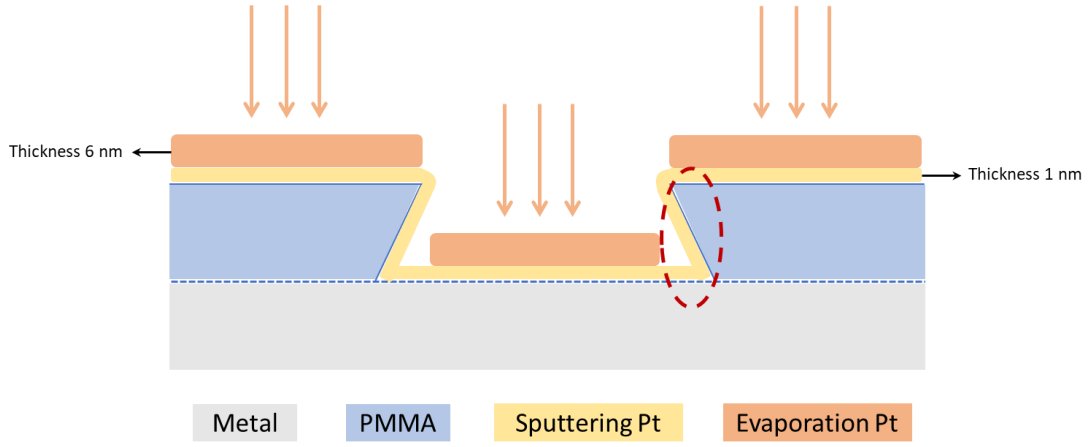

Fig. 2.24 Schematic of sputtering coating and evaporation coating of Pt.

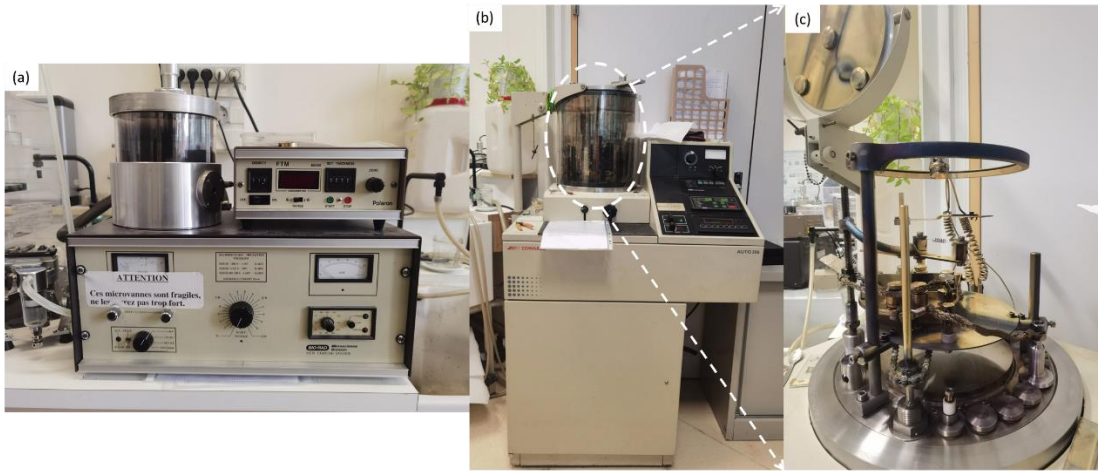

Fig. 2.25 Photos of (a) the coating system used for Pt sputtering and (b) the thermal evaporator used for Pt evaporating deposition.

(e) Dissolution of PMMA

The final step of e-beam lithography was to dissolve the rest of the PMMA resist layer so that only the thin film of Pt (thickness of about 7 nm), which formed the designed pattern, remained on the sample surface. The sample was finally put into a beaker within an ultrasonic cleaning bath with ethyl acetate as the dissolving agent.

Then the sample with Pt patterns deposited on the surface was observed using SEM as shown in Fig. 2.26. The brighter parts in the images are the patterns in platinum achieved by the e-beam lithography and the darker parts in the background are the sample surface (aluminum).

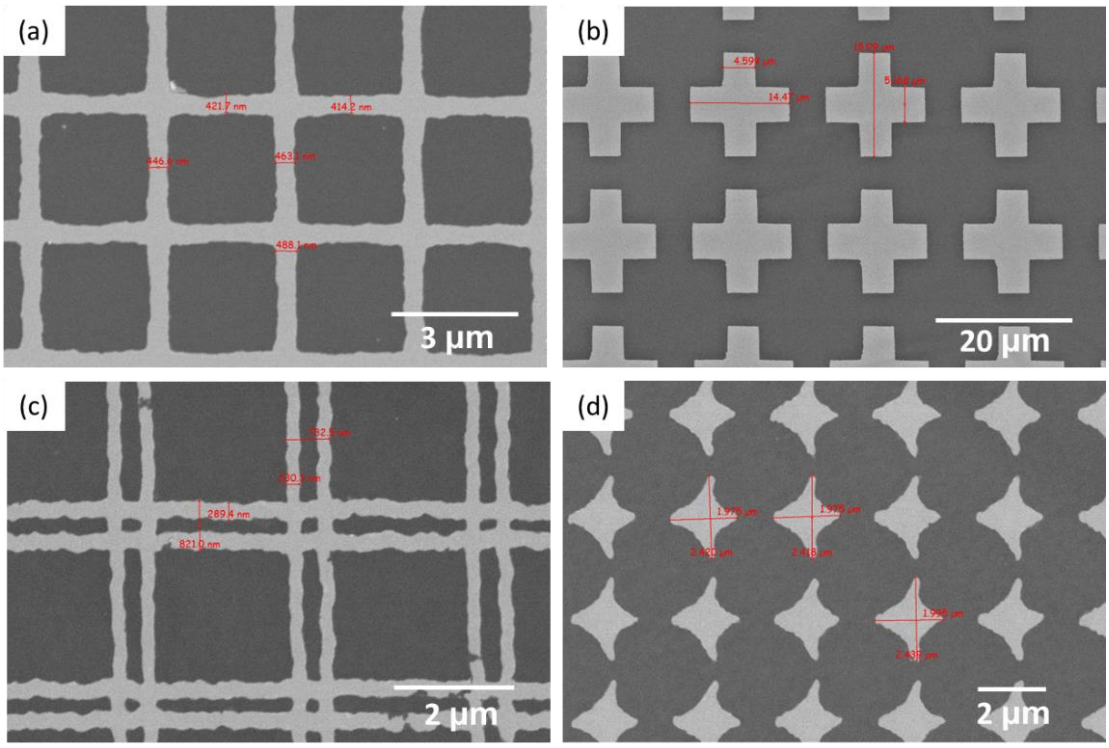

Fig. 2.26 SEM (BSE) image of the multiscale patterns designed and realized by e-beam lithography for DIC, with (a) (x10000 magnification) Grids (b) (x1600 magnification) Crosses (c) (x14000 magnification) Double-Grids and (d) (x8000 magnification) Diamonds.

It is important to note that even if the patterns were correct after exposure and developing, it does not necessarily mean that the e-beam lithography would be successful after the metal deposition and the PMMA dissolution processes.

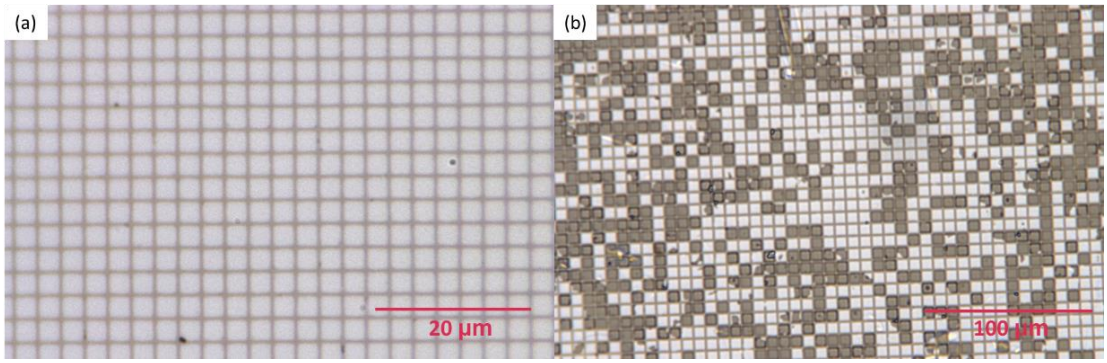

Fig. 2.27 Optical microscope images of (a) successful pattern of grids and (b) unsuccessful pattern of grids formed on the sample surface after Pt deposition and PMMA dissolution processes.

In Fig. 2.27a, a successful case, after Pt deposition and dissolution of PMMA observed with an optical microscope, is shown, in which all the PMMA that was not exposed to the e-beam dissolved while taking away the Pt layer deposited on it.

While as shown in Fig. 2.27b, the PMMA that should be removed was not completely dissolved due to the inappropriate thickness of the PMMA layer or the unsuitable electron beam parameters during the exposure process, resulting in the excess Pt layer deposited on PMMA remaining on the sample surface and thus leading to an unsuccessful pattern.

In our case, we selected two regions of interests (ROI) with different dimensions, which were ROI-macro at the size of 3 mm × 3 mm marked by crosses (shown in Fig. 2.28a) and ROI-micro (centered in the middle of ROI-macro) at the size of 1 mm × 1 mm marked by grids (shown Fig. 2.28b). The distance between two adjacent crosses was 125 µm while the grids were with a pitch of 5 µm. The crosses in ROI-macro were used to compute the overall macroscopic strain of the sample, while the grids in ROI-micro were used to calculate the local strain fields at the correlation points selected at grid intersections. The strain fields computed by DIC using this combination of patterns are presented in section 2.4.3.

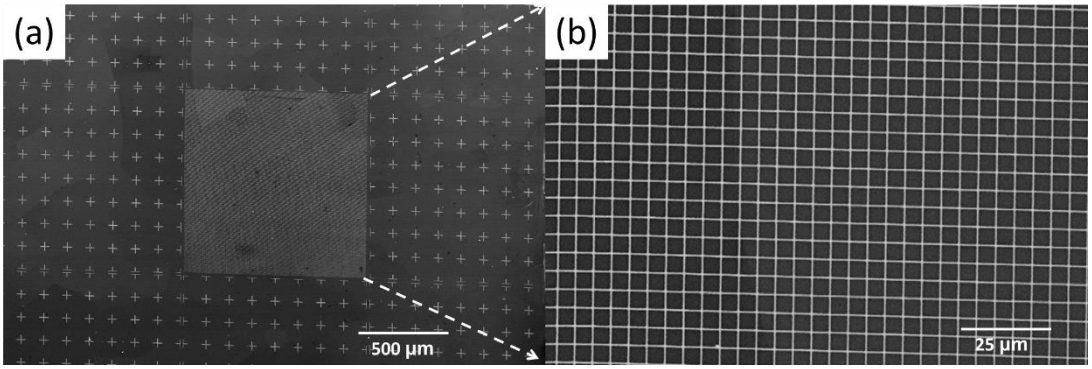

Fig. 2.28 SEM image of the two-scale patterns of (a) (x42 magnification) crosses for computing the strain field in ROI-macro and (b) (x568 magnification) grids for computing local strain field in ROI-micro.

Once the patterns were successfully deposited on the sample surface by e-beam lithography, the sample must be carefully stored to prevent any damage to the observation surface.

2.3.3. In situ SEM uniaxial compression test

In situ SEM uniaxial compression test was then performed on the $AlMn_{0.1}$ sample with patterns deposited on the ROI of the sample surface for investigation of the deformation mechanism of massive metal of aluminum and especially the behavior of interfaces and grain boundaries during deformation.

The sample was in the form of a cuboid with the size of 4 mm × 4 mm × 6 mm. The experiment was performed with the same micro compression machine described in 2.2.5, but with several changes which will be described as followed. The force was measured by a load cell (LTH300, FUTEK) with a capacity of 250 lb (1112.06 N). The compression tests were controlled via displacement with the home-built software Agnes. A standard DC motor (3557K-024C, FAULHABER) with a no-load speed of

4800 rpm combined with a gearhead was used for powering the displacement of the crosshead for the compression of the sample. The displacement was measured with a displacement sensor (LVDT Position Sensor, Solartron Metrology). An external LVDT (linear voltage displacement transducer) was chosen over the use of an extensometer because LVDT measures more accurately since it avoids end effects [130]. The setup is presented in Fig. 2.29. After mounting the setup onto the SEM stage, the stage needed to be adjusted to the lowest position in height before closing the SEM chamber to prevent any possible contact of the experimental setup with the SEM column when closing the chamber door (see Fig. 2.29a). The compression test was performed at a sample temperature of 150 ℃. As shown in Fig. 2.29b, a Pt100 temperature sensor was glued to the sample side surface by carbon conductive cement adhesive for measuring its temperature during the experiment without damaging the sample surface for observation or changing its stress state. The step of gluing the sensor to the sample required extreme caution to avoid touching the surface of the sample to be observed. At the beginning of the experimental design, we worried that the Pt100 glued to the sample could eventually detach during the deformation of the sample, which would affect the monitoring of the sample temperature. Therefore, an infrared pyrometer was initially integrated into the micro compression machine system with the Pt100. However, subsequent experiments revealed that the Pt100 temperature sensor was capable of accurately measuring the sample temperature without detaching during the entire experiment. As a result, the use of a pyrometer, which complicated the assembly process, was abandoned. The Pt100 temperature sensor alone provided sufficient temperature measurement, eliminating the need for an additional temperature measurement method as a backup. It is also worth noting that metal wires should be used to ground the sample, as shown in Fig. 2.29c. Otherwise, the imaging quality would be seriously affected, especially when using the BSE detector. A photo of the sample surface after loading is presented in Fig. 2.29d.

Experimental Protocol

First of all, the Pt100 temperature sensor was glued to the side surface of the sample by carbon conductive cement adhesive with great caution 10-15 min before the test and dried naturally to ensure a secure bond. The water circulation for cooling was set at 18 ℃ and turned on. A preload of 100 N on the force sensor was applied in order to ensure its linear response during the experiment. The sample with the Pt100 sensor was then placed between the SiC pawns with the observation surface facing upward. A preload of 15 N was added to the sample to prevent it from dropping. Note that the surface of the sample in contact with the SiC pawns needed to be carefully polished to make it flat, so as to ensure close contact between the sample and the SiC pawns, which made the heat transfer more effective, and also to ensure that the force applied on the contact surface to be

uniform during the compression. Then the SEM chamber was closed and pumped to a vacuum state with chamber pressure reaching at least the order of magnitude of 10^{-2} Pa. Then, the oven temperature was set at 167 ℃ for the sample temperature to reach 150 ℃ at a rate of 0.2 ℃/s. For heating the sample, the PI parameters were selected to be P = 120 and I = 0.35. During the heating process, the preload applied to the sample would increase due to the thermal expansion of the sample. Therefore, the displacement needed to be manually adjusted to maintain the preload. After the stabilization of the sample temperature at 150 ℃, the appropriate imaging parameters were selected and verified according to CMV requirements of image grayscale and resolution for performing digital image correlation. In this test, an accelerating voltage of 15 kV and a spot size of 4.5 were chosen for imaging. Reference (initial state) images of ROI were taken before loading. Afterward, the compression experiment began and was maintained at a displacement speed of 0.001 mm/s. SEM images (with both BSE and SE detectors) were taken of the ROI every 30 μm increase in displacement. All the images were in the size of 6144 × 4414 pixels. They were compared to the reference image for measuring the global average axial strain. The load was stopped when the global average axial strain reached the desired value.

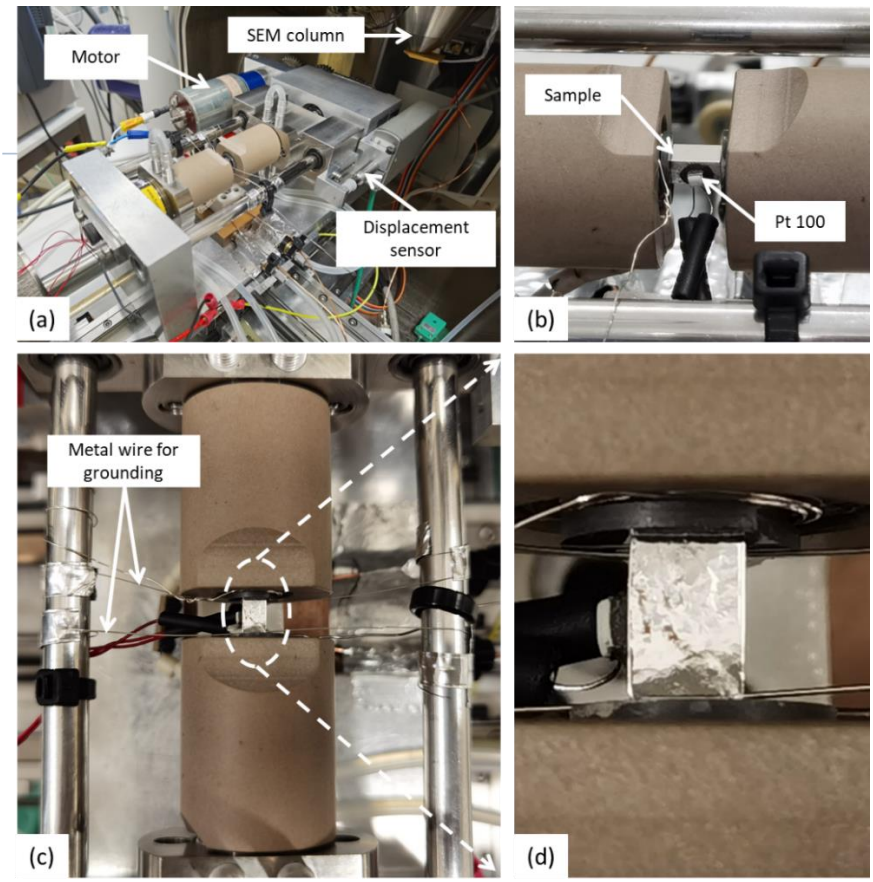

Fig. 2.29 Photos of in situ SEM uniaxial compression test setup for performing on $AlMn_{0.1}$ massive sample. (a) The overview of the experimental setup with DC-motor and LVDT. (b) Zoom on the sample (before loading) with a Pt100 temperature sensor glued to the side of the sample. (c) Top view of the setup focusing on the sample and (d) zoom on the sample surface after loading.

2.4. Characterization and analysis of metal foam

In this section, the structural characterization results of different kinds of metal foams obtained by SEM and EBSD are first presented. Then, the macroscopic, mesoscopic and microscopic deformation mechanism studied by in situ uniaxial compression test on metal foam at ambient temperature as well as at 150 ℃ with high-resolution camera and SEM are described. 2D and 3D DIC analyses were accomplished by using images recorded during in situ tests and by 2D projection images of the metal foam samples. The final part of this section presents the microscopic deformation mechanisms summarized through results obtained from the compression test on bulk aluminum samples and DIC analysis, with a particular focus on grain and grain boundary scales.

2.4.1. Structural characterization of metal foam

As mentioned in 2.2.2, the structural and surface morphology characterization of the metal foam was studied by using scanning electron microscopy (SEM). In this section, the structural properties of the metal foams used in the study are presented.

First of all, in order to describe clearly in the following parts, the nomenclature of the structural elements of the metal foam, such as the pore (or cell), cell window (or cell face) and strut (or ligament) are introduced in Fig. 2.30.

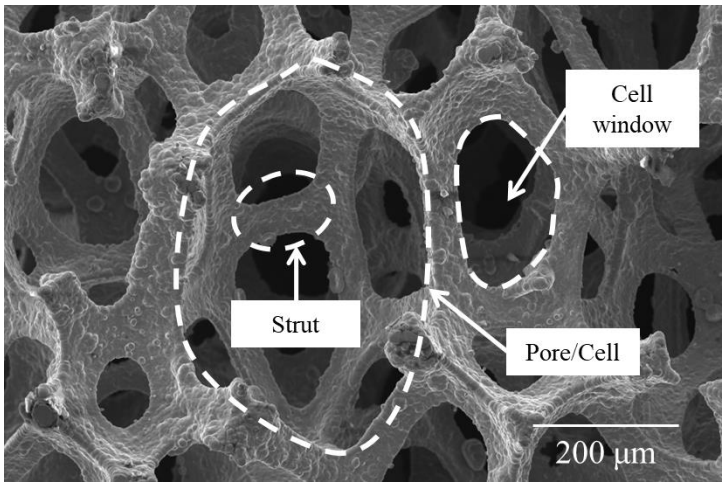

Fig. 2.30 SEM image (x127 magnification) of bulk nickel foam used in this study, with essential elements (pore/cell, cell window and strut) of open-cell metal foam marked in white.

The photographs of nickel foam, copper foam and aluminum foam are shown in Fig. 2.31a, b and c, respectively. It can be seen that the nickel foam and copper foam had more homogenous pore distribution and higher porosity, while the aluminum foam had lower porosity and highly varied pore size. This was consistent with the data provided by the supplier on the properties of the metal foam presented in Table 2.1, where nickel foam had a porosity of 96% and copper foam had a porosity of 93.5%, while the porosity of aluminum foam was only 40%. Under daylight, the nickel foam was silvery white, the copper foam was orange, and the aluminum foam

had a darker overall color than the nickel foam.

The bulk metal foam samples were observed by SEM and the BSE images are presented in Fig. 2.31d, e and f of nickel foam, copper foam and aluminum foam, respectively. The images were with the same magnification of x40 and the pixel size of these three images was also the same (0.52 μm). From the images, we can conclude that these metal foams were all open-cell metal foams. It is also clear that, for nickel foam and copper foam, not only the pores and pore size were evenly distributed, but also the thickness of the strut. Conversely, for aluminum foam, the pore shape varied from cuboids to spheres and it had a wide range of pore size distribution, from tens of micrometers to six or seven hundred micrometers. What's more, there were significant differences in the thickness and form of the aluminum foam struts. Some of the struts took the form of thin sheets, while others were large beams of solid aluminum with considerable thickness. These differences in structure will affect deeply the mechanical behavior of metal foams under loading.

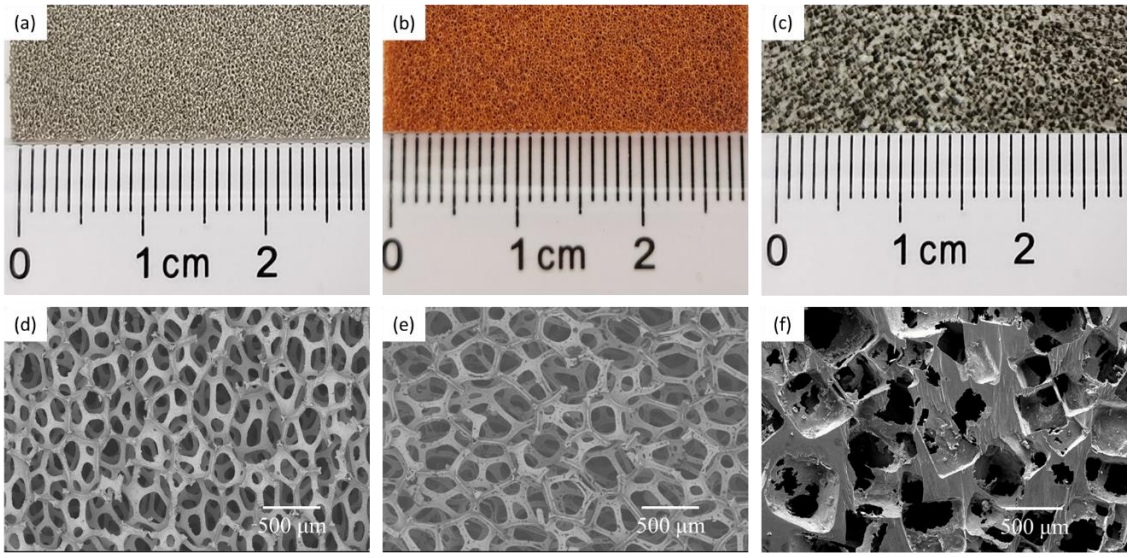

Fig. 2.31 Photo of (a) nickel foam (b) copper foam (c) aluminum foam and Backscattered Electron (BSE) image (x40 magnification) of (d) nickel foam (ρ/ρ_s = 0.04) (e) copper foam (ρ/ρ_s = 0.04) and (f) aluminum foam (ρ/ρ_s = 0.27).

The microstructure of metal foam samples are presented in the following part. For observing the microstructure of open-cell metal foam, appropriate polishing methods were applied. Mechanical polishing was used for flatting the observation surface and then the cross-section ion polishing was applied for revealing the surface microstructure, as described in 2.2.2.

In Fig. 2.32, the microstructure of copper foam is presented. The copper foam had a copper content of over 99.8%. Images shown in Fig. 2.32 were cross-section images of the copper metal foam struts. It can be clearly seen that the struts of copper metal foam were hollow and the shape of the cross-section can be seen as a triangle with three sides recessed inwards. From Fig. 2.32a and b, we can clearly see

the grains and grain boundaries on the cross-sections of struts.

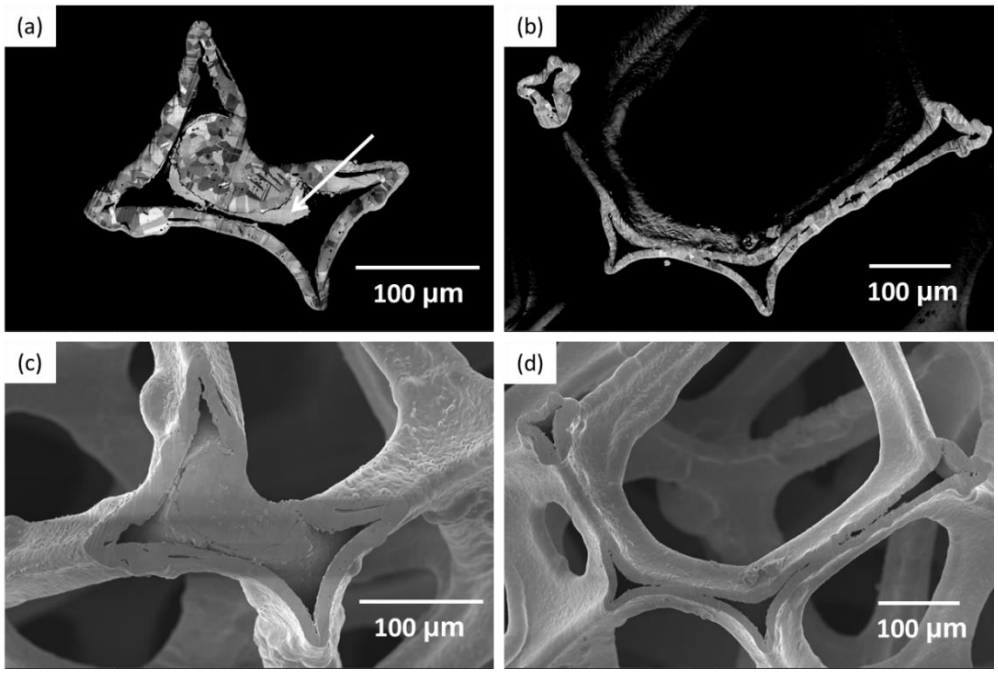

Fig. 2.32 (a) BSE image (x318 magnification), (b) BSE image (x212 magnification), (c) SE image (x318 magnification) and (d) SE image (x212 magnification) of the cross-section of copper foam strut, with (a) and (c) images of the same spot while (b) and (d) images of another spot.

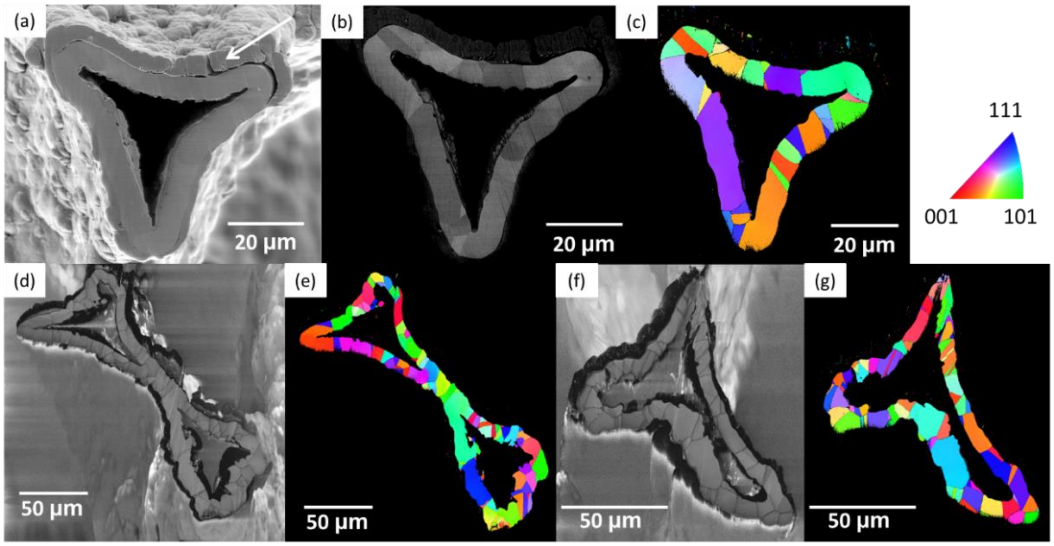

Fig. 2.33 (a) (d) (f) SE images, (b) BSE image, and (c) (e) (g) EBSD maps color-coded with IPF (inverse pole figure) coloring of strut cross-section of nickel foam at three different spots. The IPF orientation scale is shown on the upper right.

A similar microstructure was found in nickel foam. The nickel foam had a nickel content of over 99.5%. As shown in Fig. 2.33, the nickel foam struts were also in the shape of a triangle and were hollow as well. From the EBSD maps of struts cross-sections at three different spots, presented in Fig. 2.33c, e and g, the crystallographic structure of the nickel foam can be clearly seen. On each cross-section of struts, we can see grains with different orientations and distinct grain

boundaries. It is worth noting that for both nickel and copper foam, the walls of hollow struts were composed of strings of individual grains, and as a result, the grain boundaries traversed the entire thickness of the strut walls.

For aluminum foam, the microstructure was quite different from the other two kinds of metal foam described above. First of all, unlike the copper foam or the nickel foam, the struts of aluminum foam were fully solid, surrounding the pores like walls with different thicknesses. In addition, different foreign phases were observed via the BSE image of the cross-section of the strut, as shown in Fig. 2.34a, c and d. Especially when zooming on the cross-section of the strut (see Fig. 2.34d), the Z-contrast imaging provided by the BSE images clearly shows that the aluminum foam presented several phases.

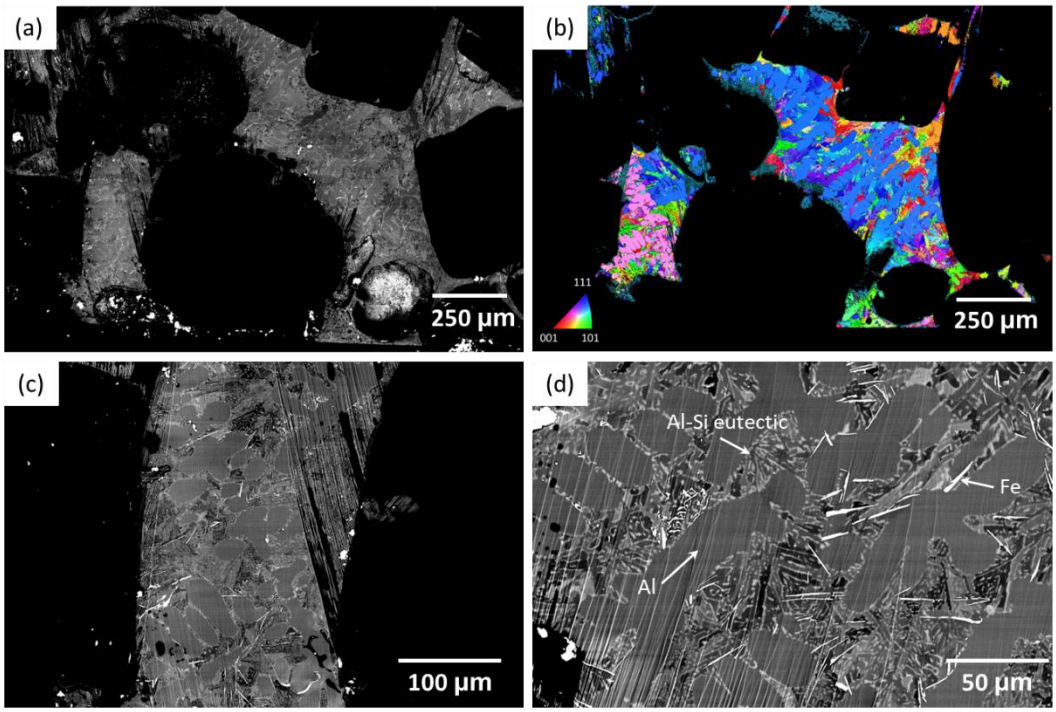

Fig. 2.34 (a) BSE image and (b) EBSD map color-coded with IPF coloring (with the insert of IPF color code) of a strut cross-section of aluminum foam, with (c) and (d) BSE image of zoom on the strut.

For identifying each phase and for proceeding with the composition analysis of the aluminum foam, the elemental analysis was conducted using the energy-dispersive X-ray spectroscopy (EDS) technique. The results demonstrated that the aluminum foam was not made of pure aluminum, but contained other elements such as silicon and iron. For more detail on Al-Si alloys, the readers are addressed to [191], who presented the microstructure and mechanical properties of Al-Si alloys. The specific constituent elements and mass fractions are shown in Table 2.6 and the spectrum obtained is shown in Fig. 2.35. The different phases determined by EDS are indicated in Fig. 2.34d. The phase of aluminum, Al-Si eutectic and Fe-containing intermetallic phase (bright, needle-like) can be observed in the microstructure of the strut. Therefore, the so-called aluminum foam was actually a foam of an

aluminum alloy, but for simplification, we still use the term “aluminum foam” to refer to this metal foam used in our study. Even though the foam was not made of pure aluminum, since it was its porous structure (especially the appropriate pore size) that we were interested in for this study, the purity was not essential. Besides, by studying such materials, we are able to gain insights into future industrial applications, particularly in the fabrication of thermochemical composites based on metal foam using recycled aluminum.

Table 2.6 Composition of aluminum foam.

Element	Symbol	Wt%
Aluminum	Al	85.73
Silicon	Si	12.40
Oxygen	O	1.31
Iron	Fe	0.55

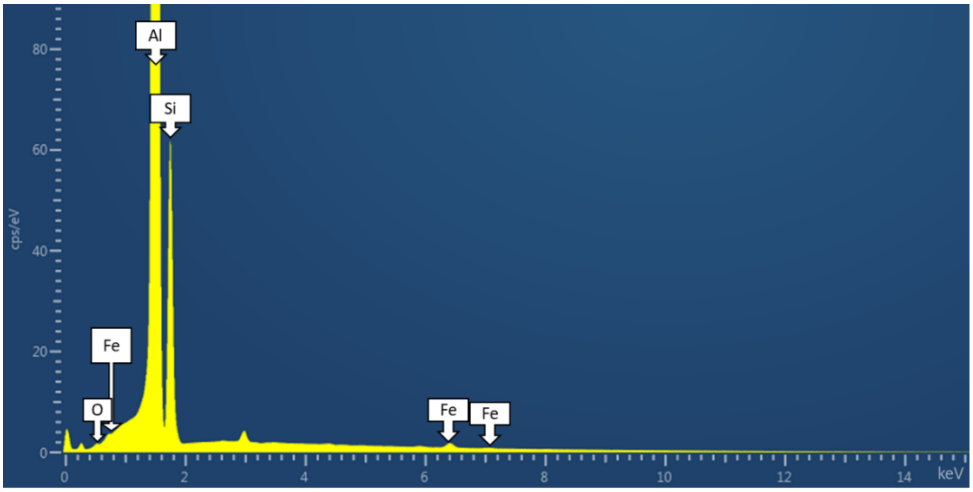

Fig. 2.35 EDX spectrum obtained for aluminum foam.

Another commercial aluminum foam (Al-0812, RECEMAT BV) with an aluminum content of 99.7% was initially chosen for study. The composition is presented in Table 2.7.

Table 2.7 Composition of Al-0812 foam.

Element	Symbol	Wt%
Aluminum	Al	99.70
Iron	Fe	0.12
Silicon	Si	0.04
Copper	Cu	0.01
Titanium	Ti	0.01

Before observing the microstructure of Al-0812 foam, the sample was prepared by mechanical polishing and planar ion polishing. Here in Fig. 2.36 we present the microstructure of cross-sections of Al-0812 foam struts. As this foam had a high purity of aluminum, grains and grain boundaries could be well identified, without noticeable secondary phases. The foam Al-0812 had a porosity of 95% with yet an

average pore size of 2.4 mm, which was estimated to be too large for serving as host matrix for salt particles, as a result, this foam was not chosen for further study. However, it provided us with meaningful information on the microstructure of almost pure aluminum foams. For instance, it can be seen that in opposition to the Ni- and Cu-foams, the aluminum foam struts were fully solid. Yet, the aluminum struts were also composed of only a few grains, for which the grain boundaries also ran through the whole thickness of the struts. As the struts ensure the structural integrity and load-bearing capacity of the foam, these observations indicate that the grain boundaries may have an important influence on the mechanical behavior of the foam struts, and hence the foam itself,

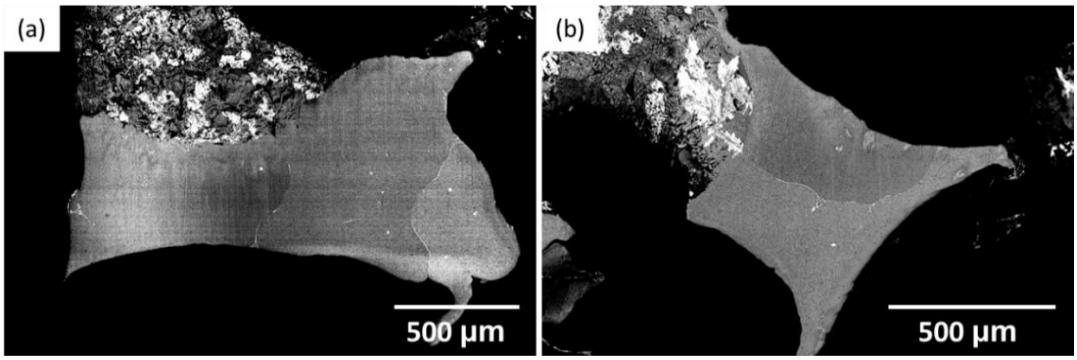

Fig. 2.36 BSE images of cross-sections of Al-0812 foam struts for observing its microstructure.

It is also noteworthy that for the copper and nickel foams, we observed a thin layer of shell-like material covering both sides of the cross-section of the strut, with one side thicker than the other, as pointed out with the white arrow in Fig. 2.32a and in Fig. 2.33a. As shown in both of these images, there were narrow gaps between the shell and the strut of metal foam. What's more, no grains or grain boundaries could be observed on the surface of this shell. We speculate that this shell may be the result of material redeposition during the cross-section ion polishing. To verify this speculation, EDS was applied for testing the composition of the shell. The results are presented in Fig. 2.37.

Three spots were chosen for study. As shown in Fig. 2.37a and b, Spot 1 was chosen on the cross-section of nickel foam strut and Spot 2 was chosen on the shell around the strut of nickel foam, while Spot 3 was chosen in the hollow of copper foam strut. Comparing their spectrums shown in Fig. 2.37c and d respectively, we can see that the main component of the shell was still the nickel but an extra titanium element appeared on the shell surrounding the strut. This element also appeared in the hollow of copper foam strut, as shown in spectrum 3 (see Fig. 2.37e). In fact, titanium was the main component of the mask of the sample used for cross-section ion polishing. We can conclude that the shell covering the metal foam strut was due to the redeposition of the metal foam and the titanium sample mask used during cross-section ion polishing, resulting in the microstructure (such as grains and grain boundaries) not being visible in the cross-section of the shell.

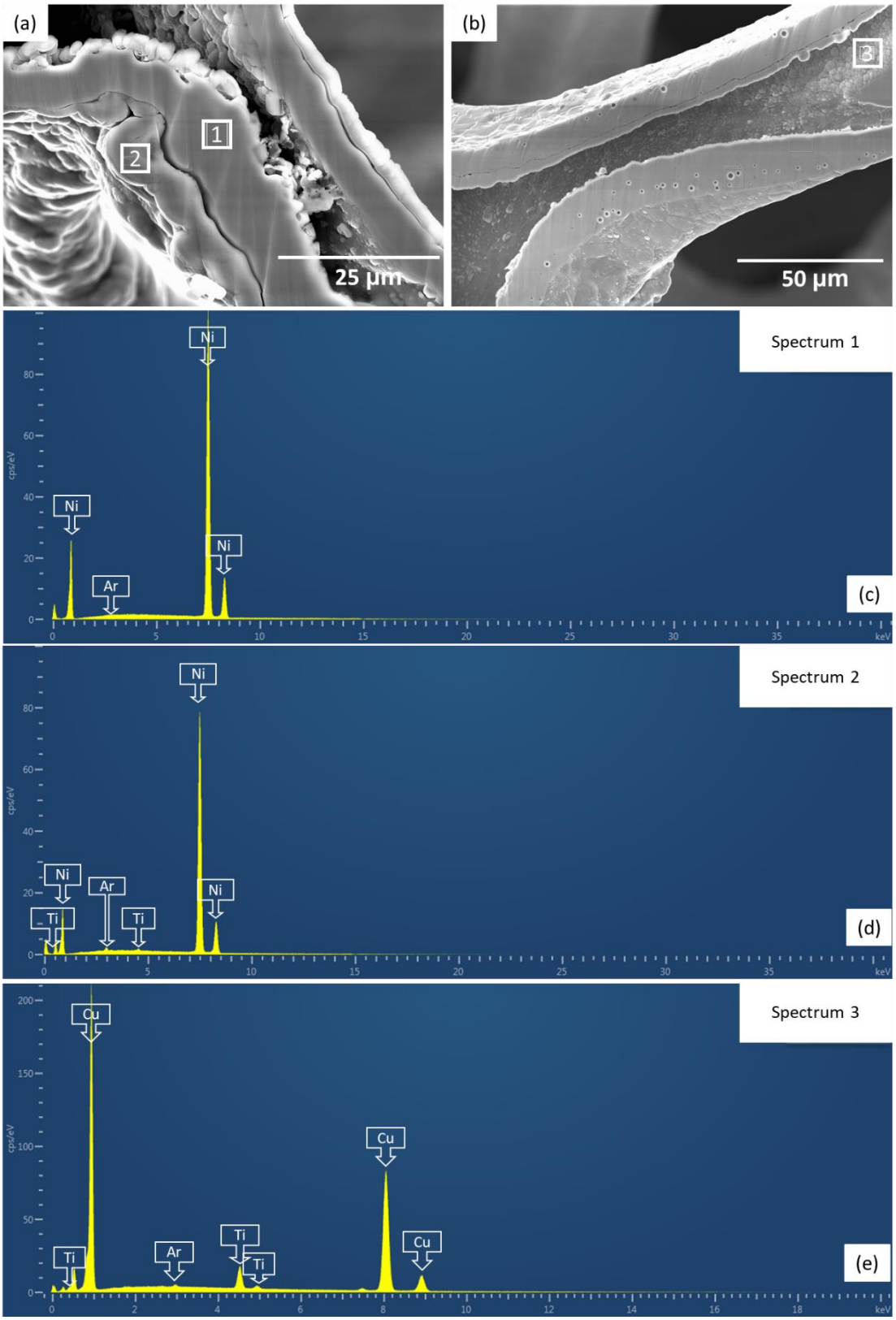

Fig. 2.37 EDS spectrum obtained for nickel foam and copper foam at 3 different chosen spots. (a) Spot 1 chosen on the cross-section of strut and Spot 2 chosen on the shell around the strut of nickel foam, with (c) and (d) their EDS spectrum obtained respectively. (b) Spot 3 chosen in the hollow of copper foam strut with (e) its EDS spectrum obtained.

As a conclusion of the structural characterization of the metal foam, copper foam, nickel foam and aluminum foam that we chose for serving as the host matrix of the salt were all open-cell metal foams. Among which, the copper foam and nickel foam had a similar mesostructure, in terms of the porosity, the shape of the pores and the homogeneity of the distribution and size of the pores, while aluminum foam exhibited quite an uneven strut thickness and irregular pore shape and size. The second type of aluminum foam (Al-0812 foam) exhibited structural characteristics similar to those of the Ni- and Cu-foam. However, due to its relatively large cell size, it was not considered suitable as a host matrix, and therefore we will not delve further into its analysis. In terms of microstructure, the copper foam and nickel foam featured hollow struts with triangular cross-sections and consistent sizes and wall thicknesses. In contrast, the aluminum foam exhibited variable strut shapes and thicknesses. All three kinds of metal foams selected for the elaboration of thermochemical composites showed distinguishable grains, grain boundaries and interfaces on the cross-section of struts, which may have a non-negligible influence on the macroscopic mechanical properties of the metal foam during compression. In fact, the mesostructure and microstructure of metal foams both play a crucial role in determining their overall mechanical properties in compression. In the following sections, we will describe how different structures of metal foams behave in compression experiments and how their structure specifically affects their mechanical properties and in particular the strain localization phenomena.

2.4.2. Mechanical properties of metal foam under compression

In this section, we present the mechanical properties of metal foam obtained from in situ uniaxial compression tests observed by optical microscope and by SEM at ambient temperature and 150 ℃. The full 2D and 3D strain fields computed by CMV 2D and 3D using the images acquired during in situ experiments and from post-mortem X-ray microtomography are presented. Among the three kinds of metal foams, we performed compression tests on copper foam and aluminum foam. As explained in 2.2.1, the nickel foam was purchased in sheets with a thickness of only 1.4 mm, which limited the possibility of performing the compression test due to the boundary effects. The comparison of the mechanical behavior under compression of different metal foams with different structures and the analysis of their advantages or inconveniences from the point of view of the potential host matrix for the metal foam-salt hydrate composites are presented in the discussion and conclusion in section 2.5.

Mechanical behavior of copper foam

(1) At ambient temperature

The uniaxial compression test performed on sample Cu01 was at ambient temperature.

The sample preparation, experimental setup and protocol were introduced in 2.2.6. In total, 1199 images with a resolution of 3296 × 2472 (pixel size at 2.75 μm) were recorded during compression at a sampling rate of one image every 5 seconds.

The strain fields at different scales were obtained via the 2D version of software CMV, based on deformation steps every 10 images recorded.

First, we compute the macroscopic strain field at the sample scale. The correlation coefficient was set to 0.3 (which is a severe criterion for correlation quality, as introduced in section 2.2.3). Scheme 1 of the integration domain, introduced in Fig. 2.6, was used for all the calculations via CMV in this section. In Fig. 2.38a, we present the image taken by the optical microscope of the initial state of the sample. This image was used as the reference image for digital image correlation. The matrix of measurement points defined on the reference image and the correlation domains (correlation window) for each point with the size of 80 × 80 pixels are represented by blue squares, shown in Fig. 2.38b. These points and correlation domains were defined for computing the mean macroscopic strain components of the observation surface. A search domain of 30 × 30 pixels was applied. The search domain represents the domain in which CMV seeks to place the measurement points and correlation domain to find the best match in the deformed images. Scheme 1 integration domain implies that the local strain gage is double of the spacing between the measurement points, so the vertical local strain gage was of 160 pixels, which corresponded to 440 μm, and the horizontal local strain gage was of 300 pixels, which corresponded to 825 μm**.** The spatial resolution of the computed strain field was limited to these values, which were larger than the pore size of the foam, and were therefore adapted to compute the macroscopic strain of the sample.

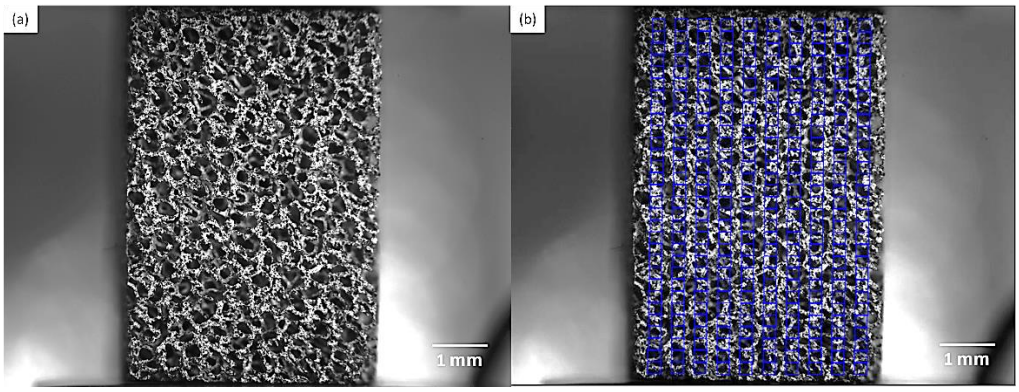

Fig. 2.38 (a) The initial state image of copper foam sample Cu01 by optical microscope and (b) the same image serving as the reference image for computing the macroscopic strain maps using CMV with the matrix of points defined and the correlation domains shown in blue squares.

The compression stress-strain curve for Cu01 is shown in Fig. 2.39. The copper foam showed three characteristic phases: first the elastic response (corresponding to elastic bending of the struts of the foam structure), second the plastic yielding with moderate strain hardening (corresponding to plastic deformation of the struts of

the metallic structure) until approximately 40% shortening, then strong stain hardening due to cell collapse and densification of the foam [131].

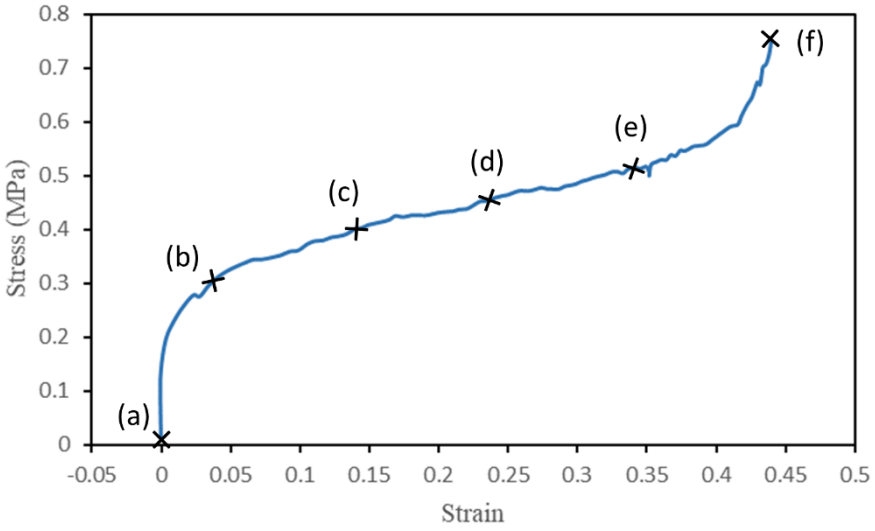

Fig. 2.39 The stress-strain curve from the uniaxial compression test on Cu01 obtained by DIC analysis.

Note that as the stress at which the copper foam changed from linear elastic to plastic yielding was not easily detected, the 0.2% offset yield strength was determined [156, 192]. By zooming in on the stress-strain curve to the elastic response regime, it is possible to estimate the Young's modulus with the slope of the initial part of the curve by using the coordinates of two points on the elastic response part of the curve (e.g., point A and point B, as marked in red marked in Fig. 2.40). Alternatively, a trendline can be fitted based on all measurement points within the elastic region, with the slope representing the Young's modulus. A line (yellow in Fig. 2.40) can be then constructed parallel to the initial portion of the stress-strain curve but offset by 0.2% from the origin. The 0.2% offset yield strength is the stress at which the constructed line intersects the stress-strain curve as shown in Fig. 2.40.

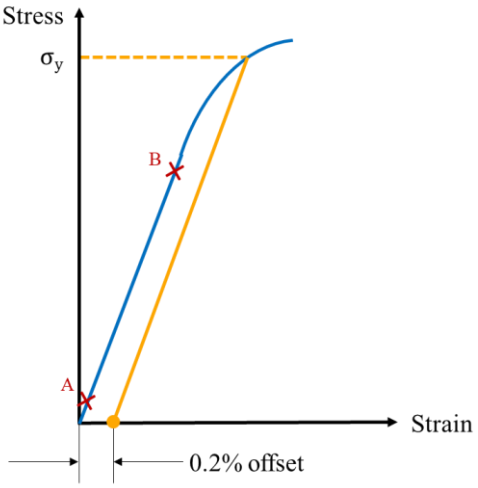

Fig. 2.40 Schematic of the definition of 0.2% offset yield stress.

For sample Cu01, Young's modulus was around 42 ± 5 MPa. This value agrees with the scaling law provided by Gibson and Ashby [130, 131], presented in Equation (4), with the relative density equal to 0.04 (presented in Table 2.1), Young's modulus of solid copper to be around 130 GPa, and the constant $\alpha \approx 0.2$. The value of α is well between the proposed theoretical range of 0.1 to 4 [130, 131]. The yield stress (0.2% offset stress) was 0.23 ± 0.02 MPa. With further loading, the copper foam stress-strain curve showed a long plastic pseudo-plateau, due to plastic deformation of the cells (pores) owing to the plastic deformation of the struts of the copper foam. In the final densification regime, the pores of copper foam completely collapsed and the stress rose rapidly from around 0.6 MPa. The sample Cu01 was unloaded until a strain of 44%.

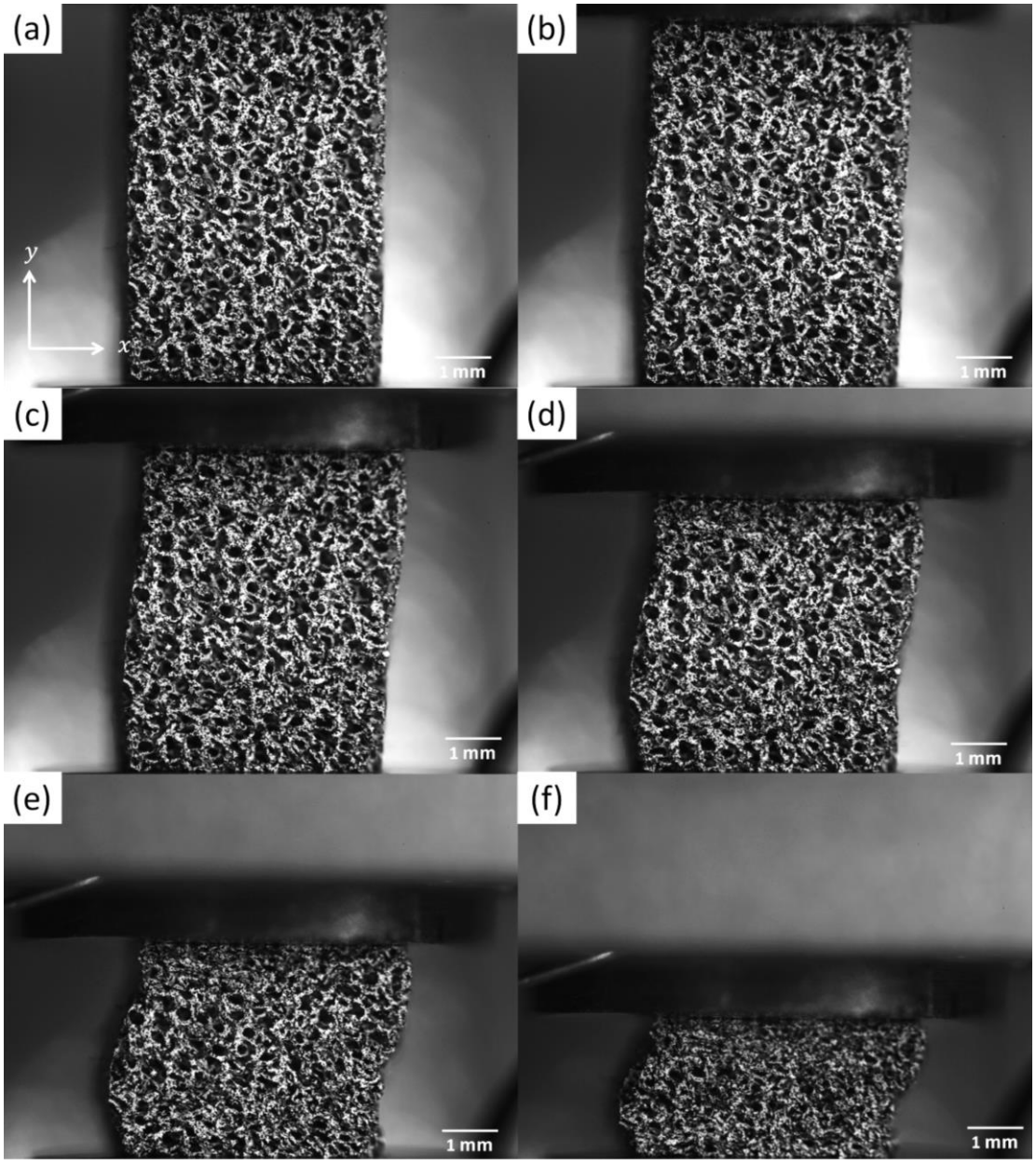

Fig. 2.41 Loaded open-cell copper foam sample Cu01 at different strains of (a) 0%, (b) 4%, (c) 14%, (d) 24%, (e) 34% and (f) 44%.

The strain states of the copper foam sample Cu01 at different deformation steps during compression are shown in Fig. 2.41, referred to as (a) to (f) and marked by crosses on the stress-strain curve shown in Fig. 2.39. The applied load was vertical, aligned with direction $-y$ on the upper face of the sample with the bottom face of the sample kept still.

In the next step, to investigate the localization of strains in metal foams at the structural scale of pores and to demonstrate the possible existence of strain bands, we computed the strain field by DIC on reducing the correlation domain from 80 × 80 pixels to 50 × 50 pixels and increasing the number of measurement points. The local strain gage was of 100 pixels in both x and y directions (scheme 1 as integration contour), which corresponded to 275 μm. The spatial resolution of the computed strain field was limited to this value, which was comparable to the pore size of the foam, and was therefore adapted to compute the local strain of the sample on the scale of pores. The correlation coefficient was kept at 0.3 and the search domain was set at 10 × 10 pixels. The reference image was still the one shown in Fig. 2.38a and the new matrix of measurement points with the correlation domains in squares are presented in Fig. 2.42.

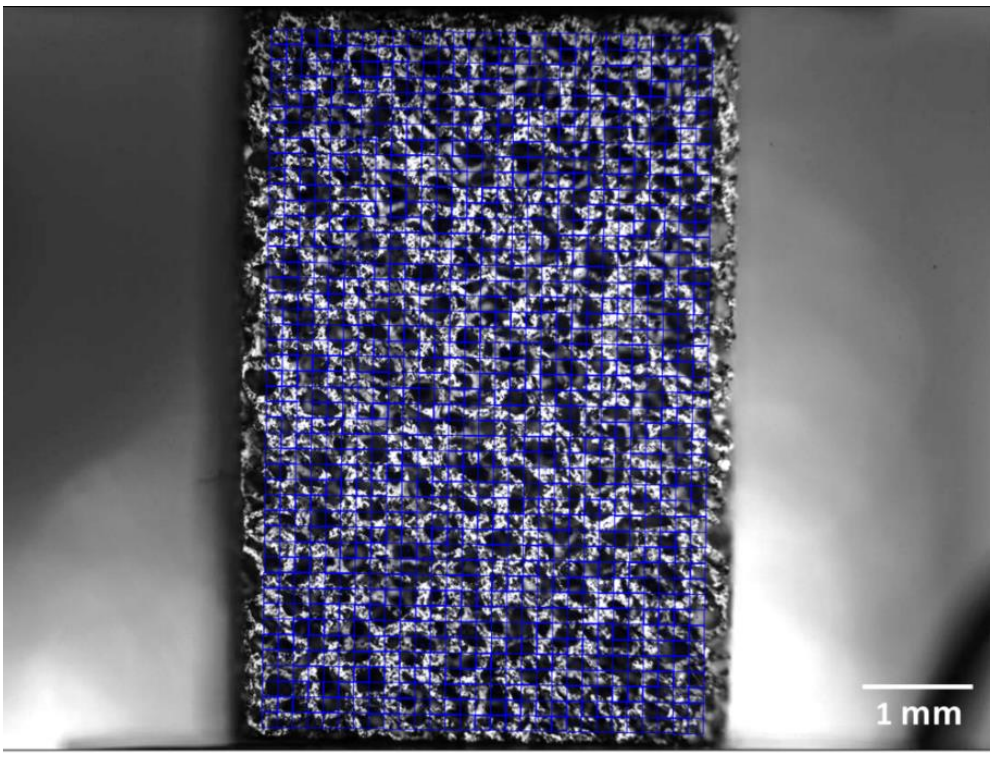

Fig. 2.42 Matrix of the measurement points defined and correlation domains in size of 50 × 50 pixels for computing the strain field at the metal foam structural scale of pores of Cu01.

Fig. 2.43 presents the equivalent strain maps for sample Cu01 computed at seven selected macroscopic strain levels of 1%, 2.4%, 4%, 6%, 8%, 10% and 14%. The equivalent strain (von Mises strain) is the second invariant of the plane strain tensor (see Equation (26) and (27) in section 2.2.3). It is a convenient scalar representation

of strain localization patterns. The macroscopic stresses corresponding to these seven strains are shown in Table 2.8. The color code we have chosen assigns warmer colors to indicate higher levels of strain, with the color red specifically representing the strongest strain localization. Note that all the strain maps displayed in Fig. 2.43 utilize the same color code scale, spanning from 0 to 20%.

Table 2.8 Selected macroscopic strains for computing the strain maps and their corresponding stresses for samples Cu01, Cu02, Al01 and Al02.

Macro. Strain (%)	Stress (MPa)			
	Cu01	Cu02	Al01	Al02
1	0.23	0.28	4.76	2.31
2.4	0.28	0.32	5.57	2.49
4	0.31	0.35	5.94	2.65
6	0.34	-	6.47	-
7	-	0.36	-	2.87
8	0.35	-	7.22	-
10	0.36	0.38	7.96	3.19
12	-	0.38	-	3.45
14	0.40	0.39	9.25	3.65
15	-	0.38	-	3.79

According to the strain maps shown in Fig. 2.43, the development of a localization band, that propagated at approximately 60° of the compression direction, between macroscopic strains from 2.4% to 6% was readily apparent (from Fig. 2.43b to d). As the deformation progresses to 8% and 10% (Fig. 2.43e and f), nearly horizontal compaction bands started to form, suggesting a high probability of pore collapse. By the time a macroscopic strain of 14% was reached (Fig. 2.43g), the deformation zone that was already observed at a strain of 10% exhibited further reinforcement. The strain maps presented in Fig. 2.43 effectively illustrate the evolution of the localization bands in a manner that is both comparable and comprehensive.

Then, we present in Fig. 2.44 the equivalent strain maps for sample Cu01 computed at three selected macroscopic strain levels of 1%, 4%, and 8% with color scale adapted to the specific range of each strain map. Fig. 2.44a demonstrates the existence of the 60° conjugate band even at 1% macroscopic strain. Additionally, these strain maps shown in Fig. 2.44 reveal that significant localizations also occurred at an early stage. The initial localizations manifested as soon as plasticity initiates and subsequently intensified over time.

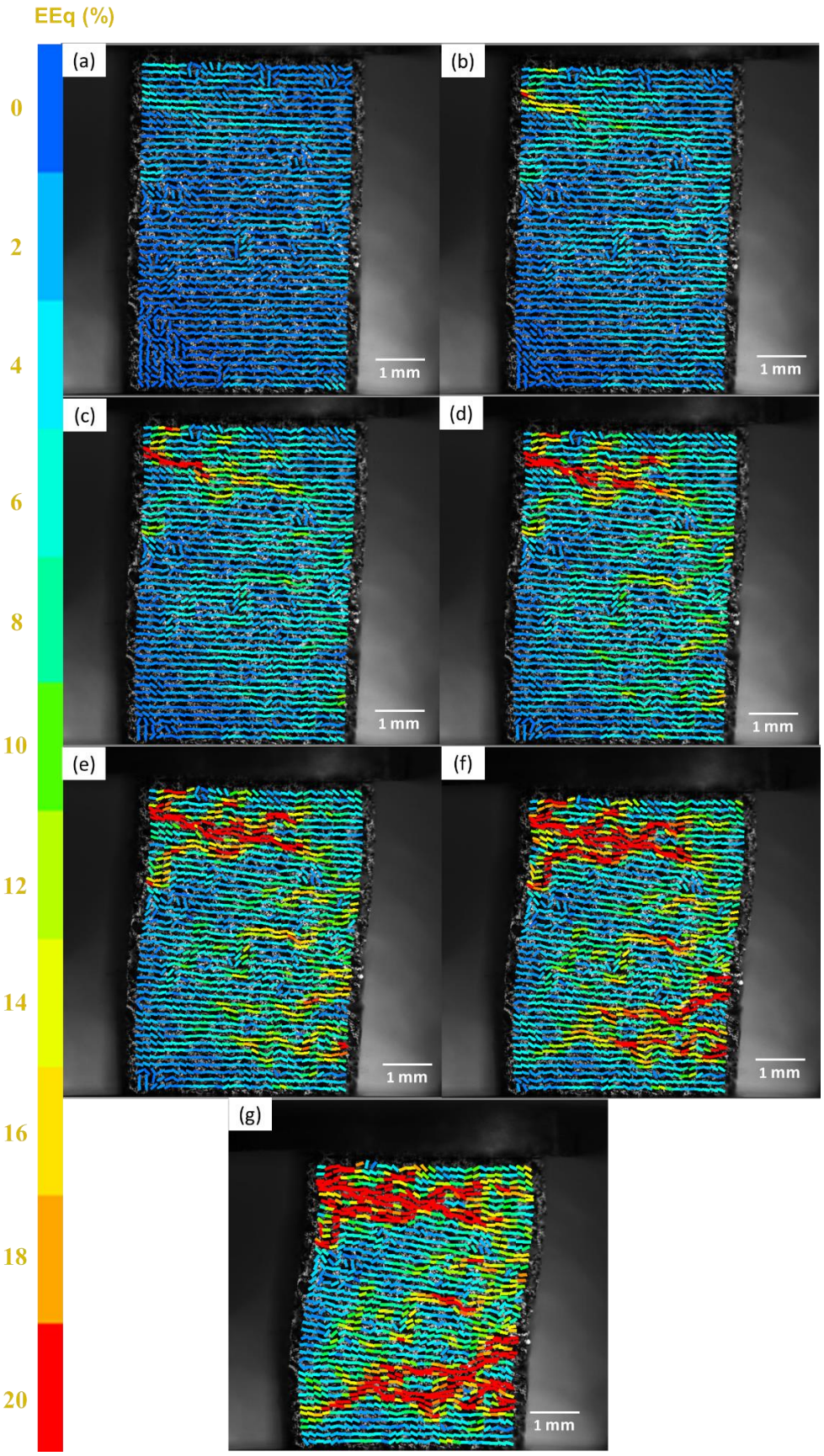

Fig. 2.43 Equivalent strain maps (correlation domain of 50 × 50 pixels) at different levels of macroscopic strain of sample Cu01 during compression (vertical) with (a) at 1% (b) at 2.4% (c) at 4% (d) at 6% (e) at 8%, (f) at 10% and (g) at 14%.

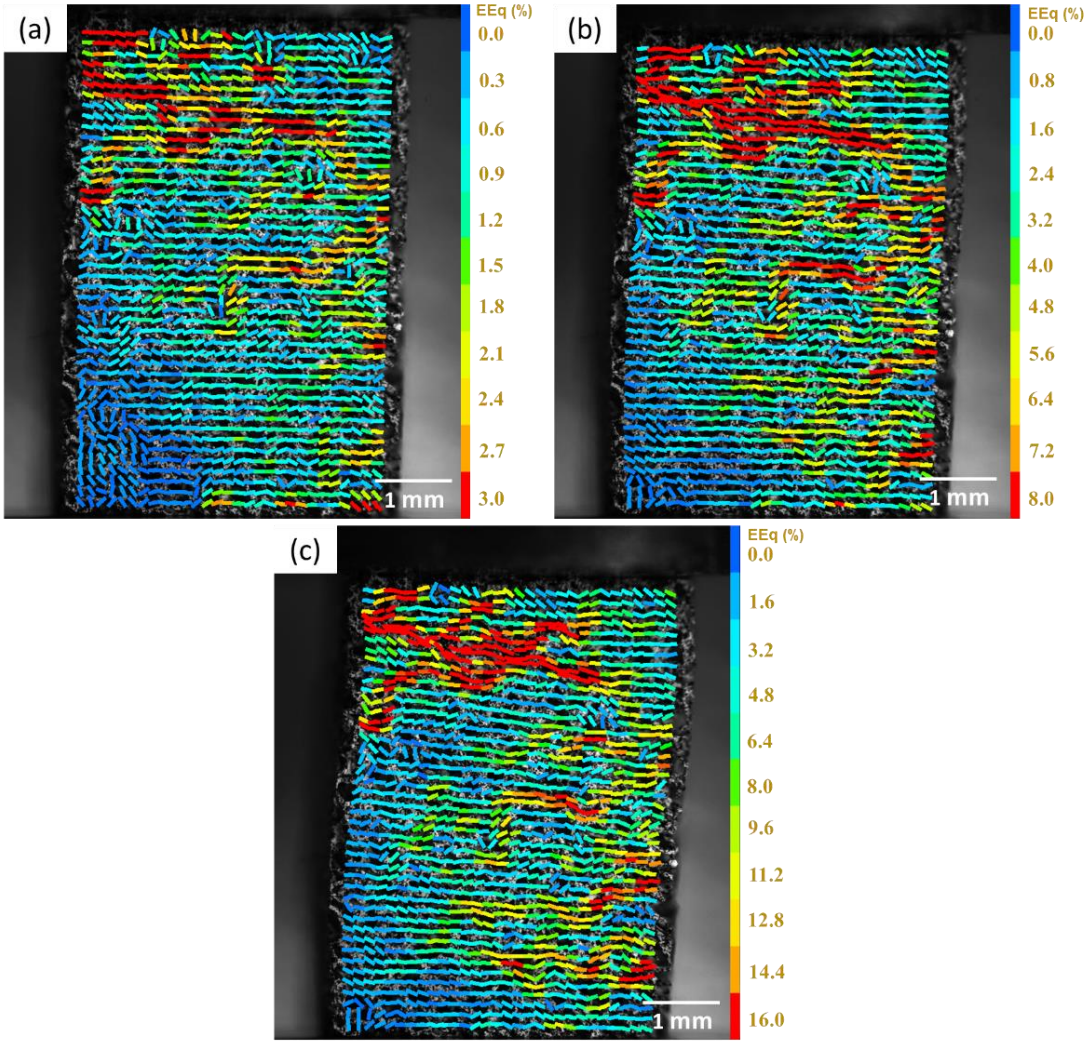

Fig. 2.44 Equivalent strain maps (correlation domain of 50 × 50 pixels) for Cu01 during compression (vertical) at macroscopic strain levels of (a) 1% (b) 4% and (c) 8% with different color code scales adapted to each strain map.

To obtain a clearer view of the deformation mechanism of the copper foam sample Cu01 at ambient temperature at a more localized scale, the local strain gage must continue to be reduced. Therefore, the matrix of points defined on the reference image in Fig. 2.45 is even denser than that in Fig. 2.42. The correlation domains for each measurement point, presented by yellow squares as shown in Fig. 2.45, were reduced to the size of 25 × 25 pixels. The strain gage was thus of 50 pixels, which corresponded to 137.5 µm. The search domain was set to 10 × 10 pixels and the correlation coefficient was set at 0.3. As the strain gage was significantly smaller than the average pore size, the computed strain field accurately represented the scale of the microstructure, such as the metal foam struts. For computing the deformation maps more precisely, only measurement points lying in the focal plane were selected for image correlation.

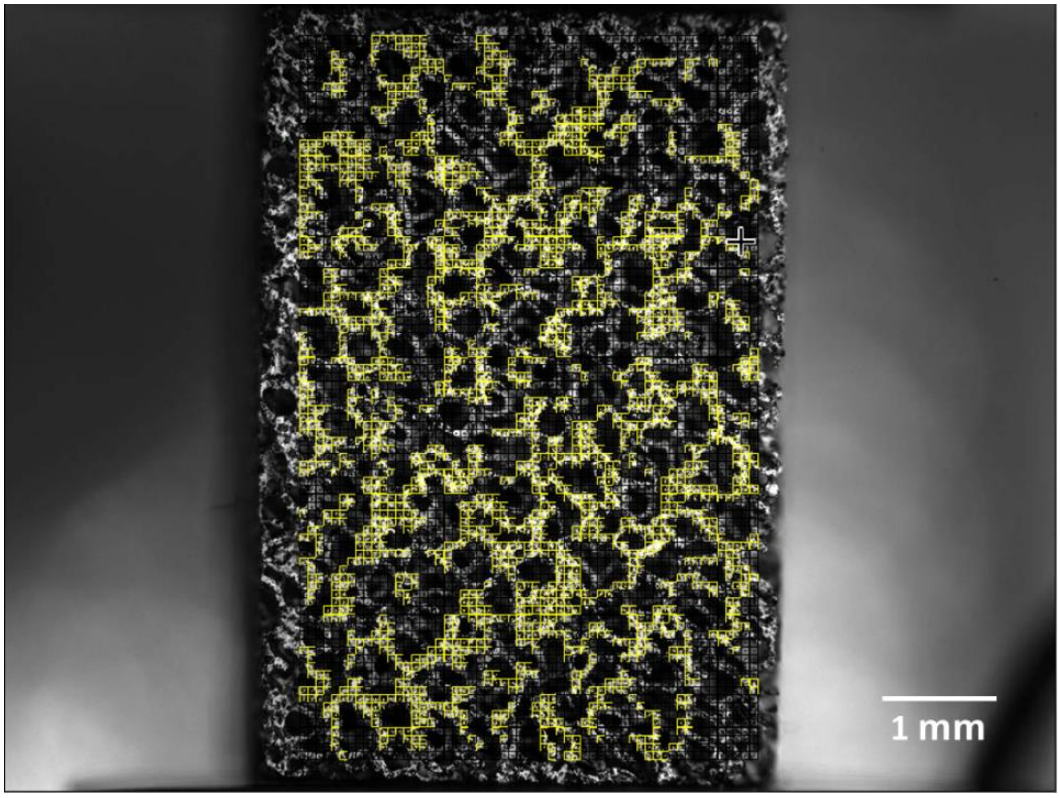

Fig. 2.45 Points and correlation domains defined on reference image for computing microscopic strain maps of copper foam sample Cu01 under uniaxial compression.

Fig. 2.46 presents the equivalent deformation maps for sample Cu01 computed at six selected macroscopic strain levels of 1%, 2.4%, 4%, 6%, 8% and 10%. The macroscopic stresses corresponding to these six strains are shown in Table 2.8. The color code we have chosen assigns warmer colors to indicate higher levels of strain, with the color red specifically representing the strongest strain localization. During the initial compression phase where the macroscopic strain level was of 1% and 2.4%, the strain field of the whole sample observation surface remained relatively homogeneous on the scale of struts (as shown in Fig. 2.46a and b). With the load increasing, strain localization zones started to appear at structural weak spots. It first started to appear on the upper part of the sample and continued to intensify as the test went on, as can be seen in Fig. 2.46c, d and e. Until the macroscopic strain reached a level of 10% (see Fig. 2.46f), strain localization was only observed in a few relatively scattered areas. Furthermore, the localization location revealed in Fig. 2.46f corresponds well with the observed localization bands in Fig. 2.43f, both occurring at a macroscopic strain of 10%. This observation suggests that the struts served as the fundamental structural units responsible for the deformation and changes in pores. The behavior and deformation of the metal foam struts directly contributed to the formation of localization bands and the overall deformation characteristics of the material.

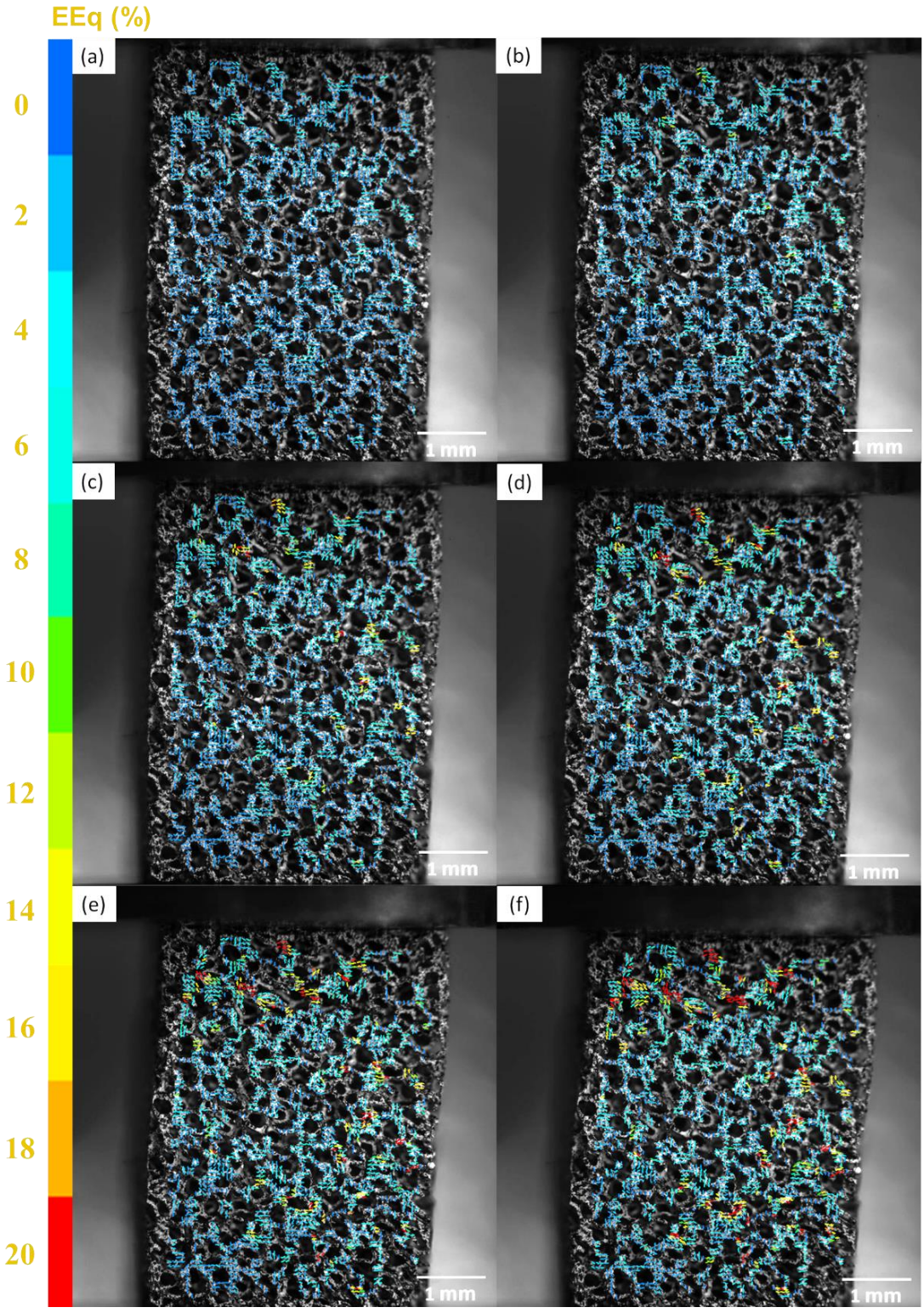

Fig. 2.46 Equivalent deformation maps at six levels of macroscopic strain of the sample Cu01 during compression (vertical) with (a) at 1% (b) at 2.4% (c) at 4% (d) at 6% (e) at 8% and (f) at 10%.

In Fig. 2.47, we present the displacement map of each correlation points defined on the observation surface of sample Cu01 during uniaxial compression at a macroscopic strain of 10%. With the selected color code, blue represents larger displacement and red represents smaller displacement. The displacement map

shows the absolute displacement of the measurement points. According to Fig. 2.47, we can conclude that the maximum absolute displacement occurred near the loading surface on the upper part of the sample and it decreased gradually along the direction of compression. Overall, the absolute displacement demonstrated a relatively uniform distribution along the compression direction, exhibiting only a minor disruption within the circled area in the dashed line. This results in the formation of a "blue" triangular region of displacement in the upper right region. This occurrence is associated with the emergence of a local strain band in the upper left region shown in Fig. 2.43, which formed and propagated at an angle of approximately 60° to the axial compression direction.

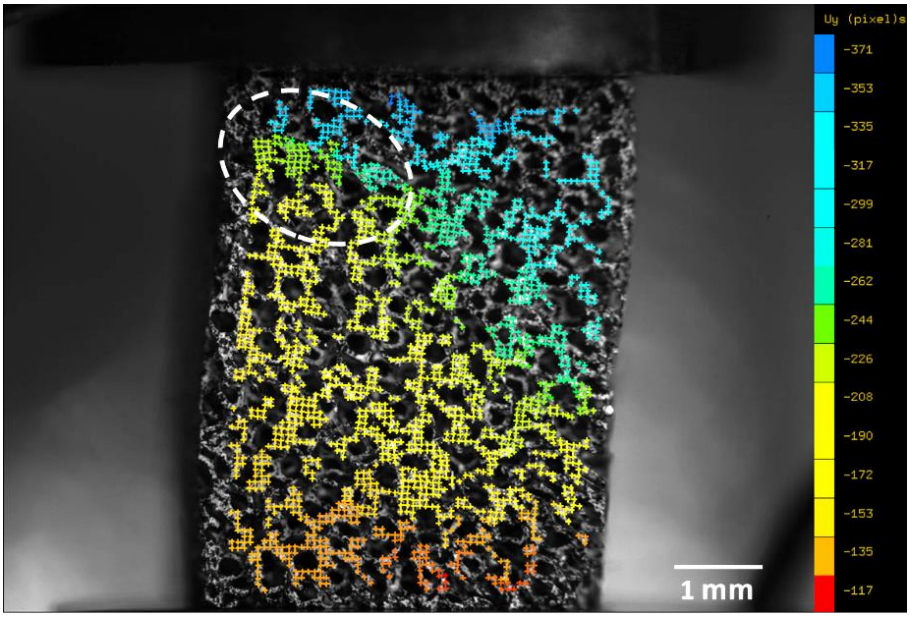

Fig. 2.47 Displacement map on the compression axis (vertical) of each correlation point of sample Cu01 at a macroscopic strain of 10%.

(2) At 150 ℃

The uniaxial compression test performed on sample Cu02 was at a temperature of 150 degrees. In total, 532 images with resolution of 2300 × 2472 (pixel size at 2.75 μm) were recorded at a sampling rate of one image every 5 seconds during the compression of the sample.

The macroscopic strain was obtained via CMV by computing the strain field of the overall observation surface for every 5 images recorded. In Fig. 2.48a, we present the image taken by optical microscope of the initial state of the sample which was used as the reference image for DIC. The matrix of measurement points defined on the reference image and the correlation domains for each point with the size of 100 × 100 pixels were presented by blue squares as shown in Fig. 2.48b. The vertical local strain gage was of 240 pixels, which corresponded to 660 μm, and the horizontal local strain gage was of 340 pixels, which corresponded to 935 μm**.** The

correlation coefficient was set at 0.3 and the search domain was set at 30 × 30 pixels.

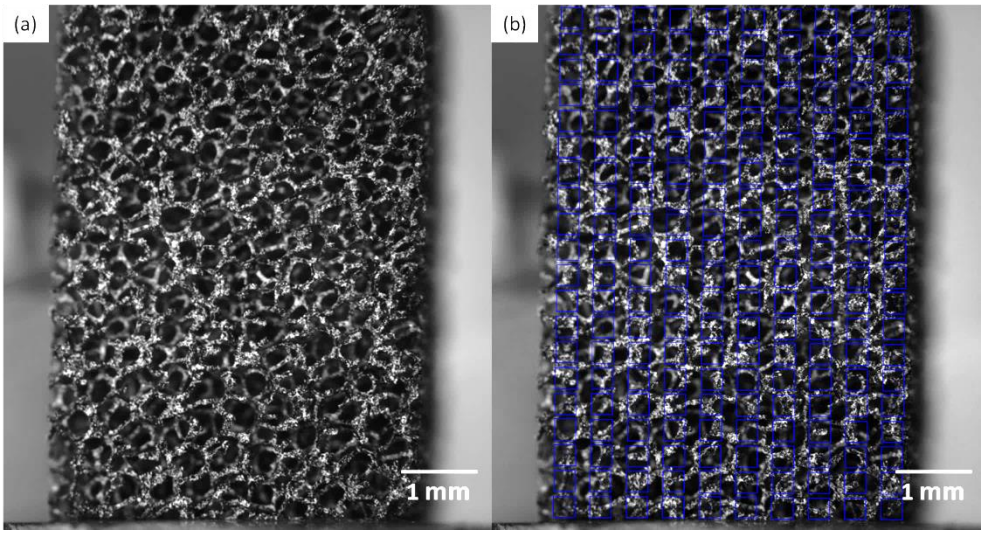

Fig. 2.48 (a) The initial state image of copper foam sample Cu02 by optical microscope and (b) the same image serving as the reference image for computing the macroscopic strain maps using CMV with the matrix of points defined and the correlation domains shown in blue squares.

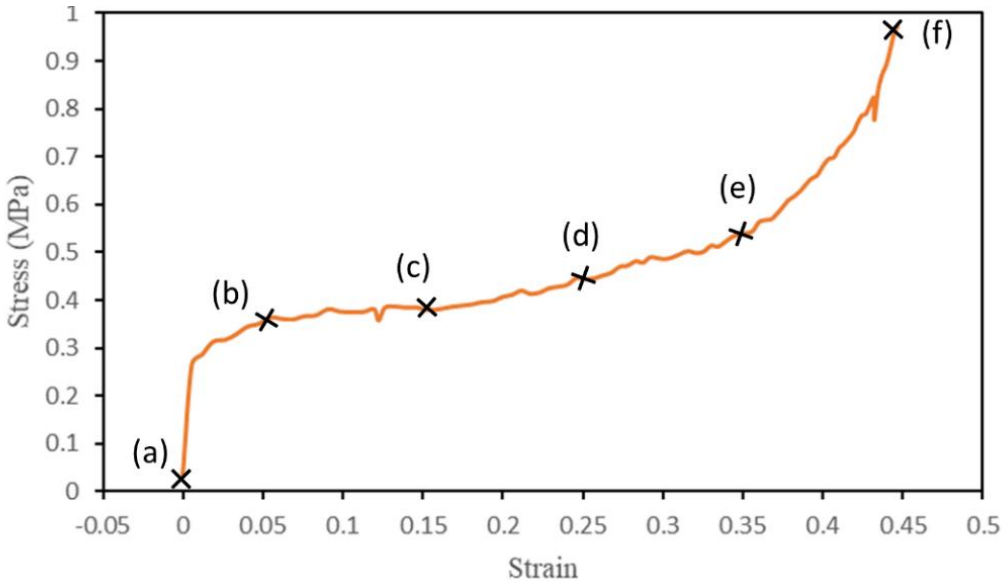

Fig. 2.49 The stress-strain curve from uniaxial compression test at 150 ℃ on Cu02 obtained by DIC analysis.

The compression stress-strain curve for Cu02 at 150 ℃ is shown in Fig. 2.49. At a temperature of 150 ℃, the behavior of the sample revealed three distinct stages. Initially, upon the initial loading, an elastic response was observed. Subsequently, after reaching the 0.2% offset yielding stress at approximately 0.27 ± 0.02 MPa (Young's modulus ~40 ± 5 MPa), a pseudo plateau phase ensued, characterized by a moderate increase in strain hardening. The third stage commenced at 0.55 MPa, where a significant rise in strain hardening was observed, corresponding to the regime of pore collapse and densification. The Cu02 sample was unloaded after experiencing a strain of approximately 45%. Note here the measured Young's

modulus agrees with the scaling law provided by Gibson and Ashby [130, 131], presented in Equation (4), with the relative density equal to 0.04 (presented in Table 2.1), Young's modulus of solid copper to be around 130 GPa, and the constant $\alpha \approx 0.2$, which lies between the proposed theoretical range of 0.1 to 4 [130, 131].

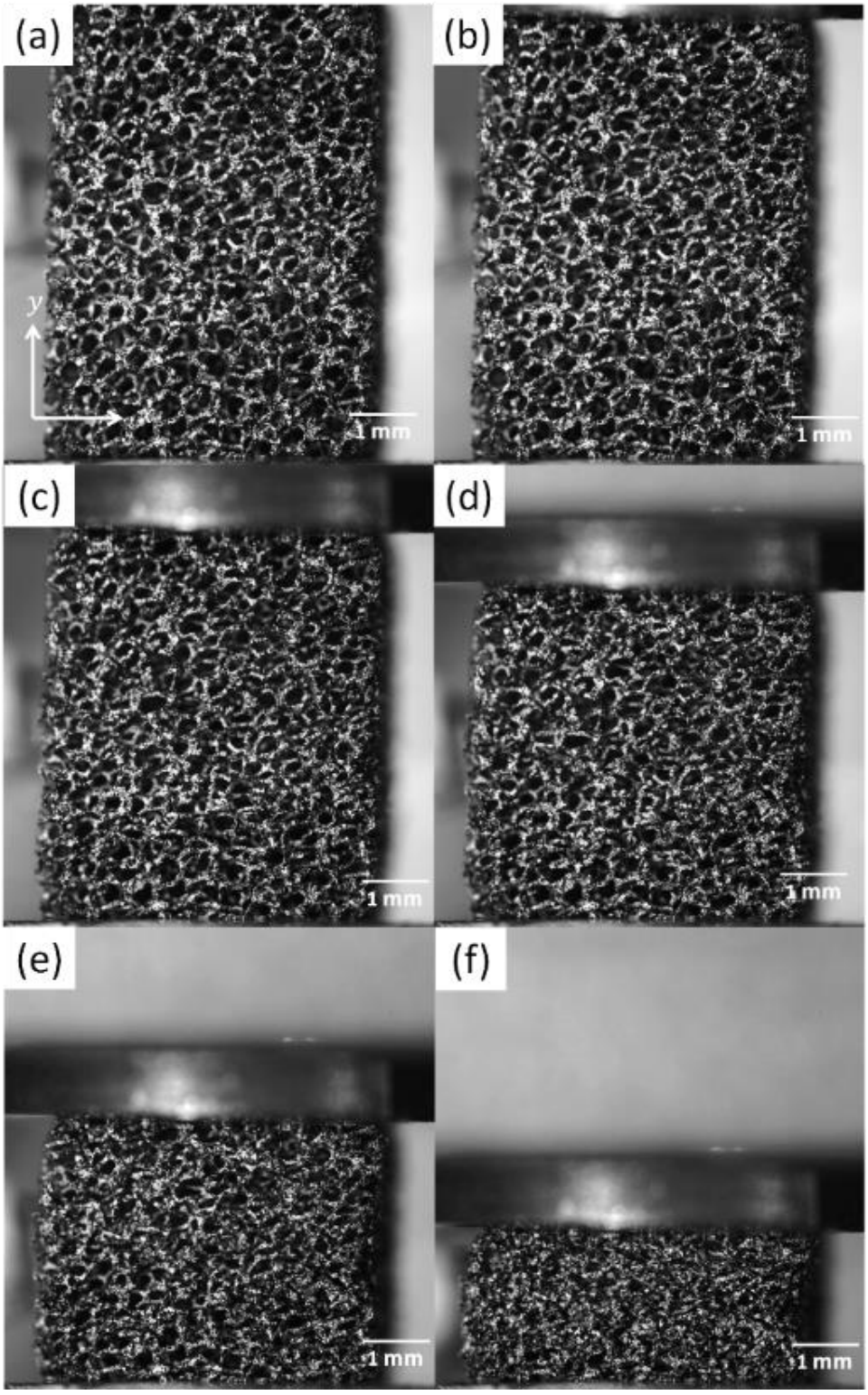

Fig. 2.50 Loaded open-cell copper foam sample Cu02 at different strain of (a) 0%, (b) 5%, (c) 15%, (d) 25%, (e) 35% and (f) 45%.

In terms of qualitative behavior, the loading curves at both room temperature and 150°C exhibit similarities. However, there are notable quantitative differences between them. At 150°C, the second stage demonstrated a nearly constant strength (around 0.4 MPa) between 5% and 15% strain. This was followed by a smooth and moderate increase in strain hardening from 15% to 35% strain, before transitioning into a rapid and significant hardening in the third stage. On the other hand, at room temperature, the second stage showed a linear and pronounced strain hardening from 5% to approximately 40% strain, before entering the third stage. The dissimilarity in strain hardening behavior during the plastic deformation of the foam could be attributed to the typical disparity between cold working and hot working conditions. In the latter case, processes such as dislocation recovery might have occurred, thereby reducing strain hardening.

The images of sample Cu02 at different stress and strain during compression are shown in Fig. 2.50, with deformation stages referred to as (a) to (f) corresponding to the crosses marked on the stress-strain curve shown in Fig. 2.49. The load was applied vertically to the upper face of the sample by the mobile piston in the $-y$ direction, while the immobile piston was positioned on the bottom face of the sample. The images illustrate the progressive plastic collapse of pores during the plastic stage, ultimately resulting in densification. The deformation of Cu02 appeared more homogeneous than that of Cu01 at room temperature, as no buckling and shearing could be directly seen. In the next step, we will try to explain this according to the strain maps obtained via DIC.

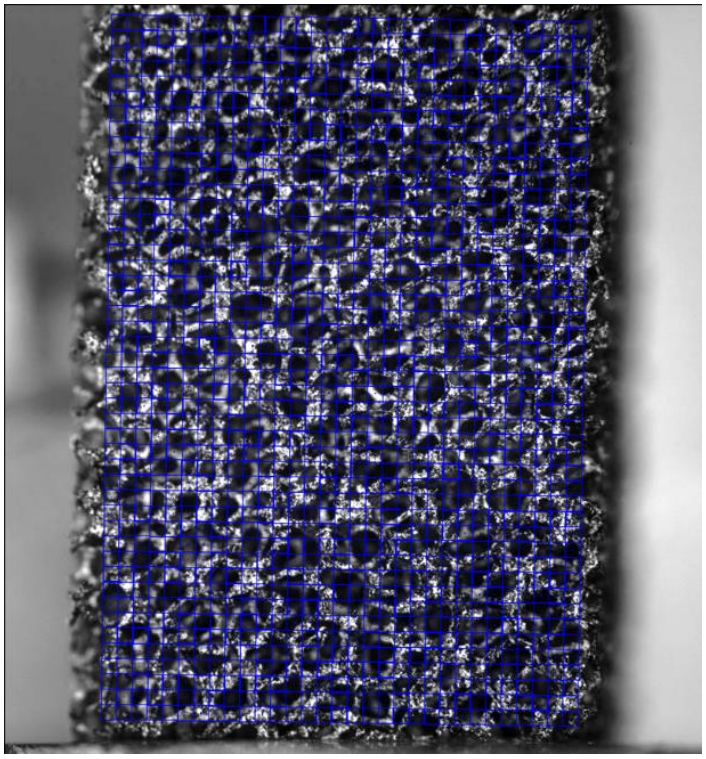

Fig. 2.51 Matrix of the measurement points defined and correlation domains in size of 50 × 50 pixels for computing the strain field at the metal foam structural scale of pores of Cu02.

To investigate the localization of strains in sample Cu02 at the structural scale of pores and to demonstrate the possible existence of strain bands, we compute the strain field by DIC on reducing the correlation domain from 100 × 100 pixels to 50 × 50 pixels and increasing the number of measurement points. The local strain gage was of 100 pixels in both x and y directions (scheme 1 as integration contour), which corresponded to 275 μm. The correlation coefficient was kept at 0.3 and the search domain was set at 10 × 10 pixels. The reference image was still the one shown in Fig. 2.48a and the new matrix of measurement points with the correlation domains in squares are presented in Fig. 2.51.

Fig. 2.52 presents the equivalent strain maps for sample Cu02 computed at six selected macroscopic strain levels of 1%, 4%, 7%, 10%, 12% and 15%. The macroscopic stresses corresponding to these six strains are shown in Table 2.8. The color code we have chosen assigns warmer colors to indicate higher levels of strain, with the color red specifically representing the strongest strain localization. Note that all the strain maps displayed in Fig. 2.52 utilize the same color code scale from 0 to 20%.

We can see from Fig. 2.52 that a distinctive, nearly horizontal strain band emerged in the middle of the sample only when the macroscopic strain reached a level of 7% (Fig. 2.52c). Simultaneously, there was the emergence of a strain band extending from the upper right corner at a 60° angle to the compression axis, accompanied by the appearance of another horizontal strain band in the lower part of the sample. These bands intensified with the progression of macroscopic strain from 10% to 15% (Fig. 2.52d to f). The deformation of Cu02 appeared more homogeneous than that of Cu01 at room temperature can be attributed to the predominant formation of strain bands that were primarily oriented horizontally.

Then, we present in Fig. 2.53 the equivalent strain maps for sample Cu02 computed at three selected macroscopic strain levels of 1%, 4%, and 7% with the color scale adapted to the specific range of each strain map. Fig. 2.53a illustrates the presence of a strain localization band propagating at a 60° angle to the axial stress direction, as well as the occurrence of a horizontal strain band even at a macroscopic strain of 1%. Similar to our observations for Cu01, the strain maps depicted in Fig. 2.53 demonstrate that certain significant localizations have already occurred early on and subsequently intensified over time. Furthermore, as the macroscopic strain increased, new localization bands emerged at later stages. For instance, the horizontal strain band situated in the lower part of the sample gradually formed during a later stage of strain (Fig. 2.53b and c).

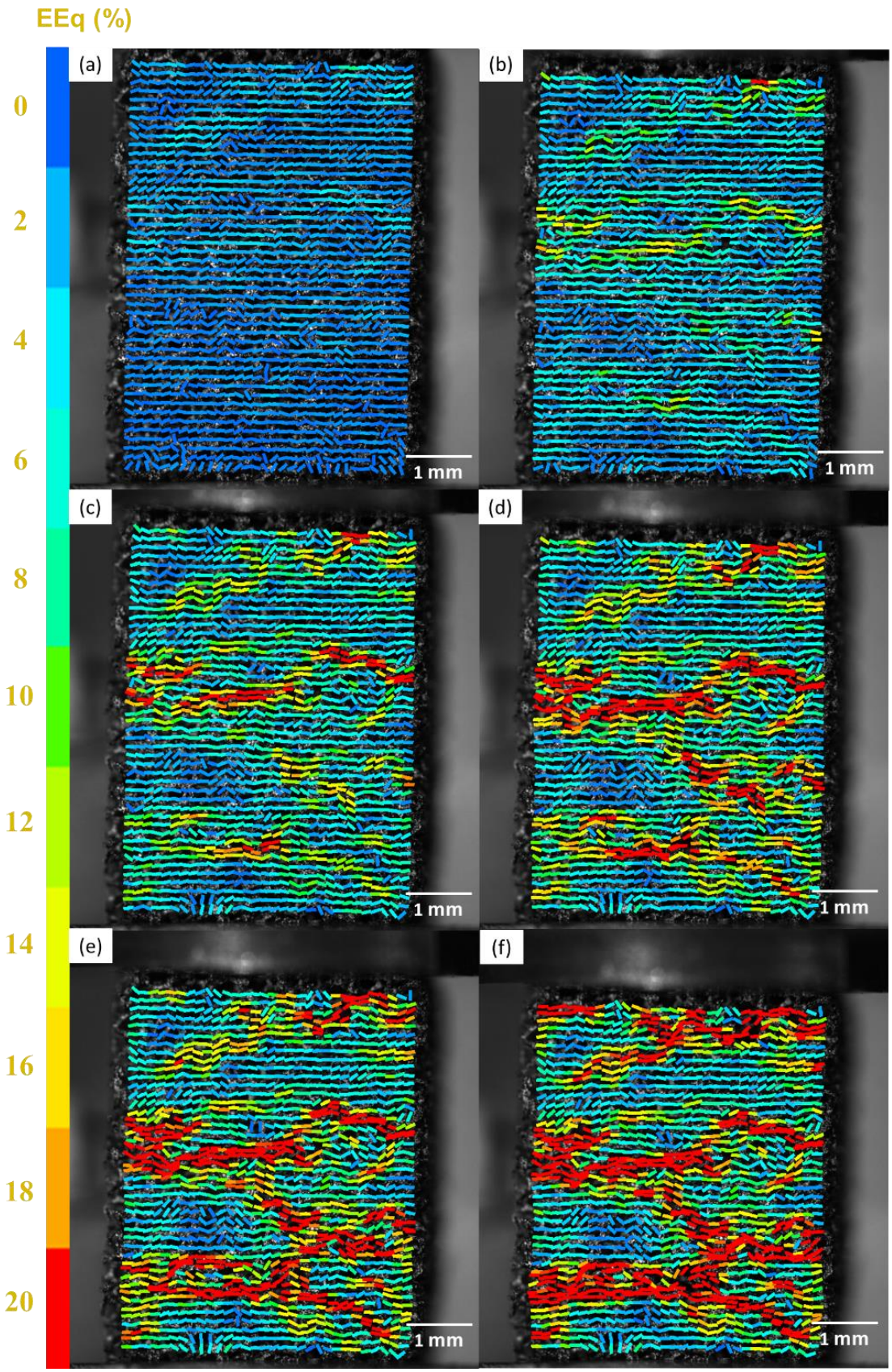

Fig. 2.52 Equivalent strain maps (correlation domain of 50 × 50 pixels) at different levels of the macroscopic strain of sample Cu02 during compression (vertical) with (a) at 1% (b) at 4% (c) at 7% (d) at 10% (e) at 12% and (f) at 15%.

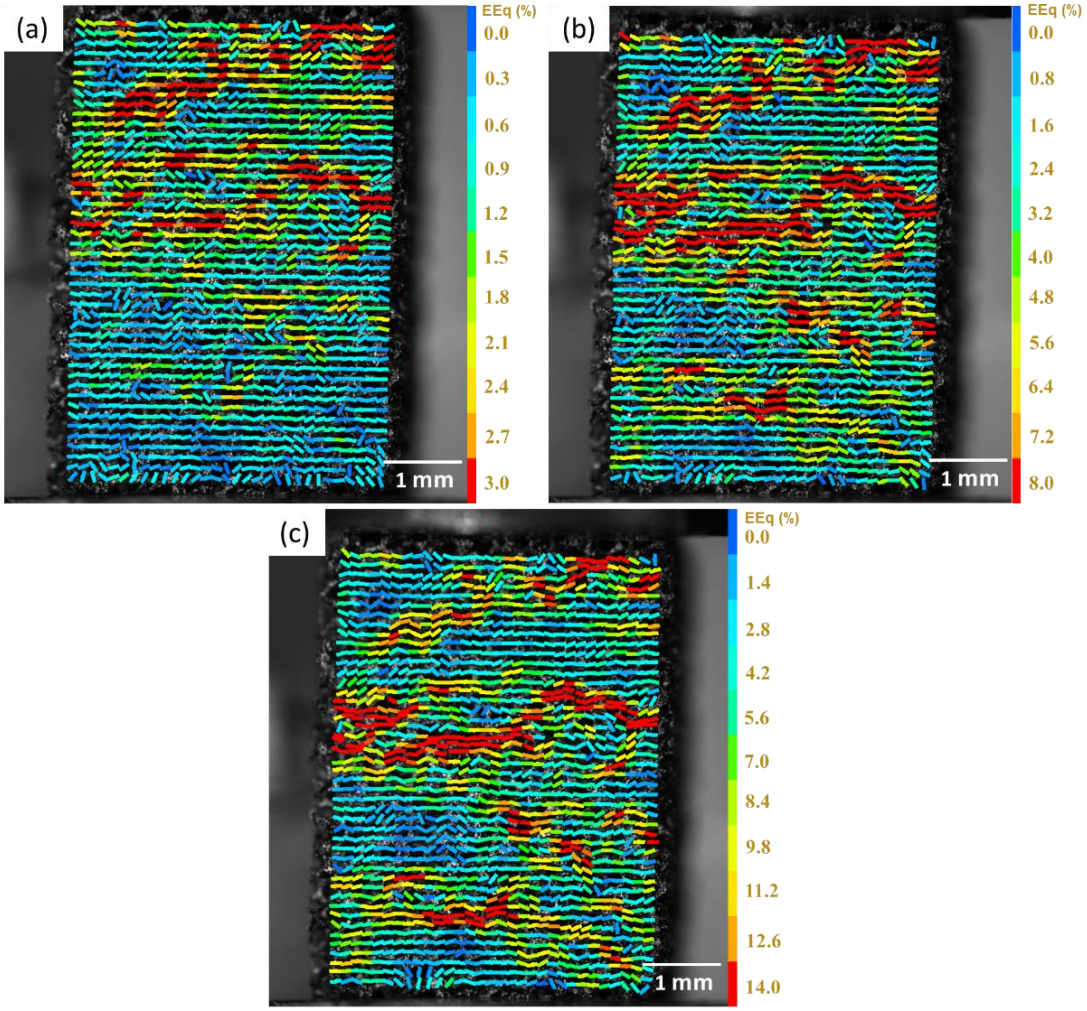

Fig. 2.53 Equivalent strain maps (correlation domain of 50 × 50 pixels) for Cu02 during compression (vertical) at macroscopic strain levels of (a) 1% (b) 4% and (c) 7% with different color code scales adapted to each strain map.

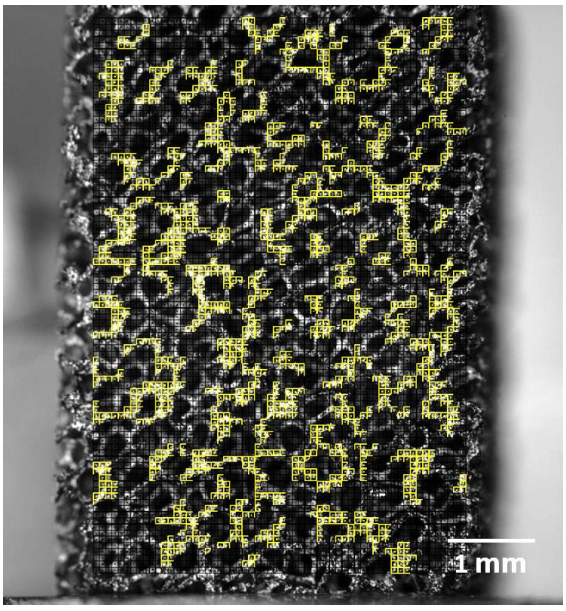

Fig. 2.54 Points and correlation domains defined on reference image for computing microscopic strain maps of copper foam sample Cu02 under uniaxial compression at 150 ℃.

To study the microscopic deformation mechanism of copper foam sample Cu02 at 150 ℃ at the scale of metal foam pores and struts, we refined the grid of correlation points and defined smaller correlation domains with the size of 25 × 25 pixels. The grid is presented by yellow squares as shown in Fig. 2.54. The local strain gage was of 50 pixels (137.5 μm). The search domain was 10 × 10 pixels and the correlation coefficient was 0.3. Only measurement points in the focal plane were selected for image correlation.

Fig. 2.55 presents the equivalent deformation maps for sample Cu02 computed at eight selected macroscopic strain levels of 1%, 2.4%, 4%, 6%, 8%, 10%, 12%, 14% and 15%. The macroscopic stresses corresponding to these strains are shown in Table 2.8. For the color code selected, the strongest localization of strain is presented in red. Note that the strain maps shown in Fig. 2.55 utilize the same color code scale, from 0 to 20%.

At the beginning of the loading where the macroscopic stress was around the 0.2% offset yield stress, the strain field didn't exhibit significant localization for the time being (as shown in Fig. 2.55a). For a stress level of around 0.32 MPa, localized deformation started to reveal at some structural weak spots, as shown in Fig. 2.55b. From this stage on, distinct equivalent strain localization sequentially developed at various spots in the dispersion of the sample observation surface, as can be seen in Fig. 2.55c and d. From Fig. 2.55e to h, the macroscopic strain was between 10% and 15%, where the sample was in the zone of the plastic plateau. We observed minimal occurrence of new localizations on the sample surface, but only a gradual intensification of the existing localizations.

In Fig. 2.56 we present the displacement field of correlation points defined on the observation surface of sample Cu02 during uniaxial compression at a macroscopic strain of 15%. With the selected color code, blue represents larger displacement and red represents smaller displacement. Similar results were obtained when comparing with sample Cu01.

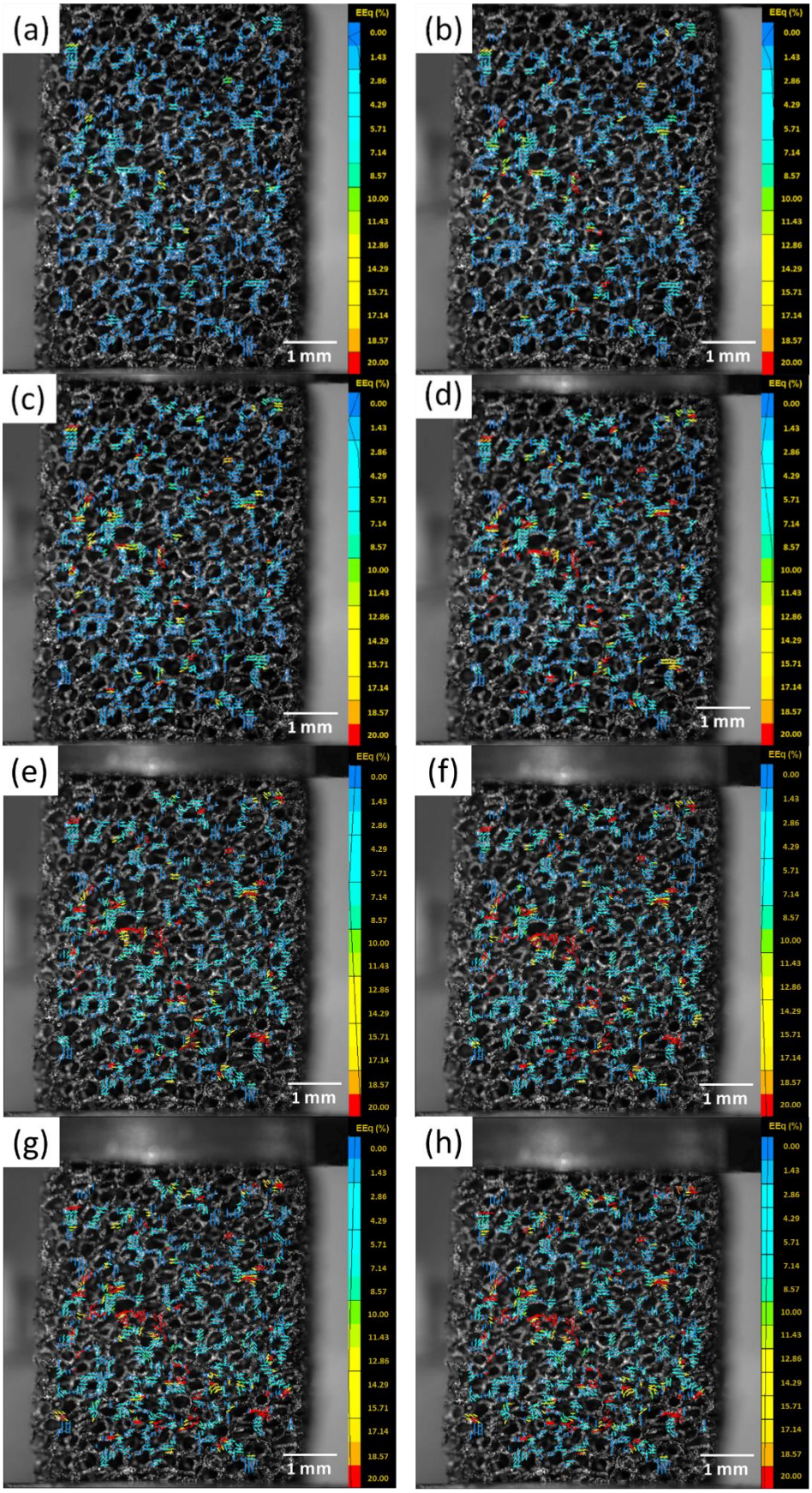

Fig. 2.55 Equivalent deformation maps at eight levels of macroscopic strain of the sample Cu02 during compression (vertical) at 150 degrees with (a) at 1% (b) at 2.4% (c) at 4% (d) at 7% (e) at 10% (f) at 12% (g) at 14% and (h) at 15%.

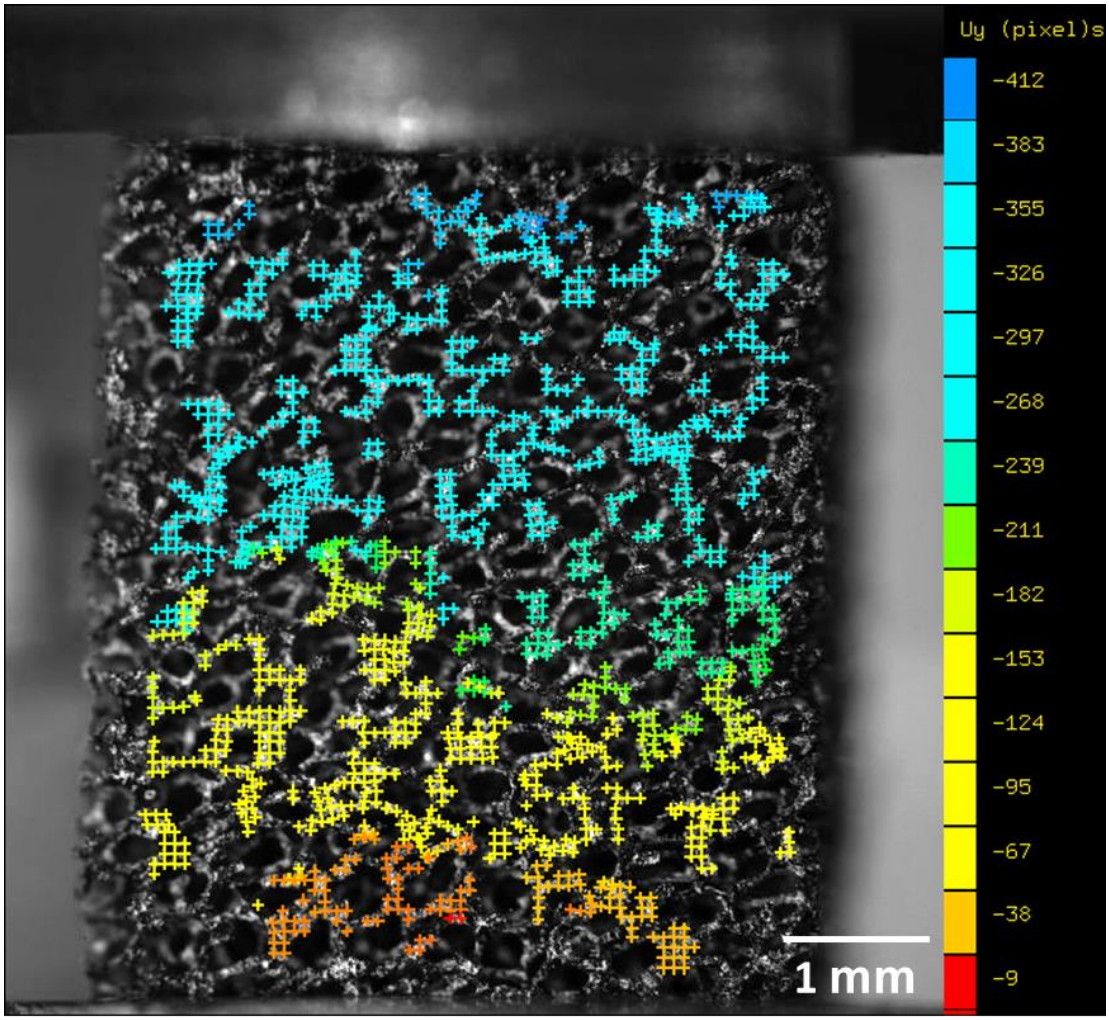

Fig. 2.56 Displacement map on the compression axis (vertical) of each correlation point of sample Cu02 at macroscopic strain of 15%.

The in situ SEM uniaxial compression test at 150 ℃ provided a clearer view of the deformation mechanism on the scale of pores and struts of the copper foam with an axial strain up to 6%, which nearly corresponds to the beginning of the pseudo-plateau of flow strength for the sample deformed at 150°C under optical observation, shown in Fig. 2.49. Images were recorded at a resolution of 6144 × 4415 pixels, with one pixel corresponding to about 1.06 µm. The SEM images shown in Fig. 2.57a, b and c correspond to loading states of 0%, 4% and 6%, respectively. The loading direction is indicated in Fig. 2.57a with red arrows. Until an axial strain of 6%, no distinct localization bands were detected. The strain localized by affecting some load-bearing struts. When looking closely at some strongly deforming cells, as shown in Fig. 2.57d to f, we can see the rupture of one strut (circled in red) during the loading steps. In Fig. 2.57g, h and i, we can see plastically deforming struts. It is worth noting that according to the literature, the plasticity of open-cell metal foam is dominated by the bending and plastic hinge of the struts [193]. This was well-observed in our experiment. For example, the strut pointed out by the red arrow bent at the sample axial strain of 4% and then formed the plastic hinge (S-

shape) at the axial strain of 6%. Both ductile bending and damage of struts can lead to substantial pore shrinking. However, at this relatively low strain level, there were no signs of complete pore collapse.

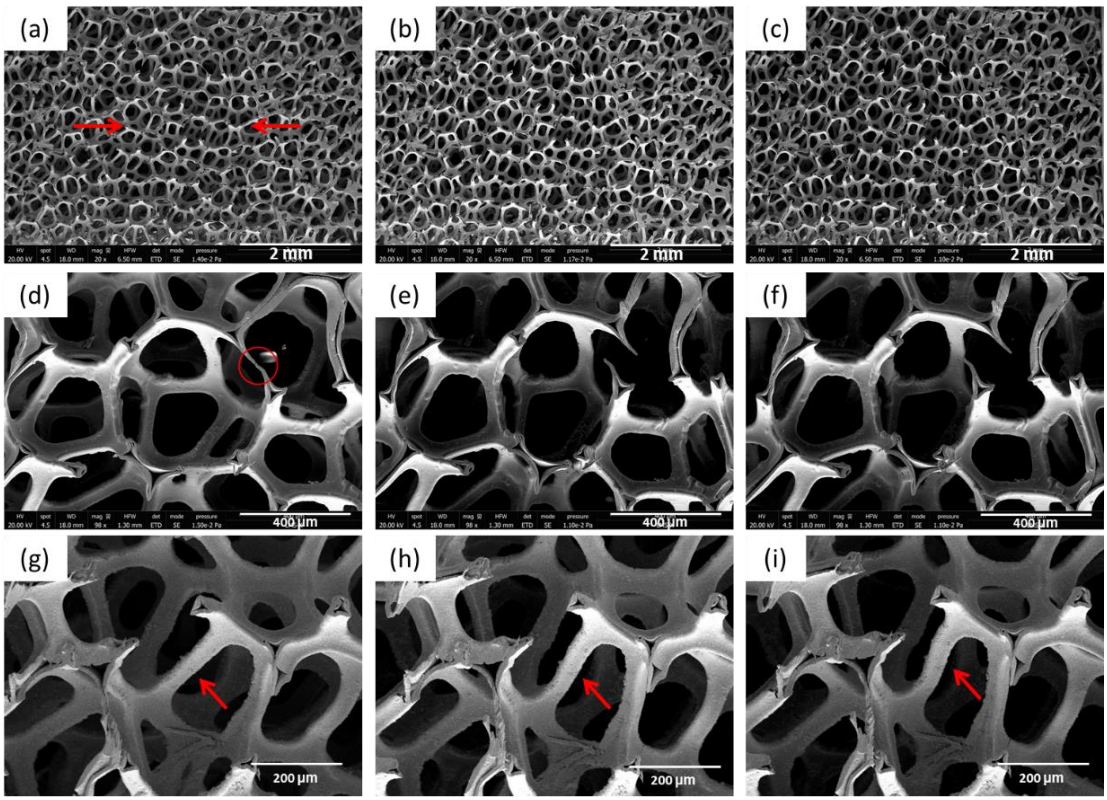

Fig. 2.57 SEM images of copper foam at the axial strain of (a) 0% (b) 4% and (c) 6% during compression test at 150 ℃, with (d) to (f) zooming on one pore located in the center, and (g) to (i) zooming on one strut.

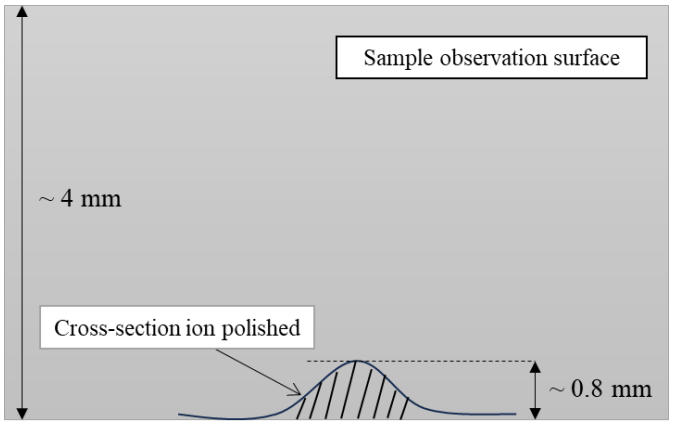

Fig. 2.58 Schematic of cross-section ion polishing of metal foam sample.

DIC analysis on the grain scale with the cross-section SEM images of the metal foam struts recorded during in situ compression tests could have been interesting. However, for depositing markers that provide strong local contrast on the struts' cross-sections (e.g., the deposition of Sn), the cross-section ion polishing has to be performed on the metal foam to achieve a sufficiently smooth sample surface. After numerous attempts, we found it impossible for the whole thickness of the metal

foam (thickness of 4 mm) cross-section to be ion-polished. The maximum achievable thickness of cross-section ion polishing for us was approximately 0.8 mm, and the polished area exhibited an irregular shape, as shown in Fig. 2.58. Thus, it was impossible to deposit the metal Sn as markers over the whole observation surface. This, in turn, resulted in the inability to perform DIC at the grain scale.

Mechanical behavior of aluminum foam

(1) At ambient temperature

The uniaxial compression test performed on sample Al01 was at ambient temperature. In total, 523 images with a resolution of 3296 × 2472 (pixel size at 2.75 μm) were recorded at a rate of one every 5 seconds during compression of the sample.

The macroscopic strain was obtained by computing via CMV the strain field of the overall observation surface of the sample from every 5 images recorded. In Fig. 2.59a, we present the image taken by the optical microscope of the initial state of the sample. This image was used as the reference image for digital image correlation. To calculate the macroscopic strain, the matrix of measurement points and the correlation domains for each point with the size of 100 × 100 pixels were defined on the reference image, as presented by blue squares shown in Fig. 2.59b. The vertical local strain gage was of 232 pixels, which corresponded to 638 μm, and the horizontal local strain gage was of 336 pixels, which corresponded to 924 μm**.** The correlation coefficient was set at 0.3 and the search domain was set at 30 × 30 pixels.

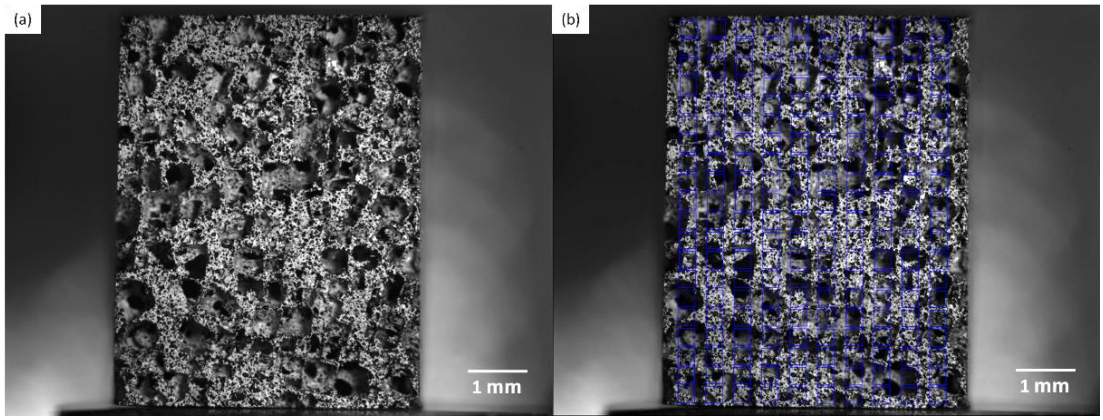

Fig. 2.59 (a) The initial state image of aluminum sample Al01 by optical microscope and (b) the same image serving as the reference image for computing the macroscopic strain maps using CMV with the matrix of points defined and the correlation domains shown in blue squares.

The compression stress-strain curve for Al01 is shown in Fig. 2.60. The aluminum foam first showed linear elasticity at low stresses and it provided a 0.2% offset yield strength of 4.48 ± 0.02 MPa and a Young's modulus of around 1217 ± 50 MPa. The measured Young's modulus agrees with the scaling law provided by Gibson and

Ashby [130, 131], presented in Equation (4), with the relative density equal to 0.27 (presented in Table 2.1), Young's modulus of solid AlSi0.12 to be around 76 GPa [194], and the constant $\alpha \approx 0.22$, which lies between the proposed theoretical range of 0.1 to 4 [130, 131]. With further loading, Al01 entered a long plastic stage, with pronounced and slightly accelerating strain hardening, resulting in a flow stress augmentation of approximately 7-8 MPa for a 20% change in deformation. The sample Al01 was unloaded when the stress reached 14.20 MPa with a macroscopic strain of 24%. At this point, the sample had not yet reached the third stage of densification, which is characterized by complete pore collapse.

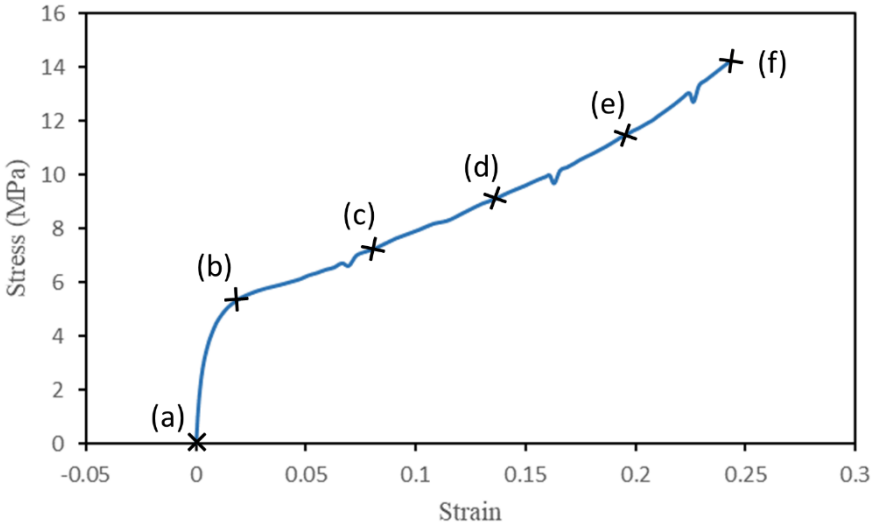

Fig. 2.60 The stress-strain curve from the uniaxial compression test at ambient temperature on Al01 obtained by DIC analysis.

The states of sample Al01 at different stress and strain states during compression are shown in Fig. 2.61, referred to as (a) to (f), with corresponding crosses marked on the stress-strain curve shown in Fig. 2.60. The load was applied vertically, on the upper face of the sample by the mobile piston, in the direction $-y$, with the bottom face loaded by the immobile piston attached to the loading frame. The regions outlined by white dashed lines in Fig. 2.61 indicate noticeable reductions and closures in pore size that can be observed visually.

To investigate the localization of strains in Al01 at the structural scale of pores and to demonstrate the possible existence of strain bands, we compute the strain field by DIC on reducing the correlation domain from 100 × 100 pixels to 50 × 50 pixels and increasing the number of measurement points. The local strain gage was of 100 pixels in both x and y directions (scheme 1 as integration contour), which corresponded to 275 µm. The correlation coefficient was set at 0.3 and the search domain was set at 10 × 10 pixels. The reference image was still the one shown in Fig. 2.59a and the new matrix of measurement points with the correlation domains in squares are presented in Fig. 2.62.

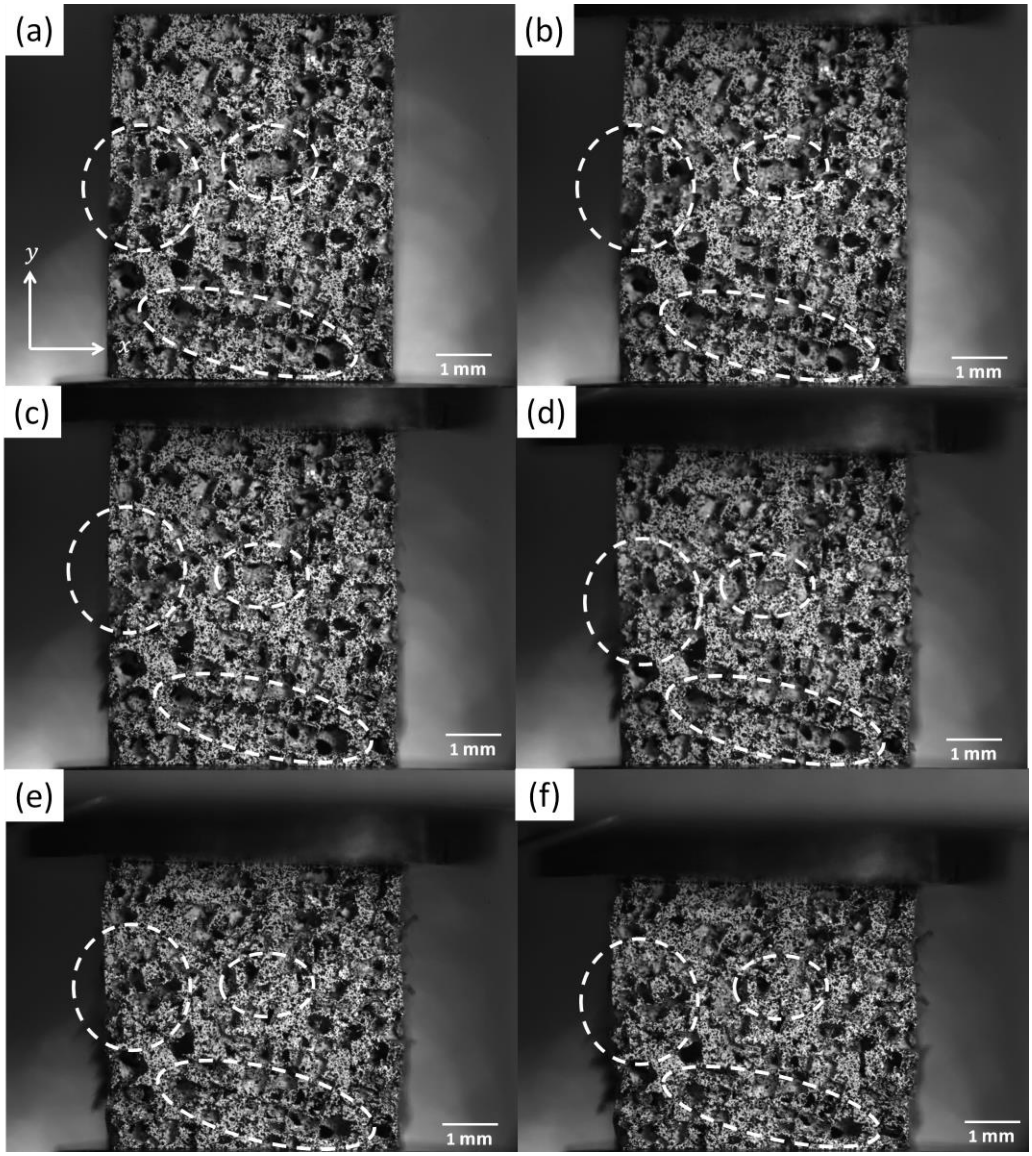

Fig. 2.61 Loaded open-cell aluminum foam sample Al01 at different strain of (a) 0%, (b) 2%, (c) 8%, (d) 14%, € 20% and (f) 24%.

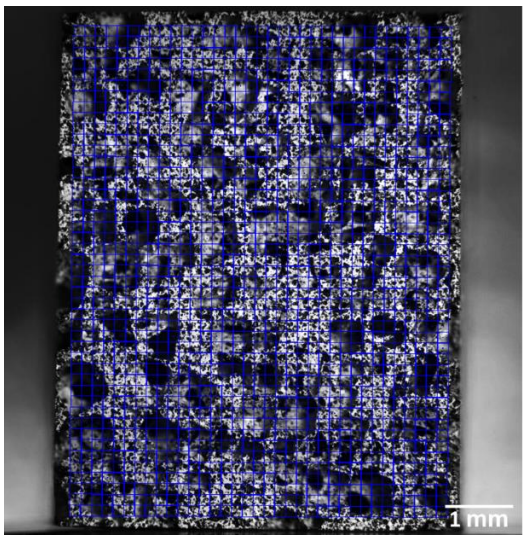

Fig. 2.62 Matrix of the measurement points defined and correlation domains in size of 50 × 50 pixels for computing the strain field at the metal foam structural scale of pores of Al01.

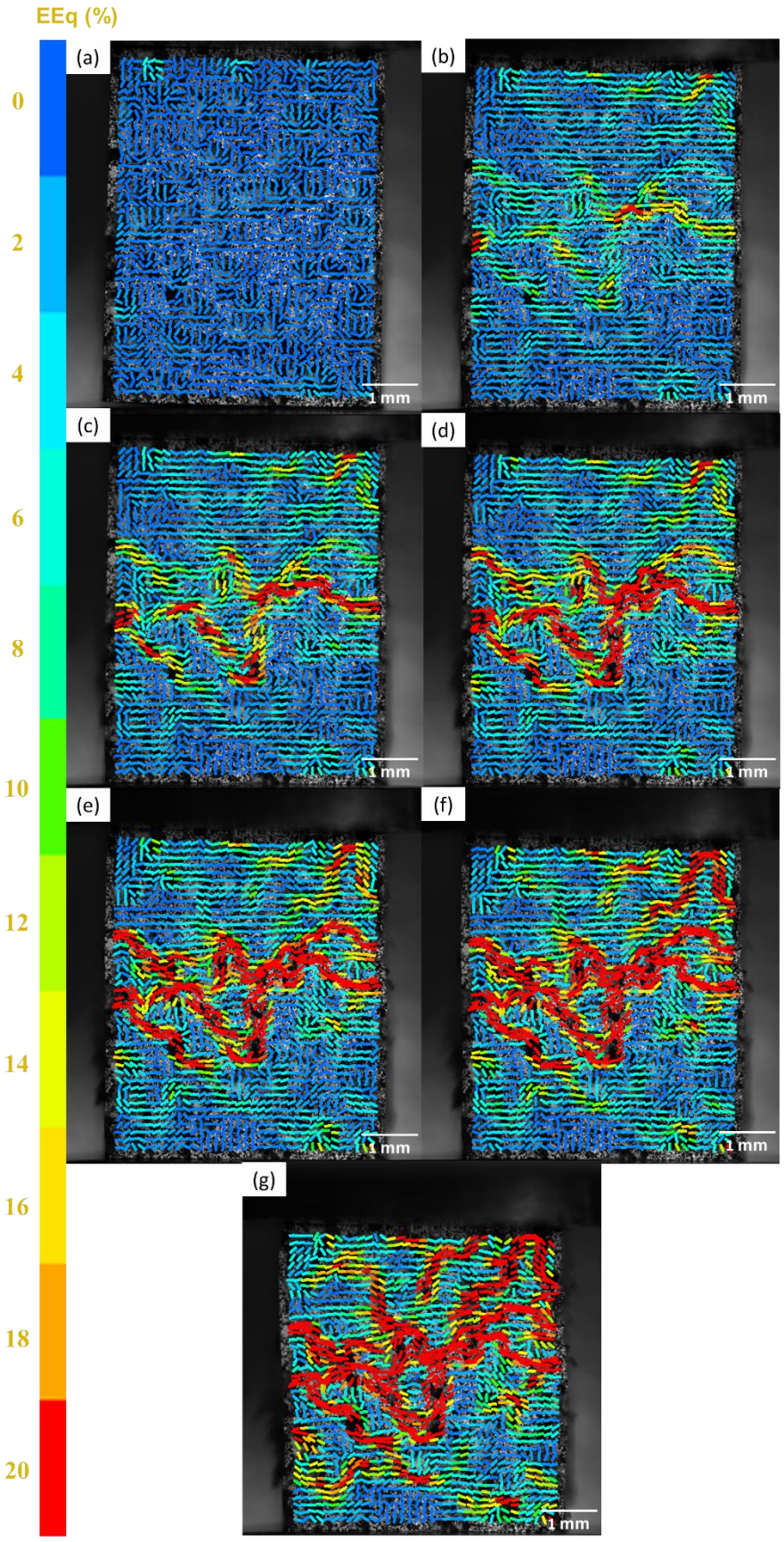

Fig. 2.63 Equivalent strain maps (correlation domain of 50 × 50 pixels) at different levels of the macroscopic strain of sample Al01 during compression (vertical) with (a) at 1% (b) at 2.4% (c) at 4% (d) at 6% (e) at 8%, (f) at 10% and (g) at 14%.

Fig. 2.63 presents the equivalent strain maps for sample Al01 computed at seven selected macroscopic strain levels of 1%, 2.4%, 4%, 6%, 8%, 10% and 14%. The macroscopic stresses corresponding to these seven strains are shown in Table 2.8. The color code we have chosen assigns warmer colors to indicate higher levels of strain, with the color red specifically representing the strongest strain localization. Note that all the strain maps displayed in Fig. 2.63 utilize the same color code scale, ranging from 0 to 20%.

As shown in Fig. 2.63a, the local deformation was relatively homogeneous at a macroscopic strain of 1%. From the macroscopic strain of 2.4% to 6% (Fig. 2.63b to d), distinct localization bands emerged and developed in the central region of the observation surface. Subsequently, these bands gradually intensified as the macroscopic strain reached between 8% and 10% (Fig. 2.63e and f). By the time the macroscopic deformation reached 15% (Fig. 2.63g), almost 50% of the entire observation surface was occupied by these strong localization bands.

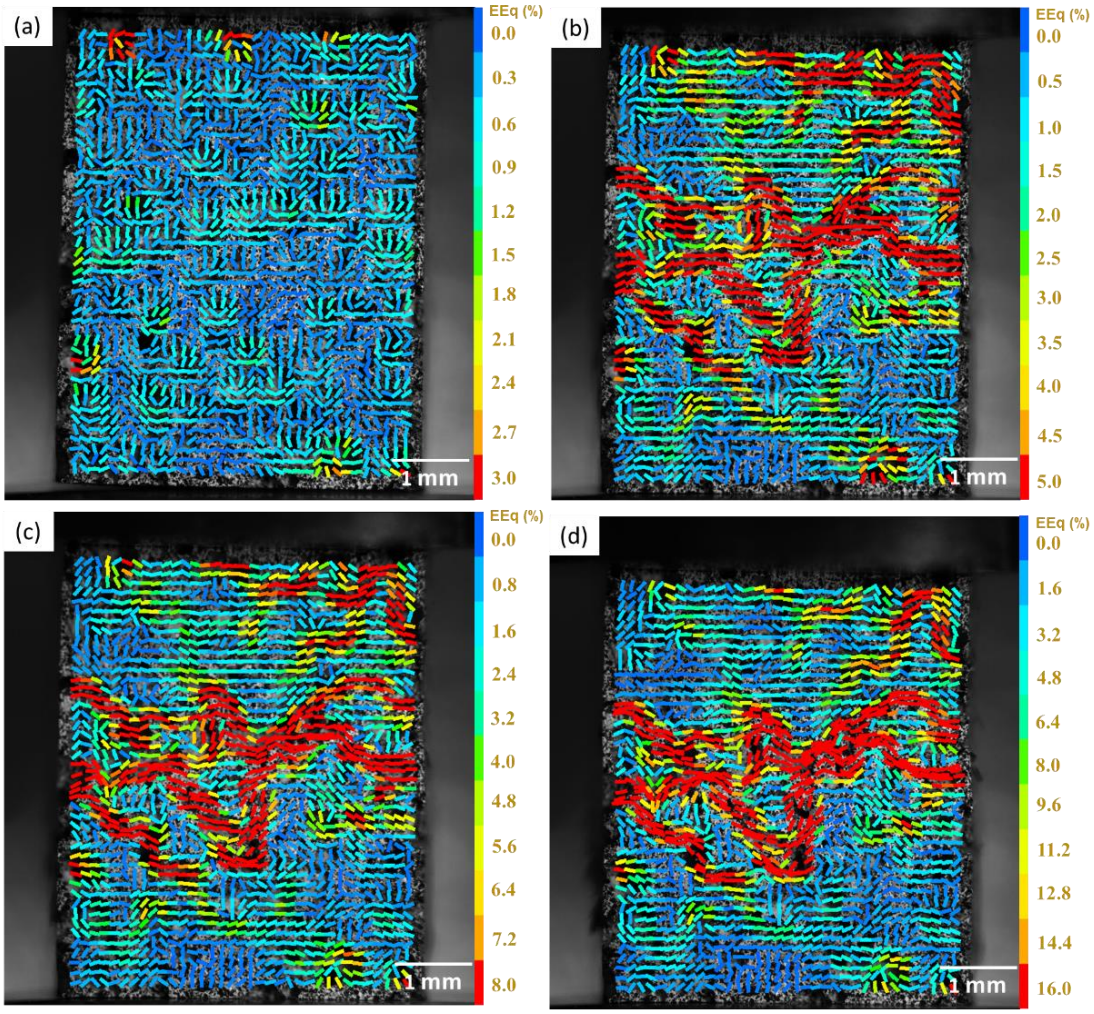

Fig. 2.64 Equivalent strain maps (correlation domain of 50 × 50 pixels) for Al01 during compression (vertical) at macroscopic strain levels of (a) 1% (b) 2.4%, (c) 4% and (d) 8% with different color code scales adapted to each strain map.

Then, we present in Fig. 2.64 the equivalent strain maps for sample Al01 computed at four selected macroscopic strain levels of 1%, 2.4%, 4%, and 8% with the color scale adapted to the specific range of each strain map. Fig. 2.64a shows that at a macroscopic strain of 1%, the deformation was still relatively homogeneous and no local strain bands were evidently visible, while Fig. 2.64b demonstrates that the strain bands exhibited at high macroscopic strains were already presented as early as 2.4% of the macroscopic strain and the bands continued to intensify over time.

To study the microscopic deformation mechanism of aluminum foam sample Al01 at ambient temperature, the grid of measurement points was refined with correlation domains of 25 × 25 pixels as shown in Fig. 2.65. The strain gage length for scheme 1 integration contour was of 50 pixels, corresponding to 137.5 μm. The correlation coefficient was set at 0.3 and the search domain was set at 10 × 10 pixels. For computing the strain fields, only measurement points of the material in the focal plane were selected for image correlation.

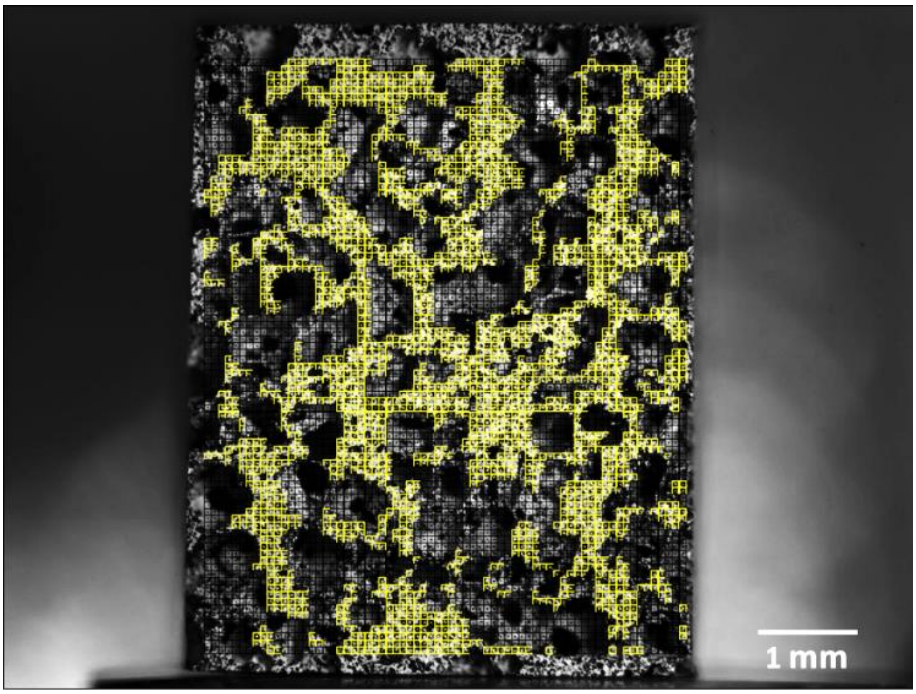

Fig. 2.65 Points and correlation domains defined on reference image for computing microscopic strain maps of aluminum foam sample Al01 under uniaxial compression.

The microscopic equivalent strain maps computed via DIC analysis for sample Al01 at six selected macroscopic strain levels of 1%, 2.4%, 4%, 6%, 8% and 10% are shown in Fig. 2.66. The macroscopic stresses corresponding to these six strains for Al01 are shown in Table 2.8. For the color code we selected, the color red represents the strongest localization of strain.

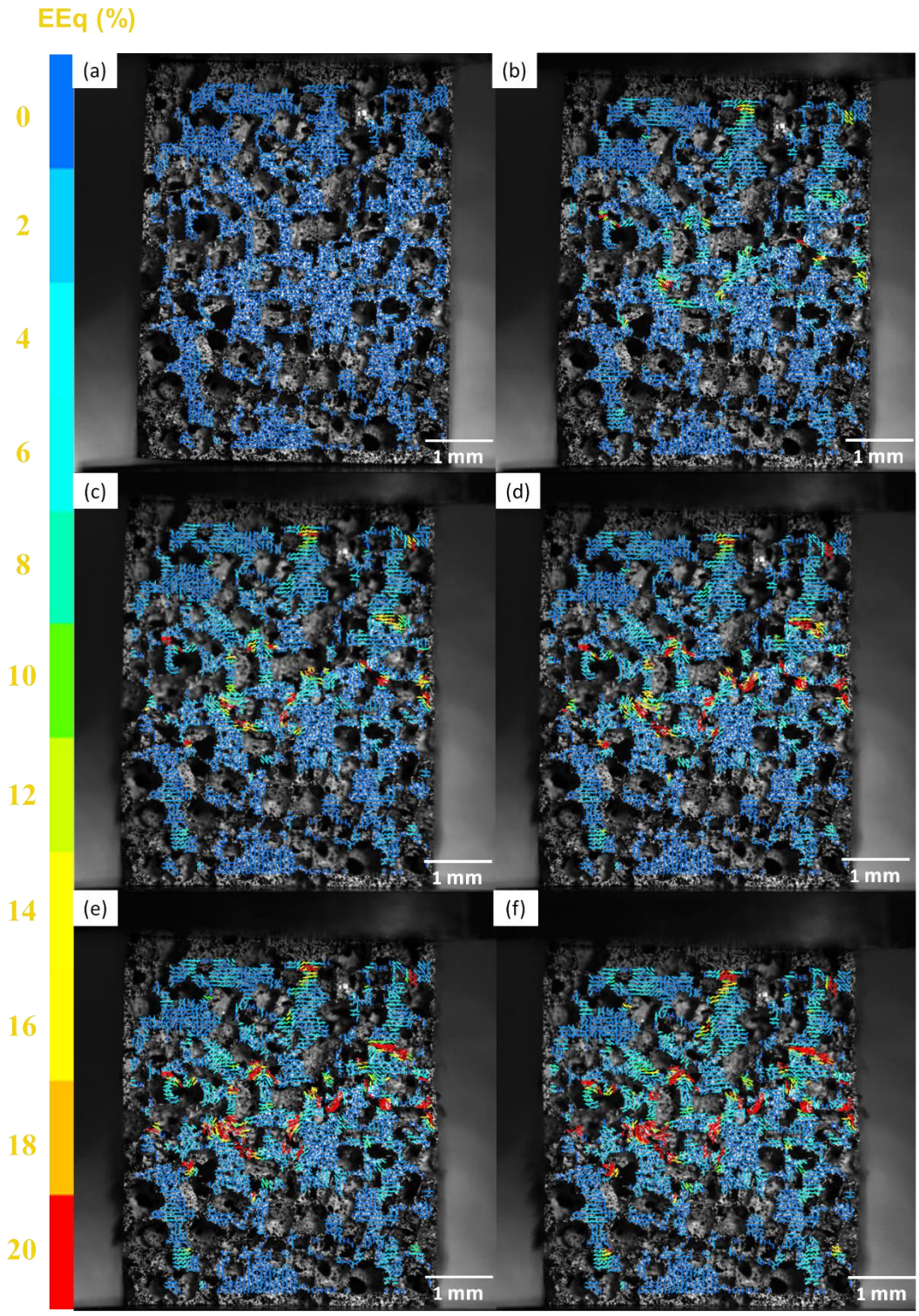

Fig. 2.66 Equivalent deformation maps at six levels of macroscopic strain of the sample Al01 during compression (vertical) with (a) at 1% (b) at 2.4% (c) at 4% (d) at 6% (e) at 8% and (f) at 10%.

As shown in Fig. 2.66a, during the initial compression phase, before the macroscopic stress reached about 5 MPa, the equivalent strain of the sample observation surface remained homogeneous. At the macroscopic stress of 5.57 MPa with a macroscopic strain of 2.4%, strain localization zones appeared on the upper and the central parts of the sample (see Fig. 2.66b). Unlike the open-cell copper

foams studied previously, the denser aluminum foam Al01 exhibited thicker and more varied structural elements. As a result, solid block-like regions were formed, which separated the pores, in contrast to the thin stick-like struts typically found in copper foams. It was found that the localizations of strain seemed to occur more easily at the junctions of these block regions. These localizations of strain continued to develop with the incensement of the macroscopic stress, as shown in Fig. 2.66c, d and e. In fact, from the state shown in Fig. 2.66c and on, the local equivalent strains may differ by more than an order of magnitude. When the macroscopic stress reached 7.96 MPa and induced a macroscopic strain of 10% (see Fig. 2.66f), such strong strain localization regions in the central and upper part of the sample observation surface can be clearly identified. These strain localizations primarily occurred in the junction areas between two block-like regions. Importantly, these weaker junctions started experiencing strain localization between 2.4% and 4% of macroscopic shortening, as shown in Fig. 2.66b and c. As the sample underwent further loading, the strain intensified within these existing localized areas with few localizations emerging up to 10% sample shortening. These observations highlighted the influence of the structural characteristics on strain localization, which became evident even at small strains. It is worth mentioning that these strain localizations in the junction areas aligned well with the localization bands observed during compression, as presented in Fig. 2.63.

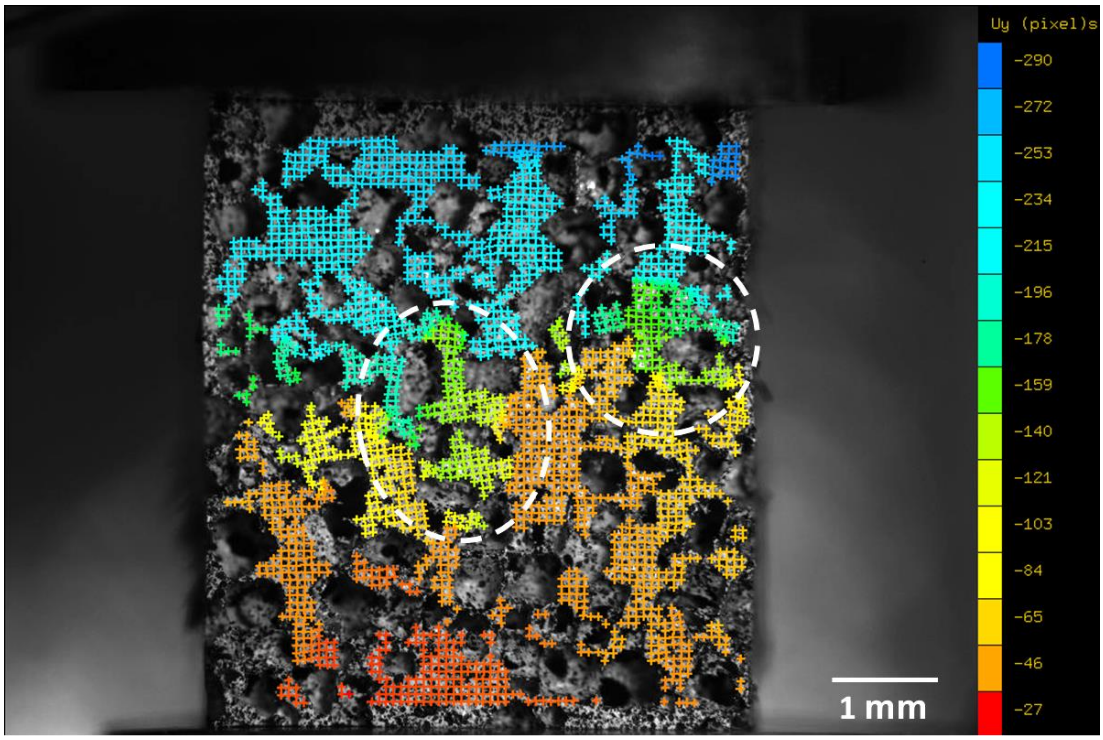

Fig. 2.67 Displacement map on the compression axis (vertical) of each correlation point of sample Al01 at the macroscopic strain of 10%.

The displacement field of each correlation point defined on the observation surface

of sample Al01 during uniaxial compression at a macroscopic strain of 10% is presented in Fig. 2.67. With the selected color code, blue represents larger displacement and red represents smaller displacement. Through this displacement field, we can see that the maximum displacement naturally occurred near the loading surface on the upper part of the sample and that it decreased gradually down to the lower part of the sample surface. However, significant discontinuities in displacement variation can be observed in the central region between the blocks circled in dashed lines in Fig. 2.67 and their neighboring blocks, as we observed in the corresponding equivalent strain map (Fig. 2.63f and Fig. 2.66f).

(2) At 150 ℃

The uniaxial compression test performed on sample Al02 was at a temperature of 150 degrees. In total, 339 images with resolution of 2300 × 2472 (pixel size at 2.75 μm) were recorded at a sampling rate of one image every 3 seconds during compression of the sample.

The macroscopic strain was obtained via CMV by computing the strain field of the overall observation surface of the sample every 3 images recorded. In Fig. 2.68a, we present the image taken by the optical microscope of the initial state of the sample. This image was used as the reference image for digital image correlation. The matrix of measurement points defined on the reference image and the correlation domains of 100 × 100 pixels were presented by blue squares as shown in Fig. 2.68b. The vertical local strain gage was of 232 pixels, which corresponded to 638 μm, and the horizontal local strain gage was of 332 pixels, which corresponded to 913 μm**.** The correlation coefficient was set at 0.3 and the search domain was set at 30 × 30 pixels.

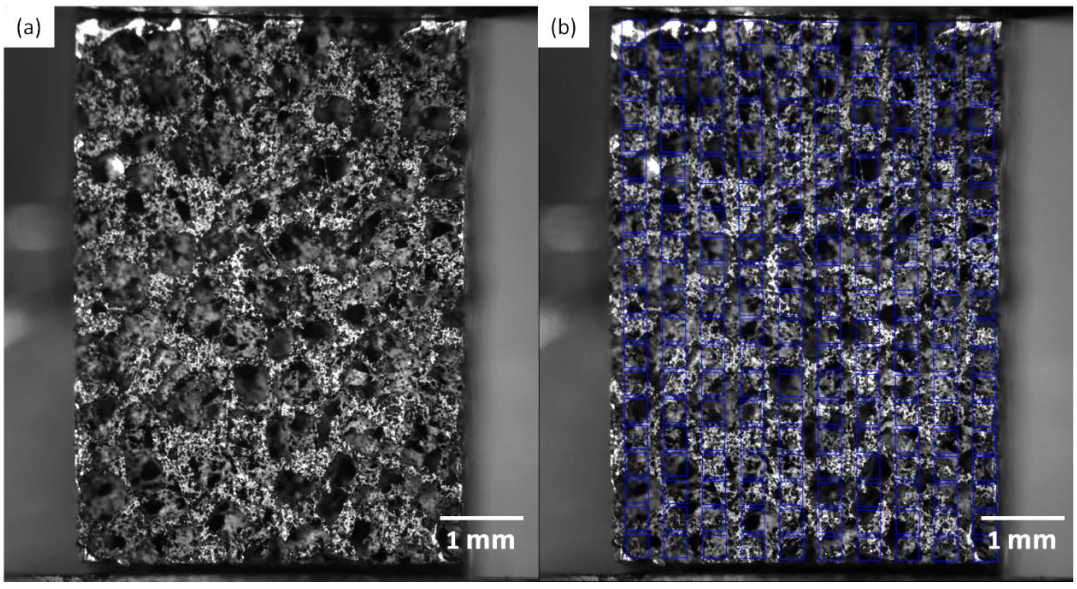

Fig. 2.68 (a) The initial state image of aluminum sample Al01 by optical microscope and (b) the same image serving as the reference image for computing the macroscopic strain maps using CMV with the matrix of points defined and the correlation domains shown in blue squares.

The compression stress-strain curve at 150 ℃ for sample Al02 is shown in Fig. 2.69. The aluminum foam first showed an elastic response at low stresses and its 0.2% offset yield strength was 2.12 ± 0.02 MPa and the Young's modulus was around 648 ± 50 MPa. The measured Young's modulus agrees with the scaling law provided by Gibson and Ashby [130, 131], presented in Equation (4), with the relative density equal to 0.27 (presented in Table 2.1), Young's modulus of solid AlSi0.12 to be around 76 GPa [194], and the constant $\alpha \approx 0.17$, which lies between the proposed theoretical range of 0.1 to 4 [130, 131]. As the loading continued to increase, the plastic deformation of the aluminum foam was initiated by the collapse of the pores. The densification stage started when the stress exceeded about 5.5 MPa with the macroscopic strain reaching approximately 24%. We stopped the loading when the stress reached 8.45 MPa and the macroscopic strain reached a level of 30%. Note the linear but moderate strain hardening with about 2 MPa strengthening upon 20% deformation shown in Fig. 2.69.

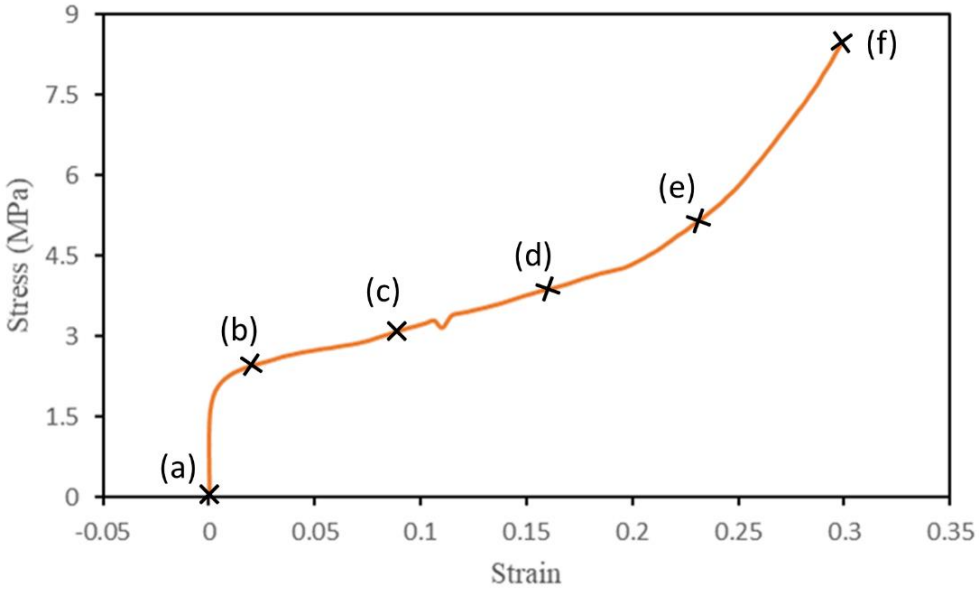

Fig. 2.69 The stress-strain curve from uniaxial compression test at 150 ℃ on Al02 obtained by DIC analysis.

The images of sample Al02 at different stress and strain during compression at 150 ℃ are shown in Fig. 2.70, referred to as (a) to (f) with corresponding crosses marked on the stress-strain curve shown in Fig. 2.69. The load was applied vertically from the upper face of the sample along the direction of $-y$ with the bottom of the sample kept still. As marked with white dashed circles in Fig. 2.70, the changes in pore shape, pore closure, and rupture of the connections between block-like solid parts of the foam can all be observed during the compression.

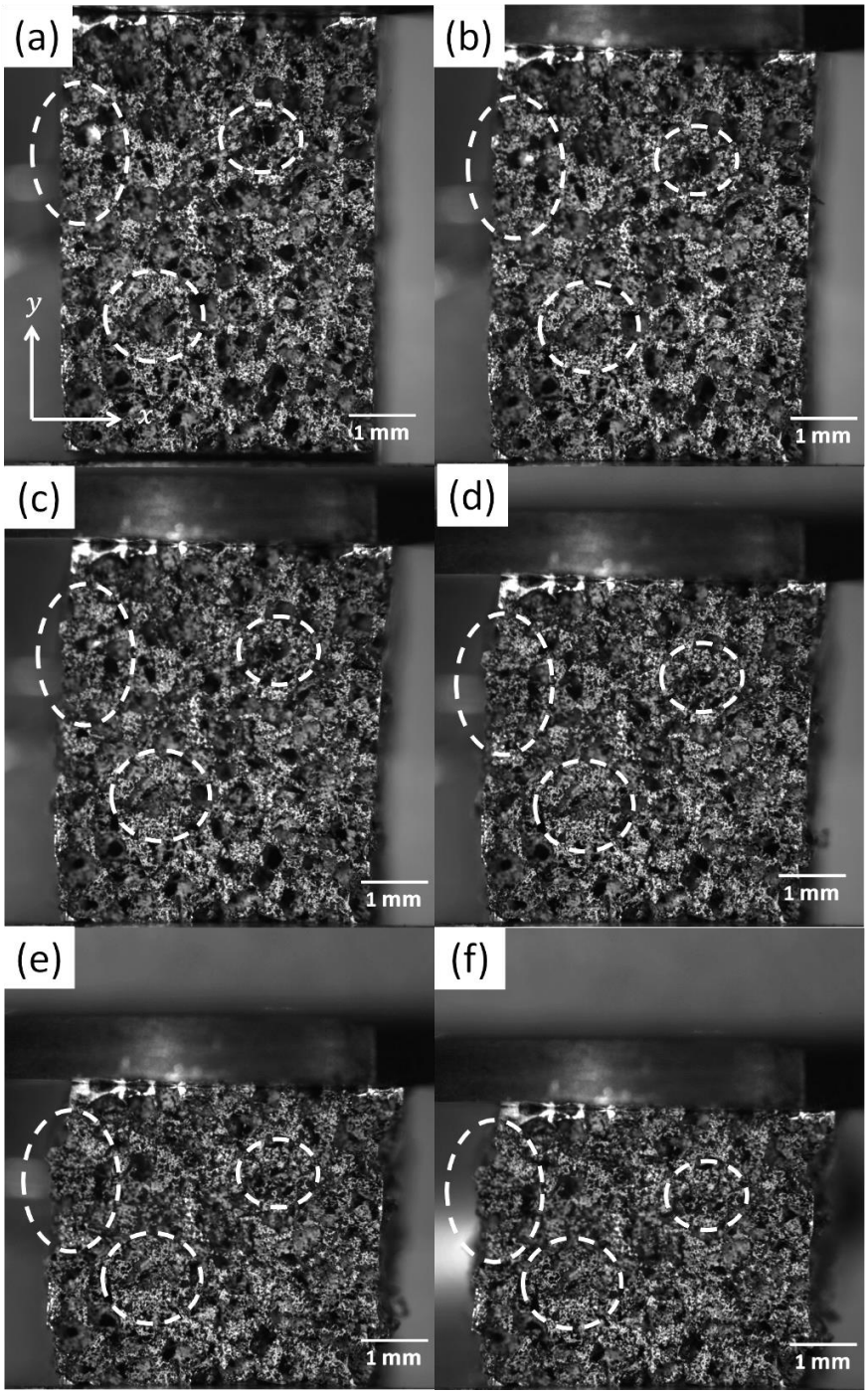

Fig. 2.70 Loaded open-cell aluminum foam sample Al02 at different strains of (a) 0%, (b) 2%, (c) 9%, (d) 16%, (e) 23% and (f) 30%.

To investigate the localization of strains in Al02 at the scale of pores and to demonstrate the possible existence of strain bands, we compute the strain field by DIC on reducing the correlation domain from 100 × 100 pixels to 50 × 50 pixels and by defining more measurement points. The local strain gage was of 100 pixels in both x and y directions (scheme 1 as integration contour), which corresponded to 275 μm. The correlation coefficient was set at 0.3 and the search domain was set at 10 × 10 pixels. The reference image was still the one shown in Fig. 2.68a and the

new matrix of measurement points with the correlation domains in squares are presented in Fig. 2.71.

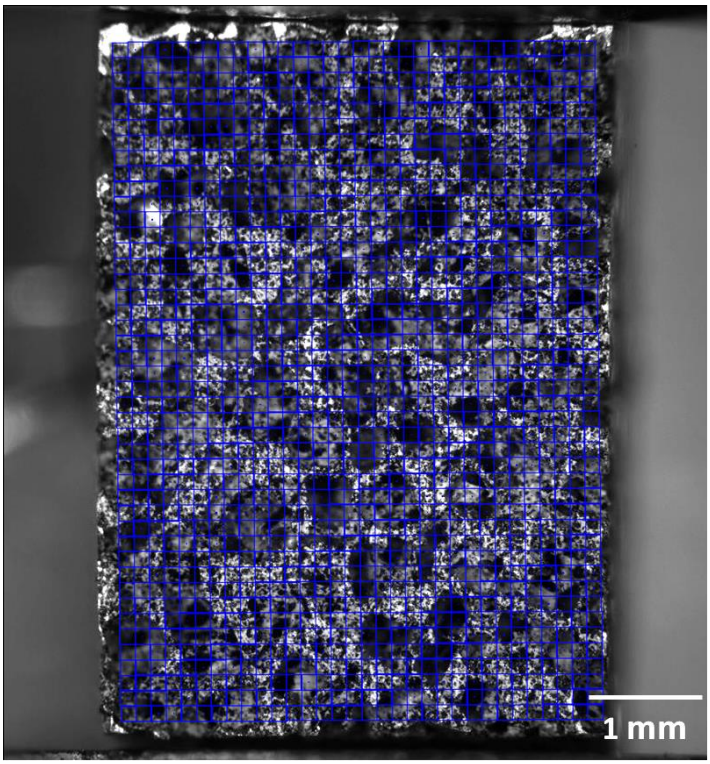

Fig. 2.71 Matrix of the measurement points defined and correlation domains in size of 50 × 50 pixels for computing the strain field at the metal foam structural scale of pores of Al02.

Fig. 2.72 shows the equivalent strain maps for sample Al02 computed at six selected macroscopic strain levels of 1%, 4%, 7%, 10%, 12% and 15%. The macroscopic stresses corresponding to these six strains are shown in Table 2.8. The color code we have chosen assigns warmer colors to indicate higher levels of strain, with the color red specifically representing the strongest strain localization. Note that all the strain maps displayed in Fig. 2.72 are presented with the same color code scale, ranging from 0 to 20%.

It can be seen from Fig. 2.72a that the shape of the three horizontal localization bands were already relatively obvious at a macroscopic strain of 1%. From the macroscopic strain of 4% to 7% (Fig. 2.72b and c), three horizontal localization bands began to develop progressively, with two of them extending almost the entire length of the observation plane. These horizontal bands subsequently intensified as the macroscopic strain continued to increase from 10% to 15% (Fig. 2.72d, e and f). At a macroscopic strain level of 10% (Fig. 2.72d), multiple localization bands initiated along the axial stress direction and progressively intensified as the macroscopic strain increased (Fig. 2.72e and f). At a macroscopic deformation of 15% (Fig. 2.72f), the strong localization bands were widely distributed and interconnected over the observation surface. These localizations were most likely accompanied by a reduction in pore size or even pore collapse.

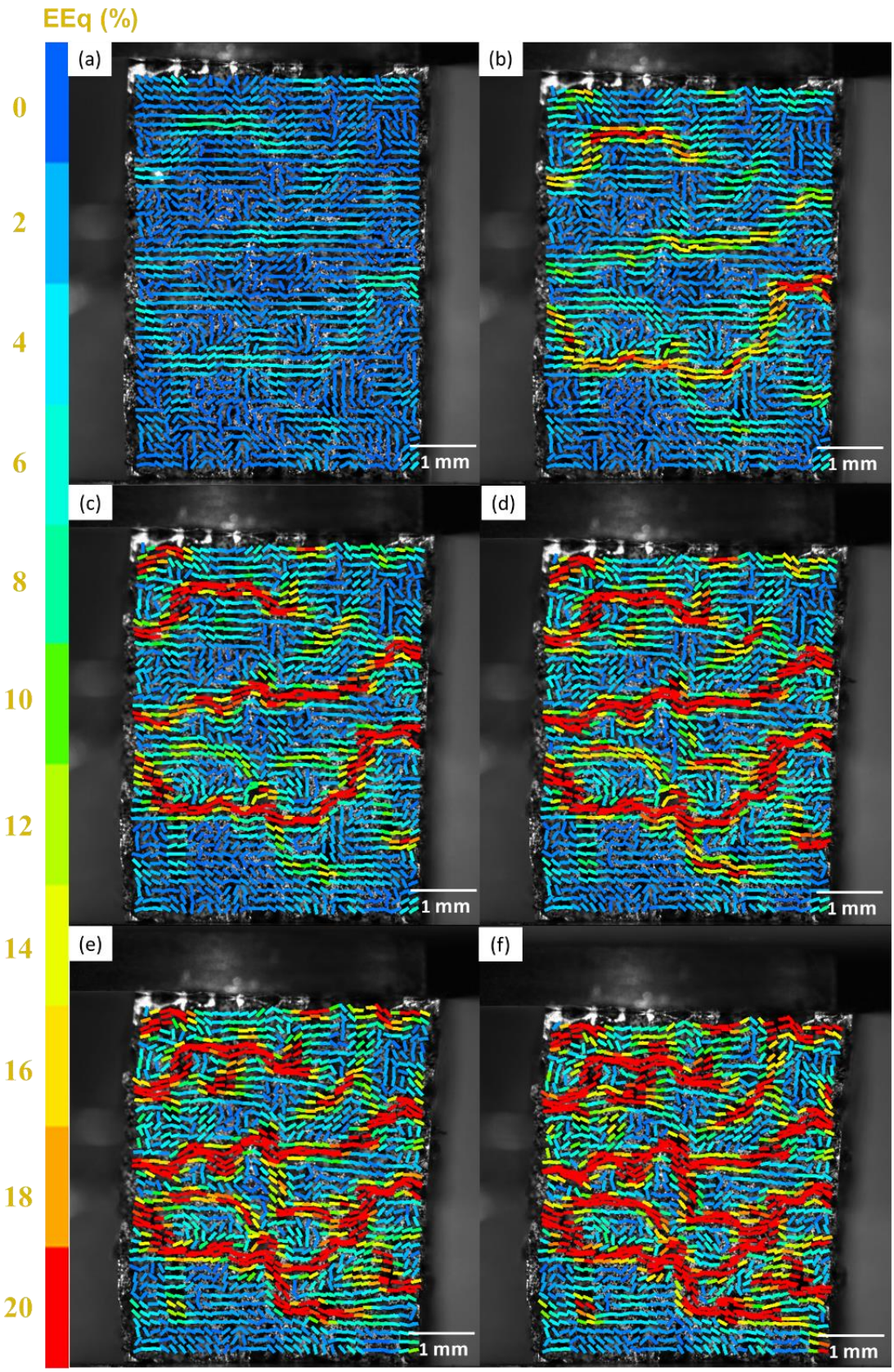

Fig. 2.72 Equivalent strain maps (correlation domain of 50 × 50 pixels) at different levels of the macroscopic strain of sample Al02 during compression (vertical) with (a) at 1% (b) at 4% (c) at 7% (d) at 10% (e) at 12% and (f) at 15%.

We present in Fig. 2.73 the equivalent strain maps for sample Al02 computed at three selected macroscopic strain levels of 1%, 4%, and 8% with color scale adapted to the specific range of each strain map. Fig. 2.73a illustrates that the localization bands have already formed at a macroscopic strain of 1% for Al02 when compressed at a temperature of 150 ℃. This is in contrast to our observations for Al01 when compressed at ambient temperature, where the localization bands did not appear until a macroscopic strain of 2.4%, indicating that temperature might have an important influence on the early-stage plastic behavior of the porous structure of the metal foam. The strain maps in Fig. 2.73 also show that significant localizations began early in the deformation process and progressively accumulated a considerable amount of strain thereafter (Fig. 2.73b and c). It can be concluded that these initial localizations were initiated at the onset of plasticity and continued to intensify as the deformation progressed.

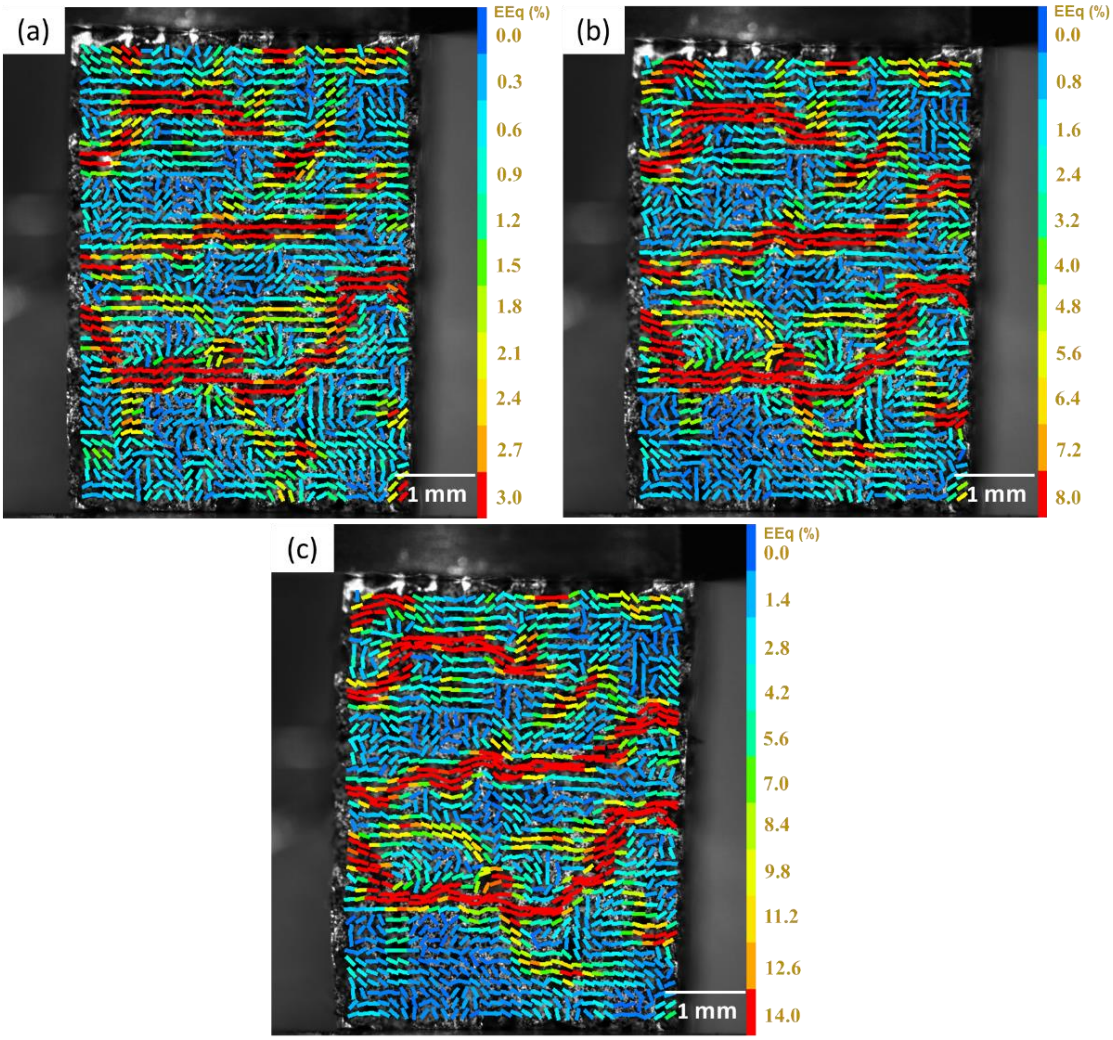

Fig. 2.73 Equivalent strain maps (correlation domain of 50 × 50 pixels) for Al02 during compression (vertical) at macroscopic strain levels of (a) 1% (b) 4% and (c) 8% with different color code scales adapted to each strain map.

To study the microscopic deformation mechanism of aluminum foam sample Al02 at 150 ℃ by DIC, the matrix of measurement points and the correlation domains of 25 × 25 pixels were defined on the reference image, as presented by yellow squares shown in Fig. 2.74. The strain gage length was of 50 pixels, corresponding to 137.5 μm. The correlation coefficient was set at 0.3 and the search domain was set at 10 × 10 pixels. For computing the strain field more precisely, only measurement points lying in the focal plane were selected for image correlation.

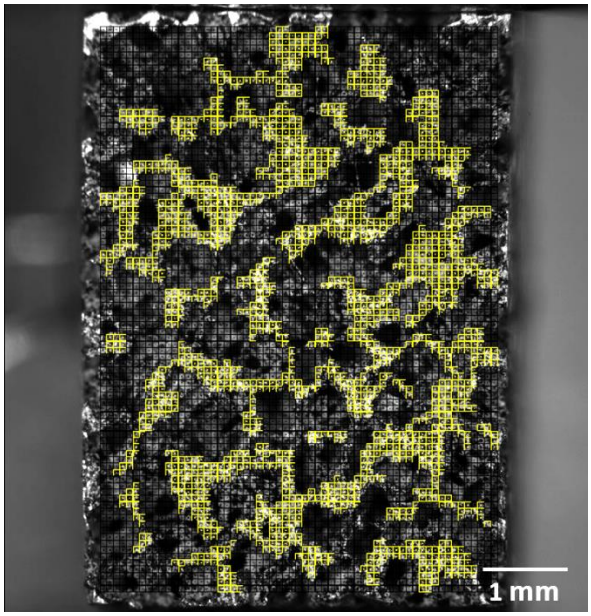

Fig. 2.74 Points and correlation domains defined on reference image for computing microscopic strain maps of aluminum foam sample Al02 under uniaxial compression at 150 ℃.

The microscopic equivalent strain fields calculated by DIC for sample Al02 at 8 selected macroscopic strain levels of 1%, 2.4%, 4%, 6%, 8%, 10%, 12%, 14% and 15% are shown in Fig. 2.75. The macroscopic stresses corresponding to these strains for Al02 are shown in Table 2.8. For the color code we selected, the color red represents the strongest localization of strain. As shown in Fig. 2.75a, during the initial compression phase, before the macroscopic stress reached 2.31 MPa, the equivalent strain of the sample observation surface remained relatively homogeneous, with a small zone of strain localization appearing in the upper part of the sample. When the macroscopic stress reached 2.49 MPa with a corresponding macroscopic strain of 2.4%, multiple strain localization zones started to appear at different parts of the sample surface (see Fig. 2.75b). Strain localization continued during further loading to develop progressively in different zones of the sample surface, as shown in Fig. 2.75c to f. Just like what we observed for Al01, the weaker zones were usually found at the junctions of adjacent solid blocks of the surface material. This can be seen clearer in Fig. 2.75g and h, where the macroscopic strain reached 14% and 15 % respectively. After reaching this level of macroscopic strain, strong localization was found at most of the junctions between two adjacent blocks that formed the walls of the pores.

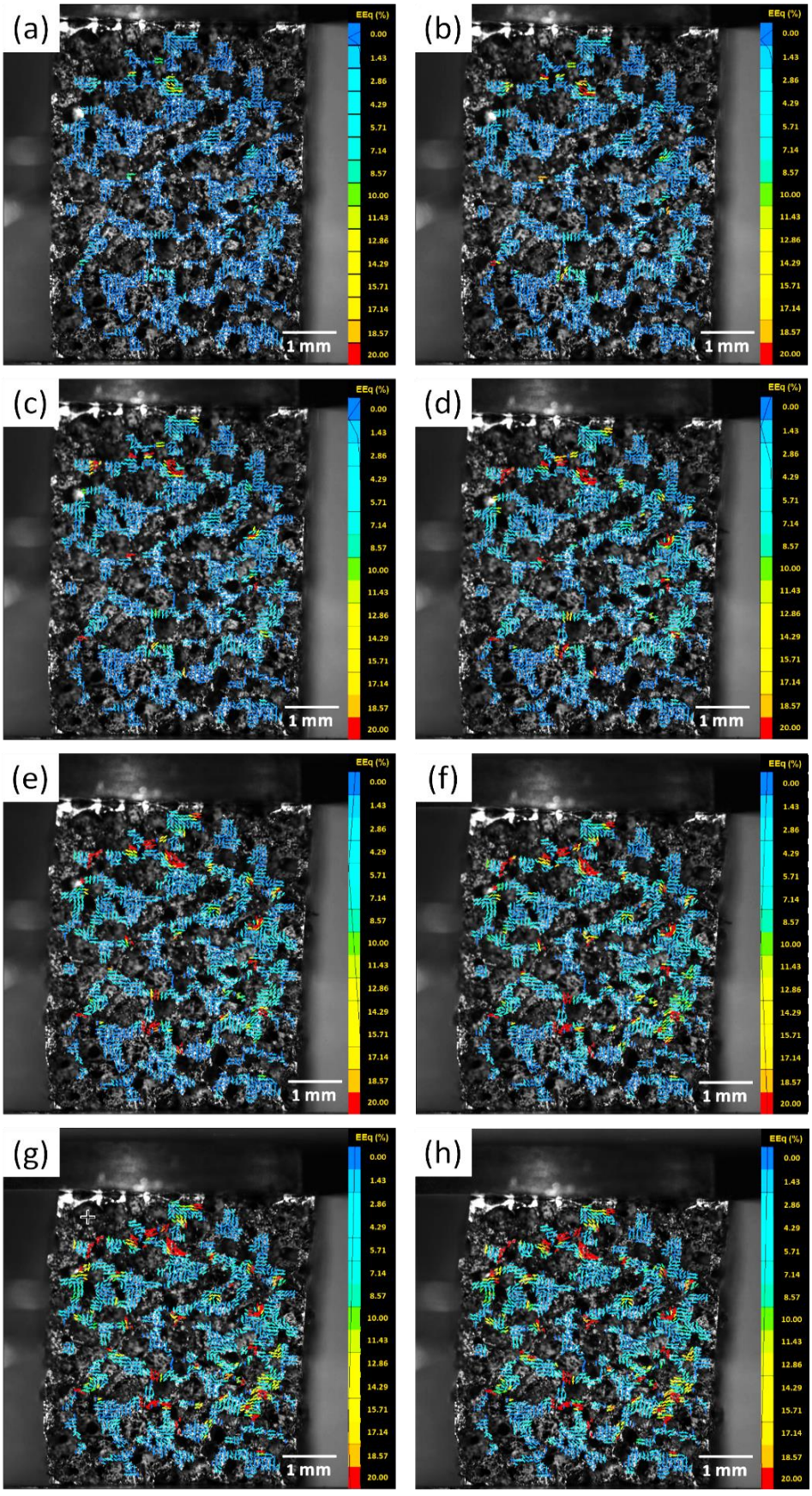

Fig. 2.75 Equivalent deformation maps at eight levels of macroscopic strain of the sample Al02 during compression (vertical) at 150 degrees with (a) at 1% (b) at 2.4% (c) at 4% (d) at 7% (e) at 10% (f) at 12% (g) at 14% and (h) at 15%.

The displacement field of each correlation point defined on the observation surface of sample Al02 during uniaxial compression at a macroscopic strain of 15% is presented in Fig. 2.76. With the selected color code, blue represents larger displacement and red represents smaller displacement. The displacement map clearly illustrates that the maximum displacement occurred in the upper region of the sample. It is evident that the solid block-like structures of the foam behaved as rigid bodies, exhibiting uniform displacement. Similar to our previous observations on Al01, notable discontinuities in displacement were observed between these blocks and their neighboring blocks, consistent with the observations shown in Fig. 2.72f and Fig. 2.75f.

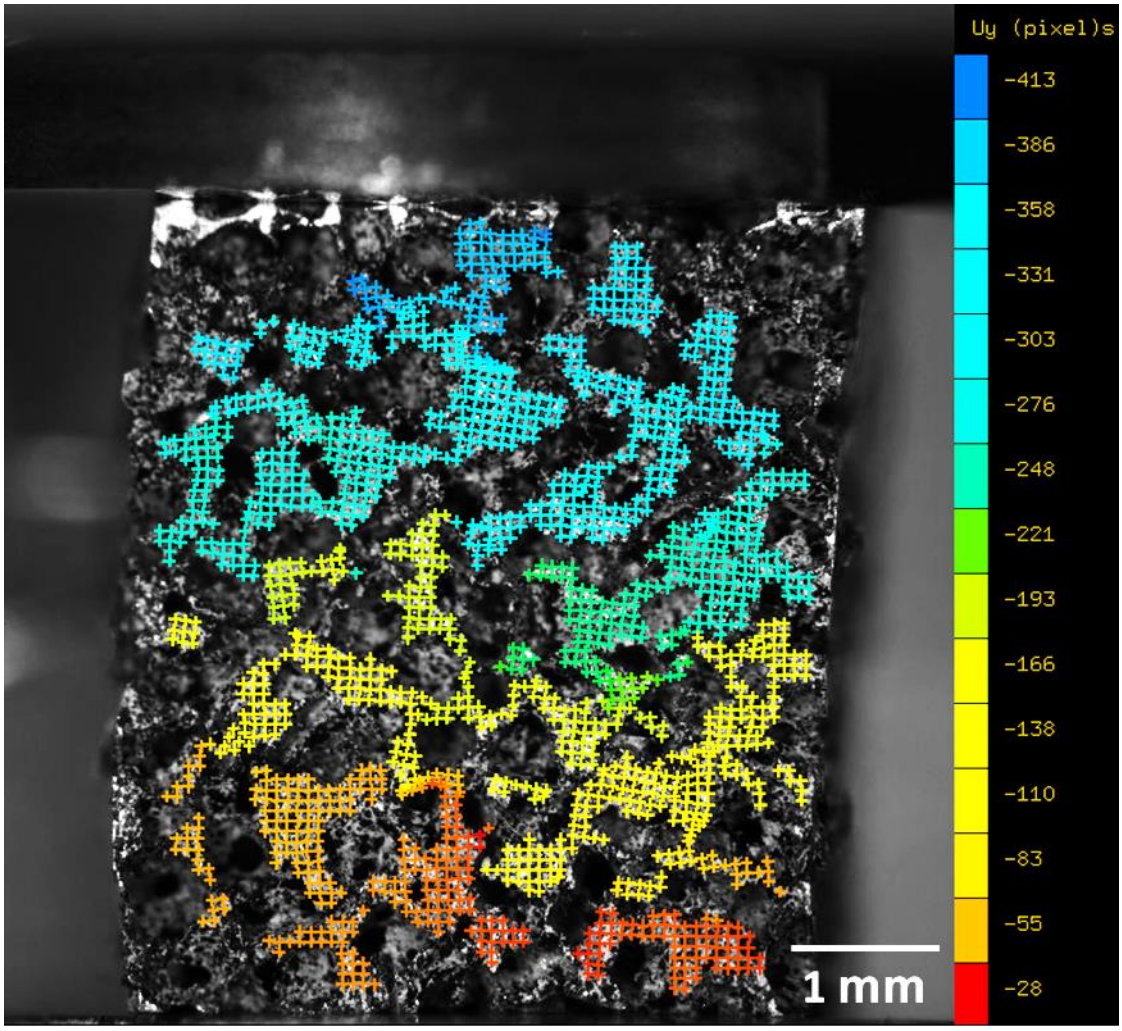

Fig. 2.76 Displacement map on the compression axis (vertical) of each correlation point of sample Al02 at a macroscopic strain of 15%.

The in situ SEM uniaxial compression test at 150 ℃ provided a clearer view of the deformation mechanism of the pores collapse in the aluminum foam. Images were recorded at a resolution of 6144 × 4415 pixels, with one pixel corresponding to about 1.06 μm. The SEM images shown in Fig. 2.77 represent the sample at various loading states. The loading direction (horizontal) is indicated in Fig. 2.77a.

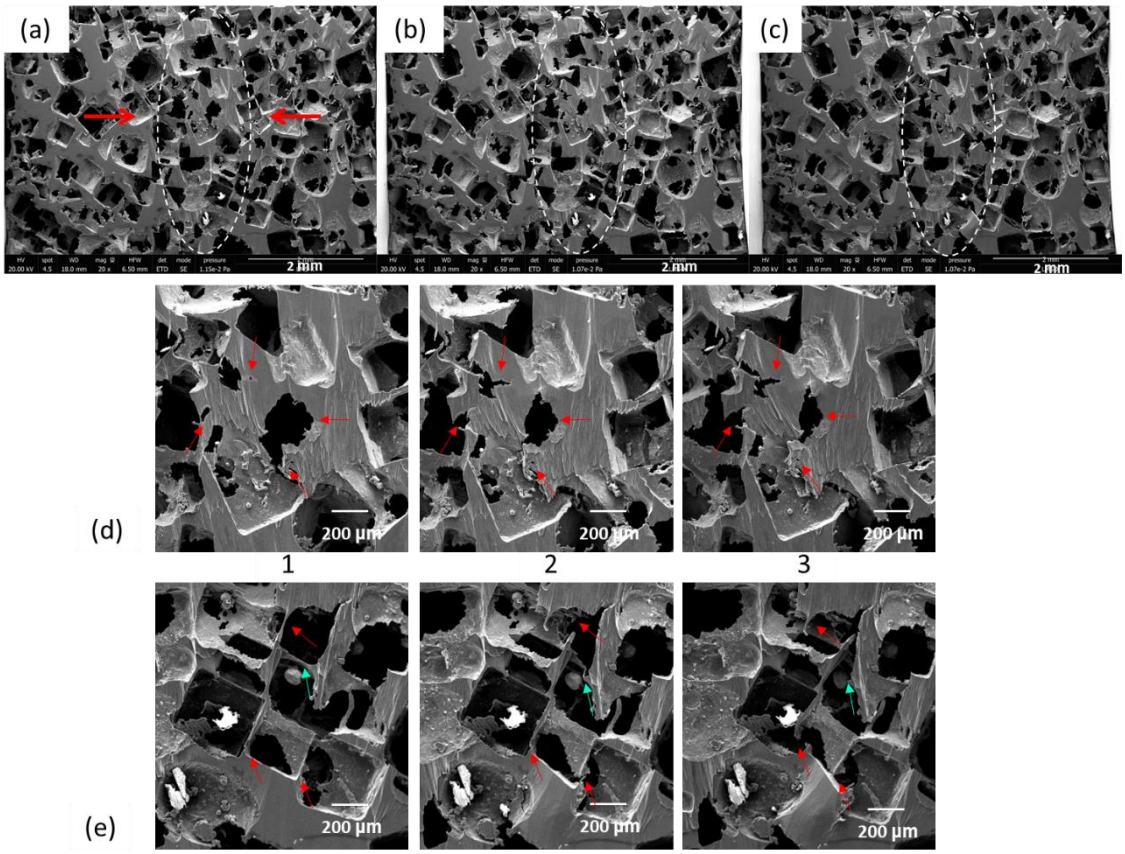

Fig. 2.77 SEM images of the aluminum foam at the axial strain of (a) 0% (b) 4% and (c) 6% during the compression test at 150 °C, with (d) and (e) zooming on several pores located on the strain localization band during these 3 steps, corresponding to the axial strain of (a) to (c) respectively.

At an axial strain of 4% (Fig. 2.77b), a clear deformation (compaction) band was observed compared to the initial state (Fig. 2.77a), located in the center of the sample surface. The deformation band is marked by circling. The strain localization developed as the loading increased to an axial strain of 6% (Fig. 2.77c). The mechanisms combined both plastic strain and local rupture of ligaments (sheets or struts) ensuring continuity between block-like solid portions. The collapse or reduction in pore size within the strain bands was a consequence of these mechanisms, including the thrusting of failed portions onto adjacent regions. Fig. 2.77d and e illustrate two zones chosen on the deformation band for presenting how the pores collapsed during loading. Firstly, as can be seen clearly from the SEM images, the aluminum foam was very heterogeneous in terms of the pore size and thickness of the struts. There also existed numerous defects on the struts. For example, in Fig. 2.77 (d1) to (d3), it is evident that fracture defects were already present in the struts of the sample in its initial state. These cracks propagated during the testing process, ultimately resulting in the complete rupture of the struts or sheet-like walls surrounding the pores. Additionally, the thrusting of the right-hand part of the aluminum foam over the left-hand part can be observed along the "compaction band" shown in Fig. 2.77d, which finally led to compaction. In Fig. 2.77 (e1) to (e3), we see ultra-thin struts (about several tens of micrometers) rupturing

during compression and thus causing the collapse of the pores. It is interesting to note that in Fig. 2.77 (e2) we were also able to observe the buckling of the strut at an axial strain of 4% (pointed out in the blue arrow) and the break of this strut at an axial strain of 6% (Fig. 2.77 (e3)).

As previously explained, it was not feasible to perform ion polishing on the entire observation surface of metal foam samples with a thickness of approximately 4 mm. Consequently, it was impossible to deposit markers for DIC, resulting in the unavailability of quantitative results for strain localization using SEM images recorded during in situ compression test.

DVC results

The DIC of optical images in 2 dimensions and the observation during in situ SEM compression tests allowed us to study the microscopic compressive deformation mechanism on the selected observation surface of the metal foams. To better understand the spatial deformation mechanism of both copper foam and aluminum foam during compression, and especially for investigating the volumetric changes inside the foams, the technique of X-ray microtomography was applied before and after the compression tests of the samples deformed in situ. The images acquired from X-ray microtomography were then used to compute the 3D strain fields by digital volume correlation (DVC).

Aluminum sample Al-to and copper foam sample Cu-to were used for applying the X-ray microtomography before and after the uniaxial compression test. The sample details are presented in Table 2.3. In Fig. 2.78, we present the cross-section image of X-Y plan and the cross-section of X-Z plan before the loading obtained by X-ray microtomography. From the cross-section images of sample Al-to shown in Fig. 2.78b and c, we can see that the shape of struts and pores of aluminum foam were very heterogeneous. Pores were rectangular, circular and triangular. Also, at some spots, the struts consisted of solid material with considerable thickness, while others may consist of just a thin layer of the material, similar to what we have observed and described in section 2.4.1. For copper foam sample Cu-to, as shown in Fig. 2.78e and f, the struts were hollow and the shape and size of pores were homogeneous. Another major difference between these two foams that can be seen clearly from the cross-section images presented is the porosity. The aluminum foam was much less porous (40% porosity) than the copper foam (93.5% porosity).

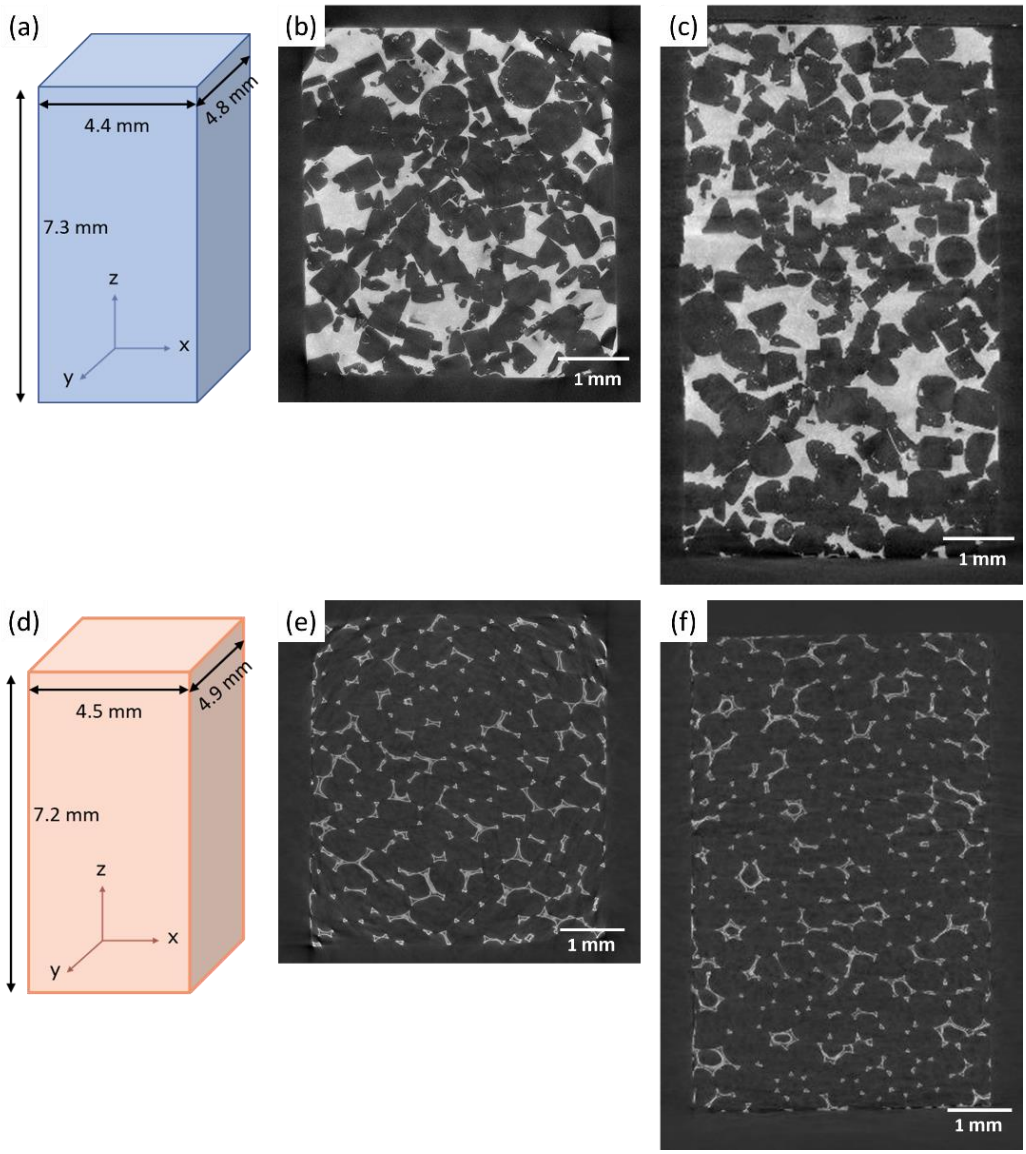

Fig. 2.78 The initial sample size of (a) aluminum foam Al-to and (d) copper foam Cu-to, with X-Y plan cross-section of (b) Al-to and (e) Cu-to, and X-Z plan cross-section of (c) Al-to and (f) Cu-to.

The macroscopic stress-strain curves presented in Fig. 2.79 for both aluminum foam sample Al-to and copper foam sample Cu-to were obtained by DIC analysis in 2 dimensions, based on optical imaging. It can be seen that the very beginning of the experiments corresponded to apparent extension deformations. This surprising observation was also reported in the work of other researchers in our lab using the same micro compression machine and the same DIC software [195, 196]. This can be explained by magnification variations: during the initial loading, the stress increased abruptly and caused out-of-plane movements of the testing machine and therefore of the sample, which changed the working distance and consequently induced a slight variation in magnification [195, 196], in the order of 10^{-4} in our case. The 0.2% offset yield stress of Al-to was 2.10 ± 0.02 MPa and 0.28 ± 0.02 MPa for copper foam sample Cu-to, which were both comparable to the 0.2% offset yield stress obtained for sample Al02 (2.12 ± 0.02 MPa) and Cu02 (0.27 ± 0.02 MPa)

compressed under the same experimental condition. Both of the samples were unloaded at a macroscopic strain of approximately 9%.

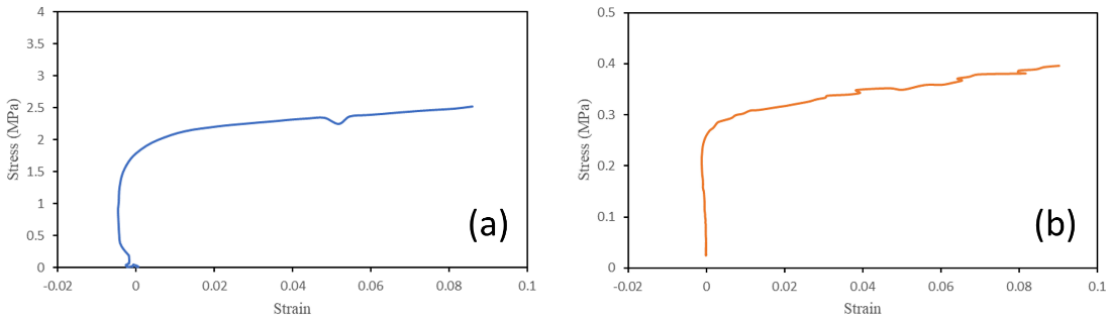

Fig. 2.79 The macroscopic stress-strain curve of (a) sample Al-to and (b) sample Cu-to under uniaxial compression test at 150 °C.

The analysis by volumetric digital image correlation was achieved by the 3D version of the software CMV. The results were visualized with Paraview. In Fig. 2.80, the longitudinal deformation maps at the final strain level are presented for both the aluminum foam sample Al-to and the copper foam sample Cu-to with the same color code scale. With the color code selected, strong strain localizations appear in red. The correlation domain size was 60 voxels and the strain gage length was set to 130 voxels, corresponding to 312 µm for a voxel size of 2.4 µm. The plastic deformation in the aluminum foam exhibited highly pronounced localized regions, characterized by large bands that extended throughout the entire volume of the sample. As shown in Fig. 2.80a and b, several strong localization bands formed in the foam with a width of about 400 µm. While copper foam deformed much more homogeneously compared to aluminum foam at the same level of macroscopic strain, with a rather homogeneous distribution of numerous thin localization bands propagated at 45° of the loading direction (vertical). This means that almost all the pores and struts in copper foam accommodated plastic deformation in comparable amounts. As can be seen from Fig. 2.80c and d, a prominent localization band was generated near the bottom surface of the sample Cu-to, specifically at the corner. Another localization region appeared at the diagonally opposite corner on the upper surface, where the load was applied. These areas were likely influenced by misalignment or a lack of parallelism between the loaded sample faces. The patterning phenomena identified in 3 dimensions are similar to those we have observed with the 2D DIC analysis.

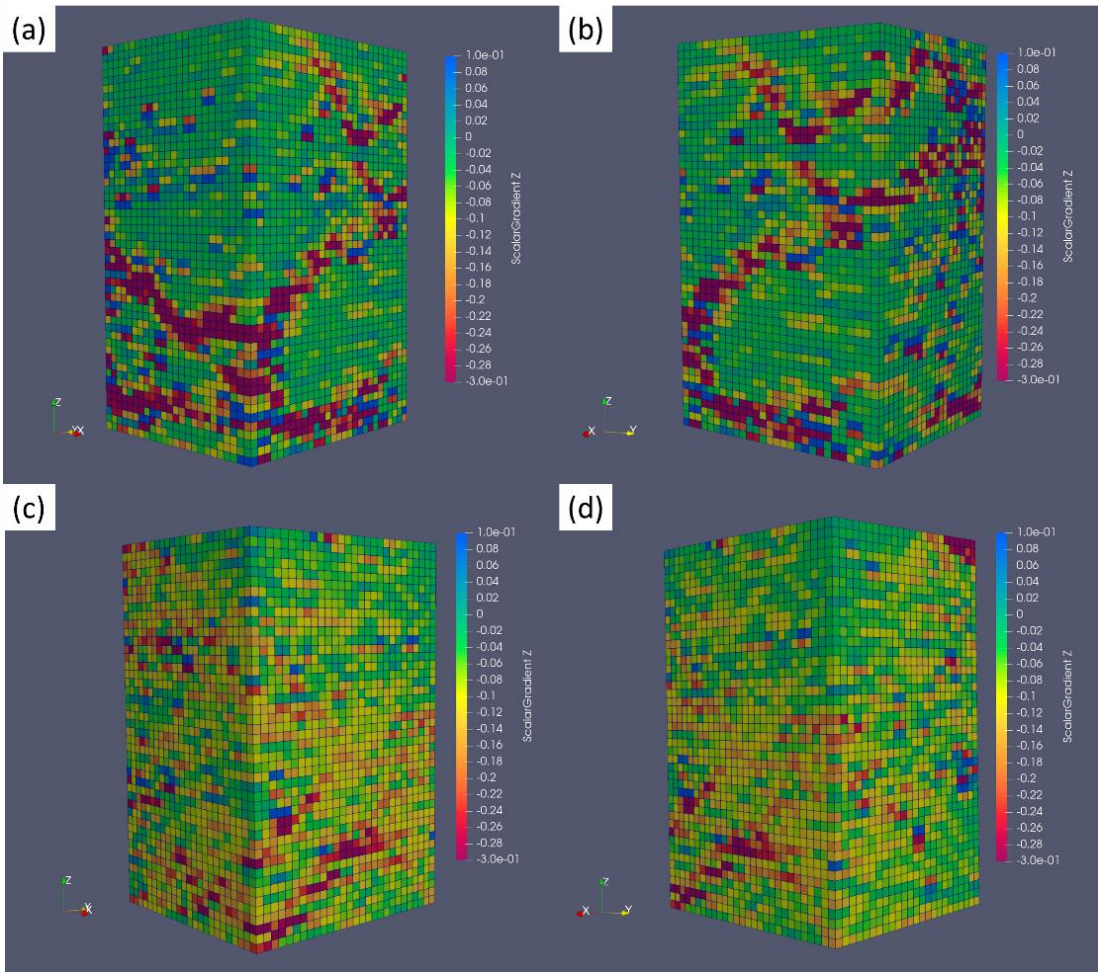

Fig. 2.80 Longitudinal deformation maps (strain gage length of 312 μm) at final macroscopic strain level of 9% for (a) (b) aluminum foam sample Al-to and (c) (d) copper foam sample Cu-to after uniaxial compression at 150 ℃.

Discussion on the uncertainty of the DIC results

There exist two types of errors when using the software CMV for digital image correlation: systematic error and random error. The systematic or periodic error mainly depends on the local contrast, initial image noise, correlation window size, as well as the interpolation of the grayscale of the images during subvoxel optimization [196, 197]. The random error is mainly governed by the noise in the images, the quality of the local contrast, and the size of the correlation domain [198]. Normally, the larger the correlation domain, which contains more information, the smaller the random error. However, a larger correlation domain may potentially obscure details on grain boundaries or interfaces and may also smooth local strain heterogeneities. However, the small correlation domain contains too little local information and almost no sufficient local contrast to achieve DIC. Therefore, a compromise needs to be found. The size of the correlation domain should be chosen based on the local contrast presented and the information that we want to obtain [196].

By imposing a known mechanical transformation, we can estimate the uncertainties in the measurement of the local surface displacement field by DIC. For example, by changing the imaging conditions, we can obtain a homogeneous transformation of a known percentage per magnification variation. The average and standard deviation of the difference between the measured displacement fields by DIC and the theoretical ones, which correspond to the apparent transformation, are then calculated.

However, in our case, the metal foam samples were deformed until at least 9~10%. At the beginning of the compression steps, the software CMV may still be able to locate the measurement points automatically on the deformed images for small deformations. However, as soon as there were significant local deformations, the software may fail to find the corresponding correlation measurement point on the deformed image or it may locate the measurement point at a completely wrong coordinate. In this case, we need to manually select the correct position of the measurement point on the deformed image based on the comparison between the deformed image and the reference image. When we manually choose the positions of the measurement points and the correlation domains, it is not possible to measure the error or uncertainty quantitatively.

During our DIC analysis on metal foam samples before and after compression, we discovered that the metal foams can exhibit significant strain localizations even with small macro strains, making the DIC process extremely complicated. Each deformed image required the manual selection of dozens of measurement points to ensure their accurate positioning. As the macro strain increased to 10%, 15%, or even higher, the number of deformed images to process also increased significantly to several hundred. Therefore, unfortunately, in our case, there is no appropriate way to provide the uncertainty or error of the DIC results presented in the previous part. Nonetheless, it is essential to note that the magnitude of the error is negligible when compared to the phenomenon we are interested in observing, which is the localization band. Additionally, subtle displacements may be occurring at a smaller scale, such as grain-level localization or deformation, that we cannot observe. However, these smaller-scale phenomena are not our primary focus.

2.4.3. Grain boundary and interface behavior

As introduced in section 2.4.1, the structural characterization of metal foam showed that all these three kinds of metal foams selected for serving as host matrix of presented distinct grains, grain boundaries and interfaces on the cross-section of struts, which may have a non-negligible influence on the macroscopic mechanical properties of the metal foam during compression. Therefore, it is essential to understand the deformation mechanism at grain boundaries or interfaces scale under compression or under extreme thermochemical solicitations, which would help us to estimate the durability of these structural metals. What's more, the

stress-strain curve obtained from uniaxial compression tests on aluminum foam presented in the previous part showed a great difference under ambient temperature and at 150 ℃. The investigation on grain boundaries and interfaces at 150 ℃ would allow us to identify the microscopic deformation mechanisms at this temperature and help us to understand the macroscopic differences in performance that may be caused. We chose to perform the experiment on bulk metallic sample instead of metal foam because of the limitation of the strut size of the metal foams. Especially with the hollow structure of the struts, it would be difficult to observe the deformation mechanism at the scale of grains. In this section, we present the experimental result obtained from the uniaxial compression test on bulk aluminum sample, with special interest in grain boundary localization phenomena. The sample information, experimental setup and procedure were introduced in section 2.3.

As presented in Fig. 2.28a and b in section 2.3.2, the ROI-macro of 3 mm × 3 mm and the ROI-micro of 1 mm × 1 mm was selected in the center of the ROI-macro. The ROI-micro was chosen where the microstructure was homogeneous and non-textured. Also, note that the grain size should be appropriate (300 µm on average) so that it contains enough grain boundaries in the ROI-micro for study. The chosen ROI-micro is shown in Fig. 2.81b.

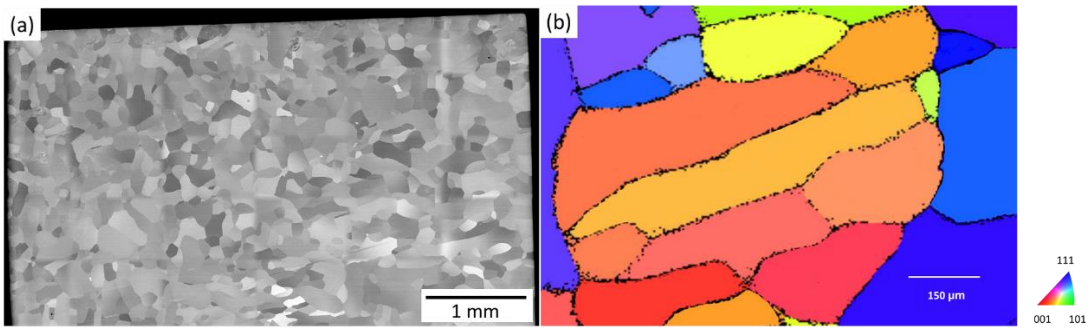

Fig. 2.81 (a) SEM image of typical microstructure of the whole sample surface and (b) the inverse pole figure (IPF) map of the region of interest (ROI)-micro obtained by EBSD with respect to the compression axis. The IPF orientation scale is shown in the right corner.

The compressive stress-strain curves at 150 ℃ obtained by two different methods are shown in Fig. 2.82. The stress-strain curve presented in Fig. 2.82a was based on the force recorded by the load cell and the displacement measured by LVDT during compression. Recall that the micro-compression machine is in the form of the letter “U” (as shown in Fig. 2.10), so the machine is very flexible and deforms easily during the compression test. As a result, the LVDT would measure the displacement of the sample plus the machine during the compression test. Therefore, this method is not able to avoid the effects associated with the compression machine itself. Thus this raw loading curve presented in Fig. 2.82a shows the mechanical behavior of the sample as well as the emplacement of the loading column and the compliance of the machine [182]. Note that the relaxation on the curve was due to the imaging duration every 30 µm increase in displacement. While the curve shown in Fig. 2.82b

was obtained from DIC analysis based on the full strain field computation realized over the ROI-macro with crosses as correlation markers (strain gage length 250 µm). This ensures the accuracy of the mean strain of the large area of ROI-macro of the sample surface. As explained previously, the apparent extension deformations at the initial state of the compression test be explained by magnification variations. During the initial loading, the stress increased abruptly and caused out-of-plane movements of the testing machine and therefore of the sample, which changed the working distance and consequently induced a slight variation in magnification [195, 196]. This observation was also reported in the work of other researchers in our lab using the same micro compression machine and the same DIC software [195, 196].

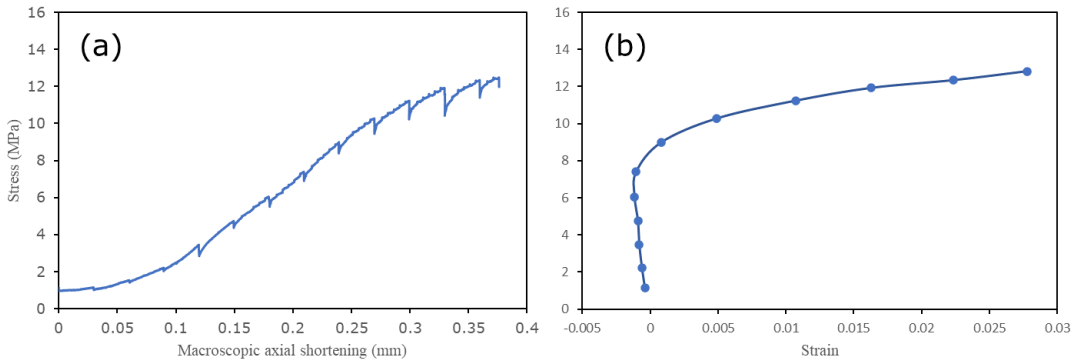

Fig. 2.82 Stress-strain curve (a) based on the force recorded by the load cell and the displacement measured by the LVDT and that (b) based on the strain computed by DIC.

The equivalent strain maps for in situ uniaxial compression test on bulk aluminum at 150 ℃ computed over ROI-macro (Fig. 2.28a) of each step of loading are presented in Fig. 2.83. The measurement points were selected on each center of the lithography marking crosses and the correlation domain was set to 60 × 60 pixels. The resolution of SEM images of ROI-macro was 3072 × 2207. The real-time strain field was computed after each relaxation and imaging of the ROI-macro to quickly obtain the mean overall strain of the sample after each loading step during the test. In this experiment, the final overall axial strain was 2.78%. The sample first showed a small expansion along the compression axial, as we observed on the stress-strain curve shown in Fig. 2.82b, which may be explained by magnification variations. Besides, the result of slight magnification problems may also be related to imperfection of the contacting surface of the sample and the pistons of the compression machine, inducing slight displacement of the sample upon initial loading. The heating of the sample may also add some emplacement effects. The initial stages of the test were influenced by this effect. However, as the test progressed, the sample started to display measurable negative strain, indicating the beginning of the compressive deformation. The crosses drawn on the strain field at each measurement point have a symbolic meaning: the major axis of the cross indicates the first eigendirection of the local deformation, associated with the largest eigenvalue in algebraic value. Note that this would be the transverse

direction for a compression test. The color and size of these crosses were related to the equivalent von Mises strain intensity which characterized the distortion in the observation plane. With the selected color code, localization is presented in red. It is observed that from the step presented in Fig. 2.83b and further on, nearly all the measurement points in the ROI-macro region began to indicate compression in the main axial compression axis. From the equivalent strain of ROI-macro change from 0.01% to 1.07%, the deformation was still relatively homogeneous in this region of 3 mm × 3 mm, as shown in Fig. 2.83a to c. Minor localization of the deformation appeared when the mean strain of the sample reached 1.63%, as can be seen in Fig. 2.83d. The localization zones developed in the following steps, as shown in Fig. 2.83e and f. From Fig. 2.83f, we can see that when the equivalent strain of ROI-macro reached 2.78%, the local strain may reach a level of 7%.

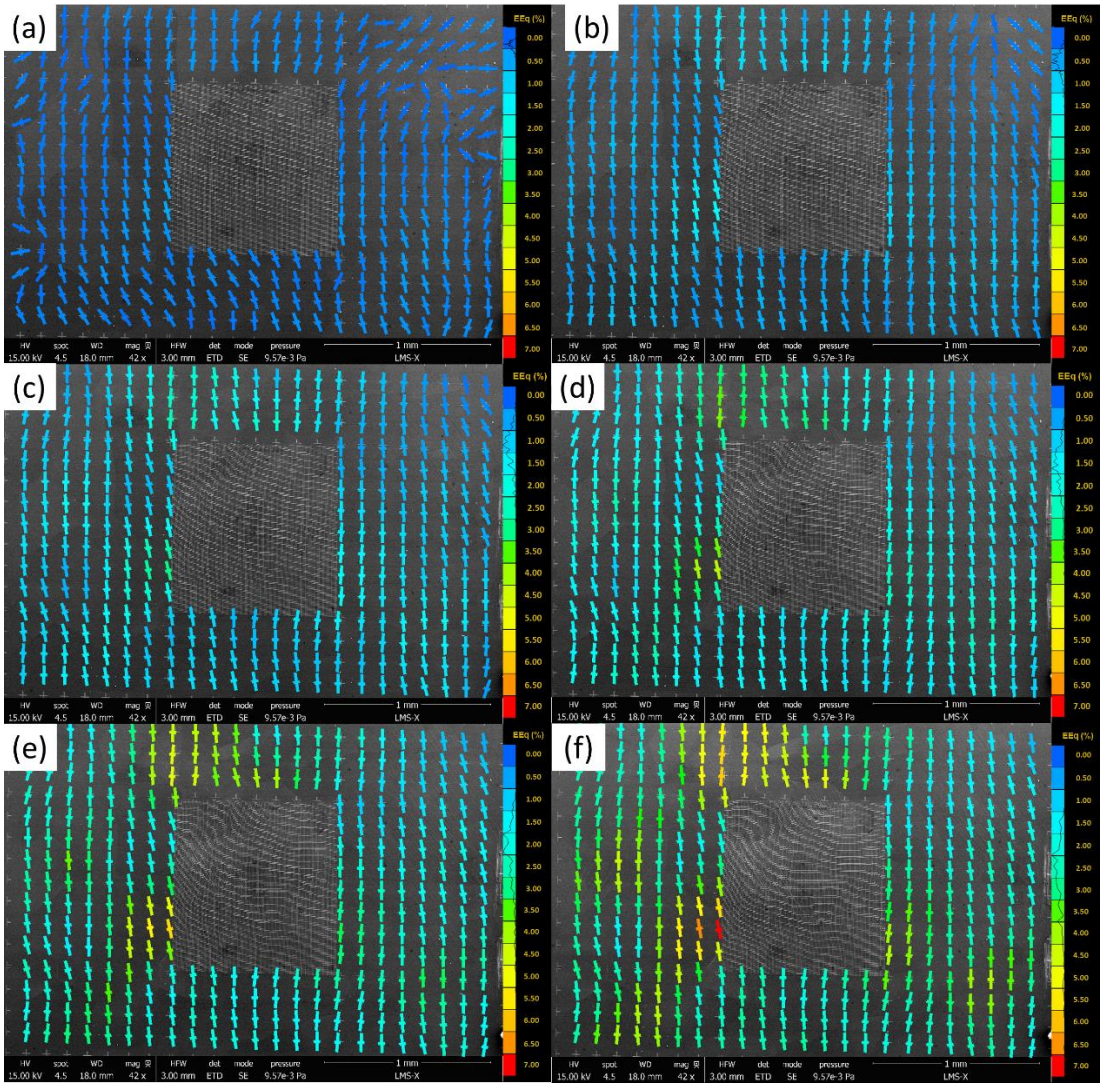

Fig. 2.83 Equivalent strain maps computed over ROI-macro representing the mean strain of the sample, with a strain of (a) 0.01% (b) 0.49% (c) 1.07% (d) 1.63% (e) 2.24% and (f) 2.78%. The compression axis was horizontal.

Fig. 2.85a to f present the equivalent von Mises strain maps computed over ROI-micro by DIC for each loading step corresponding to the macroscopic strain maps of ROI-macro presented in Fig. 2.83a to f, respectively. The square-shaped ROI-micro zone, with finely scaled grids as markers (Fig. 2.28b), was located in the central part of the ROI-macro zone (Fig. 2.28). The grid marking allowed to have a gage length of 10 µm which allowed computation of high-resolution strain field for revealing strain localization at the grain scale. The measurement points were placed on each grid intersection (as shown in Fig. 2.84). The microstructure of the investigated ROI-micro zone was presented in Fig. 2.81b. The SEM images were recorded with the highest resolution possible of our equipment which was 6144 × 4415, corresponding to a pixel size of 0.16 µm. Note that with the color code selected, strong localization is presented in red.

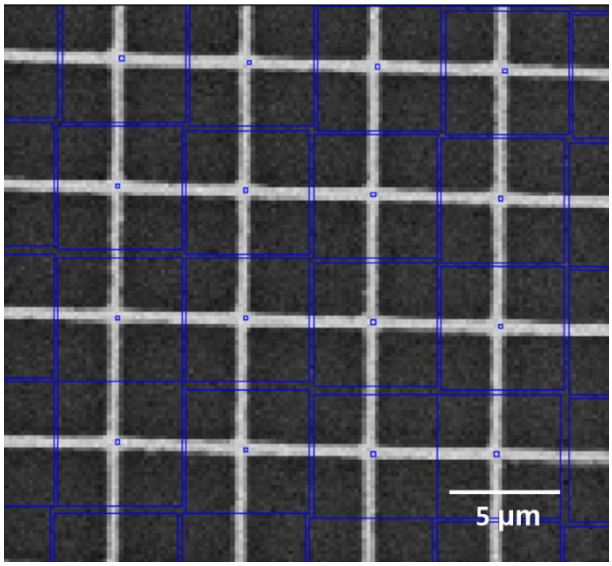

Fig. 2.84 The measurement points placed on the intersections of the grids, with small blue squares representing the measurement point and the big blue squares representing the correlation domain.

As shown in Fig. 2.85a, the equivalent strain was homogeneous at the beginning of compression, where the macroscopic strain of ROI-macro was 0.01%. Then in Fig. 2.85b, strain localization began to appear on the upper left of the ROI-micro zone with clear activations of crystal slip plasticity (CSP). Two slip bands propagated obliquely from the upper left part of the ROI-micro region to the bottom at approximately 60° of the axial stress direction (horizontal). In addition, there was a diffuse localization present, extending perpendicular to the slip bands. These localizations of strain in the ROI-micro appeared relatively early since Fig. 2.85b corresponded to an equivalent strain of ROI-macro of only 0.49%. In the following steps, we observe an intensification of the already existing patterns of strain localization and robust development of the crystal slip bands in the entire ROI-micro zone (see Fig. 2.85c to f). It is worth noting that the diffuse strain localization area, which was initially located adjacent to the first slip bands (Fig. 2.85b), continued to intensify over time and eventually formed highly localized strain bands

perpendicular to the slip bands. As shown in Fig. 2.85f, when the equivalent strain of ROI-macro reached a level of 2.78%, the localized strain in the ROI-micro zone can reach a level of 20%.

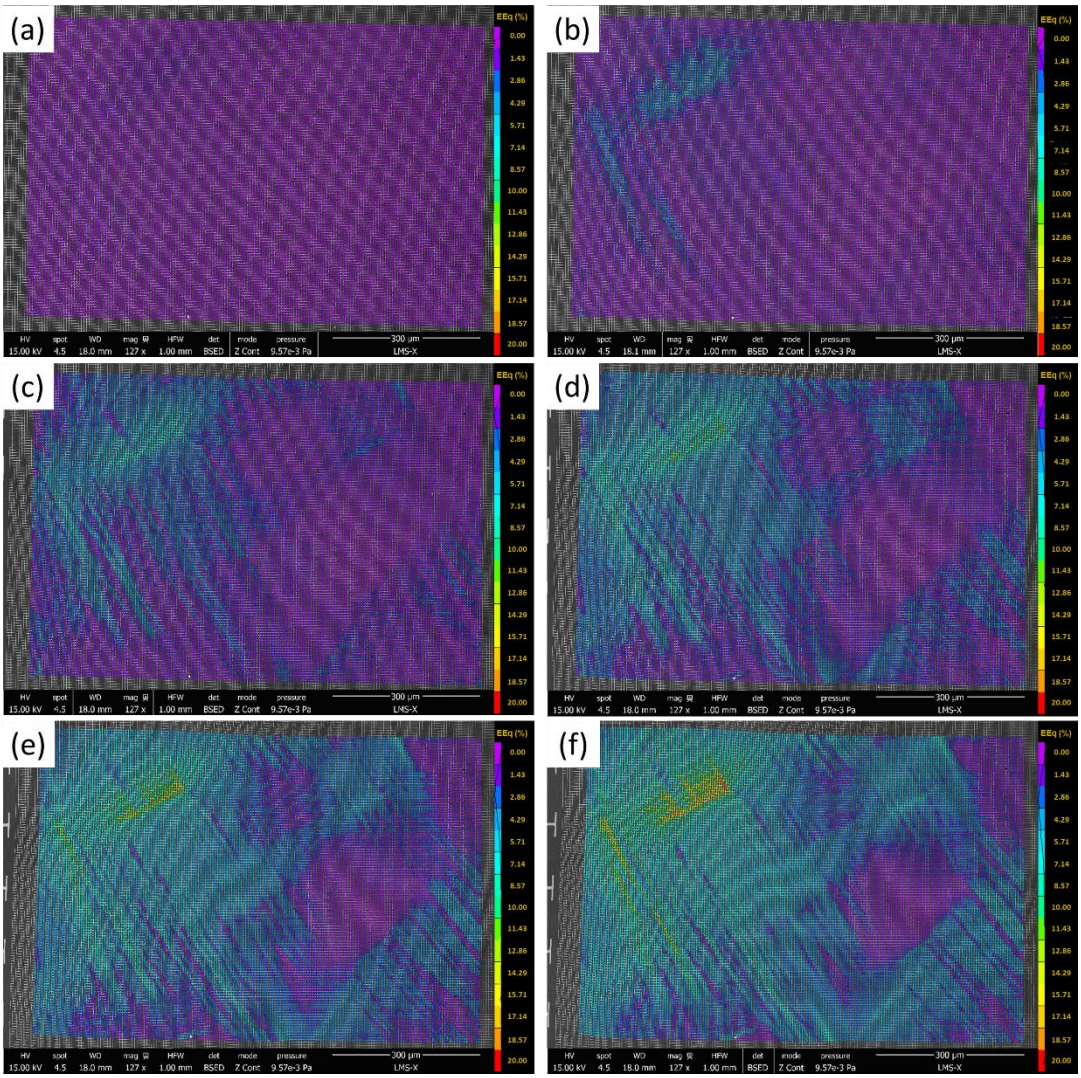

Fig. 2.85 Equivalent strain maps computed over ROI-micro (microstructure shown in Fig. 2.81b) presenting the strain localization in grain scale, corresponding to the macroscopic strain of (a) 0.01% (b) 0.49% (c) 1.07% (d) 1.63% (e) 2.24% and (f) 2.78%. The compression axis was horizontal.

To have a clearer view of the microscopic deformation mechanism with a special focus on grain boundaries, we ought to place measurement points right on the grain boundaries so that discontinuities related to potential GBS (grain boundary sliding) could be detected and quantified. However, on the reference image, in order to facilitate the later DIC with the deposited Pt markers in grids, the SEM image must maintain a suitable contrast and brightness, under which conditions we cannot distinguish between individual grains let alone find the grain boundaries directly and select the accurate locations for placing the measurement points. To solve this problem, we applied the method developed in our lab [196] to measure the deformation and compute the strain of the grain boundaries. The method was

originally developed for decoupling the intra-grain deformation from inter-grain deformation and quantifying the inter-grain deformation. It consisted of 4 steps: (1) Create an image of the ROI-micro with different grayscales assigned to each grain as their labels. (2) Replace the measurement points closest to the grain boundaries onto the grain boundaries by dichotomy and give them a different phase, distinguishing them from the measurement points within the grains. (3) Apply the method of correlation with a mask for each grain. And the last step is to (4) Calculate the average gradient of each grain. For a more detailed presentation of this method, the reader is addressed to the reference [196].

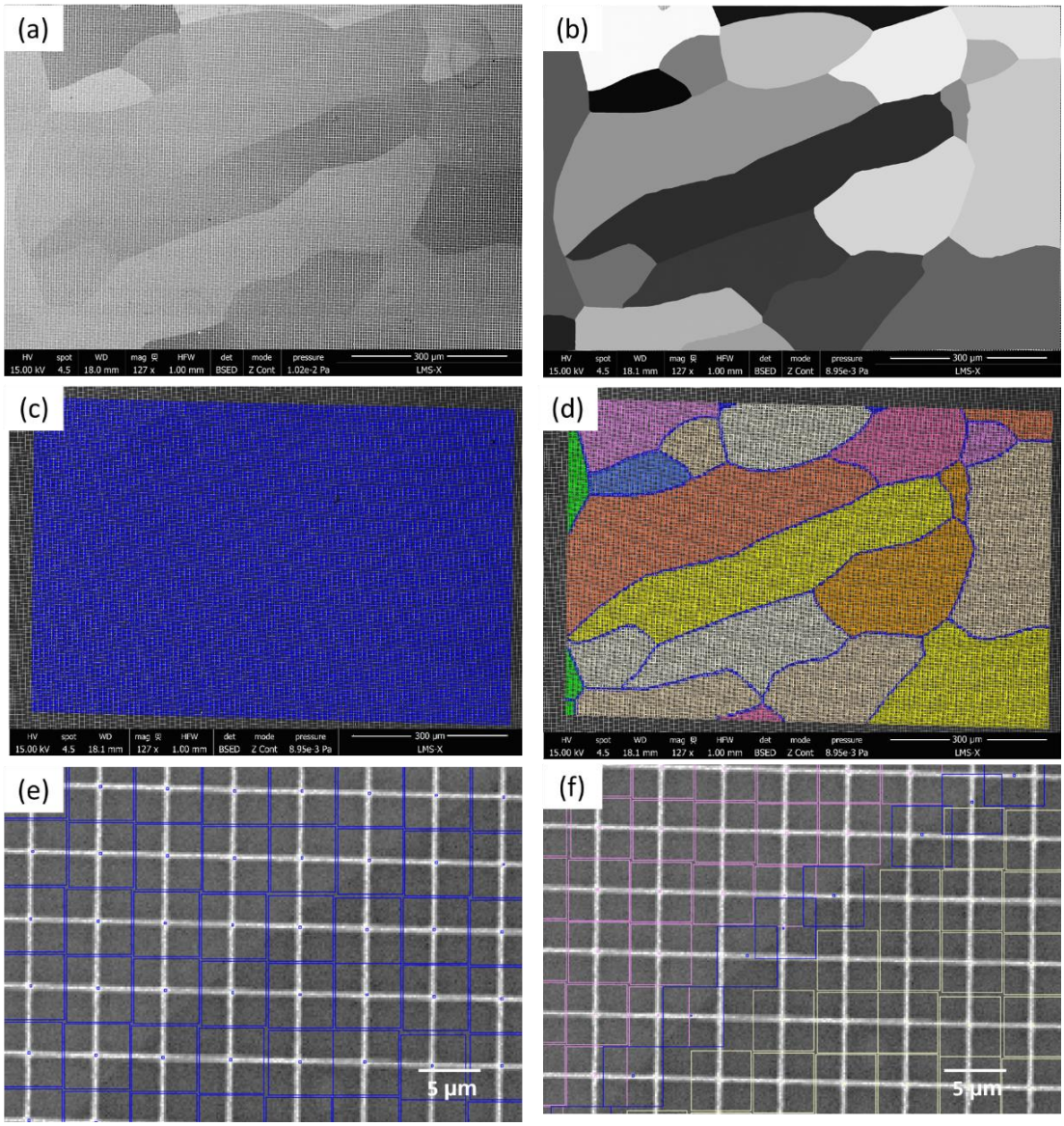

Fig. 2.86 (a) The BSE image of ROI-micro with contrast showing the grain boundaries, which was used to create (b) the image of ROI-micro with different grayscales assigned to different grains as their labels. (c) Original mesh of measurement points all in blue phase and (d) the mesh of measurement points with blue points repositioned on the grain boundaries constructed using image (b). (e) Zoom on the original mesh of measurement points near a grain boundary and (f) zoom on the same grain boundary with repositioned measurement points (in blue) on the grain boundary.

For our study, the purpose was to calculate the deformation and strain localization at grain boundaries, thus we used the first two steps of the method to generate a file where the measurement points were placed in the grains and on the grain boundaries of every grain in the ROI-micro region so that we can follow the deformation of grain boundaries for each step during compression and compute the strain by DIC. In Fig. 2.86, we present the two steps for obtaining the mesh of measurement points with certain ones placed right on the grain boundaries serving as reference points for computing the deformation and strain of grain boundaries via DIC. As shown in Fig. 2.86b, the grains in ROI-micro were assigned with different grayscale according to the high-resolution BSE image (Fig. 2.86a) and the EBSD of ROI-micro (Fig. 2.81b). With this image of labeled grain, we repositioned the original measurement points (Fig. 2.86c) by dichotomy to form a new mesh of measurement points with certain points replaced onto the grain boundaries, as shown in Fig. 2.86d, with blue points representing measurement points located right on the grain boundaries. An example shown in Fig. 2.86e and f presented clearly how the points were repositioned onto the grain boundaries.

The DIC was then performed using the new mesh of measurement points obtained from the previous steps as reference points. The correlation domain was set to 30 × 30 pixels and the gage length was still 10 μm. The results are presented in Fig. 2.87 which corresponds to the last step of loading with a macroscopic axial strain of the sample at the level of 2.78%. From the overall equivalent strain map shown in Fig. 2.87a, we can see that the major difference between this map and that shown in Fig. 2.85f is that the deformation of grain boundaries is clearer and more distinct. From Fig. 2.87a, it can be seen that the highly localized strain band perpendicular to the slip bands observed in Fig. 2.85f was due to grain boundary sliding (GBS).

The zooming-in strain fields and SEM images of Zone 1 and 2 marked on the Fig. 2.87 are presented in Fig. 2.87 (1) and Fig. 2.87 (2) respectively. The Fig. 2.87 (1-b) presents the strain map of Zone 1 and Fig. 2.87 (1-c) presents the SE image of the same zone. The GBS can be clearly seen on both the strain map and the SE image. According to the strain map presented in Fig. 2.87 (1-b), the GBS induced a local equivalent strain of 17%. While the SE image also allowed us to observe the crystal slip inside the grain on below shown in Fig. 2.87 (1-c). Note that the DIC was applied with BSE images which allowed imaging based on contrasts between different phases and also provided crystallographic contrasts, thus facilitating the correlation process and providing a more accurate result. However, GBS and intra-grain slip lines and bands also show out-of-plane components, inducing changes in the topology of the surface, which can be better observed with SE images. It can be clearly observed that the slip lines were discontinuous within the different grains, so we consider this to be an intracrystalline strain localization.

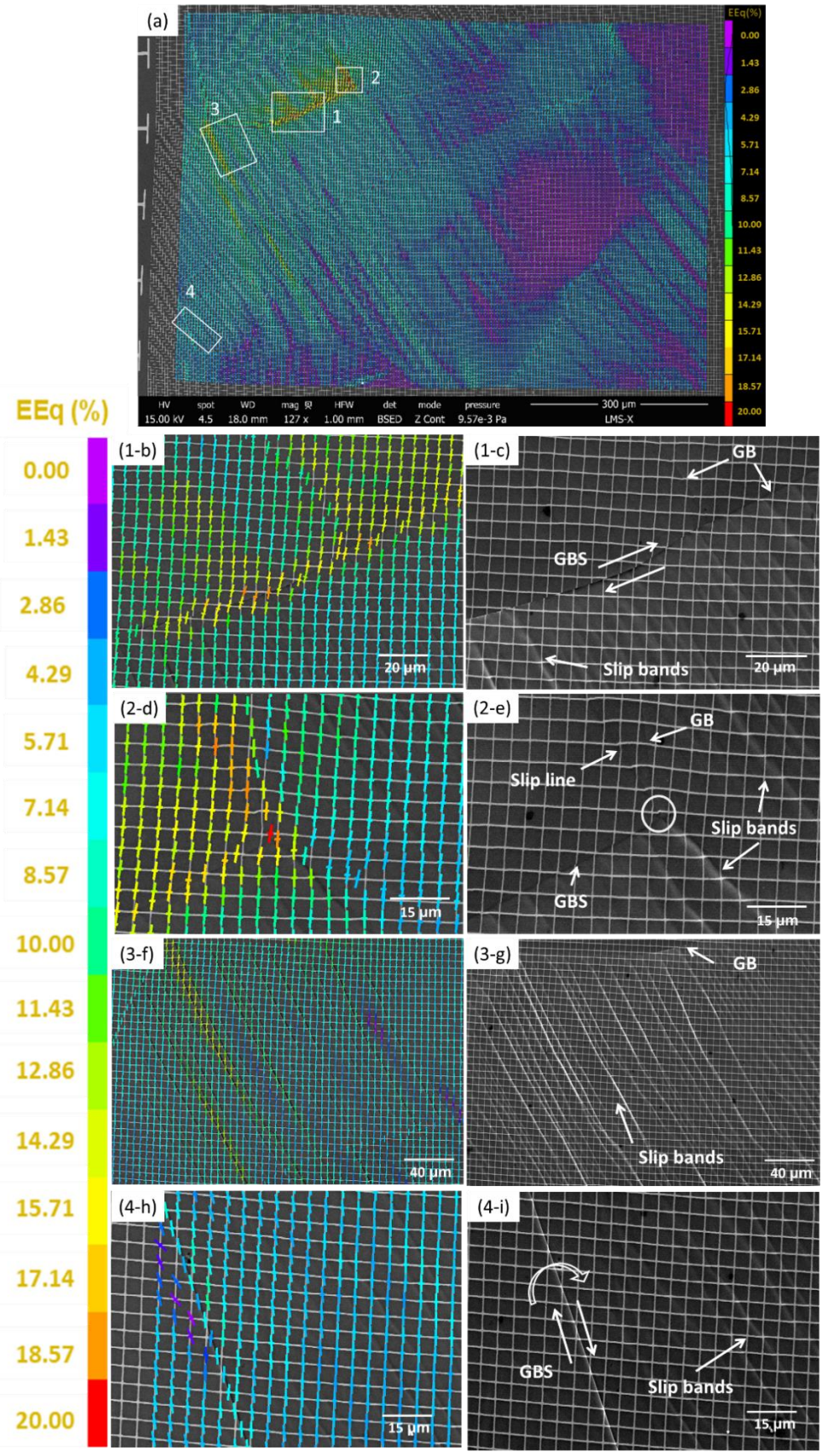

Fig. 2.87 (a) The equivalent strain map computed by DIC with measurement points repositioned onto the grain boundaries. 4 zones of interests with clear GBS and CSP phenomena were selected, the equivalent strain map (1-b) (2-d) (3-f) (4-h) and corresponding SE images (1-c) (2-e) (3-g) (4-i) are presented for each of these 4 zones.

The strain map shown in Fig. 2.87 (2-d) presents one measurement point (in red) with the highest equivalent strain in ROI-micro at the macroscopic strain of 2.78%. According to the equivalent strain map, the measurement point in red corresponded to an equivalent strain of 20% and the zone around it also had a relatively high localized equivalent strain. From the SE image of the same zone, we found that the measurement point with the highest equivalent strain was the intersection of the GBs of two adjacent grains. What's more, this point was also the end of a slip line activated in the upper grain and the beginning of another slip line of the grain on the bottom. Under the combined effect of these mechanisms, an extremely strong strain localization occurred at this point, which can be considered as either the meeting point of emerging slip lines from both grains or as the point where slip transmitted from one grain to the other.

The activation of spatial dense and intense crystal slip can be observed on the left side of the ROI-micro, as shown in Fig. 2.87 (3-f) and Fig. 2.87 (3-g). By the equivalent strain map shown in Fig. 2.87 (3-f), we can see that the slip bands had relatively high strain intensity, which was from 8% to 15%. According to the SE image Fig. 2.87 (3-g) of this same zone, the slip lines were essentially sharp. It is also worth noting that the slip lines with higher strain intensity seemed to present a non-negligible out-of-plane component, which was hard to observe in equivalent strain maps obtained by DIC.

In Zone 4 we observed similar phenomena for GBS. As shown in the strain map of Zone 4 (Fig. 2.87 (4-h)), the grain boundary exhibited an average strain localization level of approximately 7%, which was relatively consistent compared to the measurement points in the surrounding area. As a result, the level of strain localization observed at this grain boundary appeared to be relatively insignificant. However, with the SE image (Fig. 2.87 (4-i)) presenting the topography of this zone, we found that the GB presented an out-of-plane component, it seemed that if we continue to compress, the grain on the left may "climb" onto the grain on the right. This is a thrusting mechanism due to sliding onto a grain boundary which is not straight edge-on but inclined in depth. Such overlapping of one grain by another was observed during uniaxial compression tests on the same material ($AlMn_{0.1}$) at 200 ℃ and 300 ℃ with a macroscopic strain level of 5% [182, 185]. In our case, the grain boundary in Zone 4 presented an active but net strain localization, which means the grid markers hardly changed the form, thus it was difficult for DIC to detect such localization dominated by out-of-plan components.

To sum up, as the application of the designed composites with metal foams serving as host matrix cause them to be loaded in compression, it is important for us to understand the microstructural evolution of metal foams during compression. In addition, because of the numerous grain boundaries and interfaces presented in metallic foam structures, in situ SEM uniaxial compression test at 150 ℃ was

performed with bulk aluminum ($AlMn_{0.1}$) cuboid sample. This allowed us to observe and investigate the microscopic deformation mechanism of bulk aluminum with a special focus on the deformation of grain interfaces (grain boundaries).

The experimental and DIC results demonstrated that the uniaxial compression at 150 ℃ with an axial strain of 2.78% could already induce strain localization as grain boundary sliding (GBS). In our case, until the axial strain reached 2.78%, the dominant deformation mechanism would still be crystal slip plasticity (CSP), while strong strain localization appeared on limited interfaces between grains in the form of grain boundary sliding. Although GBS only appeared on a limited number of grain boundaries, the strain localization level cannot be ignored. For an axial strain of 2.78%, the strain where GBS occurred can reach a level of 20%. It is reported in the literature that as temperature increases, the flow stress tends to decrease while the intensity of slip lines increases. However, it is important to note that recovery mechanisms and grain boundary migration may also be activated under such conditions [182, 185, 199]. These phenomena may explain the decrease in mechanical strength and the relatively moderate strain hardening during the second stage of deformation of aluminum foam (Al02) under compression at 150 ℃ compared to that at ambient temperature (Al01) that we observed in the previous section.

In fact, the appearance of grain boundary sliding (GBS) with such a strong intensity (~20%) at a moderately high of 150 ℃ ($\approx$ 0.23 $T_{melting}$ of aluminum) for an axial strain of only 2.78% was surprising. Because in the literature [185], where experiments were performed on samples of the same material, it is reported that at a temperature of around 110 ℃, the GBS didn't occur until an axial strain of 5%. Besides, the observed GBS remained very limited, with an amplitude of approximately 100 nm (a local strain of ~8%). Strong GBSs (local strain > 25%) were observed at the temperature of 200 ℃ and an axial strain of 5%. It is concluded in [185] that the higher the temperature, the more likely grain boundary sliding is to occur. While our experimental result also suggests that besides the influence of temperature, there appear to be certain grain boundaries that are more prone to undergo sliding during the loading process. Though in our case we do not know the specific physical micro-mechanism responsible for GBS, it is plausible that such mechanisms involved the movement of dislocations, mass transfer through diffusion, or even frictional sliding [182]. Indeed, up to this day, there is still no consensus on which types of grain boundaries are more prone to sliding. Some studies have attempted to identify factors that may influence grain boundary sliding. For example, El Sabbagh [185] tried to study the influence on GBS of the grain boundary plane orientation relative to the applied stress. It was found that the grain boundary plans with an orientation of approximately 45° to the direction of stress are the most prone to sliding. However, this conclusion was drawn based on the observation of

15 grain boundaries on only one sample surface. Thus, the universality of this conclusion remains to be verified.

In terms of the deformation of metal foams, plastic deformation derives from the plastic hinge of the struts [193]. Based on our experimental results and analysis, it is reasonable to speculate that, on the microscopic scale of the grains that formed the struts, the strain localization on the grain boundaries and interfaces may strongly affect the deformation and failure mechanism of struts, thus inducing local pore collapse and affecting the macroscopic mechanical strength of the metal foams. It is interesting to note that even at 150°C the strain hardening of the massive aluminum was important. The fact that there was a strengthening of slightly less than 1 MPa for 1% of deformation (Fig. 2.79) suggests that the material underwent substantial plastic strengthening during the severe local plastic deformation of foam struts and walls. This enhanced plastic strengthening can potentially amplify the effects of grain boundary sliding (GBS) mechanisms and local damage within the material.

In addition, based on the comparison of the results obtained for different metal foams, it may be assumed that the extent to which grain-scale strain localization affects the macroscopic mechanical behavior of metal foams depends on the characteristics of the metal foam, such as the porosity, homogeneity or heterogeneity of pore shapes and sizes, geometrical characteristics of pore walls and struts, and temperature.

2.5. Discussion and conclusion

In our work, the metal foam is designed to serve as the host matrix, providing mechanical strength and maintaining the integrity of the porous structure in metal foam-salt hydrate composites. Specifically, the metal foam must bear the mechanical load applied during the stacking of composite sheets and the construction of units for thermochemical reactors intended for future industrial applications. Even though the estimated load applied on the bottommost layer of the upper layers determined by the composite volume required to meet the energy demand for space heating in each household in France, is in the order of several kPa, which lies well in the elastic regime of the compressive phases of the studied metal foams. However, as we explained in section 2.1.1, this estimation represents the minimum load it may experience in practical use. It is essential, to explore the complete mechanical behavior of the metal foam under compression to address various application scenarios that may arise in real engineering applications within the temperature limit of 150 ℃. The experimental results will aid in determining the appropriate stacking configurations of our designed thermochemical heat storage composite within a safe range for various operating conditions and energy density requirements. This ensures the feasibility and reliability of the practical applications in the future.

In section 2.2 and 2.3, we introduced the experimental approach of the uniaxial compression test on metal foam and the bulk aluminum sample, including the sample preparation process, the characterization and analytical techniques used and the experimental protocol of both in situ tests with observations by SEM and by optical microscopy with high-resolution camera.

Then in section 2.4, we presented the characterization and analytical results obtained through experiments. We first presented the structural characterization of various kinds of metal foams obtained with SEM and EBSD. Then, the macroscopic, mesoscopic and microscopic deformation mechanisms studied by in situ uniaxial compression test on metal foam at ambient temperature and 150 ℃ with observations by optical microscopy with high-resolution camera and by SEM were presented. 2D and 3D DIC analyses were accomplished by using images captured during in situ tests and 3D volumes acquired by X-ray microtomography technique. The final part of this section summarized the microscopic deformation mechanisms obtained from compression tests on bulk aluminum samples and DIC analysis, with a special focus on grain and grain boundary scales.

In summary, copper foam, nickel foam and aluminum foam that we chose for serving as the host matrix of the salt were all open-cell metal foams. Among which, the copper foam and nickel foam had similar macrostructures, in terms of the porosity, pore shape and homogeneity of pore distribution and size, whereas aluminum foam had quite an uneven strut thickness and irregular pore shape and size. The following results demonstrated that the homogeneous and heterogeneous structure of metal foams had a great impact on their mechanical properties.

We tested the deformation mechanism under compression at ambient temperature and 150 ℃ for both copper foam and aluminum foam. The compressive stress-strain curves demonstrated that after the elastic phase, following yielding, the foams experienced two plastic deformation stages. The first one was related to the plastic deformation of the pores, involving the folding and rupturing of pore struts and walls. The second stage was characterized by the collapse of the pores, followed by a final regime of densification, where the strength increased rapidly. The three deformation regions were consistent with the observed results in other studies [130, 131].

In terms of mechanical strength, copper foam showed a 0.2% offset yield stress of about 0.23 ± 0.02 MPa at ambient temperature and about 0.27 ± 0.02 MPa at 150 ℃. The obtained yield stress at ambient temperature was comparable with the reported yield stress of open-cell copper foam with a porosity of 96.4% and a relative density of 0.036 tested in the research of Chen et al. [192] at ambient temperature. The copper foam studied in our research and in the literature [192] has almost the same porosity and relative density. Compression tests were both

performed at a strain rate on the order of 10^{-3} s. It is thus not surprising to find that they exhibited similar mechanical properties in terms of yield stress. It is also interesting to note that the temperature up to 150 ℃ didn't have a significant impact on the yielding mechanical strength of copper foam compared to that at ambient temperature. However, the strain hardening during the first plastic deformation phases was substantially different at ambient temperature and 150 °C. It is presented in the work of Han et al. [200] that the mechanical strength of a self-produced closed-cell copper foam (with a relative density of 0.42) degrades evidently with the increase in temperature from 25 ℃ to 500 ℃. The plateau stress (average stress between a strain of 20% to 30%) decreased by 32% at 300 ℃ and 60% at 500 ℃ compared to that at 25 ℃. While the sample examined in this literature was a closed-cell copper foam, our study focused on an open-cell copper foam. Nevertheless, the information regarding the impact of temperature increase remains valuable and worthy of reference. It's a pity that there was no information on the mechanical behavior of the reported sample at 150 ℃ in this paper [200]. Note that 150 ℃ corresponds to approximately 0.14 $T_{melting}$ of copper, which is 1085 ℃. We can only speculate that perhaps this moderately high temperature was still not high enough for copper foam studied in our work to show a difference in mechanical strength. In fact, this speculation can be supported by the work of Bekoz et al. [201] in the study of the compression behavior of open-cell steel foams at the temperature range of room temperature to 600 ℃. Their experimental results indicated that the compressive yield stress of steel foam began to decline only when the temperature surpassed 400 ℃. This implies the possible existence of a threshold beyond which the influence of temperature on the mechanical properties of metal foams becomes noticeable. For the copper foams investigated in our study, this threshold temperature requires further exploration in future studies.

While for aluminum foam, the 0.2% offset yield stress at ambient temperature was 4.48 ± 0.02 MPa, but only 2.12 ± 0.02 MPa at 150 ℃, where 150 ℃ corresponds to about 0.23 $T_{melting}$ of aluminum. The yield stress decreased by 53% with the temperature increased from the ambient temperature to 150 ℃. This was also observed in the work of Tavares et al. [161] conducted compression tests on aluminum (AlMgSi0.5) open-cell foam with pore size around 2.7 mm and a porosity of 71.4%-81.8%. It is reported that the 0.2% offset yield strength of the aluminum foam decreased over 50% at 150 ℃ compared to that measured under ambient temperature, and had only 4.4% remaining at 500 ℃. Aly [157] found similar results when studying the compressive behavior of closed-cell Al foam with different relative densities (0.08, 0.09, and 1.11) within the temperature range of 25 ℃ to 620 ℃. It was observed that, regardless of the relative density, the compressive strength at 20% strain of the studied closed-cell aluminum foam began to decrease continuously at temperatures ranging from 170 ℃ to 620 ℃ (0.94 $T_{melting}$). By the temperature of 620 ℃, the remaning compressive strengths at 20% were only on the

order of 0.01 MPa for foam with all these three relative densities. Aly [157] also noted that the behavior of this closed-cell aluminum foam at high temperatures is similar to that observed in massive aluminum metal. The author also suggested that the observed softening effect with increasing test temperature is attributed to the phenomenon of grain boundary sliding in aluminum foams. However, further investigation to validate this viewpoint at the specific temperatures was not reported in this article [157]. Nevertheless, this hypothesis was confirmed in our compression experiments on the massive aluminum sample at 150 ℃.

In terms of compressive mechanical behavior during the plastic deformation regime, open-cell copper foam deformed more homogeneously with almost all pores accommodating plastic deformation in comparable amounts. For instance, for copper foam, the results obtained through digital volume correlation (DVC) revealed the formation of thin, homogeneously distributed localization bands, oriented at a 45° angle to the compression axis, carrying comparable amounts of strain. The few stronger localizations that were observed were most likely attributed to end effects and imperfections in planarity at the sample-piston interfaces. In contrast, the open-cell aluminum foam exhibited significant heterogeneity in local plastic deformations. Several pronounced localizations were observed, forming large deformation bands that extended across the entire sample with thicknesses of approximately 400 μm, which aligned with the pore size and indicated localized pore collapse.

The great difference in compressive deformation behavior of these two foams derived from their microstructures and the difference in relative density. The copper foam was much more homogeneous compared to aluminum foam, in terms of pore size, pore shape, and strut thickness. On the contrary, the microstructure of the aluminum foam was very heterogeneous. There were local variations in the morphology of the pores, of thicknesses of the struts, and of local quantity of metal compared to the pores volume. By SEM image presented in Fig. 2.77, we can even observe the existence of semi-closed cells in the aluminum foam. This heterogeneity resulted in strong localizations of the plastic deformation, which were triggered by possible defects of the microstructure, such as a “giant” pore or an angular/cubic pore morphology with locally thin walls and struts, that might have concentrated the stresses. The inhomogeneity of microstructure influencing the mechanical properties of metal foams was also observed in the research of Kaya et al. [150] and Hong et al. [156]. For instance, the difference in pore size and thickness of the struts, the defects of the cell walls, and the percentage and distribution of closed pores existing in the structure can all be regarded as a source of inhomogeneity of the metal foam microstructure.

During the observation of metal foam cross-sections using SEM, distinct grains, grain boundaries, and interfaces were found in all three types of metal foams. These

features were observed to extend throughout the entire cross-section of the struts and may have a non-negligible influence on the macroscopic mechanical properties of the metal foam during compression. It is also worth noting that the 0.2% offset yield stress of aluminum foam at ambient temperature and 150 ℃ varied greatly. It decreased by more than 50% at 150 ℃. This reduction in mechanical strength of aluminum foam at 0.23 $T_{melting}$ of aluminum is likely to be at least partly related to the influence of grain boundary sliding (GBS) at elevated temperatures [157, 185]. This possibility was investigated by compression tests on massive aluminum sample with special interest in grain boundaries.

The experimental and DIC results showed that the uniaxial compression at the temperature of only 150 ℃ with an axial strain of 2.78% could already induce strain localization as grain boundary sliding (GBS). At this temperature and axial strain level, the dominant deformation mechanism remained crystal slip plasticity (CSP), while strong strain localization appeared on some interfaces between grains due to grain boundary sliding. At high temperatures, additional microscopic deformation mechanisms related to the grain boundaries might be activated in addition to crystal slip plasticity. Based on our experimental results and analysis, it is reasonable to speculate that strain localization on the grain boundaries and interfaces may strongly influence the deformation and failure mechanisms of struts and thin cell walls, thereby affecting the macroscopic mechanical strength of the aluminum foam at 150 ℃ and undoubtedly at temperatures above. The observation of grain boundary sliding at 150 ℃ in massive aluminum within our study vividly supports and adequately explains the reported results in the literature [157, 161] concerning the degradation of compressive strength of aluminum foam at and above 150 ℃. In addition, based on the comparison of the mechanical behavior of copper foam and aluminum foam, it is assumed that the extent to which grain-scale strain localization affected the macroscopic mechanical behavior of metal foams depended on the characterization of the metal foam, such as porosity, relative density, the temperature as well as the melting point of the metal itself.

In conclusion, between the two metal foams we studied, copper foam presented clear advantages in terms of compressive mechanical behavior. However, this was primarily due to the structurally homogeneous characteristics of the foam, which enabled it to accommodate substantial plastic strain without experiencing complete pore collapse. As a result, the foam would maintain efficient water vapor transfer even after plastic yielding. On the other hand, the heterogeneities in the microstructure of the aluminum foam led to the formation of highly localized deformation bands, which would impede the mass transfer. Therefore, although the copper foam exhibited overall lower resistance compared to the aluminum foam, its more homogeneous microstructure made it mechanically more suitable as a host matrix for salts in our composite. It is worth noting that an aluminum foam with a

similarly homogeneous microstructure as the copper foam studied would have offered similar advantages as well. Additionally, a homogeneous aluminum foam with comparably high porosity would have been lighter and more cost-effective. Furthermore, the corrosion resistance of aluminum foam in the presence of salts and humidity would have been significantly better than that of copper foam. In fact, we observed rapid corrosion of the copper foam-salt hydrate composites, resulting in a greenish color even under room temperature and humidity conditions (will be further presented in section 3.2).

From a general mechanical perspective, the microstructure of the metal foam is by far more important than the metal itself. We must prioritize a metal foam with a microstructure as homogeneous as possible to ensure the success of mass transfer and to avoid catastrophic pore collapse in case of accidental plastic yielding. Secondly, the resistance of the metal to corrosion must be considered as well, since fast corrosion could rapidly degrade the advantage of the mechanical strength. This is to say, the nickel foam we presented in section 2.4.1, which had a similar homogeneous microstructure as compared to copper foam, would be an ideal candidate for serving as host matrix of salts hydrates in both terms of compressive mechanical strength and corrosion resistance. Unfortunately, these operational advantages would be somewhat offset by the higher commercial cost of nickel metal. However, this question does not address technical constraints. It is essentially concerned with economic issues, which are beyond the scope of this thesis.

3. Thermochemical properties of metal foam-salt composite

3.1. Introduction

As introduced at the beginning, pure hygroscopic salt hydrates and mixed salt hydrates are promising thermochemical materials (TCM). However, pure or mixed hygroscopic salts present non-negligible disadvantages, such as excessive swelling and agglomeration during hydration/dehydration cycles, which progressively degrade heat and mass transfer efficiency and lead to poor cyclic stability [39, 72, 73]. To alleviate the limitations mentioned above, we propose an original composite consisting of open-cell metal foam as a host matrix and calcium chloride as hygroscopic salt dispersed in the pores, specially designed for thermochemical energy storage.

In the previous part, we investigated the mechanical properties of the metal foam-salt hydrate composite, focusing on that of metal foam, which is the host matrix providing mechanical strength to the composite. In this part, we introduce the thermochemical properties of the metal foam-salt composite.

Firstly, we focus on the synthesis method of metal foam-salt hydrate composites. Secondly, we evaluate their thermochemical properties during hydration and dehydration cycles, as compared with these properties of simple salt hydrate powders of calcium chloride. In the last part, the evolution of the thermochemical properties is addressed based on their thermomechanical characteristics and in particular their microstructural/morphological evolution. For that purpose, we performed experimental measurements by differential scanning calorimetry (DSC), isothermal reaction calorimetry, and in situ environmental scanning electron microscope (ESEM) observations. The experimental setup and protocol are also introduced in detail in this part.

3.2. Synthesis of the composite

The starting material was commercial open-cell metal foams of copper, nickel, and aluminum introduced in section 2.2.1 with their structural characterization presented in detail in section 2.4.1. We recall here that copper foam and nickel foam had a homogeneous structure in terms of shape and size of the pores, while aluminum foam had fairly heterogeneous pore shape and size as well as strut thickness, as can be seen in Fig. 2.31. The hygroscopic salt $CaCl_2{\cdot}2H_2O$ (VWR Chemicals, AnalaR NORMAPUR® Reag. Ph. Eur.) was used as the active phase of the composite.

Two methods were initially tried for the synthesis of the composite.

(1) Depositing ground salt particles by sieve

Firstly, the idea of synthesizing the composite by depositing ground calcium chloride particles into the pores of metal foam using a sieve with sufficiently fine

pore size was realized. The mortar and sieve used are presented in Fig. 3.1a and b, respectively. Considering the hygroscopic nature of calcium chloride, the deposition process was carried out in a humidity-controlled glove box (see Fig. 3.1c). The relative humidity in the glove box was controlled by the saturated potassium hydroxide (KOH) solution. At room temperature, the relative humidity in the glove box can be controlled at a level of 8% [202]. The sample was then met in an oven at 90 ℃ for dehydration over 48h before use.

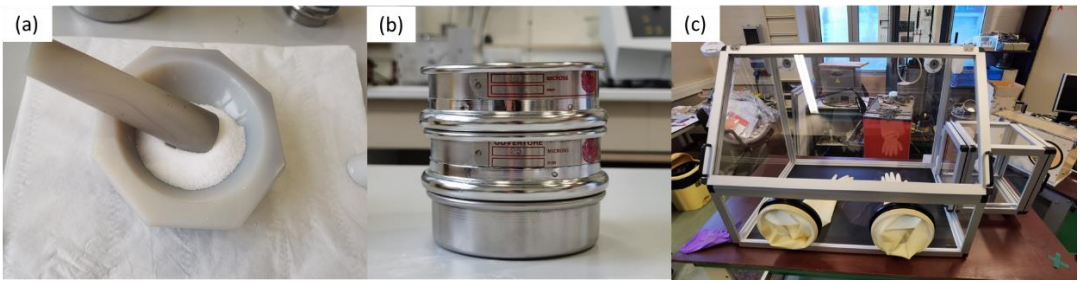

Fig. 3.1 Photo of (a) the mortar used to grind the salt, (b) the sieve used with pore size of 36 microns, and (c) the glove box used to manipulate the deposition of the salt powder into the metal foam.

The experimental results showed that the quantity of salt deposited in metal foam in this way was relatively low (around 15 wt%) and that it was difficult to distribute the salt uniformly within the metal foam matrix, so we finally opted for the synthesis method described below.

(2) Depositing salt by immersing metal foam in an oversaturated solution of calcium chloride

This method involved the deposition of salt particles into the metal foam matrix by the deposition-precipitation process. The metal foams were cut into pieces in the form of panels, measured, and weighed before depositing $CaCl_2$. They were then immersed in an oversaturated solution of calcium chloride at room temperature. Dispersion of salt particles was achieved by stirring continuously and intensively the metal foam in the oversaturated $CaCl_2$ solution for approximately 5 min. Then the composites were subjected to moderately flushed by compressed air, in order to remove the excess of salt dispersion from the pores and to avoid complete saturation of the porosity. The final step consisted of placing the composites in an oven for more than 48 h at 90 ℃. The composite sample was then kept in the oven at 90 ℃ before use for avoiding the hydration by air humidity.

The photos of the synthesized composites are presented in Fig. 3.2. Fig. 3.2a shows the nickel foam-$CaCl_2$ composite with Fig. 3.2b its side view. Fig. 3.2c shows the aluminum foam-$CaCl_2$ composite. The copper foam-$CaCl_2$ composite (after corrosion) is shown in Fig. 3.2d. At the beginning of the synthesis attempts, we didn't store the composite samples in the oven at high temperatures. The plan was to completely dehydrate the samples before use, so they were merely stored in plastic sample boxes sealed with tape at the lid and then placed in a larger

container with moisture absorbers to control humidity. However, the copper foam-$CaCl_2$ composite was found quickly corroded. Slight corrosion was already visible the next day and, in several days, a bright green compound was found to have formed on the surface of the composite samples (as shown in Fig. 3.2d). This was unacceptable for a composite designed to store heat through hydration and dehydration cycles. Firstly, considering mechanical properties, corrosion of metal significantly decreases the mechanical strength of metal foams, leading to a shortened lifespan. Secondly, after the samples rust, we found that the generated green substance on the sample surface occupies a considerable volume, which may likely affect the porosity and cause changes in the sample volume. This should be avoided in practical applications. Finally, we were also unsure whether the green compounds generated by corrosion would have an impact on the hydration and dehydration process of the salt itself. This would complicate the entire system and make it less conducive to studying the overall performance effects of metal foams serving as the host matrix. Therefore, in subsequent experiments, we did not consider using easily corroded copper as the host matrix, and the thermochemical properties of the composite were studied with nickel foam-$CaCl_2$ composite and aluminum foam-$CaCl_2$ composite.

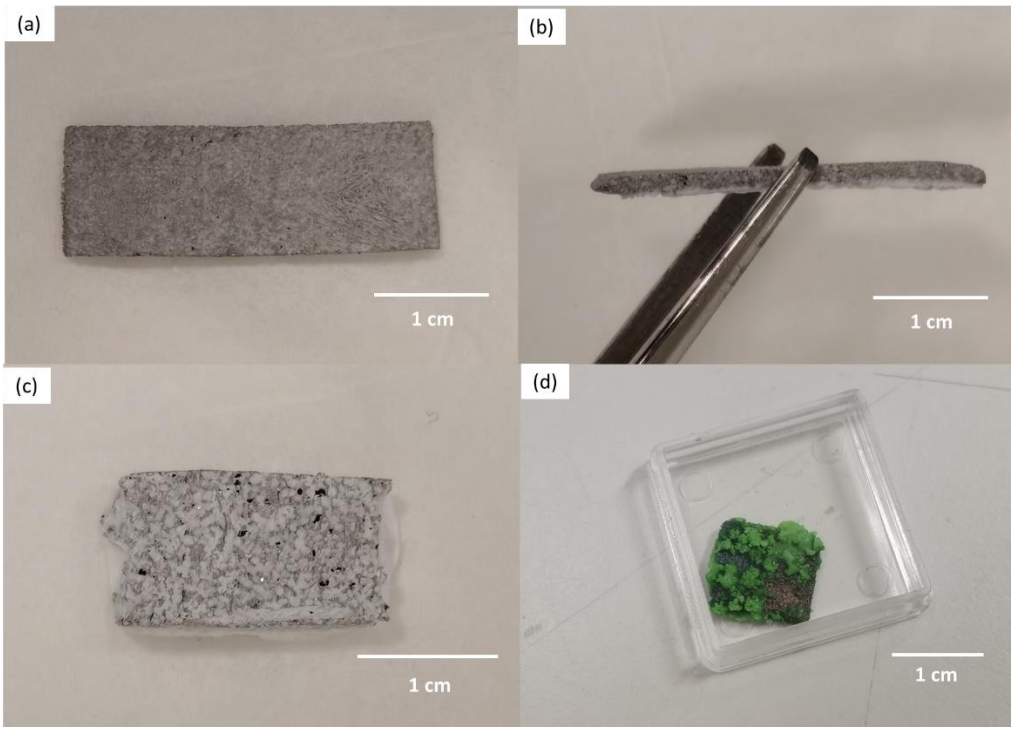

Fig. 3.2 Photo of (a) nickel foam-$CaCl_2$ composite with (b) its side view, (c) aluminum foam-$CaCl_2$ composite, and (d) the copper foam-$CaCl_2$ composite (after corrosion).

3.3. Experimental approach

In this section, we present the analysis technique as DSC and calorimeter used to study the thermal and thermochemical properties of the metal foam-salt hydrate composites, with experimental setup and experimental procedures described in

detail. In the last part, the in situ environmental scanning electron microscope (ESEM) technique and protocol for observations of the microstructural and morphological evolution of composite during the hydration and dehydration process are presented.

3.3.1. DSC: thermal properties analysis

Differential scanning calorimetry (DSC) is a thermal analysis technique that measures the change of heat flow rate difference between the sample and a reference under a controlled temperature program [203]. The term DSC was first used in 1963 by the company Perkin-Elmer on the first differential scanning calorimeter [204]. Besides the measurement of heat and heat flow rate, DSC can also provide us with information on the characteristic temperatures of a reaction or a phase-change process, such as the melting and crystallization temperature. In Fig. 3.3 we present a typical DSC curve and the definition of important characteristic terms for describing the curve. The DSC curve usually plots the heat flow rate versus the temperature.

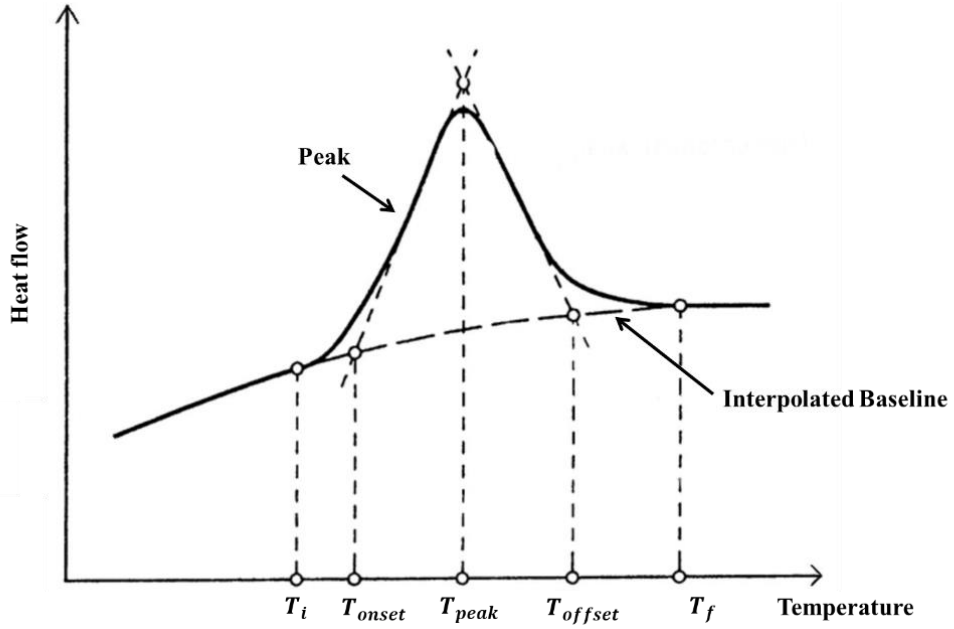

Fig. 3.3 Definition of characteristic terms of DSC curves [203].

The peak appears when the thermal activation as heat production or consumption occurs in the sample. For example, a reaction or a phase change process would induce an appearance of a peak in the measured curve. The interpolated baseline connects the DSC curve at the beginning and the end of the peak, as if no peak was developed. We consider the beginning of the peak to be at T_i, which is the temperature where the curve first deviates from the baseline. The peak onset temperature T_{onset} is defined as the intersection temperature of the auxiliary line through the ascending peak slope and the interpolated baseline. Similarly, the peak offset temperature T_{offset} is defined as the intersection temperature of the auxiliary

line through the descending peak slope and the interpolated baseline. The temperature T_{peak} represents the maximum value of the difference between the measured curve and the interpolated baseline, which may not be the maximum value of the curve. For more information on DSC curves, the reader is referred to this book on DSC [203].

In our study, the thermal properties analysis of the composite was realized by performing thermal cycling tests on a DSC device (Micro-DSC VII, SETARAM). The DSC device was equipped with a double chamber that serves as the calorimetric block. It contained one vessel for the sample and a second one for reference. Both vessels consisted of an 850 µl cylindrical crucible made of Hastelloy®. They were sealed with elastomer seals retained by anti-extrusion rings. The heat flow measurement sensor consisted of a high-sensitivity planar flow meter, which surrounded the two experimenting vessels and kept a tight thermal connection to the calorimetric block, ensuring identical temperature between the experimenting vessels and the calorimetric block. The temperature sensor was composed of Peltier elements with Joule effect calibration and provided measurement accuracy of a level up to ± 0.07 ℃ for the temperature range between -45 ℃ and 120 ℃.

We performed cyclic thermal experiments on a nickel foam-$CaCl_2$ composite sample with a mass of 78.92 mg. The sample was heated up to 115 ℃ and cooled down to -40 ℃ at the heating/cooling rate of 0.5 ℃/min for 4 cycles. The temperature range was chosen to cover the temperature range of possible working conditions for the composite serving as thermochemical material for thermal energy storage. To reduce the errors related to the thermal lag between the sample and the sensor, a relatively low heating and cooling rate of 0.5 ℃/min was chosen [205]. The thermal properties of the composite were then analyzed based on the DSC curve recorded during the crystallization and melting process of the salt.

Fig. 3.4 Photo of the Micro-DSC VII device used for thermal properties analysis of composite.

3.3.2. Calorimeter: isothermal thermochemical reaction analysis

a) Experimental setup

Heat flow measurements during hydration and dehydration cycles were carried out on a Calvet-type calorimeter (C80, SETARAM). The sample and reference vessels of 12.5 ml were connected to a gas circulation tubing circuit. They were surrounded by 3D Calvet sensors based on thermocouples with Joule effect calibration which provided a temperature measurement accuracy of ± 0.1 °C and precision of ± 0.15 °C. The operating temperature range was between the ambient temperature and 300 °C.

Before depositing the salt, metal foam samples in form of panels were cut from the metal foam sheets, measured, and weighed. The metal foam-salt composite samples were kept dry in the oven at 90 °C and re-weighed before use. Samples were then placed directly into the sample vessel of the calorimeter and sealed to prevent the hydration of the sample due to ambient air humidity. Every two samples of metal foam-salt composite panels were stacked in the sample vessel to simulate their practical industrial application conditions. For our experiment, we chose to perform the hydration/dehydration cycles at an isothermal condition at 23 °C. The schematic diagram and photo of this experimental setup are shown in Fig. 3.5 and Fig. 3.6 respectively. The sample vessel presented in Fig. 3.6c was equipped with an inlet and an outlet valve, as well as a switch knob for controlling the gas flow rate that circulated in the sample vessel. A bottle of dry nitrogen gas (N_2 ⩾ 99.999%, ALPHAGAZ™ 1 Nitrogen, Air Liquide) was connected to two gas circuits controlled by a valve. During the dehydration process, the dry nitrogen gas served as the purge gas. For the hydration process, the dry nitrogen gas passed through a gas bubbler filled with a saturated solution of magnesium nitrate kept at a constant temperature of 23 °C by water bath, which allowed the nitrogen gas to be humidified to a constant relative humidity of 54% [202]. The nitrogen gas then passed a flowmeter (R-2-15-AA, Sho-Rate™ 1355, BROOKS) connected to the gas inlet valve of the sample vessel for measuring the gas flow rate. It can be controlled by adjusting the switch knob of the gas circulation tube attached to the sample vessel. For both the cyclic hydration and dehydration processes, the gas flow rate was controlled at 128 ml min^{-1}. Note that the inlet pipe connecting to the entrance of the sample vessel was heated by a water bath glass tube and heat-insulated to ensure that the humidified gas could still enter the reaction chamber at the temperature of 23 °C, in order to avoid fluctuations of heat flow in the reaction chamber due to temperature differences. The gas outlet valve of the sample vessel was then linked to a vacuum pump to realize the gas circulation throughout the experimental setup. At the beginning and the end of each hydration/dehydration process, we waited for at least 15 min for the signal to stabilize.

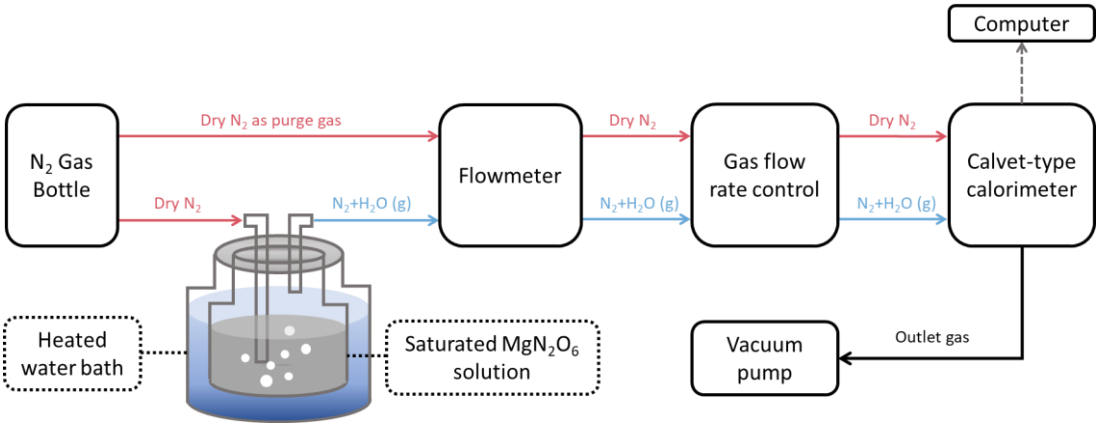

Fig. 3.5. Schematic diagram of the experimental setup.

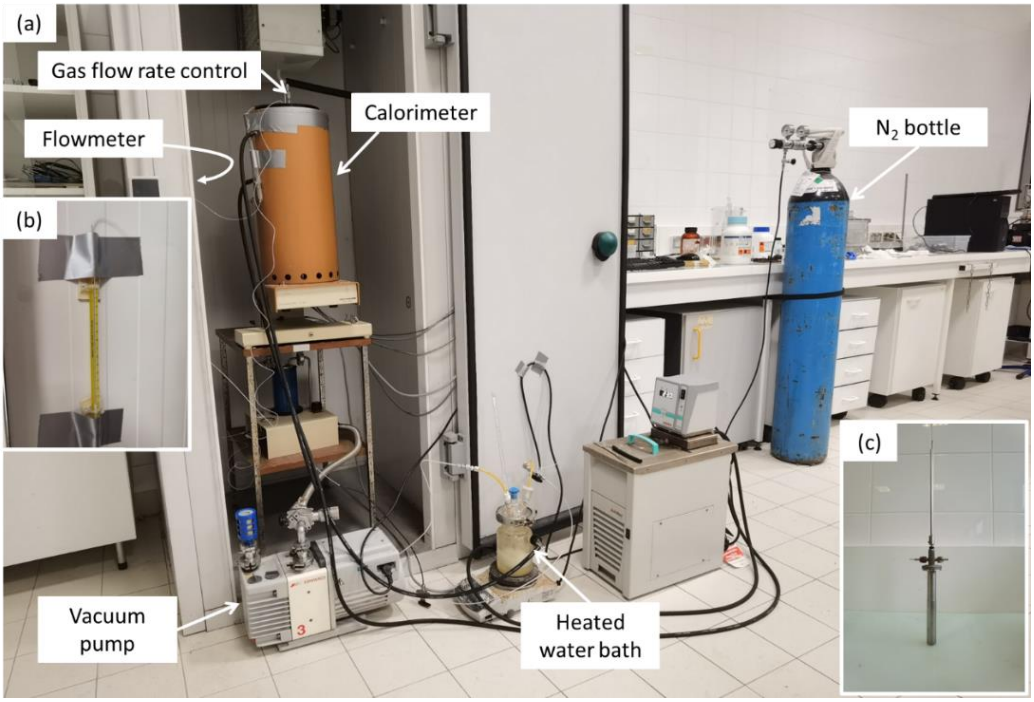

Fig. 3.6 Photo of (a) experimental setup for hydration/dehydration cycles performed on composite, with (b) the flowmeter stuck to the side wall (not visible in photo (a)) and (c) the photo of the sample vessel.

Discussion on the choice of experimental conditions

Note that, in our study, the humidified nitrogen gas was chosen as the source of water vapor instead of ambient air for the following reasons. First, to avoid introducing other unnecessary variables regarding our experiment purpose, it is important to control the relative humidity of the gas serving as the source of water vapor. This control is impossible when using ambient air, which changes its relative humidity with the weather. Second, approximately 80% of the ambient air is composed of nitrogen, with the remaining 20% being mainly oxygen. The presence of oxygen can significantly affect the corrosion mechanism of metal foams. Since the experiment aims to validate the enhancement in terms of cyclic and thermal

storage performance with metal foam serving as the host matrix, introducing potential corrosion issues would complicate the system and we believe that it is better to study the corrosion problem separately.

As for the choice of the experimental temperature of 23 ℃, it can be seen in the experimental setup photo Fig. 3.6 that the calorimeter machine's surface was in direct contact with the laboratory air. Since its temperature sensor was very sensitive, external temperatures can greatly influence the temperature inside the reaction (sample) vessel. To maintain a stable temperature inside the reaction vessel, it is necessary to equilibrate the temperature inside the vessel with the ambient air temperature in the laboratory. Since our laboratory temperature was typically controlled around 23 ℃ throughout the year, and this temperature is a common indoor temperature, we decided to set the experimental temperature at 23 ℃.

As for the choice of relative humidity of the humidified N_2 gas serving as the source of water vapor, we first tested the relative humidity of ambient air in the laboratory. During summer and winter time, the relative humidity in our laboratory was between 47% and 65%, while for most days the RH was around 54%. As explained in the previous paragraph, it is necessary to control the relative humidity of the source gas to a certain constant value. So we chose to conduct our experiment at a relative humidity of 54% by sending the dry nitrogen gas passing through a saturated salt solution to serve as the source of water vapor. Actually, in practical use, an analysis should be done according to the climate condition to define whether the ambient relative humidity is sufficiently high for a good heat-releasing rate [31]. For instance, in regions with very dry climates, it may be necessary to use an additional humidifier to moisten the gas used for salt hydration.

Another point to note is that the dehydration process was achieved by continuously purging with dried nitrogen gas, while in real applications, the total dehydration could be done by heating the samples to a relatively high temperature. For example, it is reported in the literature [107] that hexahydrate of calcium chloride can be completely dehydrated at 200 ℃ by raising the temperature from 20 ℃ to 300 ℃ with a rate of 2 ℃/min. In our work, heating for dehydration was not applied considering two factors: first, without using thermogravimetric analysis, we were uncertain about the temperature at which the salt in the sample would completely dehydrate. Second, due to the relatively low melting points of hexahydrate and tetrahydrate of calcium chloride (around 30 ℃ and 45 ℃, respectively), the melting of the salt should be avoided during the experiment because we were unsure of the potential impact of salt melting on the microstructure of the composite. Furthermore, salt melting is an endothermic process. To avoid introducing additional variables, we opted to proceed with salt dehydration at a constant temperature of 23 ℃.

b) Experimental protocol

For analyzing the thermal cycling performance of the composite and compare its performance with that of bulk $CaCl_2$ salt during hydration and dehydration cycles, we performed experiments on three kinds of samples, which were nickel foam-$CaCl_2$ composite (48.5 wt% $CaCl_2$), aluminum foam-$CaCl_2$ composite (21.0 wt% $CaCl_2$) and bulk $CaCl_2$ salt powder. We designed two kinds of experimental procedures described as follows.

1) Long hydration/dehydration cycles

To avoid the irreversible structural damage of the composite during complete hydration related to $CaCl_2$ deliquescence, each composite sample was partially hydrated by the circulation of hydrated nitrogen gas with a constant relative humidity at 54% for different hydration duration Δt_{hydr} under isothermal conditions for 12 cycles (see Table 3.1).

Table 3.1 Long hydration/dehydration cycles experimental procedure.

Cycle number	Hydration duration Δt_{hydr} (min)
1	360
2	180
3	180
4	180
5	90
6	90
7	90
8	90
9	45
10	45
11	45
12	360

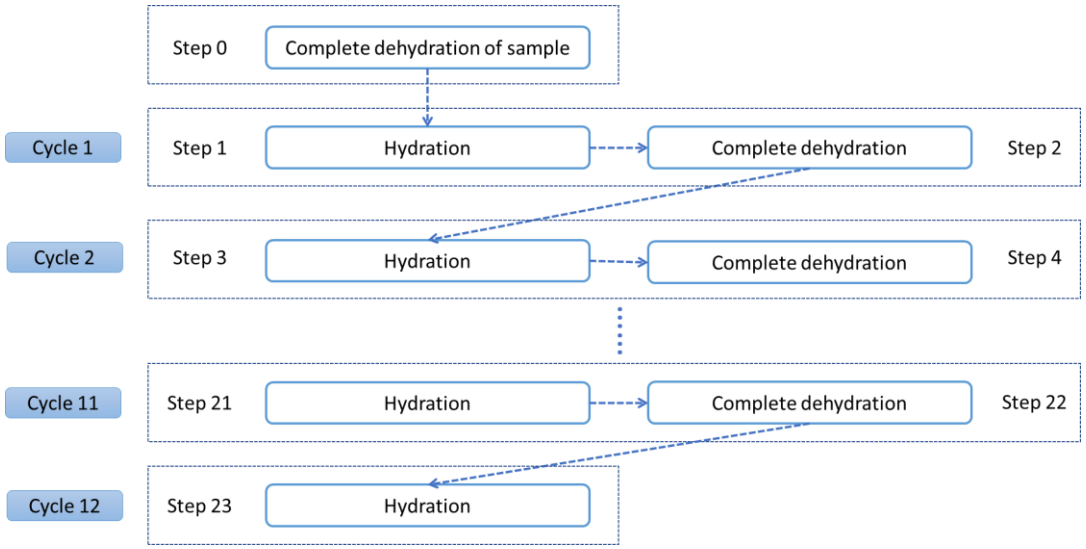

Fig. 3.7. Graphical flow chart of the long hydration/dehydration cycles experimental procedure.

After every hydration, the samples were completely dehydrated by the circulation of dry nitrogen. The time necessary to completely dehydrate the sample depended on the hydration duration, the type of sample, and the mass of salt contained in the sample. The same experimental procedure was applied to bulk salt powder for comparison. The graphical flow chart of the long hydration/dehydration cycles experimental procedure in shown in Fig. 3.7.

2) Short hydration/dehydration cycles

In this procedure, each sample was hydrated by the circulation of hydrated nitrogen gas with a constant relative humidity at 54% for 45 min under isothermal conditions and was completely dehydrated by the circulation of dry nitrogen after every hydration process. Six cycles of this experiment were performed for each kind of sample, and two repetition tests were conducted.

Heat flows during these cycles were recorded and the quantity of thermal energy released/stored during hydration/dehydration cycles was obtained by integrating the heat flow signal over the time duration of each experiment, respectively. Experimental errors were estimated according to the data acquired through repetition tests as well as resolution limitations of the instrument given by manufacturers.

The mass of samples used in both long and short hydration/dehydration cycles are presented in Table 3.2.

Table 3.2 Mass of samples used in long and short hydration/dehydration tests.

Cycle type	Sample mass (mg)		
	Ni-$CaCl_2$ composite	Al-$CaCl_2$ composite	Bulk $CaCl_2$
Long cycle	430.1	653.6	209.1
Short cycle	440.4	718.3	209.1
	431.2	703.8	209.1

3.3.3. SEM: in situ hydration/dehydration cycling test

In situ hydration/dehydration cycling tests of the metal foam-salt composites were performed using a scanning electron microscope (FEI QUANTA 650 FEG-ESEM) to investigate their microstructural evolution. The observation and the image recording in real-time during the process were done under controlled relative humidity (RH), which is made possible with the environmental scanning electron microscope (ESEM) mode and using a gaseous secondary electron detector (GSED). The water vapor is injected into the SEM chamber via a separate vacuum pump that is able to control the chamber pressure with great accuracy, in addition to a Peltier stage for keeping the sample at a constant temperature, the RH can be thus controlled [206, 207]. In addition to RH control, the ESEM mode also allowed for avoiding coating the poorly conductive salt particles with conductive metal foam, hence preserving their original characteristics.

The nickel foam-$CaCl_2$ composite sample (7 mm × 7 mm × 1.4 mm) fresh out of the oven was mounted on a cooling stage using the Peltier effect with a thermocouple in contact with the sample's upper surface to monitor the actual temperature of the sample. For reproducing the experimental conditions of thermochemical tests mentioned in section 3.3.2, the sample was controlled at a constant temperature of 23 ℃ by adjusting the temperature of the Peltier stage. During the hydration process, the humidity around the sample was gradually increased from 0 to about 54% RH. This was achieved and controlled by increasing the vapor pressure in the SEM chamber. Likewise, for the dehydration process, the humidity was decreased to 0 by reducing the vapor pressure in the chamber. Highly resolved images (3072 × 2207 pixels per image with a pixel size of 0.08 µm) were taken for the region of interest (ROI) at the initial and final states for both hydration and dehydration cycles. Lower resolution images (1536 × 1113 pixels per image with a pixel size of 0.77 µm) were also recorded automatically every 5 seconds during the hydration/dehydration cycles

3.4. Results and discussion

In this part, the thermal and thermochemical properties of metal foam-salt hydrate composites are presented and analyzed. In addition, the thermochemical properties of the composites were compared with that of bulk salt hydrate powders. In the final part, we present the results obtained during hydration/dehydration cycling tests performed on the composite with the in situ environmental scanning electron microscope (ESEM) technique and provide insight into the possible working mechanisms of the metal foam-salt hydrate composite.

3.4.1. Thermal properties analysis of the composite

Thermal properties and thermal cyclic reliability of metal foam-salt composite were analyzed by DSC. Fig. 3.8 presents the DSC curves of nickel foam-$CaCl_2$ composite during 4 cycles of heating and cooling in the temperature range of -40 ℃ to 120 ℃ at a constant rate of 0.5 ℃/min. The onset temperature, offset temperature, and peak temperature of melting and crystallization and their average value of 4 heating/cooling cycles are listed in Table 3.3. Fig. 3.8 shows that one exothermic peak with an onset temperature of 18.2 ± 0.8 ℃ during the cooling process and one endothermic peak with an onset temperature of 44.3 ± 0.2 ℃ during the heating process were detected, which corresponded to the crystallization and the melting of salt embedded in the metal foam, respectively. The onset crystallization temperature and onset melting temperature detected are compatible with the values for calcium chloride tetrahydrate reported in the literature [208, 209]. The difference between onset crystallization temperature and onset melting temperature is defined as the supercooling degree ΔT_s of a phase change material and can be evaluated by a hysteresis equation [210] :

$$\Delta T_s = T_M - T_C \tag{29}$$

where T_M and T_C are the melting and crystallization temperatures, respectively. As shown in Table 3.3, $\Delta T_s \approx 26$ ℃ was detected for the composite during the heating and cooling process. It is also notable that the supercooling degree of the first cycle (about 27.5 ℃) was nearly 2 ℃ higher than that of the following cycles (about 25.5 ℃). It is possible that during the first melting process, the salt particles were redistributed in the host matrix in a way favoring nucleation during the following cycles, for instance by revealing more open pores as well as metal foam struts and strut ends, thus resulting in a lower supercooling degree from the second cycle and on [211, 212].

Table 3.3 Thermal properties of the composite obtained by DSC cyclic tests.

Cycle No.	Heating			Cooling		
	Onset T_M (℃)	T_{Peak} (℃)	Offset T_M (℃)	Onset T_C (℃)	T_{Peak} (℃)	Offset T_C (℃)
1	44.5	47.6	48.6	16.8	16.4	15.7
2	44.1	47.0	47.8	18.4	18.1	17.4
3	44.2	47.1	47.9	18.8	18.4	17.7
4	44.2	47.1	47.9	18.9	18.7	17.9
Average	44.3 ± 0.2	47.2 ± 0.2	48.1 ± 0.3	18.2 ± 0.8	17.9 ± 0.9	17.2 ± 0.9

* T_M = melting temperature, T_C = crystallization temperature, T_{Peak} = maximum peak temperature

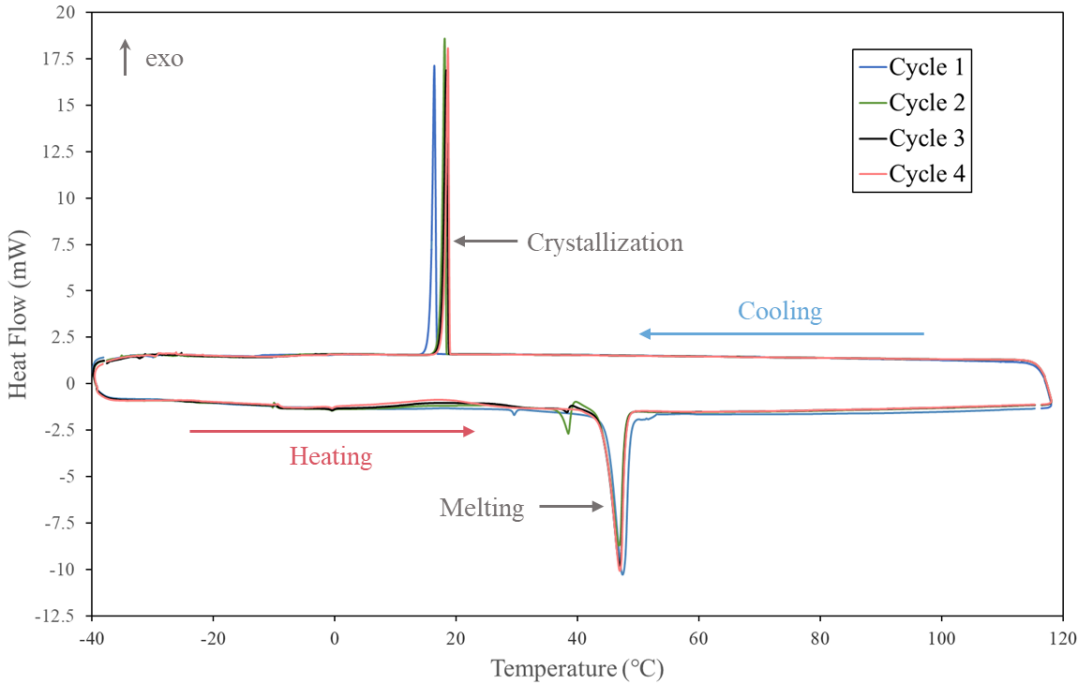

Fig. 3.8. DSC curves of nickel foam-salt composite during 4 cycles of heating and cooling.

It can be clearly seen in Fig. 3.8 that except for the first cycle, the DSC curves for the following 3 cycles are closely coincident with each other, indicating that the

enthalpy of fusion and crystallization almost remained unchanged during heating and cooling cycles. In addition, the phase change temperatures were rather steady (see Table 3.3). These results demonstrated that the composite has sufficiently good cycling thermal stability and reliability over a large temperature range of -40 ℃ and 120 ℃.

3.4.2. Thermochemical properties analysis during cyclic tests

a) Analysis of long hydration/dehydration cycles

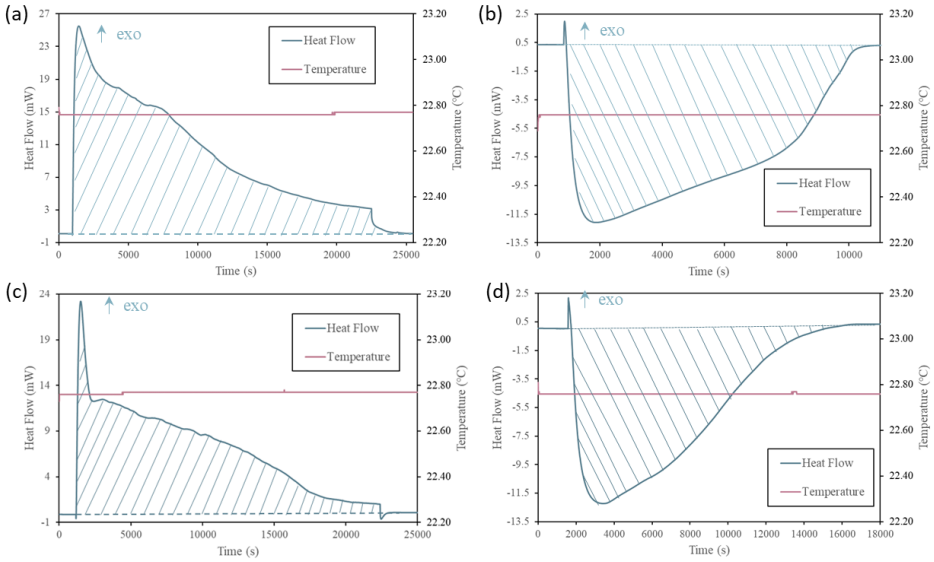

Fig. 3.9. Typical curves of heat flow over time during (a) hydration and (b) dehydration process of bulk calcium chloride powder and during (c) hydration and (d) dehydration process of composite (here we present the curves of nickel foam-$CaCl_2$ composite for example).

We present in Fig. 3.9 the typical curves of heat flow over time during the hydration/dehydration process of both composite and bulk salt powder. The curves obtained for the nickel foam-salt composite and the aluminum foam-salt composite had identical forms, so here we present the curves of the nickel foam-salt composite as an example. In fact, it can be seen in Fig. 3.9 that the curves obtained for bulk salt powder and composites also have similar forms. For curves obtained during the hydration process (see Fig. 3.9a and c), the signal of heat flow stabilized during the first 15 min which provided us with a steady state baseline value of the heat flow ϕ_{bl} for evaluating the integration of heat flow over time. Then the humidified nitrogen entered the reaction vessel at t_i and a rapidly increasing heat flow signal was detected. The heat flow reached a maximum peak value of ϕ_p in 5-7 min and then decreased slowly over time. The circulation of humidified nitrogen was stopped at t_f when the humidification process time reached the target duration set by our experimental plan. Then the heat flow signal dropped immediately and rapidly. It gradually stabilized near the baseline in 30 min. For the following dehydration process (see Fig. 3.9b and d), the dry nitrogen gas entered the reaction vessel after the signal stabilized. The circulation of dry nitrogen

continued until the signal of heat flow gradually returned to the baseline. Note that the small exothermic peak during the beginning of the dehydration process, as shown in Fig. 3.9b and d, is caused by the small amount of residual humidified nitrogen gas in the tube during the hydration process. The energy released corresponding to this small peak is negligible compared to the thermal energy restored during the entire dehydration process. During the whole process, the temperature of the sample was controlled at 22.76 ℃.

The quantity of thermal energy Q released/restored during hydration/dehydration processes is estimated as follows:

$$Q(t) = \int_{t_i}^{t_f} [\phi(t) - \phi_{bl}]dt \tag{30}$$

The normalized quantity of thermal energy Q_N released/restored during each cycle is defined as follows:

$$Q_N = \frac{Q}{m_{CaCl_2}} \tag{31}$$

where m_{CaCl_2} is the mass of $CaCl_2$ contained in each sample.

Hydration process

We first analyze the normalized thermal energy released during the hydration process for these three kinds of samples.

The normalized thermal energy Q_N released during 12 cyclic hydration processes (see Table 3.1) for bulk $CaCl_2$ salt powder, nickel foam-$CaCl_2$ composite, and aluminum foam-$CaCl_2$ composite are presented in Fig. 3.10. For the first cycle of 360 min hydration, the bulk $CaCl_2$ powder outperformed the other two composite significantly by reaching 1074.3 kJ/kg^{salt} in terms of thermal energy released during this time range, while for nickel foam-$CaCl_2$ composite, the value was 730.8 kJ/kg^{salt} and 811.0 kJ/kg^{salt} for aluminum foam-$CaCl_2$ composite. Yet, in the following cycles, especially from the 5th cycle, the performance of bulk $CaCl_2$ powder exhibited a clear disadvantage compared to the other two composites. For a hydration time range of 90 min (cycle N°5, 6, 7 and 8), the average Q_N released by nickel foam-$CaCl_2$ composite and by aluminum foam-$CaCl_2$ composite was 705.3 kJ/kg^{salt} and 525.7 kJ/kg^{salt}, which improved 146.1% and 83.5% respectively compared to that of bulk $CaCl_2$ powder (286.5 kJ/kg^{salt}). In the following cycles, for hydration time range of 45 min (cycle N°9, 10, 11), the advantage of composites' performances became increasingly apparent. In particular, the composite with aluminum foam as the matrix released up to 351.2 kJ/kg^{salt} for the average Q_N of these 3 cycles, which was 4.9 times more than the amount released by bulk $CaCl_2$ powder (72.0 kJ/kg^{salt}), while the nickel foam-$CaCl_2$ also released up to 4.0 times more thermal energy than the

bulk salt powder, which was 288.3 kJ/kg^{salt}. Then, in the last cycle, we reproduced exactly the same experimental conditions of the first cycle, which means the samples were re-humidified for 360 min as in the first cycle, to investigate how the samples performed after 11 hydration/dehydration cycles. Results showed that nickel foam-$CaCl_2$ composite provided a Q_N of 903.9 kJ/kg^{salt}, which improved 23.7% compared to that of the first cycle, while aluminum foam-$CaCl_2$ composite provided a Q_N of 834.1 kJ/kg^{salt} in the 12th cycle, which slightly increased by 2.8% compared to the first cycle. In contrast, Q_N of bulk $CaCl_2$ powder decayed by 63.2% after 11 cycles, by providing a Q_N of only 395.8 kJ/kg^{salt} in the 12th cycle.

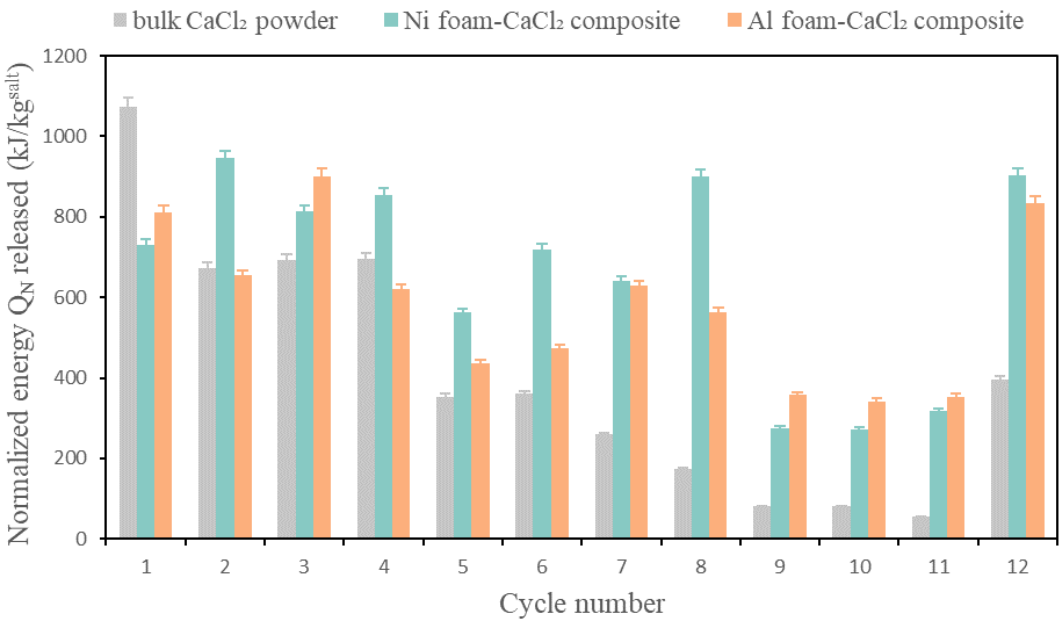

Fig. 3.10. Normalized thermal energy released during 12 cyclic hydration/dehydration processes of nickel foam-$CaCl_2$ composite, aluminum foam-$CaCl_2$ composite and bulk $CaCl_2$ powder.

In order to better compare the trends in performance of these 3 kinds of samples during the 12 hydration/dehydration cycles by eliminating the influence on Q_N due to the difference in hydration time during different cycles, the values of normalized thermal energy Q_N released for each kind of sample were calculated and compared for the first 45 minutes of each humidification as presented in Fig. 3.11. Although bulk $CaCl_2$ powder provided the highest Q_N in the first cycle, it is clearly seen that the performance of bulk $CaCl_2$ powder decreased from the 2nd cycle and continued to decline sharply after 6 cycles, resulting in a performance degradation of 78.5% at the 12th cycle compared to the 1st cycle (from 265.6 to 57.2 kJ/kg^{salt}). While the performance of both composites was found to be much more stable. Both composites provided a lower Q_N compared to the bulk $CaCl_2$ powder in the first cycle, however, in the following cycles, the composites showed superior performance and enhanced cycling stability. After 12 cycles, Q_N improved from 179.3 to 299.6 kJ/kg^{salt} for nickel foam-$CaCl_2$ composite and from 225.6 to 346.5

kJ/kg^{salt} for aluminum foam-$CaCl_2$ composite, which indicates a 67.1% and a 53.6% increase in Q_N, respectively. Moreover, there wasn't any tendency for Q_N to degrade for both composites after these 12 cycles. The results also demonstrate that for the first 45 min of the 12th cycle, Q_N of nickel foam-$CaCl_2$ composite and of aluminum foam-$CaCl_2$ composite improved substantially to 5.2 and 6.1 times that of bulk $CaCl_2$ powder.

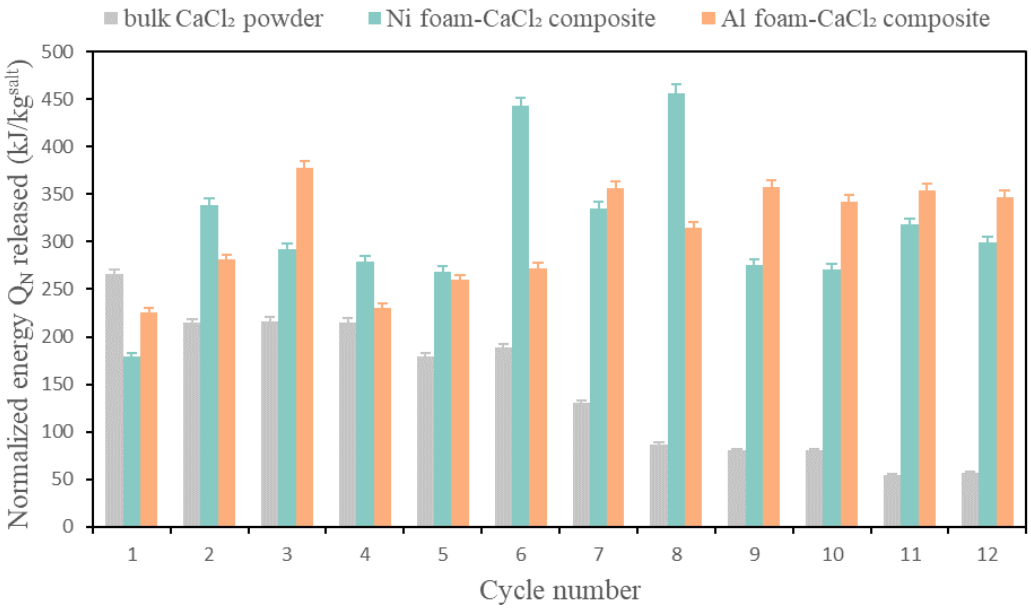

Fig. 3.11. Normalized thermal energy released during the first 45 min of each humidification process for 12 hydration/dehydration cycles of nickel foam-$CaCl_2$ composite, aluminum foam-$CaCl_2$ composite and bulk $CaCl_2$ powder.

Dehydration process

In this part, we focus on the normalized thermal energy restored during the dehydration process for composites and bulk salt powder during long cyclic tests.

As the experimental procedures for long hydration/dehydration presented in 3.3.2, the samples were completely dehydrated at 23 °C with dry nitrogen gas serving as purge gas before the cyclic hydration/dehydration test and after every hydration process, as shown in Fig. 3.7.

The normalized thermal energy Q_N restored during each dehydration process for bulk $CaCl_2$ salt, nickel foam-$CaCl_2$ composite and aluminum foam-$CaCl_2$ composite are presented in Fig. 3.12. It can be seen that the heat storage performance of bulk $CaCl_2$ salt and the two composites were comparable at the beginning of the cyclic experiment. For the dehydration corresponding to the first hydration process of 360 min, the normalized thermal energy Q_N restored of bulk $CaCl_2$ powder, nickel foam-$CaCl_2$ composite and aluminum foam-$CaCl_2$ composite reached 728.0 kJ/kg^{salt}, 746.8 kJ/kg^{salt} and 822.4 kJ/kg^{salt}, respectively. However, the difference between the Q_N stored of bulk salt and the two composites during each dehydration process

became more and more significant as the cycle continued. For example, for the dehydration process in cycle N°5, 6, 7 and 8 which correspond to the hydration process of 90 min, the average Q_N restored for $CaCl_2$ powder was 232.2 kJ/kg^{salt}, while this value of nickel foam-$CaCl_2$ composite and aluminum foam-$CaCl_2$ composite remained 697.7 kJ/kg^{salt} and 519.2 kJ/kg^{salt}, respectively, which were 3 times and 2.2 times that of $CaCl_2$ powder. In the following cycles, the advantage of composites' performances in terms of energy storage capacity became more apparent. In particular, aluminum foam-$CaCl_2$ composite restored up to 340.6 kJ/kg^{salt} for the average Q_N of cycle N°9, 10 and 11 (corresponding to 45min hydration), which was 5.3 times compared to that of bulk $CaCl_2$ powder (64.6 kJ/kg^{salt}), while the nickel foam-$CaCl_2$ also restored an average Q_N of 284.4 kJ/kg^{salt} during these last 3 cycles, which was 4.4 times compared to that of bulk $CaCl_2$ powder.

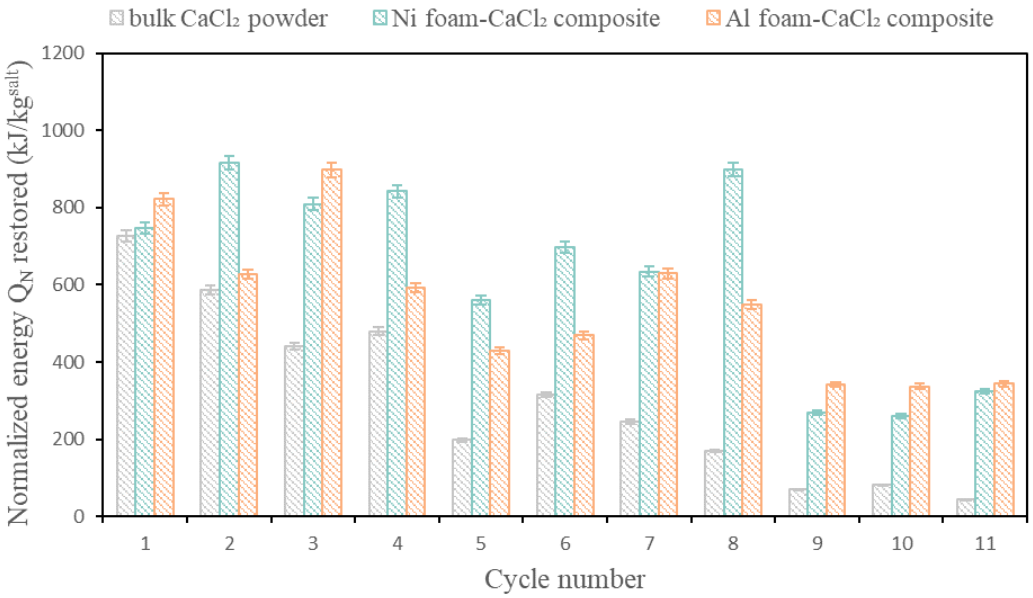

Fig. 3.12. Normalized thermal energy restored during long cyclic hydration/dehydration process of nickel foam-$CaCl_2$ composite, aluminum foam-$CaCl_2$ composite and bulk $CaCl_2$ powder.

Summary

By summing up the normalized thermal energy released during long cycles of hydration and that restored during dehydration, we obtain total Q_N released and restored for bulk $CaCl_2$ powder, nickel foam-$CaCl_2$ composite and aluminum foam-$CaCl_2$ composite as shown in Table 3.4.

By calculation, we have the result that bulk $CaCl_2$ powder had the capability of restoring 74.7% of the thermal energy released during long cyclic hydration/dehydration tests. While for both composites, they were able to restore 99.0% and 98.3% (for nickel foam-$CaCl_2$ composite and aluminum foam-$CaCl_2$, respectively) of the total thermal energy released through these 12 cycles of hydration and dehydration. If we consider the experimental error derived from the

resolution limitations of the calorimeter given by the manufacturer, which was 2%, the composites were almost capable of restoring all the thermal energy released during long cyclic hydration/dehydration tests.

Table 3.4 Total normalized thermal energy released and restored during long cyclic tests for bulk $CaCl_2$ powder, nickel foam-$CaCl_2$ composite and aluminum foam-$CaCl_2$ composite.

Sample type	Total Q_N released (kJ/kg^{salt})	Total Q_N restored (kJ/kg^{salt})
Bulk $CaCl_2$ powder	4496.7	3360.1
Ni foam-$CaCl_2$ composite	7029.6	6959.5
Al foam-$CaCl_2$ composite	6143.4	6039.2

The results obtained from the long hydration/dehydration cycles provided us with fundamental data allowing for comparison of the cyclic thermal properties on bulk $CaCl_2$ powder, nickel foam-$CaCl_2$ composite and aluminum foam-$CaCl_2$ composite.

For bulk $CaCl_2$ powder, though it provided relatively high thermal energy in the first hydration process, Q_N dropped substantially and continuously during the following humidification cycles due to deliquescence and agglomeration, inducing specific surface loss, which yielded poor cyclic stability and a relatively low capability of restoring the thermal energy released during cycles compared to composites [92, 213].

Conversely, on the one hand, for nickel foam-$CaCl_2$ composite and aluminum foam-$CaCl_2$ composite, there was no degradation in terms of Q_N after 12 cycles of hydration/dehydration. On the other hand, surprisingly, both of them showed a significant increase in Q_N in the last and longest cycle of hydration (N°12) compared to the first longest cycle (N°1). In general, except for the first cycle, the thermal energy storage/release capacity of the composites compared to the bulk salt was substantially improved in all the rest of the cycles, and this advantage tended to increase with the number of cycles. The results of long cyclic hydration/dehydration experiment clearly demonstrated that the composites combining a hygroscopic salt crystal (such as calcium chloride) dispersed in metal foam as a host matrix exhibited excellent cyclic stability and superior thermal energy storage capacity compared to bulk $CaCl_2$ powder. This improvement is undoubtedly attributable to the use of the metal foam as a porous matrix, which might have preserved the salt particles from agglomeration and compaction effects related to deliquescence and swelling during hydration cycles. As a result, the metal foam matrix might have preserved the specific reaction surface and provided more efficient pathways for mass and heat transfer.

Maximum peak value during hydration

We define $\phi_{p,N}$ the normalized maximum peak of heat flow during the hydration process as follows:

$$\phi_{p,N} = \frac{Max[\phi(t)]}{m_{CaCl_2}} \quad (32)$$

In the case of composites, the value of $\phi_{p,N}$ is considered to be strongly influenced by the spatial distribution, size, and morphology of salt crystals deposited in the composite. As for bulk salt, it is also considered to be influenced by the degree of dispersion and agglomeration of the salt crystals. In both cases, the value of $\phi_{p,N}$ can be seen as an implicit indicator of the heat and mass transfer efficiency of each sample.

Fig. 3.13 illustrates the $\phi_{p,N}$ of hydration process for these three kinds of samples during 12 hydration/dehydration cycles. For all samples, the trends of $\phi_{p,N}$ were almost the same as these of the respective Q_N during hydration over 12 cycles. For the bulk salt, the average of $\phi_{p,N}$ was 64.4 W/kg^{salt} and the maximum $\phi_{p,N}$ for the 12 cycles appeared during the first hydration process. $\phi_{p,N}$ continued to decrease in the following cycles and reached by the last cycle a degradation of 73.5%, as compared to its maximum value obtained at the first cycle. This indicates that during the initial phase of the experiment, the bulk salt particles were more uniformly dispersed in the sample vessel, providing a larger specific surface area for hydration. As the cycles progressed, the bulk salt underwent deliquescence and agglomeration, resulting in a decreasing surface area and thus reducing its cycling stability in terms of Q_N, as shown in Fig. 3.11 and in terms of $\phi_{p,N}$, as shown in Fig. 3.13. For nickel foam-$CaCl_2$ composite and aluminum foam-$CaCl_2$ composite, the average of $\phi_{p,N}$ over 12 cycles were 140.2 W/kg^{salt} and 139.9 W/kg^{salt} respectively, which was about 2.2 times higher than that for the bulk salt. In addition, no evidence of $\phi_{p,N}$ degradation was detected in either composite throughout the 12 cycles and the minimum $\phi_{p,N}$ was that of the first hydration for both composites, resulting in an increase of 27.5% and 51.9% in terms of $\phi_{p,N}$ in the last cycle for nickel foam-$CaCl_2$ composite and aluminum foam-$CaCl_2$ composite, respectively.

The conclusions drawn from Fig. 3.13 regarding $\phi_{p,N}$ correspond well to the previous conclusions regarding Q_N, which illustrate the influence of the distribution and deposition morphology of the salt particles on the cyclic stability and energy storage properties, validating the superiority offered by open-cell metal foams as a host matrix for the composites.

These results also suggest that during the first hydration cycle, the topological parameters (spatial distribution and morphology) of the salt particles deposited in the composites have evolved in a way improving the thermochemical performances. We can also infer that if the topological evolutions continued in the following cycles, it did not affect the performances of the composites in thermochemical terms (Q_N) related to the specific reaction area, nor in kinetic terms ($\phi_{p,N}$) related to mass

transfer capability, which means the portion of accessible open pores in the metal foam did not decrease during the cycles, thus leading to a better performance in terms of cyclic stability and quantity of thermal energy released.

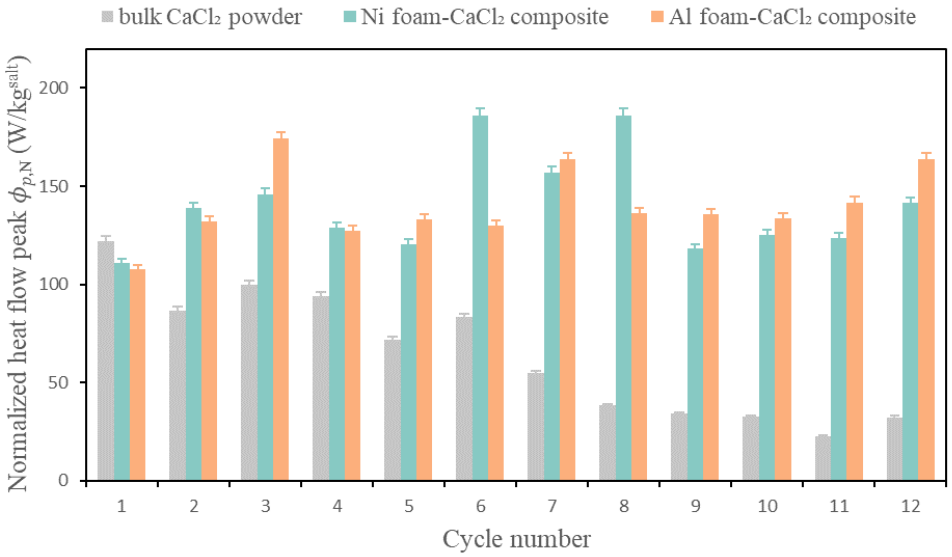

Fig. 3.13. Normalized maximum heat flow peak of hydration process during 12 hydration/dehydration cycles of nickel foam-$CaCl_2$ composite, aluminum foam-$CaCl_2$ composite and bulk $CaCl_2$ powder.

b) Short hydration/dehydration cycles

In order to better verify the superior performance of the metal foam-$CaCl_2$ composites compared to that of bulk $CaCl_2$ salts, 2 repetition experiments were performed for each kind of sample. The experiment consisted of 6 cycles, as described in section 3.3.2, where the samples were humidified for 45 minutes per cycle with other experimental conditions remaining unchanged, and the normalized thermal energy Q_N released during the process was then calculated and analyzed. Experimental errors were analyzed by standard deviation according to the data acquired through repetition tests.

Fig. 3.14 illustrates that from the 2nd cycle onwards for both composites Q_N was significantly higher than that of bulk $CaCl_2$ powder. For cycle N°2 to N°6, the improvement of normalized thermal energy Q_N released by aluminum foam-$CaCl_2$ composite to bulk $CaCl_2$ powder was between 77.9% to 129.6%, while for nickel foam-$CaCl_2$ composite, the improvement was between 54.5% to 85.9% (see Fig. 3.15). For nickel foam-$CaCl_2$ composite, Q_N varied from 256.7 kJ/kg^{salt} (N°1) to 314.3 kJ/kg^{salt} (N° 6), which increased by 22.4%, with the highest Q_N appeared in the 4th cycle (323.2 kJ/kg^{salt}). As for aluminum foam-$CaCl_2$ composite, Q_N increased from 299.3 kJ/kg^{salt} (N°1) to the highest of 389.5 kJ/kg^{salt} (N°6), achieving an improvement of 30.1%. In general, the results confirm an improved cyclic stability of the composites in comparison with bulk $CaCl_2$ powder. After the first hydration, it can be seen that for both composites Q_N stabilized or slightly increased, while it decreased

for bulk $CaCl_2$ powder. These opposite evolutions relate to microstructural changes of the reactive material which we will further discuss in section 3.4.3.

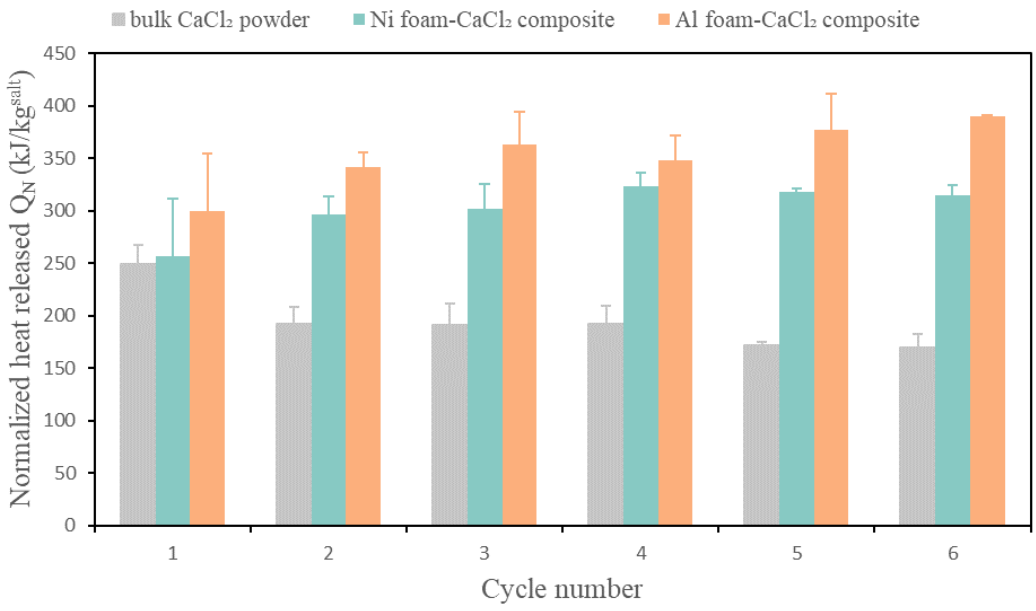

Fig. 3.14. Normalized thermal energy released during 6 hydration/dehydration cycles of nickel foam-$CaCl_2$ composite, aluminum foam-$CaCl_2$ composite and bulk $CaCl_2$ powder.

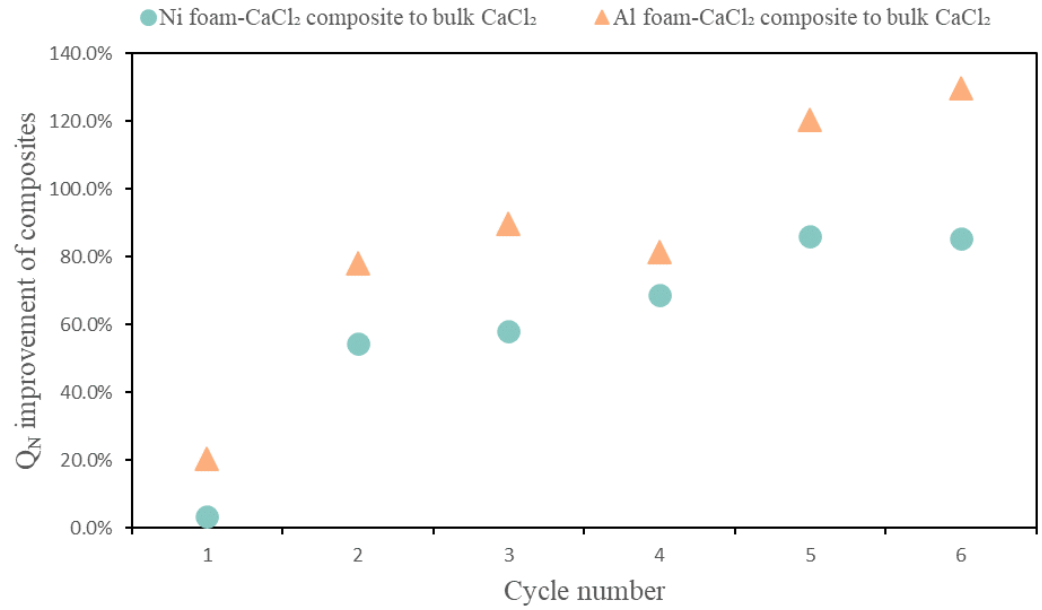

Fig. 3.15. Q_N improvement of composites compared to bulk $CaCl_2$ powder during 6 hydration/dehydration cycles.

Dehydration

Fig. 3.16 presents the normalized thermal energy restored during the dehydration process of bulk $CaCl_2$ powder, nickel foam-$CaCl_2$ composite and aluminum foam-$CaCl_2$ composite for short cycles. The results illustrate that the heat storage capacity of bulk $CaCl_2$ salt started to show a disadvantage compared to that of the two composites even after the first hydration cycle. For the dehydration corresponding to the first hydration process of 45 min, the normalized thermal energy Q_N restored for bulk $CaCl_2$ powder, nickel foam-$CaCl_2$ composite and aluminum foam-$CaCl_2$ composite were 184.1 kJ/kg^{salt}, 260.3 kJ/kg^{salt} and 305.0 kJ/kg^{salt}, respectively. In the following cycles, the energy storage capacity of the bulk salt powder declined a little bit and then kept at a level relatively steady around 160 kJ/kg^{salt}. While the storage capacity continued to increase for both composites in the subsequent cycles. For nickel foam-$CaCl_2$ composite, its thermal energy storage capacity reached 297.2 kJ/kg^{salt} in the second cycle and reached a maximum level of 319.1 kJ/kg^{salt} in the last cycle. For aluminum foam-$CaCl_2$ composite, its thermal storage capacity reached a maximum level of 368.2 kJ/kg^{salt} at the third cycle. The average normalized thermal energy storage capacity Q_N of bulk $CaCl_2$ powder, nickel foam-$CaCl_2$ composite and aluminum foam-$CaCl_2$ composite were 168.6 kJ/kg^{salt}, 298.6 kJ/kg^{salt}, and 344.3 kJ/kg^{salt}, respectively, which corresponds to a respective improvement of 80% and 108% for nickel foam-$CaCl_2$ composite and aluminum foam-$CaCl_2$ composite compared to that of the bulk $CaCl_2$ powder.

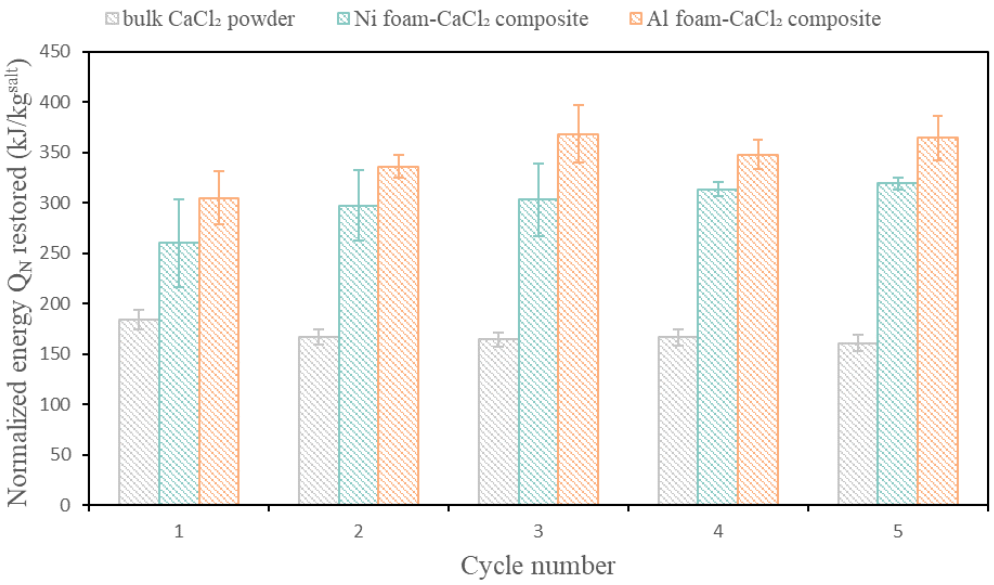

Fig. 3.16. Normalized thermal energy restored during short cyclic hydration/dehydration process of nickel foam-$CaCl_2$ composite, aluminum foam-$CaCl_2$ composite and bulk $CaCl_2$ powder.

Summary

By summing up the normalized thermal energy released during 6 cycles of 45 min

hydration and that restored during dehydration, we obtain total Q_N released and restored for bulk $CaCl_2$ powder, nickel foam-$CaCl_2$ composite and aluminum foam-$CaCl_2$ composite as shown in Table 3.5.

Table 3.5 Total normalized thermal energy released and restored during short cyclic tests for bulk $CaCl_2$ powder, nickel foam-$CaCl_2$ composite and aluminum foam-$CaCl_2$ composite.

Sample type	Total Q_N released (kJ/kg^{salt})	Total Q_N restored (kJ/kg^{salt})
Bulk $CaCl_2$ powder	994.9	842.9
Ni foam-$CaCl_2$ composite	1497.1	1493.2
Al foam-$CaCl_2$ composite	1728.9	1721.6

For bulk $CaCl_2$ powder, it had the capability of restoring 84.7% of the thermal energy released during short cyclic hydration/dehydration tests. While for both composites, they were able to retore 99.7% and 99.6% (for nickel foam-$CaCl_2$ composite and aluminum foam-$CaCl_2$, respectively) of the total thermal energy released through these 6 short cycles of hydration and dehydration. We can conclude that both composites were able to restore almost all the thermal energy released during short cyclic hydration/dehydration tests.

The results of the short hydration/dehydration cycle experiments once again verified the superior quantity of thermal energy stored/released and enhanced cycling stability of composites compared to bulk salt powder under the same experimental conditions. Compared to the previous experimental results concerned with long cycles, we found that after the first cycle of hydration, the bulk salt did not show strong degradation of performances during the short hydration/dehydration cycles. This observation is consistent with time-dependent microstructural evolution, related to the swelling of hydrated salt crystallites and corresponding agglomeration or compaction, which naturally depends on the number and duration of cycles.

In terms of thermal energy storage/release capacity, the performance of the composites is improved significantly compared to that of the bulk salt powder. For the composites, we found performance trends similar to those shown during the long-cycle (Fig. 3.11). In both cyclic processes, the Q_N was minimum for the first cycle, then increased for the following. It is therefore presumed that the metal foam-salt composites need a certain duration of time to optimize their thermochemical properties. This time-lapse represents a maturation period, during which the microstructure evolves owing to topological changes concerning salt hydrate deliquescence, swelling, agglomeration, and local redistribution within the metal foam.

This interpretation is strengthened by the fact that the thermal energy released

during the first hydration of the composites varied relatively widely for different samples under the same experimental conditions. For example, the error in Q_N of the first hydration was 21.5% for the nickel foam-$CaCl_2$ composite and 18.4% for the aluminum foam-$CaCl_2$ composite. Conversely, during the subsequent cycles, the error for different samples decreased considerably and the thermochemical properties became relatively stable. The larger differences in thermochemical performances during the initial hydration might be due to differences in the initial distribution of salt crystallites in the metal foam, resulting from the preparation process. Such differences are expected to vanish after the maturation period of the first hydration, owing to salt hydrate deliquescence redistribution within the metal foam network.

c) Comparison of thermal energy release and storage capacity

In this part, we compare the thermal energy release and storage capacity during each hydration and dehydration cycle for bulk $CaCl_2$ powder, nickel foam-$CaCl_2$ composite and aluminum foam-$CaCl_2$ composite in both long cycle and short cycle.

The normalized thermal energy released and stored during long cyclic hydration and dehydration process of bulk $CaCl_2$ powder, nickel foam-$CaCl_2$ composite and aluminum foam-$CaCl_2$ composite is shown in Fig. 3.17. For bulk $CaCl_2$ powder (see Fig. 3.17a), it was capable of restoring only 67.8% of the thermal energy released during the first hydration process. This percentage varied between 56.0% and 87.4% until the 6th cycle. From the 7th cycle and on, the bulk $CaCl_2$ powder was able to restore more than 90% of the Q_N released during hydration process through dehydration. However, the Q_N had already declined to a very large extent at the 7th cycle and the cycles followed compared to the beginning. On the contrary, both of the composites were capable of restoring almost 100% of the Q_N released during hydration through the following dehydration for the entire 11 cycles (see Fig. 3.17b and c).

Similar trends were found in results obtained for the short cyclic hydration and dehydration process for these three types of samples. The normalized thermal energy released/stored during the short cyclic hydration/dehydration process of bulk $CaCl_2$ powder, nickel foam-$CaCl_2$ composite and aluminum foam-$CaCl_2$ composite is shown in Fig. 3.18. For bulk $CaCl_2$ powder (see Fig. 3.18a), it restored 74.0% of the thermal energy released during the first hydration process through the first dehydration process. This ratio was the lowest among the 5 cycles for the short cyclic hydration/dehydration test. In the last cycle, this ratio recovered to a level of 93.9%. While for both composites, they remained the capability of restoring almost all the thermal energy released during the hydration process, as shown in Fig. 3.18b and c.

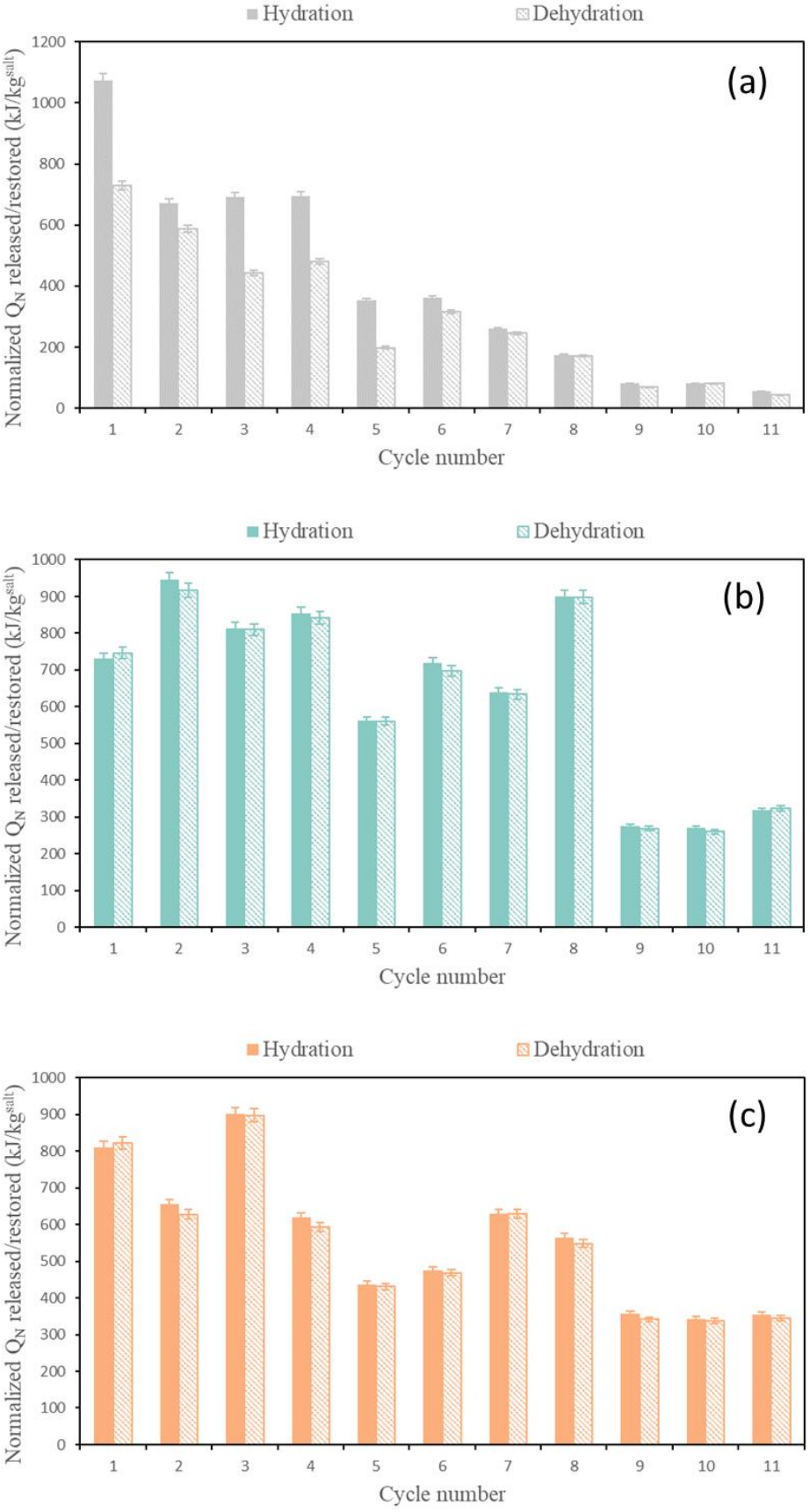

Fig. 3.17 Normalized thermal energy released/stored during long cyclic hydration/dehydration process of (a) bulk $CaCl_2$ powder, (b) nickel foam-$CaCl_2$ composite and (c) aluminum foam-$CaCl_2$ composite.

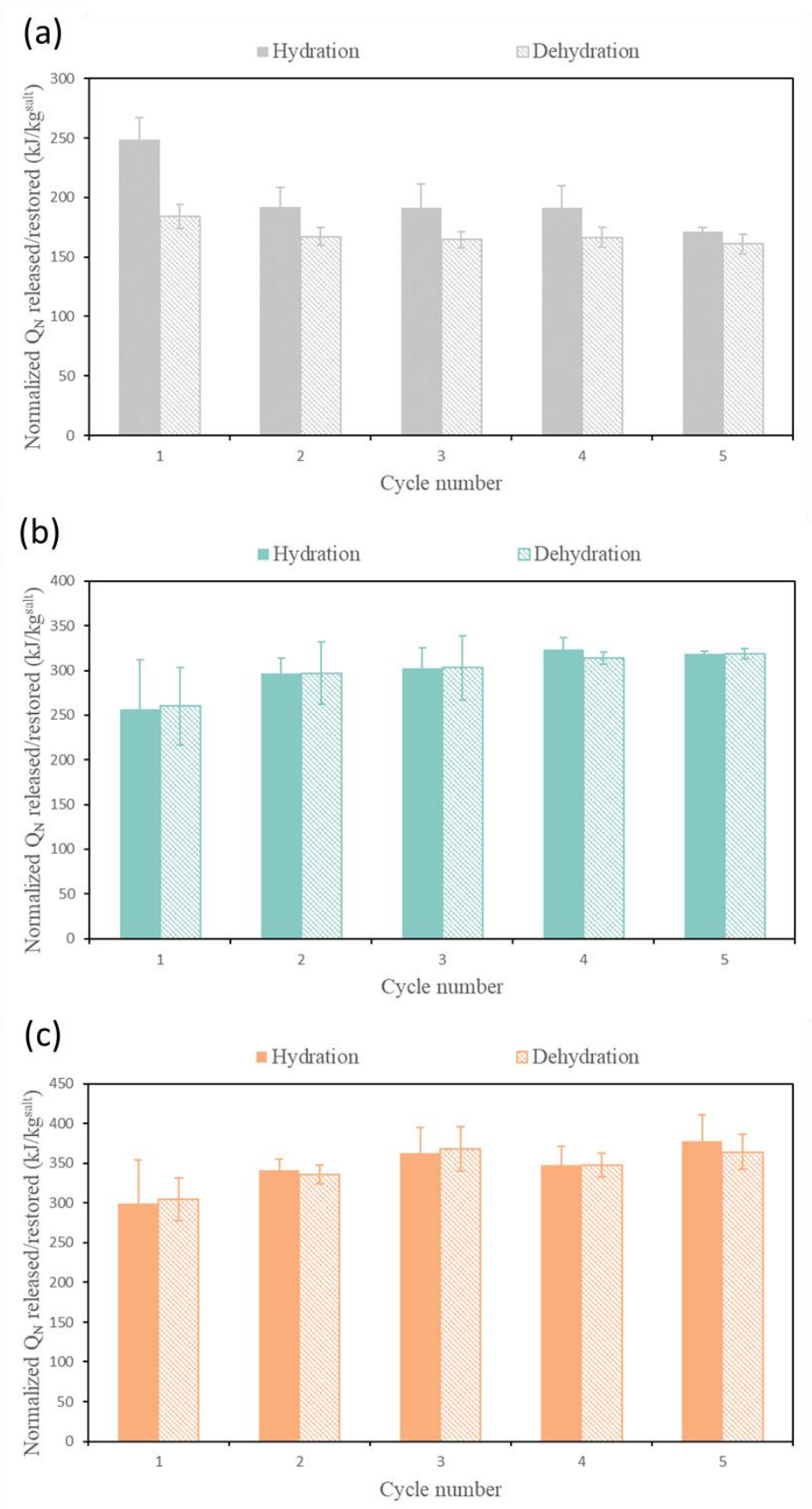

Fig. 3.18 Normalized thermal energy released/stored during short cyclic hydration/dehydration process of (a) bulk $CaCl_2$ powder, (b) nickel foam-$CaCl_2$ composite and (c) aluminum foam-$CaCl_2$ composite.

From the comparison of the thermal energy storage and release capacity for bulk $CaCl_2$ powder, nickel foam-$CaCl_2$ composite and aluminum foam-$CaCl_2$ composite in both long cycle and short cycle, we can conclude that the bulk $CaCl_2$ powder typically experiences a severe irreversible decay in thermal storage capacity after the first hydration, which may be due to deliquescence and agglomeration of the salt. The decay in the thermal storage capacity of bulk $CaCl_2$ powder is consistent with the decline of its thermal energy release capacity in the second and subsequent cycles, as demonstrated by the previous results. On the contrary, both composites have the ability to restore as much thermal energy as they have released during each cycle, which corresponds well to the enhanced cyclic stability of the composites during cyclic hydration/dehydration tests.

In section 3.4.3, we will specifically address the possible reasons and explanations for the superior performance and the enhanced cyclic stability of the designed composites by characterization based on in situ ESEM hydration/dehydration cycling test.

d) The apparent energy density of Ni/Al foam-$CaCl_2$ composite

In this part, the apparent energy density of nickel foam-$CaCl_2$ composite and aluminum foam-$CaCl_2$ composite is presented. We define the apparent energy density $E_{d,a}$ as followed:

$$E_{d,a} = \frac{Q}{V_{sample}} \tag{33}$$

where Q is the quantity of thermal energy released/restored during the hydration/dehydration process as defined in equation (30) and V_{sample} is the total volume of the composite sample. The apparent energy density provides an intuitive idea of the amount of energy that a given volume of composite material can provide.

Fig. 3.19 presents the apparent energy density of both composites in hydration/dehydration cycles. It is clear that the $E_{d,a}$ of nickel foam-$CaCl_2$ (48.5 wt%) composite exceeded that of aluminum foam-$CaCl_2$ (21.0 wt%) composite in both long and short hydration/dehydration cycles. In long hydration/dehydration cycles (as shown in Fig. 3.19a), as hydration duration Δt_{hydr} differed from 45 min to 360 min for different cycles, the $E_{d,a}$ of Ni foam-$CaCl_2$ composite was between 82.3 MJ/m^3 (N°10 - Δt_{hydr} of 45 min) and 286.9 MJ/m^3 (N°2 - Δt_{hydr} of 180 min), while the $E_{d,a}$ of Al foam-$CaCl_2$ composite was between 78.5 MJ/m^3 (N°10 - Δt_{hydr} of 45 min) and 206.8 MJ/m^3 (N°3 - Δt_{hydr} of 180 min). During the 12th cycle (Δt_{hydr} of 360 min), Ni foam-$CaCl_2$ composite provided a $E_{d,a}$ of 274.2 MJ/m^3, improved by 43% compared to that of Al foam-$CaCl_2$ composite, which provided a $E_{d,a}$ of 191.5 MJ/m^3. The results of short cycles (Δt_{hydr} of 45 min) shown in Fig. 3.19b once again confirmed the superiority of Ni foam-$CaCl_2$ composite over Al foam-$CaCl_2$

composite in terms of energy density. $E_{d,a}$ provided by Ni foam-$CaCl_2$ composite was between 76.6 MJ/m^3 (N°1) and 96.4 MJ/m^3 (N°4), with an average $E_{d,a}$ of 90.0 MJ/m^3 for 6 cycles. While $E_{d,a}$ provided by Al foam-$CaCl_2$ composite was between 65.8 MJ/m^3 (N°1) and 84.6 MJ/m^3 (N°6), with an average $E_{d,a}$ of 76.8 MJ/m^3 for 6 cycles. An improved $E_{d,a}$ of 17% was obtained for Ni foam-$CaCl_2$ composite compared to Al foam-$CaCl_2$ composite for 6 cycles of hydration/dehydration process with Δt_{hydr} of 45 min for each cycle. The summary of $E_{d,a}$ of both composites for all cycles are shown in Table 3.6.

Obviously, the difference in apparent energy density of these two composites meanly derives from the different morphology and microstructure of the host matrix (metal foam), especially the porosity. The porosity of nickel foam used is about 96%, while the porosity is about 40% for aluminum foam. The difference in porosity greatly affected the content of salt deposited in the metal foam, thus affecting the apparent energy density.

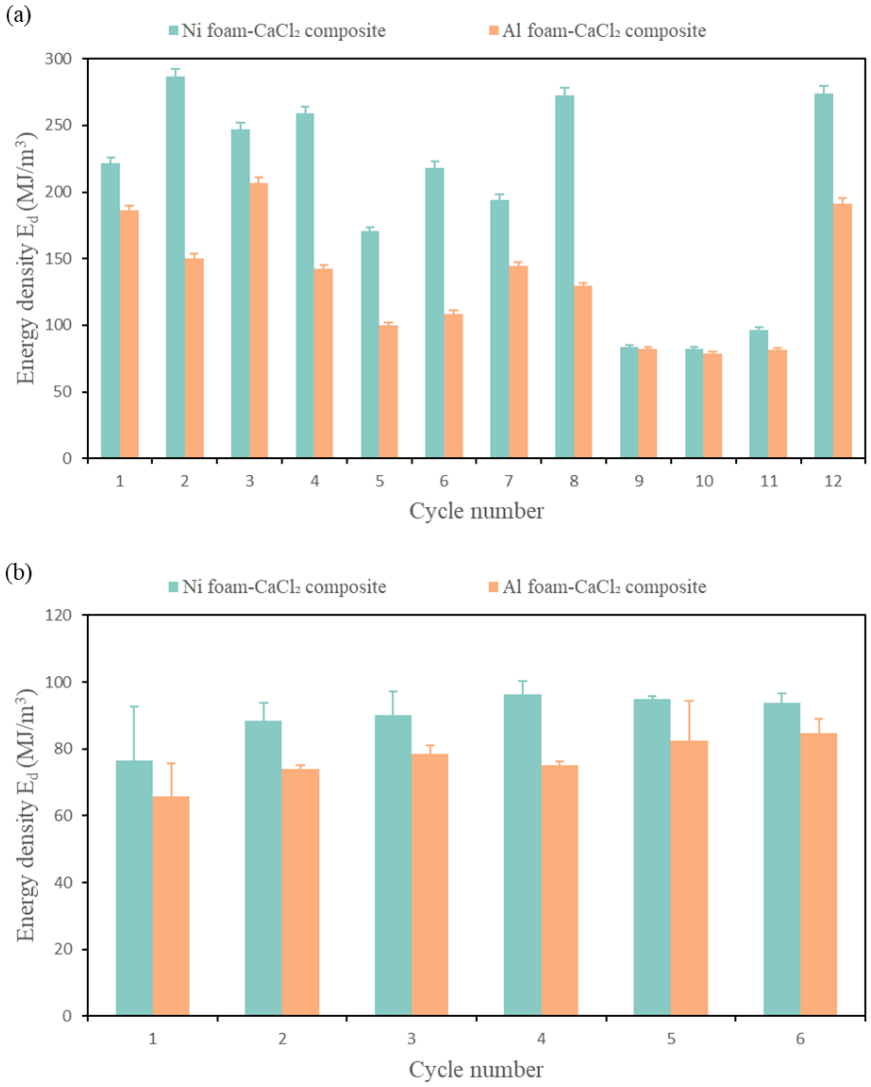

Fig. 3.19. The apparent energy density of nickel foam-$CaCl_2$ composite and aluminum foam-$CaCl_2$ composite in (a) 12 hydration/dehydration cycles of different hydration duration and in (b) 6 hydration/dehydration cycles of 45 min hydration duration.

Table 3.6 Apparent energy density results of both composites for all cycles.

Cycle No.	Apparent energy density $E_{d,a}$ (MJ/m^3)			
	Ni foam-$CaCl_2$ composite		Al foam-$CaCl_2$ composite	
	Long cycle	Short cycle*	Long cycle	Short cycle*
1	221.7	76.6	186.2	65.8
2	286.9	88.4	150.4	74.0
3	246.8	90.1	206.8	78.5
4	259.0	96.4	142.3	75.3
5	170.4	94.9	100.1	82.4
6	218.4	93.7	108.8	84.6
7	194.1	-	144.3	-
8	272.8	-	129.5	-
9	83.6	-	82.1	-
10	82.3	-	78.5	-
11	96.5	-	81.3	-
12	274.2	-	191.5	-

*Average value calculated from repetition tests.

From the perspective of cyclic stability and thermochemical energy density, the most effective thermochemical composite is the nickel foam-$CaCl_2$. Such composite, based on nickel foam as host matrix offers the highest porosity proportion as well as appropriate pore size and would be a promising choice for thermochemical heat storage systems. However, the source, cost, and mechanical properties should also be taken into account. Not to mention the corrosion problem of metal [122, 140, 214]. These aspects still need further exploration.

e) Energy storage density of metal foam-$CaCl_2$ composite and other TCM

In this section, we aim to demonstrate a comparison between the metal foam-$CaCl_2$ composite studied in our work and other TCM materials in terms of energy storage density.

Yu et al. [31] have provided us with a summary of the energy storage density of different TCMs reported in various research, as shown in Fig. 3.20. In this review, 12 papers and around 40 thermochemical materials were compared in this same diagram. Note that the reference numbers in the lower right corner boxes in Fig. 3.20 correspond to the original citation numbers in reference [31] and the details of the data can be found in Table 2 of the review paper [31].

The energy storage density of nickel foam-$CaCl_2$ composite (average Q_N of cycle 2, 3 and 4 for a hydration duration of 3 hours during long cycles) is marked in a red cross on the diagram shown in Fig. 3.20. At a discharge temperature of 23 °C, the nickel foam-$CaCl_2$ composite showed an energy storage density of 130 Wh/kg for a 3-hour hydration process. Note that the unit of the vertical axis, representing the energy storage density, is in Wh/kg. Here, the energy storage density is normalized by the mass of the whole sample. Therefore, the mass concentration of salt in the composite can have a significant impact on the energy storage density. It is also important to emphasize that the red cross represents the energy density presented

during only a 3-hour hydration process, which certainly does not represent the energy release limitation of the composite.

So, at this point, we are only providing a rough estimate to illustrate approximately where the energy storage density of the metal foam-salt composite stands in comparison to other TCMs. It can also be seen that, with only a 3-hour hydration process, the energy storage density of this material is already quite promising.

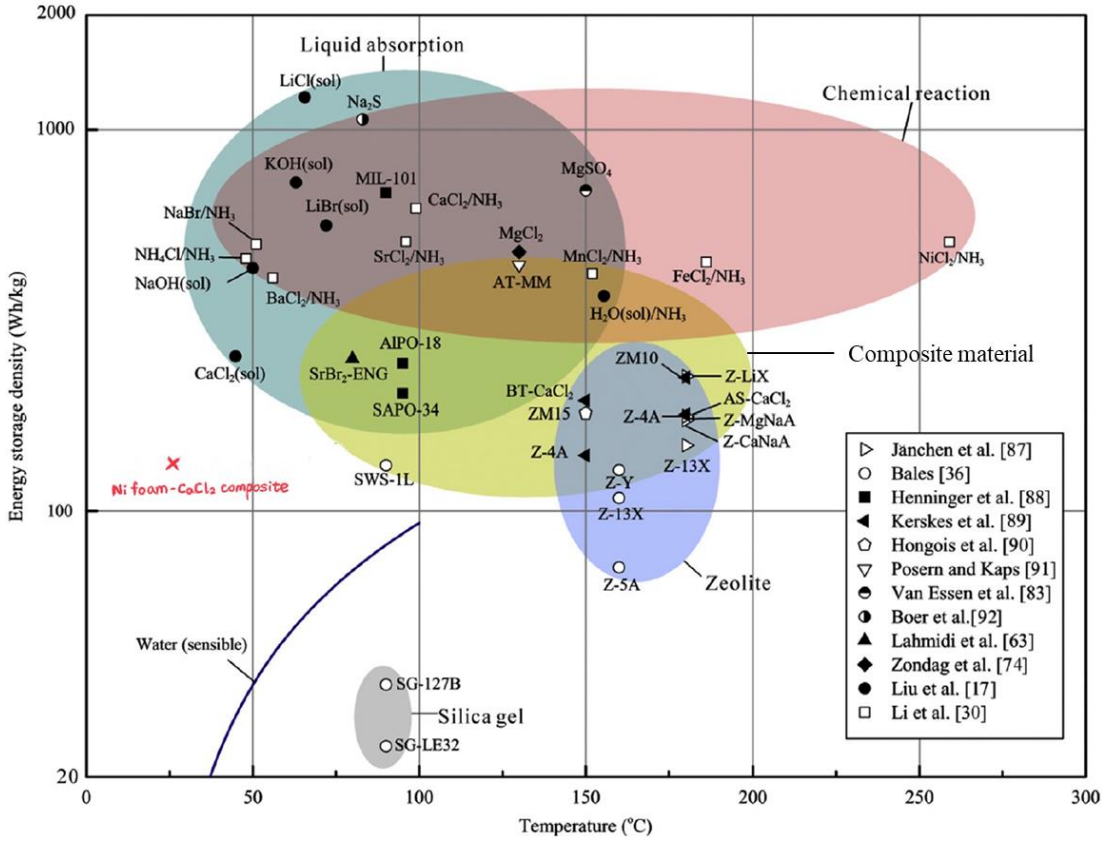

Fig. 3.20 Energy storage density of different TCMs [31] with the energy storage density of nickel foam-$CaCl_2$ composite studied in our work marked with a red cross. The horizontal axis represents the discharge temperature.

3.4.3. Performance improvement mechanism of composites

In this section, we present results obtained during hydration/dehydration cycling tests, performed with in situ ESEM, in order to investigate the topological behavior of salt hydrates in the composite. The aim is to observe the possible redistribution of salt during hydration processes and to provide explanations for the performance improvement in terms of cyclic stability and quantity of thermal energy released during hydration of metal foam-salt composites compared to bulk salt powder.

As introduced in section 3.3.3, the experimental conditions of cyclic hydration/dehydration tests performed in the differential scanning calorimeter were reproduced during in situ ESEM observation with images recorded every 5 seconds. Fig. 3.21 illustrates the continuous evolution of the sample surface as the relative

humidity increased from 0 to approximately 54% under an isothermal condition for the nickel foam-$CaCl_2$ composite.

In the region of interest (ROI) presented in Fig. 3.21, it is clearly seen that not all the open pore spaces of the metal foam matrix were filled with salt at the initial state, which ensured that the water vapor could pass smoothly through the metal foam and thus come into contact with the salt crystallites distributed within the metal foam, thereby promoting the hydration process and releasing the thermal energy. Besides the open pores of the metal foam, we observed the entrapped salt particles at the initial state with 0.4% RH, where the cross-sections of the metal foam struts protruding from the salt layer were also clearly visible, as shown in Fig. 3.21a. As introduced in 3.3.3, by controlling the pressure and temperature around the sample, we control the relative humidity. As the Peltier stage assures us the sample temperature is to be kept at 23 ℃, we adjust the chamber pressure to control the relative humidity for the hydration and dehydration process.

As the hydration process began, the salt on the surface of the sample gradually absorbed water with increasing humidity. When the RH reached about 45%, we observed the part of the salt layer denoted by the dashed line shrieked and formed a hole (see Fig. 3.21b). This hole formed on the surface salt layer continued to expand as the RH increased to 51.4% (see the part circled by the dashed line in Fig. 3.21c). When the relative humidity reached 54.7%, which was approximately the same condition as in the cyclic hydration/dehydration tests for thermal analysis (54% RH), we stopped raising the vapor pressure in the SEM chamber. The sample was kept under this condition for about 30 minutes, during which no further changes in the ROI were detected. Fig. 3.21d showed that compared to lower RH conditions, the hole in the salt layer continued expanding before the RH reached 54.7%, which is also indicated by the higher proportion of metal foam struts that can be observed under the surface salt layer compared to the former states. As no further changes in the ROI were detected under this condition for 30 min, we assume that the hydration reaction was completed in the ROI and the subsequent redistribution of salt hydrates within the metallic foam network has been achieved. This suggests that once a certain hydration degree is reached, the redistribution and relocation process of the surface salt layer stops. This in turn means that hydration kinetics are very fast and may be achieved within a few minutes. This speculation, however, needs to be validated through future experiments.

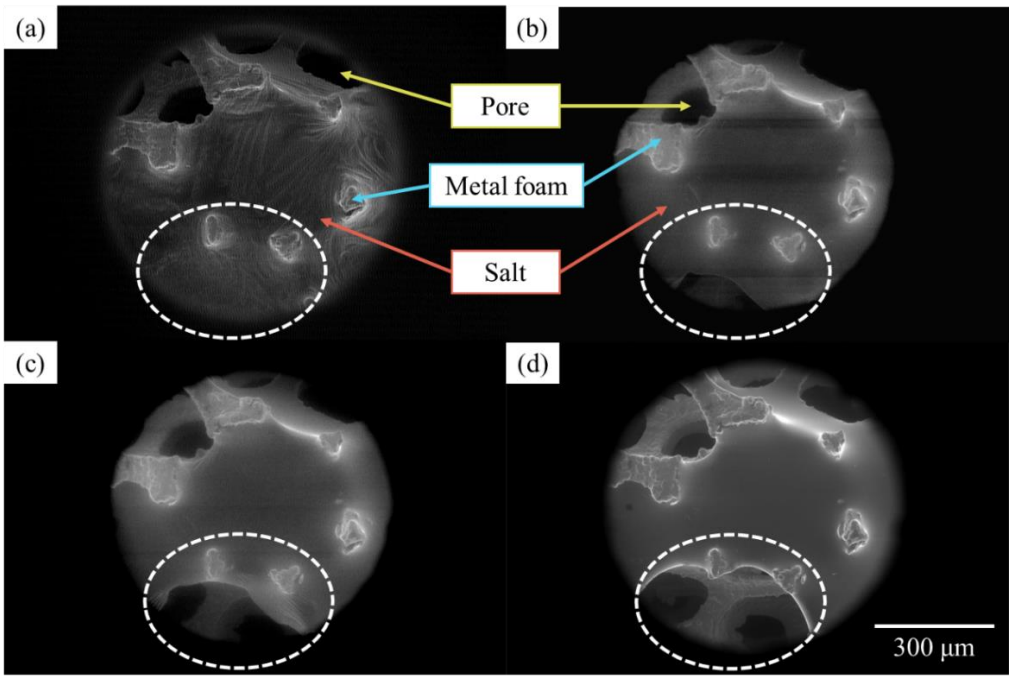

Fig. 3.21. GSED images (x107 magnification) of the nickel foam-$CaCl_2$ composite sample surface with the relative humidity increasing from (a) 0.4%, (b) 45.3%, (c) 51.4%, to (d) 54.7% under isothermal condition.

A different nickel-based composite was observed at higher magnification, with a smaller horizontal field width (HFW) of 250 µm chosen as the region of interest (ROI), in order to focus on the evolution of the interfaces between the metal foam and the salt layer during hydration/dehydration cycles (Fig. 3.22).

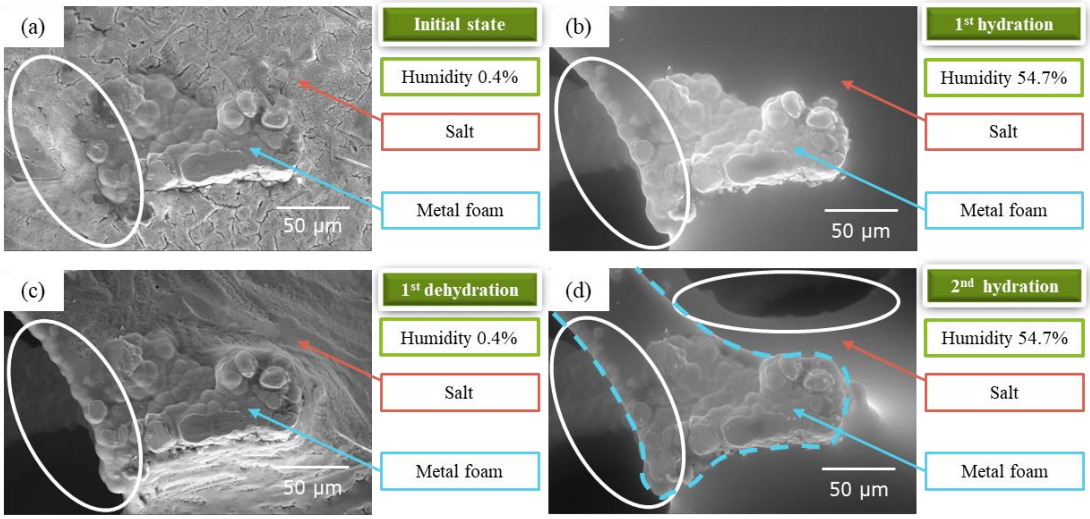

Fig. 3.22. GSED images (x508 magnification) of the nickel foam-$CaCl_2$ composite sample surface during 2 hydration/dehydration cycles with (a) the initial state (0.4% RH), (b) after the first hydration (54.7% RH), (c) after the first dehydration (0.4% RH) and (d) after second hydration (54.7% RH) under isothermal condition. Redistribution of salt during the hydration/dehydration cycles is marked in circle.

At the initial state with a relative humidity of 0.4%, as shown in Fig. 3.22a, a layer of dry salt crystals could be observed tightly surrounding the strut of the metal foam. The fine fissures formed during sample preparation and drying for preservation

were visible on the surface of the salt layer. At this point, there were no observable open pores of the metal foam in the ROI. Then the vapor pressure was raised in the SEM chamber for the relative humidity to increase. During the increase of relative humidity, the deliquescence of the salt was observed at approximately 30% RH, which is in accordance with the deliquescence relative humidity (DRH) of hexahydrate ($CaCl_2 \cdot 6H_2O$) at about 23 ℃ [64, 215, 216]. Fig. 3.22b illustrates the ROI after 30 min's stabilization when RH reached 54.7%. In this figure, the deliquescence of the salt layer after the first hydration process can be clearly seen. It is also worth noting in Fig. 3.22b that the salt which was originally located in the left area of the ROI, surrounding the strut of metal foam, separated from it along the struts and redistributed in the host matrix, thus forming a hole in the salt layer revealing the original pores and struts of metal foam (see the part marked in circle). In the next step, the relative humidity was reduced to 0.4% then remained at this RH for 30 min to dry the samples. As shown in Fig. 3.22c, the salt layer that still surrounded the struts of the metal foam after the first hydration process dehydrated and formed a salt layer with a thickness gradient. Compared to Fig. 3.22b, the hole formed during the first hydration process remained unchanged (the part marked in circle) and no additional holes in the salt layer were formed in the ROI during this process. The second hydration cycle was then carried out and the ROI after the second hydration process is presented in Fig. 3.22d. It can be clearly seen that the salt layer was again deliquescent, allowing the salt to flow in the metal foam either along the struts or through the pores. The change in the thickness of the salt layer in the ROI allowed us to see the shape of the metal foam strut (see the mark in blue dashed lines in Fig. 3.22d). Most notably, another hole was formed in the salt layer in the upper part of the ROI (marked in circles in Fig. 3.22d), indicating that the salt layer continued to relocate in the metal foam matrix during this second hydration process, as was observed during the first hydration process (shown in Fig. 3.22b).

Observations from in situ hydration/dehydration cycle tests on nickel foam-$CaCl_2$ composites show that after sample preparation and drying process, the salt tended to be deposited surrounding the struts of the metal foam pores or in the metal foam cells. The distribution of salt crystallites was irregular, some of the pores of the metal foam were filled, while others remained open. During the hydration process at a constant temperature (approximately 23°C), $CaCl_2$ became deliquescent when the relative humidity reached about 30%. The resulting gel-like salt flowed along the struts driven by surface tension forces and hence redistributed homogeneously in the metal foam. Most importantly, the redistribution favored restoring the open porosity. According to observation, this reorganization mechanism of the salt may be activated during each hydration process. It can also be inferred that as the number of hydration/dehydration cycles increases, the distribution of salt in the metal foam matrix tends to homogenize the salt dispersion along the metal foam struts, hence reaching a stable topology, with an optimum surface-to-volume ratio

and preserving the interconnections of the foam porosity.

By observing at different scales, it is noted that not all the deliquescent salt necessarily redistributes during the first hydration process, as shown in Fig. 3.23. By comparing the initial state (Fig. 3.23a) and the state after the first hydration process (Fig. 3.23b), it is clearly observed that the salt completely embedded in a small cell (< 200 µm) remained trapped even after hydration and deliquescence. This local behavior is contrasting with observations shown in Fig. 3.21, where the deliquescent salt massively migrated from a larger cell (> 300 µm). However, the smaller cell in Fig. 3.23 was nearly complete and offered only a cell window to the observation surface, while the large pore shown in Fig. 3.21 was incomplete and largely opened to the observation surface. These observations indicate the strong role of capillary effects and suggest that the local structure of the foam will control the actual salt redistribution. This aspect highlights the microstructural importance of the metal foam, for instance, the size and the size distribution of the metal foam cells, or the size of the struts and cell windows.

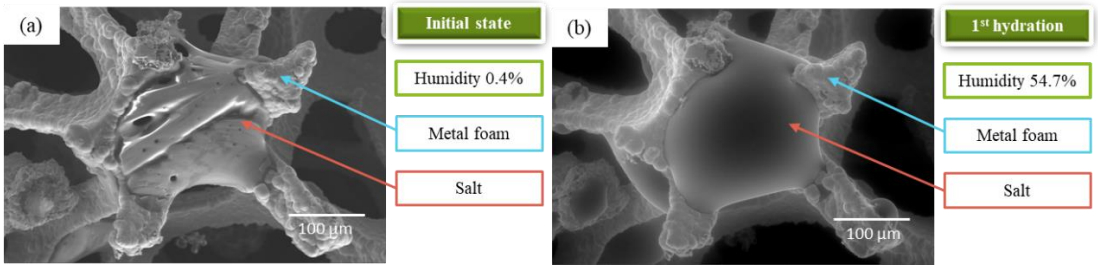

Fig. 3.23. GSED images (x254 magnification) of the nickel foam-$CaCl_2$ composite sample surface focused on the interface of salt and metal foam with (a) the initial state (0.4% RH) and (b) after first hydration (54.7% RH).

The conclusions obtained from observations during the in situ hydration/dehydration cycling test give a reasonable explanation and a possible mechanism for the improvements of the composites compared to bulk salt in terms of thermochemical performance. The enhanced performance of the metal foam-salt composite can be partially attributed to the porous structure of the metal foam. On the one hand, the porous matrix serves for salt deposition. On the other hand, the open pores increase the specific reaction area, which facilitates mass and heat transfer while effectively avoiding the degradation of performance due to salt swelling and agglomeration. What's more, thanks to the pore size of the selected metal foam and the proportion of free pores after each cycle, the host matrix ensures that the salt can be relocated and reorganized in the composite even if agglomeration or even deliquescence occurs, which greatly enhances its cyclic stability as well as the mass and heat transfer efficiency. The composite offers a dynamic microstructure, with local topological evolutions during hydration cycles, while allowing the maintenance of statistically stable proportions of interconnected open pores and specific reaction areas. In this case, the global thermochemical performances might remain stable over time. Without the metal foam serving as

host matrix, the cyclically swelling salt crystallites would undoubtedly lead to progressive compaction, with loss of open porosity and specific reaction area, which would lead to progressively decreasing thermochemical performances. Actually, these contrasting scenarios for composites and bulk salt powder are wholly supported by our thermochemical measurements (section 3.4.2).

The observations from the in situ experiments can also explain some of the conclusions drawn from the thermal analysis experiments related to the composite performance. In section 3.4.2, results suggested that for both composites the minimum value of the normalized thermal energy released Q_N during cycles usually occurred at the first hydration process and tended to increase and stabilize in the subsequent cycles. Meanwhile, the experimental data presented in section 3.4.2b) showed relatively large errors in Q_N of the first hydration process for both composites during repetition tests on different samples. Based on the in situ ESEM observations, this is possibly due to the differences in the position of salt deposited on the surface of the sample during the preparation and drying process, as well as the percentage of free open pores remaining in the composite after salt deposition. All these factors resulted in a greater variation in performance exhibited by the initial hydration process for different samples. However, as seen in the in situ hydration/dehydration experiment, salts without sufficient structural support provided by the initial deposition location are more likely to relocate after the first cycle of hydration. It can be presumed that as the hydration/dehydration cycle continues, salts continue to relocate and reorganize, thus resulting in a more dispersed and rational deposition in the composite, which increases the specific surface area while leaving more pathways for heat and mass transfer, thus improving and gradually stabilizing the performance of the composites after the first hydration. This mechanism well explained the experimental results mentioned in section 3.4.2, where Q_N was usually at a minimum during the first hydration cycle, and the reduction of the experimental error in the different samples to a reasonable range after a few cycles. The in situ ESEM observations also may explain the initial stage of improvement of the thermochemical heat storage capacity reported after the very first hydration cycle (see Fig. 3.11 and Fig. 3.14 as well as previous sections 3.4.2a) and b)). The latter may be considered as an activation (or maturation) cycle, allowing for an optimum salt redistribution, hence ensuring the most effective salt topology in terms of the specific reaction area, which in turn ensures the stability of the thermochemical heat capacity during further cycling.

In addition, the metallic framework of the metal foam provides improved thermal conductivity and mechanical strength to the overall system. All of the above results indicate that the metal foam-salt composite introduced in this paper is a suitable and promising thermochemical material.

3.4.4. Estimation of $CaCl_2$ hydrates composition during cyclic tests

In this section, we aim to estimate, approximately, the composition of calcium chloride hydrates in the initial state and after hydration with different durations, to provide an idea of the reactions that took place during the release of thermal energy.

As introduced in section 1.6.1, there are 5 known states of calcium chloride with generic formula $CaCl_2 \cdot nH_2O$, where n = 0, 1, 2, 4, 6, naming anhydrate, monohydrate, dihydrate, tetrahydrate, and hexahydrate, respectively. The calculated enthalpies of hydration reactions between different calcium chloride hydrates were shown in Table 1.1.

Then, we try to estimate the composition of calcium chloride hydrates in the initial state. Here we recall the experimental procedure of cyclic hydration/dehydration tests via isothermal calorimetry as introduced in Fig. 3.7. Before the first hydration of the samples, they were completely dehydrated. We therefore define this state of the samples after the first complete dehydration and before the first hydration as the initial state. We approximate the composition by combining the quantity of thermal energy released during the first long hydration (360 min) and the theoretical enthalpies for hydration reactions of calcium chloride.

In the previous sections, we found that composites usually require an activation or maturation cycle, so it may be difficult to estimate what proportion of the salt in the composite is involved in the first hydration reaction. On the contrary, the bulk $CaCl_2$ powder can be considered to have taken part in the first hydration process in its entirety. According to the curve obtained for heat flow over time of bulk $CaCl_2$ powder in the first hydration of 360 min shown in Fig. 3.9a, the heat flow after 360 min was 3.13 mW, which was already close enough to the baseline. By estimation, the bulk $CaCl_2$ powder sample has already released about 94% of the total thermal energy stored in the sample, which indicates that nearly all the salt has already been totally hydrated (reaching the highest degree of hydration of calcium chloride: hexahydrate) after hydration at 54% RH for 360 min. Thus, for estimating the composition of the calcium chloride hydrates in the initial state, we make the first assumption that all the salt of bulk $CaCl_2$ sample have been hydrated to hexahydrate ($CaCl_2 \cdot 6H_2O$) after the hydration process at 54% RH for 360 min. In fact, on one hand, this assumption is consistent with the observation via ESEM during the cyclic hydration/dehydration process presented in 3.4.3, where we found the salt started to deliquesce at approximately 30% RH, which is in accordance with the deliquescence relative humidity (DRH) of hexahydrate ($CaCl_2 \cdot 6H_2O$) at about 23 ℃ [64, 215, 216]. This proves the existence of $CaCl_2 \cdot 6H_2O$ at the final state of the first hydration process. On the other hand, we assume that all the salts were hydrated to hexahydrate compounds because the samples were constantly exposed to 54% RH nitrogen during the experiment and it is not reasonable to assume that with

sufficient hydration time, some of the salts would only be hydrated to tetrahydrate compounds without further hydration.

According to the phase diagram presented in Fig. 1.12 and Fig. 1.13, we speculate that the starting material was calcium chloride dihydrate ($CaCl_2 \cdot 2H_2O$) and that the pure salt sample had a mass M of 0.209 g and that 225 J of thermal energy Q was released during the first hydration. We make the second assumption that the bulk salt sample remained dihydrate and was completely hydrated to hexahydrate during the first hydration of 360 min, this means that the sample has undergone hydration reactions No.3 and No.4 shown in Table 1.1, corresponding to a $\Delta H_{reaction}$ of 237.8 kJ/mol^{salt} (by summing up the $\Delta H_{reaction}$ of reaction No.3 and No.4). The molar mass of $CaCl_2 \cdot 2H_2O$ is 147.02 g/mol, so the reaction enthalpy for dihydrate to hexahydrate $\Delta H_{reaction\,(3+4)}$ is 1617.47 kJ/kg^{salt}. As we assumed that all of the 0.209 g $CaCl_2 \cdot 2H_2O$ was hydrated to $CaCl_2 \cdot 6H_2O$, if this assumption holds true, the corresponding thermal energy released would be

$$Q = M \times \Delta H_{reaction\,(3+4)} \tag{34}$$

with M = 0.209 g and $\Delta H_{reaction\,(3+4)}$ = 1617.47 kJ/kg^{salt}, we have a thermal energy released of 338 J, which is much higher than that obtained by the experiment (225 J).

This shows that the second assumption is not valid, which means the bulk salt sample before the first hydration didn't totally exist in the form of calcium chloride dihydrate. In fact, as reported in the literature, the X-ray diffractograms of calcium chloride obtained at 25℃ during dehydration (Fig. 3.24) shows that the tetrahydrate and the dihydrate are the major hydrated forms available at this temperature in a moisture-free atmosphere [217]. Thus, we modify the second assumption to be that there existed tetrahydrate ($CaCl_2 \cdot 4H_2O$) compound of mass x as well as dihydrate ($CaCl_2 \cdot 2H_2O$) compound of mass $(M - x)$ in the sample before the first hydration. Combining the first assumption that the sample was completely hydrated to hexahydrate ($CaCl_2 \cdot 6H_2O$) during the first hydration of 360 min, we obtain the following equation

$$Q = x \times \Delta H_{reaction\,(4)} + (M - x) \times \Delta H_{reaction\,(3+4)} \tag{35}$$

with Q = 225 J, M = 0.209 g, $\Delta H_{reaction\,(4)}$ = 659.40 kJ/kg^{salt} and $\Delta H_{reaction\,(3+4)}$ = 1617.47 kJ/kg^{salt}, we obtain x = 0.118 g. Therefore, the composition of calcium chloride hydrates in the initial state is 0.118 g tetrahydrate (56% of M) and 0.091 g dihydrate (44% of M) of calcium chloride.

Now we consider approximating the composition of calcium chloride hydrates for composites after different durations of hydration using the estimation of hydrates composition in the initial state. Since the sample was always completely dehydrated after each hydration, we can assume that the composition of hydrates remained the same after each dehydration as that of the initial state.

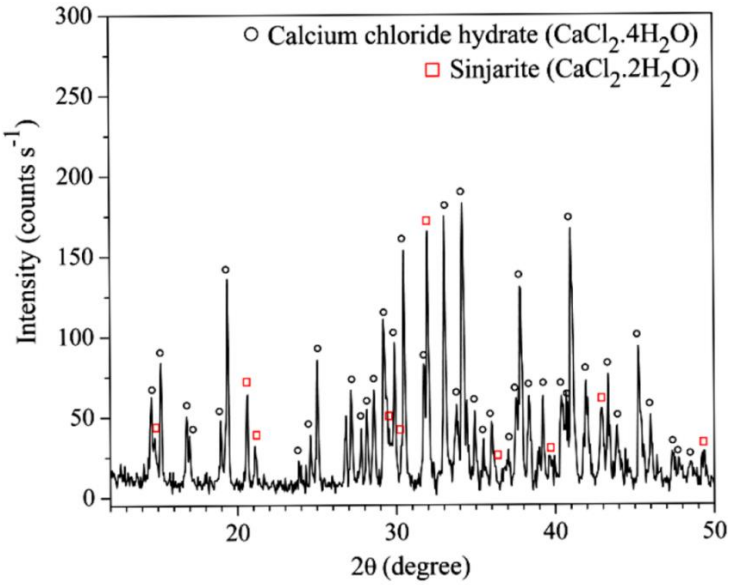

Fig. 3.24 X-ray diffractograms of $CaCl_2$ during complete dehydration at 25 ℃ [217].

As nickel foam-$CaCl_2$ composite and aluminum foam-$CaCl_2$ composite have similar cyclic performance in terms of the normalized thermal energy released during hydration processes, we take nickel foam-$CaCl_2$ composite as an example for approximating the composition after hydration of different durations. The sample nickel foam-$CaCl_2$ contained the same amount of salt compared to the bulk $CaCl_2$ sample, which was also 0.209 g. By results obtained from the long cyclic hydration/dehydration process on nickel foam-$CaCl_2$ composite, we have the average $\bar{Q}$ released during 180 min, 90 min and 45 min to be 182 J, 147 J, and 60 J, respectively. For estimating the composition at the final state, we first apply the estimated portion of tetrahydrate and dihydrate in the salt, then we make assumptions of the final state composition of the hydrates and compare the thermal energy released to that obtained via experiment.

For the salt deposited in the metal foam matrix, they can be divided into two groups, the ones deposited on the surface open pores that can directly interact with the humidified gas, and the ones that are embedded in the inner pores of metal foam that rely on pathways (cell windows) to be hydrated. We can reasonably speculate that it's the salts deposited on the surface open pores that are likely to be tetrahydrate in the initial state, while the dihydrates are embedded in the inner space of metal foam. If we assume that during the hydration process, the water vapor first interacts with the salt on the surface and then passes through the pathways to interact with the salt embedded in the middle of the metal foam, we may have the following estimation of the final state composition of calcium chloride hydrates after different durations of hydration process, as shown in Table 3.7.

Table 3.7 Estimation of final state composition of calcium chloride hydrates after different durations of hydration process, on supposing the tetrahydrate hydrated before the dihydrate.

Hydration time	Dihydrate		Tetrahydrate		Hexahydrate	
	Mass (g)	Portion	Mass (g)	Portion	Mass (g)	Portion
180 min	0	0	0.042	16%	0.213	84%
90 min	0.0033	1%	0.108	43%	0.140	56%
45 min	0.091	40%	0.026	12%	0.109	48%

*Portion: mass of a given hydrate as a percentage of the whole salt mass in its final state of hydration

To be clear, the estimation shown in Table 3.7 is obtained by assuming that, firstly, the tetrahydrate would totally hydrate to hexahydrate if not contradicted by experimental results in terms of the quantity of thermal energy released. Then we determine whether or how much of the dihydrate is to be hydrated into tetrahydrate or hexahydrate according to the experimental result on the quantity of thermal energy released for different durations.

Now, if we do not suppose that the hydration of the tetrahydrate precedes the dihydrate, but rather the reverse, which means changing the assumption to that the dihydrate precedes the tetrahydrate, then the result is as follows,

Table 3.8 Estimation of final state composition of calcium chloride hydrates after different durations of hydration process, on supposing the dihydrate hydrated before the tetrahydrate.

Hydration time	Dihydrate		Tetrahydrate		Hexahydrate	
	Mass (g)	Portion	Mass (g)	Portion	Mass (g)	Portion
180 min	0	0	0.043	18%	0.199	82%
90 min	0	0	0.096	42%	0.135	58%
45 min	0.016	7%	0.210	93%	0	0

To be clear, the estimation shown in Table 3.8 is obtained by assuming that, firstly, the dihydrate would totally hydrate to tetrahydrate if not contradicted by experimental results in terms of the quantity of thermal energy released. The quantity of thermal energy released for different durations that we measured during experiments then determine whether or how much of this part of the salt continues to be hydrated into hexahydrate.

In practice, it is likely that dihydrate and tetrahydrate are hydrated simultaneously. However, it is impossible to determine from the available data the portion of dihydrate and tetrahydrate being hydrated in the final state for actual experiments. Thus, by assuming the two extreme cases described above, we obtain a possible

interval for the proportion of each hydrate of calcium chloride in the final state.

As a conclusion, for composites, at the final state of hydration of 180 min, the estimated composition of calcium chloride hydrates is 16%~18% of tetrahydrate and 82%~84% of hexahydrate. At the final state of hydration of 90 min, the estimated composition of calcium chloride hydrates is 42%~43% of tetrahydrate and 56%~58% of hexahydrate. While for hydration of 45 min, this method doesn't provide a sufficiently specific percentage interval. There might exist three kinds of hydrates at the final state of 45 min hydration, which are dihydrate (7%~40%), tetrahydrate (12%~93%) and hexahydrate (0~48%).

To sum up, in this section, we approximately estimated the composition of calcium chloride hydrates in the initial state and after hydration with different durations, in order to provide an idea of the reactions that took place during the thermal energy releasing process. Note that the results we obtained are based on several strong assumptions. To better and more precisely detect the composition of calcium chloride hydrates at each phase during hydration and dehydration requires the implementation of other techniques, such as Thermal Gravimetric Analysis (TGA/DTA) or X-ray powder diffraction technique as presented in the literature [217].

3.5. Conclusion

To overcome the drawbacks of pure calcium chloride as thermochemical material, this study presented a newly designed metal foam-salt hydrate composite consisting of open-cell metal foam with a pore size of 350 µm as host matrix and calcium chloride as hygroscopic salt dispersed in the pores for thermochemical heat storage. The aim was to investigate the feasibility of the newly designed composite as a TCM and to compare its performance with that of pure calcium chloride. The main results are shown as follows:

(1) An appropriate synthesis method of the composite was developed, specifically tailored to our research subject. This method enabled the embedding of hygroscopic salts within the metal foams while maintaining sufficient porosity for efficient water vapor transfer during hydration and dehydration cycles. The method involves using the oversaturated salt solution and immersing the metal foam sample in. Intensive and continuous stirring was required to achieve an even distribution of salt. The composite sample should be kept in the oven for more than 48 h at 90 °C before experiments.

(2) Sufficiently good cyclic thermal reliability and stability were proven valid for the metal foam-salt composite over a large temperature range of -40 °C and 120 °C by DSC analysis.

(3) Metal foam-salt composites showed significant improvement in terms of cyclic

stability and quantity of thermal energy released/stored compared to bulk calcium chloride in both long and short hydration/dehydration cycles. For cyclic stability, composites presented a slight increase and stabilization of thermal energy released and restored upon cycles, while salt showed substantial and continuous degradation in performance. For thermal energy storage capacity, composites outperformed considerably the bulk calcium chloride in all cycles, except for the first cycle, which may be considered as an activation cycle allowing to reach the optimum composite microstructure. The result also indicated that for discharging/charging the same amount of thermal energy, metal foam-salt composites were more efficient than bulk calcium chloride.

(4) Nickel foam-$CaCl_2$ composite provided better performance in terms of apparent energy density as compared to aluminum foam-$CaCl_2$ composite. The difference in apparent energy density of these two composites meanly derives from the different porosity of the host matrix (96% for nickel foam, 40% for aluminum foam). The difference in porosity greatly affects the wt% of salt deposited in the metal foam, thus affecting the energy density.

(5) After confirming the feasibility of the designed metal foam-salt composite as TCM and its improvement in thermochemical performance compared to that of bulk salt powder, the performance enhancement mechanism of the composite was investigated by in situ ESEM hydration/dehydration cycling test. The observation indicated that the open-cell metal foam with a pore size of 350 μm provided sufficient salt deposition sites, allowing the salt to be relocated and reorganized in the metal foam cells even after deliquescence during the hydration process while preventing the swelling and agglomeration of salt, which effectively increased the cyclic stability of the composite. In addition, large open volumes and multiple flow paths provided by the metal foam increased the specific reaction surface, favored heat and mass transfer, and ensured no volume change even if swelling and agglomeration of salt occurred. Moreover, metal foam provided high thermal conductivity. All of the above-mentioned advantages led to a significant improvement in the thermochemical performance of the composite compared to that of bulk salt powder.

(6) The composition of calcium chloride hydrates in the initial state and after hydration with different durations has been approximately estimated, providing an idea of the reactions that took place during the thermal energy releasing process. For metal foam-salt composites, at the final state of hydration of 180 min, the estimated composition of calcium chloride hydrates is 16%~18% of tetrahydrate and 82%~84% of hexahydrate. At the final state of hydration of 90 min, the estimated composition of calcium chloride hydrates is 42%~43% of tetrahydrate and 56%~58% of hexahydrate.

As a conclusion, the metal foam-salt hydrate composites designed in this research is proved to be a promising choice of thermochemical material that can be implanted in thermal energy storage systems with its advantages in terms of cyclic stability, energy density, mechanical strength, thermal conductivity and cost.

4. Conclusions and perspectives

4.1. Conclusions

Rapid expansion in solar energy capacity leads to the prompt development of low-cost and reliable thermal energy storage (TES) systems for coping with the mismatch between energy demand and supply, thereby compensating for the intermittent nature of renewable energy and providing energy on demand [3]. Among the existing TES technologies, thermochemical heat storage (THS) has been attracting more attention in past decades, thanks to advantages such as high energy density, small heat losses, daily to seasonal heat storage flexibility and significant cost reduction [14, 27-29]. Compared to other thermochemical storage systems, THS systems based on hydration/dehydration reactions between water vapor and hygroscopic salts are the simplest, least expensive ones, with minimal environmental impact [34, 46-50]. However, hygroscopic salts have non-negligible drawbacks such as excessive swelling and agglomeration of the crystalline salt particles during hydration/dehydration cycles [69-71], which progressively leads to decreasing specific reaction surface and kinetics of heat and mass transfer, thus resulting in efficiency degradation due to poor cyclic performance and mediocre stability [39, 72, 73].

To alleviate the limitations mentioned above, we propose a composite "salt in porous matrix" (CSPM) type selective water sorbent (SWS), based on open-cell metal foam (pore size ~ 350 μm) as host matrix, containing calcium chloride as hygroscopic salt dispersed in the pores. With an adapted microstructure avoiding agglomeration during swelling and shrinking of the salt crystallites related to hydration and dehydration respectively, this composite material is expected to facilitate the transfers of water vapor and heat and prevents loss of specific reaction surface, thus improving the performance of the thermochemical heat storage system. A metal foam matrix offers additional advantages related to its elevated mechanical strength and high thermal conductivity, which ensures mechanical resistance, but also improves heat transfer kinetics [128]. The mechanical strength and relatively low density of metal foam serving as host matrix ensure the possibility of manufacturing lightweight and durable components, adapted to handling, stacking and mounting operations [124, 125, 127], which are necessary for adequate dimensioning and fabrication of flexible and polyvalent thermochemical reactors for future industrial and commercial TCM applications.

As this composite TCM would be stacked with variable volumes to fulfill the needs of flexible commercial usage, it is essential to make sure that the whole system maintains structural reliability under the condition of application. For instance, the porous structure of the composite system should not collapse under its own weight. Since it is the metal foam serving as host matrix that provides the mechanical

strength to the composite, in the first part we focused on the mechanical properties of various metal foams.

The multiscale deformation behavior of different types of metal foams was studied at room temperature and 150 °C by compression tests realized with in situ surface observation by optical microscopy with high-resolution camera (pixel size of 2.75 μm) and scanning electron microscopy (SEM). Laboratory X-ray microtomography technique was also applied before and after the compression tests. The images were analyzed by 2D and 3D Digital Image Correlation (DIC) for the computation of 2D and 3D full displacement fields and the corresponding strain fields. Additionally, the microscopic deformation behavior of a massive aluminum sample was studied by in situ SEM compression test and analyzed by 2D Digital Image Correlation, with a special focus on investigating the grain boundary behavior at 150 ℃.

The results showed that with respect to the mechanical integrity, the microstructure of the metal foam is by far more important than the metal itself. According to observations by SEM, copper foam, nickel foam and aluminum foam that we chose for serving as the host matrix of the salt hydrates were all open-cell metal foams. Among which, the copper foam and nickel foam had similar structures, in terms of the porosity, pore shape and homogeneity of pore distribution and size, whereas aluminum foam had quite an uneven strut thickness and irregular pore shape and size. The results obtained through uniaxial compression tests on the metal foams demonstrated that the structural homogeneity of the metal foams had a strong impact on their mechanical properties. In terms of mechanical strength, copper foam showed a 0.2% offset yield stress of about 0.23 ± 0.02 MPa at ambient temperature and about 0.27 ± 0.02 MPa at 150 ℃, showing that the moderately high temperature did not strongly impact the yield stress of the copper foam, but affected the strain hardening behavior. For aluminum foam, the 0.2% offset yield stress at ambient temperature was about 4.48 ± 0.02 MPa, but only about 2.12 ± 0.02 MPa at 150 ℃. Strain localization in metal foams with a homogeneous microstructure was rather homogeneously distributed in thin localization bands at a 45° to 60° angle to the loading direction, precluding complete pore collapse, thus preserving the mass transfer properties of the metal foam. In opposition, the highly heterogeneous metal foam microstructure led to the formation of a few extremely strong localization bands, which resulted in local pore collapse that might impede the water vapor transfer, thus affecting the performance of the designed composite. In conclusion, metal foams with homogeneous microstructure are best suited for the application of thermochemical heat storage (THS) materials.

In the second part, the thermochemical properties of the metal foam-salt composites were investigated. Firstly, an appropriate synthesis method of the composite was developed, specifically tailored to our research subject. This method enabled the embedding of hygroscopic salts within the metal foams while

maintaining sufficient porosity for efficient water vapor transfer during hydration and dehydration cycles. The thermochemical properties of the composites during hydration/dehydration cycles were studied by the isothermal reaction calorimetry and they were compared with those of salt hydrate powders of calcium chloride. The observed evolution of the measured thermochemical properties was further analyzed, based on in situ observations of the microstructural and morphological evolution of the composite during hydration/dehydration cycling tests in an environmental scanning electron microscope (ESEM). The experimental results demonstrated that metal foam-salt composites showed significant improvement in terms of cyclic stability and quantity of thermal energy released/stored compared to bulk calcium chloride during numerous hydration/dehydration cycles. For cyclic stability, composites presented a slight increase and stabilization of thermal energy released and restored upon cycles, while bulk salt powder of calcium chloride showed substantial and continuous degradation in performance. For thermal energy storage capacity, composites outperformed considerably the bulk calcium chloride powder in all cycles, except for the first cycle, which may be considered as an activation cycle allowing to reach the optimum composite microstructure.

The conclusions obtained from observations during the in situ ESEM hydration/dehydration cycling tests give a reasonable explanation and a possible mechanism for the improvements of the composites compared to bulk salt in terms of cyclic stability and thermal energy storage/release capacity and efficiency. The improved performance of the metal foam-salt composite can be largely attributed to the porous structure of the metal foam. On the one hand, the porous matrix serves for salt deposition. On the other hand, by maintaining the salt particles partly apart from each other, the foam with open pores 1) results in a large specific reaction area, 2) limits salt agglomeration and effectively avoids degradation of performance due to salt swelling and agglomeration upon hydric cycling, 3) facilitates mass and heat transfer through the wide open-porosity and the metallic network, respectively. In addition, thanks to the intermediate pore size of the selected metal foams, the capillarity effects of the host matrix ensure that during swelling and deliquescence, the salt crystallites can redistribute and reorganize locally within the composite, without extensive migration throughout the foam structure or extensive agglomeration, which are essential prerequisite properties to preserve the porosity and the specific reaction area. These properties ensure the cyclic stability of composites in terms of thermochemical energy capacity, as well as mass and heat transfer efficiency. The composite offers a sort of dynamic microstructure, with local topological evolutions upon hydric cycling, but allowing for the maintenance of statistically stable proportions of open interconnected pores and specific reaction areas. In such cases, the global thermochemical performance of the composite remains stable over operational cycles. Without the metallic foam host structure, the salt crystallites that undergo cyclic swelling may progressively

compact, leading to a loss of porosity and specific reaction area. This, in turn, results in a gradual decrease in thermochemical performance, which aligns with our observations. It can be speculated that structures with excessively large pores may not effectively limit the extensive migration of salt hydrates during deliquescence and/or melting. Conversely, structures with overly small pores may struggle to maintain open porosity during deliquescence and swelling of salt hydrates, thereby limiting mass transfer properties. These questions, however, require further investigation in future studies.

In conclusion, the metal foam-salt hydrate composite developed in our work is suitable and promising for thermochemical energy storage, offering both mechanical and thermochemical advantages. On the one hand, the metallic foam ensures structural integrity allowing for flexible industrial handling of thermochemical storage units. On the other hand, the metal foam guarantees the microstructural stability of the reactive material, hence preserving an economically durable life span of the composite. Lastly, the thermochemical composites exhibit a low environmental footprint. The reactive calcium chloride hydrates used in the composites are environmentally friendly and are widely employed as snow-clearing products, with a lower environmental impact compared to sodium chloride. Moreover, both the salt hydrates and the metallic foam materials used in the composites are fully recyclable, further contributing to their eco-friendliness.

4.2. Perspectives

From a general point of view, the objectives of the thesis have been achieved. The proposed metal foam-salt hydrate composite was proven to be a promising thermochemical material, providing both mechanical and thermochemical benefits.

However, there remain several challenges and several aspects that can be studied in depth for obtaining a reliable and efficient thermal storage system using the SWS-type metal foam-salt hydrate composite proposed in this work.

Firstly, the corrosion of metal foam host matrix needs to be addressed. Corrosion is a non-negligible corrosion issue when using metal foams in a salty environment [218]. In our study, the metal foam contacts directly with not only the salts but also water vapor which increased the complexity of the working environment of metal foam and also increased the potential for it to corrode. Besides, in practical applications, the working environment would be under ambient pressure with the ambient air serving as the source of hydration, it is therefore essential to take into account the influence of oxygen on the corrosion of the metal foam. We have already observed in our work the corrosion of copper foam-salt composite being corroded under the ambient environment (Fig. 3.2d). The results of studies on the corrosion rates of different metals with calcium chloride solutions or liquid calcium chloride exist in the literature [112, 122, 214, 219, 220], but since the experimental

conditions are set up differently from the actual environment in which the metal foam-salt composite is used, these previous conclusions are informative, but it is better to be aware of the corrosion situation under the identical conditions of use of the composite. We need to understand how and to what extent corrosion may affect the mechanical and thermochemical properties of metal foams. Besides, the corrosion might also increase the maintenance cost of the system. If necessary, the metal foam needs to be treated with corrosion protection through corrosion inhibitors, packaging, coating, or other effective methods [219].

Secondly, the possible influence of different metal foams on the thermochemical properties can be further investigated, in terms of the material, porosity and pore size of metal foam. For the material of metal foam, we studied the copper, nickel and aluminum foam with pore sizes around 350 µm, where copper and nickel foam had homogeneous microstructure and had similar porosity (>90%), while aluminum foam was quite heterogeneous and had a porosity of only 40%. However, as we weren't able to find a commercial aluminum foam that meets the requirements of a small enough pore size (~350 µm), a large enough porosity (>90%) and a homogeneous microstructure, we couldn't compare the difference of thermochemical performance resulted from the difference of the metal foam material. Besides, if the corrosion problem of copper foam can be ameliorated, the copper foam might also be a valid candidate thanks to its high thermal conductivity. Therefore, this point could be further studied if possible. In addition, our work proved the feasibility and good thermochemical performance of the composite with a metal foam of pore size around 350 µm and high porosity (>95%), it would be interesting to know how the pore size and porosity of metal foam may influence its performance. Note that it has been already demonstrated that metal foam with homogeneous microstructure is more suitable for our application of composite in terms of a more effective mass transfer. Consequently, it is better to choose a metal foam with a homogeneous microstructure for further investigation.

Thirdly, the impact of salt content in the composite on thermochemical performance can be explored. In section 1.6.2, we explained that in order to use metal foam as host matrix in SWS composites, it is essential to ensure that a sufficient portion of pores remain empty and free of the salt so that the heat and mass (water vapor) transfer properties can be guaranteed. The synthesis method developed in our work allows a salt content of 48.5% with high porosity (>90%) metal foam and a salt content of 21% with low porosity (40%) metal foam. In the future study, we can try to vary the salt content of the composite and try to find the most suitable equilibrium between salt content and free pore volume after salt impregnation in order to achieve optimal heat and mass transfer efficiency and thus improve the cyclic stability and thermochemical properties of the composite.

Additionally, exploring the influence of salt deposition in the composite on its

mechanical properties would be interesting. It would be meaningful to determine whether the hydration or dehydration process induces additional strain in the metal foam and if it does, to understand how and why this would affect the compressive behavior of the metal foam.

Finally, the experimental conditions for isothermal hydration/dehydration tests (e.g., the relative humidity, the temperature, etc.) in our study can be further discussed and investigated. The choice of our experimental conditions for isothermal hydration/dehydration cycling tests on both composites and bulk salt powder was introduced and explained in detail in section 3.3.2 a). As explained, the experimental conditions used may differ from the conventional large-scale application conditions for thermochemical heat storage. Nevertheless, it is crucial to emphasize that our study's main objective is to confirm the viability of metal foam-salt hydrate composites as thermochemical materials. This does not dictate the necessity for applying the composites under the same experimental conditions used in our study, nor does it suggest that copper, nickel, aluminum foam, or calcium chloride are inherently the optimal choices for composing the metal foam-salt hydrate composite. Therefore, the performance of the composites can be further investigated under different experimental conditions and with different compositions.

REFERENCES

[1] IEA(**2022**), Renewables 2022, IEA, Paris, https://www.iea.org/reports/renewables-2022, License: CC BY 4.0.

[2] IEA(**2022**), World Energy Outlook 2022, IEA, Paris, https://www.iea.org/reports/world-energy-outlook-2022, License: CC BY 4.0 (report); CC BY NC SA 4.0 (Annex A).

[3] Carrillo, A.J., et al., Solar Energy on Demand: A Review on High Temperature Thermochemical Heat Storage Systems and Materials. Chemical Reviews, **2019**. 119(7): p. 4777-4816.

[4] Romero, M. and J. González-Aguilar, Solar thermal CSP technology. Wiley Interdisciplinary Reviews: Energy and Environment, **2014**. 3(1): p. 42-59.

[5] Weinstein, L.A., et al., Concentrating solar power. Chemical Reviews, **2015**. 115(23): p. 12797-12838.

[6] Allouhi, A., et al., Energy consumption and efficiency in buildings: current status and future trends. Journal of Cleaner production, **2015**. 109: p. 118-130.

[7] Alva, G., Y. Lin, and G. Fang, An overview of thermal energy storage systems. Energy, **2018**. 144: p. 341-378.

[8] Aydin, D., S.P. Casey, and S. Riffat, The latest advancements on thermochemical heat storage systems. Renewable and Sustainable Energy Reviews, **2015**. 41: p. 356-367.

[9] Donkers, P., et al., A review of salt hydrates for seasonal heat storage in domestic applications. Applied energy, **2017**. 199: p. 45-68.

[10] Wood, T. and D. Blowers, Sundown, sunrise: how Australia can finally get solar power right. **2015**.

[11] Wong, B., A. Snijders, and L. McClung. Recent Inter-seasonal Underground Thermal Energy Storage Applications in Canada. in 2006 IEEE EIC Climate Change Conference. **2006**.

[12] Nguyen, M.H. and S. Bennici, Recent progress in thermochemical heat storage: materials and applications. Recent Advances in Renewable Energy Technologies, **2021**: p. 281-310.

[13] Fernández, A., et al., Selection of materials with potential in sensible thermal energy storage. Solar energy materials and solar cells, **2010**. 94(10): p. 1723-1729.

[14] Kuravi, S., et al., Thermal energy storage technologies and systems for concentrating solar power plants. Progress in Energy and Combustion Science, **2013**. 39(4): p. 285-319.

[15] Parameshwaran, R., et al., Sustainable thermal energy storage technologies for buildings: a review. Renewable and Sustainable Energy Reviews, **2012**. 16(5): p. 2394-2433.

[16] Khare, S., et al., Selection of materials for high temperature latent heat energy storage. Solar energy materials and solar cells, **2012**. 107: p. 20-27.

[17] Wentworth, W. and E. Chen, Simple thermal decomposition reactions for storage of solar thermal energy. Solar Energy, **1976**. 18(3): p. 205-214.

[18] Wu, J. and X.F. Long, Research progress of solar thermochemical energy storage. International Journal of Energy Research, **2015**. 39(7): p. 869-888.

[19] Zhang, Y. and R. Wang, Sorption thermal energy storage: Concept, process, applications and perspectives. Energy Storage Materials, **2020**. 27: p. 352-369.
[20] Hasnain, S., Review on sustainable thermal energy storage technologies, Part I: heat storage materials and techniques. Energy conversion and management, **1998**. 39(11): p. 1127-1138.
[21] Sarbu, I. and C. Sebarchievici, A comprehensive review of thermal energy storage. Sustainability, **2018**. 10(1): p. 191.
[22] Abhat, A., Low temperature latent heat thermal energy storage: heat storage materials. Solar energy, **1983**. 30(4): p. 313-332.
[23] Zhou, D., C.-Y. Zhao, and Y. Tian, Review on thermal energy storage with phase change materials (PCMs) in building applications. Applied energy, **2012**. 92: p. 593-605.
[24] Sharma, A., et al., Review on thermal energy storage with phase change materials and applications. Renewable and Sustainable energy reviews, **2009**. 13(2): p. 318-345.
[25] Zalba, B., et al., Review on thermal energy storage with phase change: materials, heat transfer analysis and applications. Applied thermal engineering, **2003**. 23(3): p. 251-283.
[26] Lane, G.A. and N. Shamsundar, Solar Heat Storage: Latent Heat Materials, Vol. I: Background and Scientific Principles. Journal of Solar Energy Engineering-transactions of The Asme, **1983**. 105: p. 467-467.
[27] Cabeza, L.F., A. Solé, and C. Barreneche, Review on sorption materials and technologies for heat pumps and thermal energy storage. Renewable Energy, **2017**. 110: p. 3-39.
[28] Ma, Z., H. Bao, and A.P. Roskilly, Electricity-assisted thermochemical sorption system for seasonal solar energy storage. Energy Conversion and Management, **2020**. 209: p. 112659.
[29] Aydin, D., Z. Utlu, and O. Kincay, Thermal performance analysis of a solar energy sourced latent heat storage. Renewable and Sustainable Energy Reviews, **2015**. 50: p. 1213-1225.
[30] Thermal Energy Storage for Solar and Low Energy Buildings: State of the Art, ed. Series. **2005**: IEA.
[31] Yu, N., R. Wang, and L. Wang, Sorption thermal storage for solar energy. Progress in Energy and Combustion Science, **2013**. 39(5): p. 489-514.
[32] Scapino, L., et al., Sorption heat storage for long-term low-temperature applications: A review on the advancements at material and prototype scale. Applied Energy, **2017**. 190: p. 920-948.
[33] McBain, J.W., XCIX. The mechanism of the adsorption ("sorption") of hydrogen by carbon. The London, Edinburgh, and Dublin Philosophical Magazine and Journal of Science, **1909**. 18(108): p. 916-935.
[34] Kerskes, H., et al., Chemical energy storage using reversible solid/gas-reactions (CWS) – results of the research project. Energy Procedia, **2012**. 30: p. 294-304.
[35] Neveu, P. and J. Castaing, Solid-gas chemical heat pumps: Field of application and performance of the internal heat of reaction recovery process. Heat Recovery Systems and CHP, **1993**. 13(3): p. 233-251.
[36] Meunier, F., Solid sorption heat powered cycles for cooling and heat pumping

applications. Applied Thermal Engineering, **1998**. 18(9): p. 715-729.
[37] Chan, C., J. Ling-Chin, and A. Roskilly, A review of chemical heat pumps, thermodynamic cycles and thermal energy storage technologies for low grade heat utilisation. Applied thermal engineering, **2013**. 50(1): p. 1257-1273.
[38] N'Tsoukpoe, K.E., et al., A review on long-term sorption solar energy storage. Renewable and Sustainable Energy Reviews, **2009**. 13(9): p. 2385-2396.
[39] Li, W., et al., Salt hydrate–based gas-solid thermochemical energy storage: Current progress, challenges, and perspectives. Renewable and Sustainable Energy Reviews, **2022**. 154: p. 111846.
[40] Pons, M., et al., Thermodynamic based comparison of sorption systems for cooling and heat pumping: Comparaison des performances thermodynamique des systèmes de pompes à chaleur à sorption dans des applications de refroidissement et de chauffage. International Journal of Refrigeration, **1999**. 22(1): p. 5-17.
[41] Linder, M., Using thermochemical reactions in thermal energy storage systems, in Advances in Thermal Energy Storage Systems. **2021**, Elsevier. p. 477-495.
[42] Gommed, K. and G. Grossman, Experimental investigation of a liquid desiccant system for solar cooling and dehumidification. Solar Energy, **2007**. 81(1): p. 131-138.
[43] Xiong, Z.Q., Y.J. Dai, and R.Z. Wang, Development of a novel two-stage liquid desiccant dehumidification system assisted by CaCl2 solution using exergy analysis method. Applied Energy, **2010**. 87(5): p. 1495-1504.
[44] Abedin, A.H. and M.A. Rosen, Closed and open thermochemical energy storage: Energy-and exergy-based comparisons. Energy, **2012**. 41(1): p. 83-92.
[45] Hauer, A. and E.L. avemann. OPEN ABSORPTION SYSTEMS FOR AIR CONDITIONING AND THERMAL ENERGY STORAGE. in Thermal Energy Storage for Sustainable Energy Consumption. **2007**. Dordrecht: Springer Netherlands.
[46] Jiang, L., et al., Thermophysical characterization of magnesium chloride and its application in open sorption thermal energy storage system. Solar Energy Materials and Solar Cells, **2022**. 236: p. 111528.
[47] Zondag, H., et al., Prototype thermochemical heat storage with open reactor system. Applied energy, **2013**. 109: p. 360-365.
[48] Johannes, K., et al., Design and characterisation of a high powered energy dense zeolite thermal energy storage system for buildings. Applied Energy, **2015**. 159: p. 80-86.
[49] Mukherjee, A., et al., Performance evaluation of an open thermochemical energy storage system integrated with flat plate solar collector. Applied Thermal Engineering, **2020**. 173: p. 115218.
[50] Michel, B., P. Neveu, and N. Mazet, Comparison of closed and open thermochemical processes, for long-term thermal energy storage applications. Energy, **2014**. 72: p. 702-716.
[51] Sögütoglu, L.C., et al., In-depth investigation of thermochemical performance in a heat battery: Cyclic analysis of K2CO3, MgCl2 and Na2S. Applied Energy, **2018**. 215: p. 159-173.
[52] Marias, F., et al., Thermodynamic analysis and experimental study of solid/gas reactor operating in open mode. Energy, **2014**. 66: p. 757-765.

[53] Houben, J., et al., K2CO3 in closed heat storage systems. Renewable Energy, **2020**. 166: p. 35-44.
[54] Pathak, A.D., et al., A DFT-based comparative equilibrium study of thermal dehydration and hydrolysis of CaCl2 hydrates and MgCl2 hydrates for seasonal heat storage. Physical Chemistry Chemical Physics, **2016**. 18(15): p. 10059-10069.
[55] Mamani, V., et al., Industrial carnallite-waste for thermochemical energy storage application. Applied Energy, **2020**. 265: p. 114738.
[56] Michel, B. and M. Clausse, Design of thermochemical heat transformer for waste heat recovery: Methodology for reactive pairs screening and dynamic aspect consideration. Energy, **2020**. 211: p. 118042.
[57] Solé, A., I. Martorell, and L.F. Cabeza, State of the art on gas–solid thermochemical energy storage systems and reactors for building applications. Renewable and Sustainable Energy Reviews, **2015**. 47: p. 386-398.
[58] Fumey, B., R. Weber, and L. Baldini, Sorption based long-term thermal energy storage – Process classification and analysis of performance limitations: A review. Renewable and Sustainable Energy Reviews, **2019**. 111: p. 57-74.
[59] Ferchaud, C., et al. Study of the reversible water vapour sorption process of MgSO4. 7H2O and MgCl2. 6H2O under the conditions of seasonal solar heat storage. in Journal of Physics: Conference Series. **2012**. IOP Publishing.
[60] Sögütoglu, L., et al., In-depth investigation of thermochemical performance in a heat battery: Cyclic analysis of K2CO3, MgCl2 and Na2S. Applied Energy, **2018**. 215: p. 159-173.
[61] Fopah-Lele, A. and J.G. Tamba, A review on the use of SrBr2· 6H2O as a potential material for low temperature energy storage systems and building applications. Solar Energy Materials and Solar Cells, **2017**. 164: p. 175-187.
[62] Donkers, P., L. Pel, and O. Adan, Experimental studies for the cyclability of salt hydrates for thermochemical heat storage. Journal of Energy Storage, **2016**. 5: p. 25-32.
[63] Luo, L. and N. Le Pierrès, Chapter 3 - Innovative Systems for Storage of Thermal Solar Energy in Buildings, in Solar Energy Storage, Bent Sørensen, Editor. **2015**, Academic Press: Boston. p. 27-62.
[64] Peng, C., L. Chen, and M. Tang, A database for deliquescence and efflorescence relative humidities of compounds with atmospheric relevance. Fundamental Research, **2021**.
[65] Piqué, F., L. Dei, and E. Ferroni, Physicochemical aspects of the deliquescence of calcium nitrate and its implications for wall painting conservation. Studies in Conservation, **1992**. 37(4): p. 217-227.
[66] Girnik, I.S., et al., Composite “LiCl/MWCNT/PVA” for adsorption thermal battery: Dynamics of methanol sorption. Renewable and Sustainable Energy Reviews, **2020**. 123: p. 109748.
[67] Sögütoglu, L.-C., et al., Understanding the Hydration Process of Salts: The Impact of a Nucleation Barrier. Crystal Growth & Design, **2019**. 19(4): p. 2279-2288.
[68] Tatsidjodoung, P., N. Le Pierrès, and L. Luo, A review of potential materials for thermal energy storage in building applications. Renewable and Sustainable

Energy Reviews, **2013**. 18: p. 327-349.
[69] Donkers, P.A.J., L. Pel, and O.C.G. Adan, Experimental studies for the cyclability of salt hydrates for thermochemical heat storage. Journal of Energy Storage, **2016**. 5: p. 25-32.
[70] Ferchaud, C., Experimental study of salt hydrates for thermochemical seasonal heat storage. Technische Universiteit Eindhoven, **2016**.
[71] Zhao, Q., et al., Optimization of thermochemical energy storage systems based on hydrated salts: A review. Energy and Buildings, **2021**. 244: p. 111035.
[72] Lu, Z.S., et al., Performance analysis of an adsorption refrigerator using activated carbon in a compound adsorbent. Carbon, **2006**. 44(4): p. 747-752.
[73] Wang, L.W., R.Z. Wang, and R.G. Oliveira, A review on adsorption working pairs for refrigeration. Renewable and Sustainable Energy Reviews, **2009**. 13(3): p. 518-534.
[74] Aristov, Y.I., et al., A family of new working materials for solid sorption air conditioning systems. Applied Thermal Engineering, **2002**. 22(2): p. 191-204.
[75] Aristov, Y.I., et al., Selective water sorbents for multiple applications, 10. Energy storage ability. Reaction Kinetics and Catalysis Letters, **2000**. 69: p. 345-353.
[76] Gordeeva, L. and Y.I. Aristov, Composites 'salt inside porous matrix'for adsorption heat transformation: a current state-of-the-art and new trends. International Journal of Low-Carbon Technologies, **2012**. 7(4): p. 288-302.
[77] Mohapatra, D. and J. Nandanavanam, Salt in matrix for thermochemical energy storage-A review. Materials Today: Proceedings, **2023**. 72: p. 27-33.
[78] Frazzica, A., et al., Development of "salt in porous matrix" composites based on LiCl for sorption thermal energy storage. Energy, **2020**. 208: p. 118338.
[79] Aristov, Y.I., New family of solid sorbents for adsorptive cooling: material scientist approach. Journal of Engineering Thermophysics, **2007**. 16: p. 63-72.
[80] Gordeeva, L.G., et al., Adsorption properties of composite materials (LiCl+LiBr)/silica. Microporous and Mesoporous Materials, **2009**. 126(3): p. 262-267.
[81] Courbon, E., et al., A new composite sorbent based on SrBr2 and silica gel for solar energy storage application with high energy storage density and stability. Applied Energy, **2017**. 190: p. 1184-1194.
[82] Zhang, Y.N., et al., Development and thermochemical characterizations of vermiculite/SrBr2 composite sorbents for low-temperature heat storage. Energy, **2016**. 115: p. 120-128.
[83] Sutton, R.J., et al., Characterising the discharge cycle of CaCl2 and LiNO3 hydrated salts within a vermiculite composite scaffold for thermochemical storage. Energy and Buildings, **2018**. 162: p. 109-120.
[84] Permyakova, A., et al., Design of salt–metal organic framework composites for seasonal heat storage applications. Journal of Materials Chemistry A, **2017**. 5(25): p. 12889-12898.
[85] Zhang, Y.N., R.Z. Wang, and T.X. Li, Thermochemical characterizations of high-stable activated alumina/LiCl composites with multistage sorption process for thermal storage. Energy, **2018**. 156: p. 240-249.
[86] Ejeian, M., A. Entezari, and R.Z. Wang, Solar powered atmospheric water harvesting with enhanced LiCl /MgSO4/ACF composite. Applied Thermal

Engineering, **2020**. 176: p. 115396.
[87] Mahon, D., et al., Feasibility study of MgSO4 + zeolite based composite thermochemical energy stores charged by vacuum flat plate solar thermal collectors for seasonal thermal energy storage. Renewable Energy, **2020**. 145: p. 1799-1807.
[88] Xu, J.X., et al., High energy-density multi-form thermochemical energy storage based on multi-step sorption processes. Energy, **2019**. 185: p. 1131-1142.
[89] Casey, S.P., et al., Salt impregnated desiccant matrices for 'open' thermochemical energy storage—Hygrothermal cyclic behaviour and energetic analysis by physical experimentation. Energy and Buildings, **2015**. 92: p. 128-139.
[90] Grekova, A.D., L.G. Gordeeva, and Y.I. Aristov, Composite "LiCl/vermiculite" as advanced water sorbent for thermal energy storage. Applied Thermal Engineering, **2017**. 124: p. 1401-1408.
[91] Casey, S.P., et al., Salt impregnated desiccant matrices for 'open'thermochemical energy conversion and storage–Improving energy density utilisation through hygrodynamic & thermodynamic reactor design. Energy Conversion and Management, **2017**. 142: p. 426-440.
[92] Korhammer, K., et al., Sorption and thermal characterization of composite materials based on chlorides for thermal energy storage. Applied Energy, **2016**. 162: p. 1462-1472.
[93] Dawoud, B. and Y. Aristov, Experimental study on the kinetics of water vapor sorption on selective water sorbents, silica gel and alumina under typical operating conditions of sorption heat pumps. International Journal of Heat and Mass Transfer, **2003**. 46(2): p. 273-281.
[94] Tokarev, M., et al., New composite sorbent CaCl2 in mesopores for sorption cooling/heating. International Journal of Thermal Sciences, **2002**. 41(5): p. 470-474.
[95] Sharma, S.D., H. Kitano, and K. Sagara, Phase change materials for low temperature solar thermal applications. Res. Rep. Fac. Eng. Mie Univ, **2004**. 29(1): p. 31-64.
[96] Kaygusuz, K., Experimental and theoretical investigation of latent heat storage for water based solar heating systems. Energy Conversion and Management, **1995**. 36(5): p. 315-323.
[97] Wang, R. and R.G. Oliveira, Adsorption refrigeration—an efficient way to make good use of waste heat and solar energy. Progress in energy and combustion science, **2006**. 32(4): p. 424-458.
[98] Khudhair, A.M. and M.M. Farid, A review on energy conservation in building applications with thermal storage by latent heat using phase change materials. Energy conversion and management, **2004**. 45(2): p. 263-275.
[99] Liang, J.-D., et al., Experimental investigation of a liquid desiccant dehumidification system integrated with shallow geothermal energy. Energy, **2020**. 191: p. 116452.
[100] Bansal, P., S. Jain, and C. Moon, Performance comparison of an adiabatic and an internally cooled structured packed-bed dehumidifier. Applied Thermal Engineering, **2011**. 31(1): p. 14-19.

[101] John, M., et al., Performance of Calcium Chloride-Ammonia Adsorption Refrigeration System. Tanzania Journal of Engineering and Technology, **2021**. 40(1).
[102] Wei, S., et al., Development of pomegranate-type CaCl2@C composites via a scalable one-pot pyrolysis strategy for solar-driven thermochemical heat storage. Energy Conversion and Management, **2020**. 212: p. 112694.
[103] Barsk, A., et al., Exceptionally high energy storage density for seasonal thermochemical energy storage by encapsulation of calcium chloride into hydrophobic nanosilica capsules. Solar Energy Materials and Solar Cells, **2023**. 251: p. 112154.
[104] The Dow Chemical Company. Calcium Chloride Handbook. **2003**; Available from: https://www.sciencemadness.org/talk/files.php?pid=234855&aid=17338.
[105] Wagman, D.D., et al., Erratum: The NBS tables of chemical thermodynamic properties. Selected values for inorganic and C1 and C2 organic substances in SI units [J. Phys. Chem. Ref. Data 11, Suppl. 2 (1982)]. Journal of Physical and Chemical Reference Data, **1989**. 18(4): p. 1807-1812.
[106] Iyimen-Schwarz, Z. and M.D. Lechner, Energiespeicherung durch chemische reaktionen. I. DSC-messungen zur quantitativen verfolgung der enthalpieänderungen von speicherstoffen für die hin- und rückreaktion. Thermochimica Acta, **1983**. 68(2): p. 349-361.
[107] Jabbari-Hichri, A., S. Bennici, and A. Auroux, Enhancing the heat storage density of silica–alumina by addition of hygroscopic salts (CaCl2, Ba(OH)2, and LiNO3). Solar Energy Materials and Solar Cells, **2015**. 140: p. 351-360.
[108] Levitskij, E.A., et al., "Chemical Heat Accumulators": A new approach to accumulating low potential heat. Solar Energy Materials and Solar Cells, **1996**. 44(3): p. 219-235.
[109] Polyachenok, O.G., et al., Formation of super disperse phase and its influence on equilibrium and thermodynamics of thermal dehydration. Thermochimica Acta, **2008**. 467(1): p. 44-53.
[110] Tso, C.Y. and C.Y.H. Chao, Activated carbon, silica-gel and calcium chloride composite adsorbents for energy efficient solar adsorption cooling and dehumidification systems. International Journal of Refrigeration, **2012**. 35(6): p. 1626-1638.
[111] Gruszkiewicz, M.S. and J.M. Simonson, Vapor pressures and isopiestic molalities of concentrated CaCl2(aq), CaBr2(aq), and NaCl(aq) to T=523 K. The Journal of Chemical Thermodynamics, **2005**. 37(9): p. 906-930.
[112] Cabeza, L.F., et al., Immersion corrosion tests on metal-salt hydrate pairs used for latent heat storage in the 32 to 36°C temperature range. Materials and Corrosion, **2001**. 52(2): p. 140-146.
[113] Wang, R.Z. and R.G. Oliveira, Adsorption refrigeration—An efficient way to make good use of waste heat and solar energy. Progress in Energy and Combustion Science, **2006**. 32(4): p. 424-458.
[114] Fujioka, K. and H. Suzuki, Thermophysical properties and reaction rate of composite reactant of calcium chloride and expanded graphite. Applied Thermal Engineering, **2013**. 50(2): p. 1627-1632.
[115] Courbon, E., et al., Further improvement of the synthesis of silica gel and CaCl2

composites: Enhancement of energy storage density and stability over cycles for solar heat storage coupled with space heating applications. Solar Energy, **2017**. 157: p. 532-541.
[116] Zhang, H., et al., Inorganic composite adsorbent CaCl2/MWNT for water vapor adsorption. RSC Advances, **2015**. 5(48): p. 38630-38639.
[117] Baumann, A.E., et al., Metal-organic framework functionalization and design strategies for advanced electrochemical energy storage devices. Communications Chemistry, **2019**. 2(1): p. 86.
[118] Touloumet, Q., et al., Water sorption and heat storage in CaCl2 impregnated aluminium fumarate MOFs. Solar Energy Materials and Solar Cells, **2021**. 231: p. 111332.
[119] Shi, W., et al., Water sorption properties of functionalized MIL-101(Cr)-X (X=-NH2, –SO3H, H, –CH3, –F) based composites as thermochemical heat storage materials. Microporous and Mesoporous Materials, **2019**. 285: p. 129-136.
[120] Gaeini, M., et al., Characterization of microencapsulated and impregnated porous host materials based on calcium chloride for thermochemical energy storage. Applied Energy, **2018**. 212: p. 1165-1177.
[121] Jabbari-Hichri, A., S. Bennici, and A. Auroux, CaCl2-containing composites as thermochemical heat storage materials. Solar Energy Materials and Solar Cells, **2017**. 172: p. 177-185.
[122] N'Tsoukpoe, K.E., et al., A review on the use of calcium chloride in applied thermal engineering. Applied Thermal Engineering, **2015**. 75: p. 513-531.
[123] Sing, K.S., Reporting physisorption data for gas/solid systems with special reference to the determination of surface area and porosity (Recommendations 1984). Pure and applied chemistry, **1985**. 57(4): p. 603-619.
[124] Lefebvre, L.P., J. Banhart, and D.C. Dunand, Porous metals and metallic foams: current status and recent developments. Advanced engineering materials, **2008**. 10(9): p. 775-787.
[125] Banhart, J., Manufacture, characterisation and application of cellular metals and metal foams. Progress in materials science, **2001**. 46(6): p. 559-632.
[126] Zhang, S., et al., A review of phase change heat transfer in shape-stabilized phase change materials (ss-PCMs) based on porous supports for thermal energy storage. Renewable and Sustainable Energy Reviews, **2021**. 135: p. 110127.
[127] García-Moreno, F., Commercial Applications of Metal Foams: Their Properties and Production. Materials, **2016**. 9(2): p. 85.
[128] Tan, W.C., et al., Overview of porous media/metal foam application in fuel cells and solar power systems. Renewable and Sustainable Energy Reviews, **2018**. 96: p. 181-197.
[129] Patel, P., P. Bhingole, and D. Makwana, Manufacturing, characterization and applications of lightweight metallic foams for structural applications. Materials Today: Proceedings, **2018**. 5(9): p. 20391-20402.
[130] Metal foams: a design guide, ed. Series. **2000**: Elsevier.
[131] Gibson, L.J. and M.F. Ashby, The mechanics of foams: basic results, in Cellular Solids: Structure and Properties, Lorna J. Gibson and Michael F. Ashby, Editors. **1997**, Cambridge University Press: Cambridge. p. 175-234.

[132] Kulshreshtha, A. and S.K. Dhakad, Preparation of metal foam by different methods: A review. Materials Today: Proceedings, **2020**. 26: p. 1784-1790.
[133] Giani, L., et al., Washcoating method for Pd/γ-Al2O3 deposition on metallic foams. Applied Catalysis B: Environmental, **2006**. 62(1-2): p. 121-131.
[134] Khouri, S., et al., Metallurgical brownfields re-use in the conditions of Slovakia–A case study. Metalurgija, **2016**. 55(3): p. 500-502.
[135] Huang, X., et al., Shape-stabilized phase change materials based on porous supports for thermal energy storage applications. Chemical Engineering Journal, **2019**. 356: p. 641-661.
[136] Aramesh, M. and B. Shabani, Metal foam-phase change material composites for thermal energy storage: A review of performance parameters. Renewable and Sustainable Energy Reviews, **2022**. 155: p. 111919.
[137] Righetti, G., et al., Phase change materials embedded in porous matrices for hybrid thermal energy storages: Experimental results and modeling. International Journal of Refrigeration, **2019**. 106: p. 266-277.
[138] Mallow, A., O. Abdelaziz, and S. Graham, Thermal charging performance of enhanced phase change material composites for thermal battery design. International Journal of Thermal Sciences, **2018**. 127: p. 19-28.
[139] Xiao, X., P. Zhang, and M. Li, Preparation and thermal characterization of paraffin/metal foam composite phase change material. Applied energy, **2013**. 112: p. 1357-1366.
[140] Xiao, X., P. Zhang, and M. Li, Effective thermal conductivity of open-cell metal foams impregnated with pure paraffin for latent heat storage. International Journal of Thermal Sciences, **2014**. 81: p. 94-105.
[141] Ferfera, R.S. and B. Madani, Thermal characterization of a heat exchanger equipped with a combined material of phase change material and metallic foams. International Journal of Heat and Mass Transfer, **2020**. 148: p. 119162.
[142] Huang, X., et al., Thermal properties and thermal conductivity enhancement of composite phase change materials using myristyl alcohol/metal foam for solar thermal storage. Solar Energy Materials and Solar Cells, **2017**. 170: p. 68-76.
[143] Wang, Z., et al., Paraffin and paraffin/aluminum foam composite phase change material heat storage experimental study based on thermal management of Li-ion battery. Applied Thermal Engineering, **2015**. 78: p. 428-436.
[144] Li, X., et al., Preparation of stearic acid/modified expanded vermiculite composite phase change material with simultaneously enhanced thermal conductivity and latent heat. Solar Energy Materials and Solar Cells, **2016**. 155: p. 9-13.
[145] Miyoshi, T., et al., ALPORAS Aluminum Foam: Production Process, Properties, and Applications. Advanced Engineering Materials, **2000**. 2(4): p. 179-183.
[146] Aluminium foam - Production, Properties and Recycling Possibilities, ed. Series. Vol. 56. **2003**. 658-662.
[147] ODYSSEE-MURE(**2021**), France energy efficiency & Trends policies | France profile, https://www.odyssee-mure.eu/publications/efficiency-trends-policies-profiles/france.html,
[148] Banhart, J. and J. Baumeister, Deformation characteristics of metal foams. Journal of Materials Science, **1998**. 33(6): p. 1431-1440.

[149] Gibson, L.J., Mechanical Behavior of Metallic Foams. Annual Review of Materials Science, **2000**. 30(1): p. 191-227.
[150] Kaya, A.C. and C. Fleck, Deformation behavior of open-cell stainless steel foams. Materials Science and Engineering: A, **2014**. 615: p. 447-456.
[151] Papadopoulos, D.P., et al., Mechanical properties of Al metal foams. Materials Letters, **2004**. 58(21): p. 2574-2578.
[152] Onck, P.R., E.W. Andrews, and L.J. Gibson, Size effects in ductile cellular solids. Part I: modeling. International Journal of Mechanical Sciences, **2001**. 43(3): p. 681-699.
[153] Bart-Smith, H., et al., Compressive deformation and yielding mechanisms in cellular Al alloys determined using X-ray tomography and surface strain mapping. Acta Materialia, **1998**. 46(10): p. 3583-3592.
[154] Deshpande, V.S. and N.A. Fleck, High strain rate compressive behaviour of aluminium alloy foams. International Journal of Impact Engineering, **2000**. 24(3): p. 277-298.
[155] Park, C. and S.R. Nutt, Strain rate sensitivity and defects in steel foam. Materials Science and Engineering: A, **2002**. 323(1): p. 358-366.
[156] Hong, K., et al., Comparison of morphology and compressive deformation behavior of copper foams manufactured via freeze-casting and space-holder methods. Journal of Materials Research and Technology, **2021**. 15: p. 6855-6865.
[157] Aly, M.S., Behavior of closed cell aluminium foams upon compressive testing at elevated temperatures: Experimental results. Materials Letters, **2007**. 61(14): p. 3138-3141.
[158] Mansoor, B., et al., Three dimensional forming of compressed open-cell metallic foams at elevated temperatures. Materials Science and Engineering: A, **2015**. 628: p. 433-441.
[159] Xiao, L., et al., High temperature compression properties of open-cell Ni–20Cr foams produced by impregnation. Materials & Design, **2015**. 85: p. 47-53.
[160] Kocks, U.F., A. AS, and A. MF, Thermodynamics and kinetics of slip. **1975**.
[161] Tavares, M., et al., Mechanical behavior of steel and aluminum foams at elevated temperatures. Local buckling based approach toward understanding of the material system behavior. International Journal of Mechanical Sciences, **2020**. 181: p. 105754.
[162] Pan, B., et al., Two-dimensional digital image correlation for in-plane displacement and strain measurement: a review. Measurement science and technology, **2009**. 20(6): p. 062001.
[163] Zhou, J., et al., Effects of heat treatment on the compressive deformation behavior of open cell aluminum foams. Materials Science and Engineering: A, **2004**. 386(1): p. 118-128.
[164] A beginners' guide to scanning electron microscopy, ed. Series. Vol. 1. **2018**: Springer.
[165] Chu, T., W. Ranson, and M.A. Sutton, Applications of digital-image-correlation techniques to experimental mechanics. Experimental mechanics, **1985**. 25: p. 232-244.
[166] Sutton, M.A., et al., Determination of displacements using an improved digital

correlation method. Image and vision computing, **1983**. 1(3): p. 133-139.
[167] Bornert, M., P. Doumalin, and É. Maire. Mesure tridimensionnelle des champs de déformation par corrélation d'images microtomographiques. in Photomécanique 2004: étude du comportement des matériaux et des structures. **2004**. GAMAC.
[168] Bornert, M., et al., Mesure tridimensionnelle de champs cinématiques par imagerie volumique pour l'analyse des matériaux et des structures. Instrumentation, Mesure, Métrologie, **2004**. 4(3-4): p. 43-88.
[169] Hounsfield, G.N., Computerized transverse axial scanning (tomography): Part 1. Description of system. The British journal of radiology, **1973**. 46(552): p. 1016-1022.
[170] Elliott, J.C. and S. Dover, X-ray microtomography. Journal of microscopy, **1982**. 126(2): p. 211-213.
[171] Bay, B.K., et al., Digital volume correlation: three-dimensional strain mapping using X-ray tomography. Experimental mechanics, **1999**. 39: p. 217-226.
[172] Dimanov, A., et al. Strain localization in ductile shear zones: This is a crystal plasticity's world, but it wouldn't be nothing without a micro-cracking or a sliding grain. in EGU. **2019**.
[173] Dautriat, J., et al., Localized deformation induced by heterogeneities in porous carbonate analysed by multi-scale digital image correlation. Tectonophysics, **2011**. 503(1-2): p. 100-116.
[174] Nguyen, T.T., et al., Initiation and propagation of complex 3D networks of cracks in heterogeneous quasi-brittle materials: Direct comparison between in situ testing-microCT experiments and phase field simulations. Journal of the Mechanics and Physics of Solids, **2016**. 95: p. 320-350.
[175] Lenoir, N., et al., Volumetric digital image correlation applied to X-ray microtomography images from triaxial compression tests on argillaceous rock. Strain, **2007**. 43(3): p. 193-205.
[176] Gane, N. and F. Bowden, Microdeformation of solids. Journal of Applied Physics, **1968**. 39(3): p. 1432-1435.
[177] Dingley, D., A simple straining stage for the scanning electron microscope. Micron (1969), **1969**. 1(2): p. 206-210.
[178] Gianola, D.S., et al., In situ nanomechanical testing in focused ion beam and scanning electron microscopes. Review of Scientific Instruments, **2011**. 82(6): p. 063901.
[179] Uchic, M.D., et al., Sample dimensions influence strength and crystal plasticity. Science, **2004**. 305(5686): p. 986-989.
[180] Greer, J.R., J.-Y. Kim, and M.J. Burek, The in-situ mechanical testing of nanoscale single-crystalline nanopillars. Jom, **2009**. 61: p. 19-25.
[181] Dong, Y.L. and B. Pan, A Review of Speckle Pattern Fabrication and Assessment for Digital Image Correlation. Experimental Mechanics, **2017**. 57(8): p. 1161-1181.
[182] Dimanov, A., et al., Deformation of aluminum in situ SEM and full field measurements by digital image correlation: evidence of concomitant crystal slip and grain boundary sliding. Available at SSRN 3922862, **2021**.
[183] Yang, D., et al., Dependence of elastic properties of argillaceous rocks on

moisture content investigated with optical full-field strain measurement techniques. International Journal of Rock Mechanics and Mining Sciences, **2012**. 53: p. 45-55.
[184] Yang, D., et al. Optimized optical setup for DIC in rock mechanics. in EPJ Web of Conferences. **2010**. EDP Sciences.
[185] El Sabbagh, A., In situ SEM caracterization of the grain boundary sliding mechanism in aluminum at high temperature by field measurement. Caractérisation du mécanisme de glissement aux joints de grains dans l'aluminium à haute température par mesures de champs in situ MEB. **2018**, Université Paris Saclay (COmUE).
[186] Dessolier, T., et al., Effect of temperature on deformation mechanisms of AZ31 Mg-alloy under tensile loading. Materials Science and Engineering: A, **2020**. 775: p. 138957.
[187] Chen, Y., Nanofabrication by electron beam lithography and its applications: A review. Microelectronic Engineering, **2015**. 135: p. 57-72.
[188] Sahin, O., M. Ashokkumar, and P.M. Ajayan, Micro-and nanopatterning of biomaterial surfaces, in Fundamental Biomaterials: Metals. **2018**, Elsevier. p. 67-78.
[189] Arrigan, D.W., Nanoelectrode arrays for electroanalysis, in Frontiers of Nanoscience. **2021**, Elsevier. p. 49-86.
[190] Prakash, S. and J. Yeom, Chapter 4 - Advanced Fabrication Methods and Techniques, in Nanofluidics and Microfluidics, Shaurya Prakash and Junghoon Yeom, Editors. **2014**, William Andrew Publishing. p. 87-170.
[191] Zamani, M. Al-Si Cast Alloys - Microstructure and Mechanical Properties at Ambient and Elevated Temperatures. **2015**.
[192] Chen, J., et al., Study on the Compression Properties and Deformation Failure Mechanism of Open-Cell Copper Foam Advanced Engineering Materials, **2017**. 19(11): p. 1600861.
[193] Gibson, L.J., Cellular solids. Mrs Bulletin, **2003**. 28(4): p. 270-274.
[194] Nikanorov, S.P., et al., Structural and mechanical properties of Al–Si alloys obtained by fast cooling of a levitated melt. Materials Science and Engineering: A, **2005**. 390(1): p. 63-69.
[195] Doumalin, P., Local Microextensometry by digital image correlation. Application to micromechanical studies by scanning electron microscopy. Microextensométrie locale par corrélation d'images numériques. Application aux études micromécaniques par microscopie électronique à balayage. **2000**, Ecole Polytechnique X.
[196] Gaye, A., Micromechanics of halite investigated by 2D and 3D multiscale full field measurements. Analyse multiéchelle des mécanismes de déformation du sel gemme par mesures de champs surfaciques et volumiques. **2015**, Université Paris-Est.
[197] Hubert, W.S., R.B. Joachim, and A.S. Michael, Systematic errors in digital image correlation caused by intensity interpolation. Optical Engineering, **2000**. 39(11): p. 2915-2921.
[198] Bornert, M., et al., Assessment of Digital Image Correlation Measurement Errors: Methodology and Results. Experimental Mechanics, **2009**. 49(3): p. 353-370.

[199] Linne, M., et al., Grain boundary sliding and slip transmission in high purity aluminum. Experimental Mechanics, **2019**. 59: p. 643-658.
[200] Han, B., et al. Temperature Effects on the Compressive Behaviors of Closed-Cell Copper Foams Prepared by Powder Metallurgy. Materials, **2021**. 14,
[201] Bekoz, N. and E. Oktay, High temperature mechanical properties of low alloy steel foams produced by powder metallurgy. Materials & Design, **2014**. 53: p. 482-489.
[202] Greenspan, L., Humidity fixed points of binary saturated aqueous solutions. Journal of research of the National Bureau of Standards. Section A, Physics and chemistry, **1977**. 81(1): p. 89.
[203] Differential scanning calorimetry, ed. Series. Vol. 2. **2003**: Springer.
[204] Differential scanning calorimetry (DSC), ed. Series. Vol. 7. **2009**: Wiley, Hoboken, NJ.
[205] Gallagher, P.K., Chapter 4 - Thermogravimetry and Thermomagnetometry, in Handbook of Thermal Analysis and Calorimetry, Michael E. Brown, Editor. **1998**, Elsevier Science B.V. p. 225-278.
[206] Danilatos, G., Introduction to the ESEM instrument. Microscopy research and technique, **1993**. 25(5-6): p. 354-361.
[207] Donald, A.M., The use of environmental scanning electron microscopy for imaging wet and insulating materials. Nature materials, **2003**. 2(8): p. 511-516.
[208] Ushak, S., et al., Characterization of calcium chloride tetrahydrate as a phase change material and thermodynamic analysis of the results. Renewable Energy, **2016**. 95: p. 213-224.
[209] Meisingset, K.K. and F. Grønvold, Thermodynamic properties and phase transitions of salt hydrates between 270 and 400 K IV. CaCl2· 6H2O, CaCl2· 4H2O, CaCl2· 2H2O, and FeCl3· 6H2O. The Journal of Chemical Thermodynamics, **1986**. 18(2): p. 159-173.
[210] Cao, F. and B. Yang, Supercooling suppression of microencapsulated phase change materials by optimizing shell composition and structure. Applied Energy, **2014**. 113: p. 1512-1518.
[211] Faucheux, M., et al., Influence of surface roughness on the supercooling degree: Case of selected water/ethanol solutions frozen on aluminium surfaces. International journal of refrigeration, **2006**. 29(7): p. 1218-1224.
[212] Safari, A., et al., A review on supercooling of Phase Change Materials in thermal energy storage systems. Renewable and Sustainable Energy Reviews, **2017**. 70: p. 905-919.
[213] Mohapatra, D. and J. Nandanavanam, Salt in matrix for thermochemical energy storage-A review. Materials Today: Proceedings, **2022**.
[214] Ren, S., et al., Corrosion testing of metals in contact with calcium chloride hexahydrate used for thermal energy storage. Materials and Corrosion, **2017**. 68(10): p. 1046-1056.
[215] Kelly, J.T. and A.S. Wexler, Thermodynamics of carbonates and hydrates related to heterogeneous reactions involving mineral aerosol. Journal of Geophysical Research: Atmospheres, **2005**. 110(D11).
[216] National Research Council, International Critical Tables of Numerical Data, Physics, Chemistry and Technology, ed. Series. **1930**, Washington, DC: The

National Academies Press.
[217] Karunadasa, K.S., et al., Relative stability of hydrated/anhydrous products of calcium chloride during complete dehydration as examined by high-temperature X-ray powder diffraction. Journal of Physics and Chemistry of Solids, **2018**. 120: p. 167-172.
[218] Zhao, C.Y. and Z.G. Wu, Heat transfer enhancement of high temperature thermal energy storage using metal foams and expanded graphite. Solar Energy Materials and Solar Cells, **2011**. 95(2): p. 636-643.
[219] Liu, M., et al., Review of research progress on corrosion and anti-corrosion of phase change materials in thermal energy storage systems. Journal of Energy Storage, **2023**. 63: p. 107005.
[220] Liu, H., Inter-seasonal solar energy storage for buildings by absorption. **2010**, Université de Savoie.

APPENDICES

A. Study of metal foam-NaCl composite

The metal foam-NaCl composite was studied before the metal foam-$CaCl_2$ composite to assess the feasibility of the synthesis method for metal foam-salt composites. This choice was due to the fact that NaCl is a non-hygroscopic salt, making it much easier to handle compared to $CaCl_2$ under room temperature and ambient humidity.

A1. Synthesis of metal foam-NaCl composite

First, a sugar film was deposited onto the surface of metal foam. The metal foam sample was immersed in a sugar solution (sucrose as solute) with a concentration of 0.6 g/ml, forming a thin film on the surface of the metal foam. This film acted as an adhesive layer to bind the salt particles in the following step. The metal foam sample was then dried and gently flushed with compressed air to clear any pores that might have been filled with sugar. This process ensured that all pores in the metal foam remained completely unblocked and available for depositing the salt particles. Note that the metal foam must be completely before the deposition of salts to ensure an evenly distribution. The ground NaCl particles were then deposited on the surface of the struts of the metal foam using a sieve with 36 µm. The mortar and sieve used are the same as presented in Fig. 3.1a and b, respectively. The states of sample after each synthesis process are shown in Fig. A.1. The sample obtained from this synthesis method was composed of 74 wt% copper foam, 13 wt% sugar binder and 13 wt% NaCl.

A2. In situ cyclic thermal test on metal foam-NaCl composite

The in situ cyclic thermal test was performed on metal foam-NaCl composite with SEM to investigate the thermal stability of the composite (especially the sugar binder) between the temperature range of 25 ℃ to 150 ℃.

The experimental setup is presented in Fig. A.2. The sheet-like composite sample, measuring 6 mm x 6 mm, was placed onto the heating stage, and a Pt100 thermocouple was affixed to the sample's surface to monitor its temperature during the test. The sample underwent four cycles within a range of 25 to 150 °C over a duration of 200 minutes. The results indicate that throughout the four thermal cycles, the structure of the composite has largely retained its original arrangement, with only subtle variations in the sugar layer and salt particle positions evident under SEM observation, as shown in Fig. A.3 (circled with white dashed lines).

In order to achieve a more precise observation of the states and potential alterations in the interfaces among the metal foam, sugar layer, and salt particles during temperature variations between 25 to 150 °C, we conducted cross-section

ion polishing of the composite sample. In Fig. A.4, the copper foam appears white, the sugar film appears black, and the salt particles appear gray.

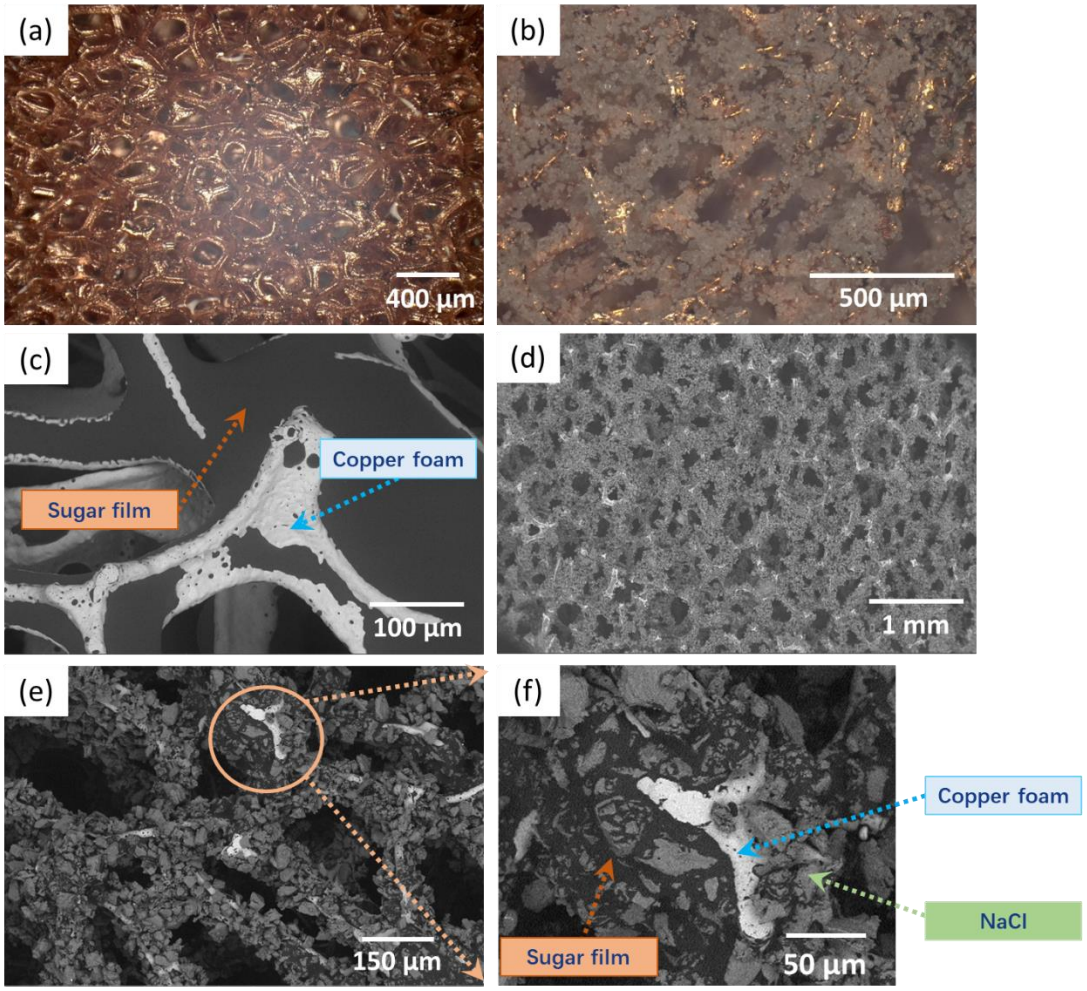

Fig. A.1. Optical microscopy image of copper foam (a) after deposition of sugar film and (b) after deposition after NaCl. (c) BES image of copper foam after deposition of sugar film as binder, with sugar film in black and copper foam in white. (d) (e) BSE images of copper foam-NaCl composite with sugar as binder and (f) zooming on interfaces of copper foam-sugar binder-NaCl particles. The copper foam is in white, NaCl particles are in gray and the sugar film is in black as indicated with arrows.

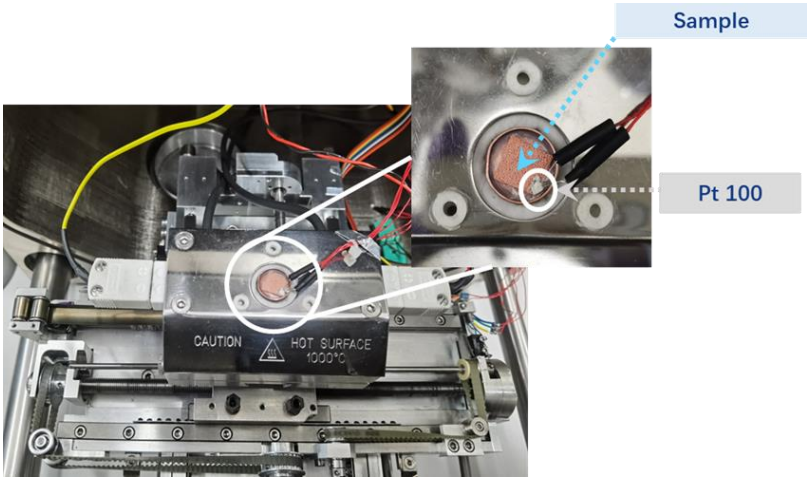

Fig. A.2. Experimental setup of in situ SEM cyclic thermal test on copper foam-NaCl composite.

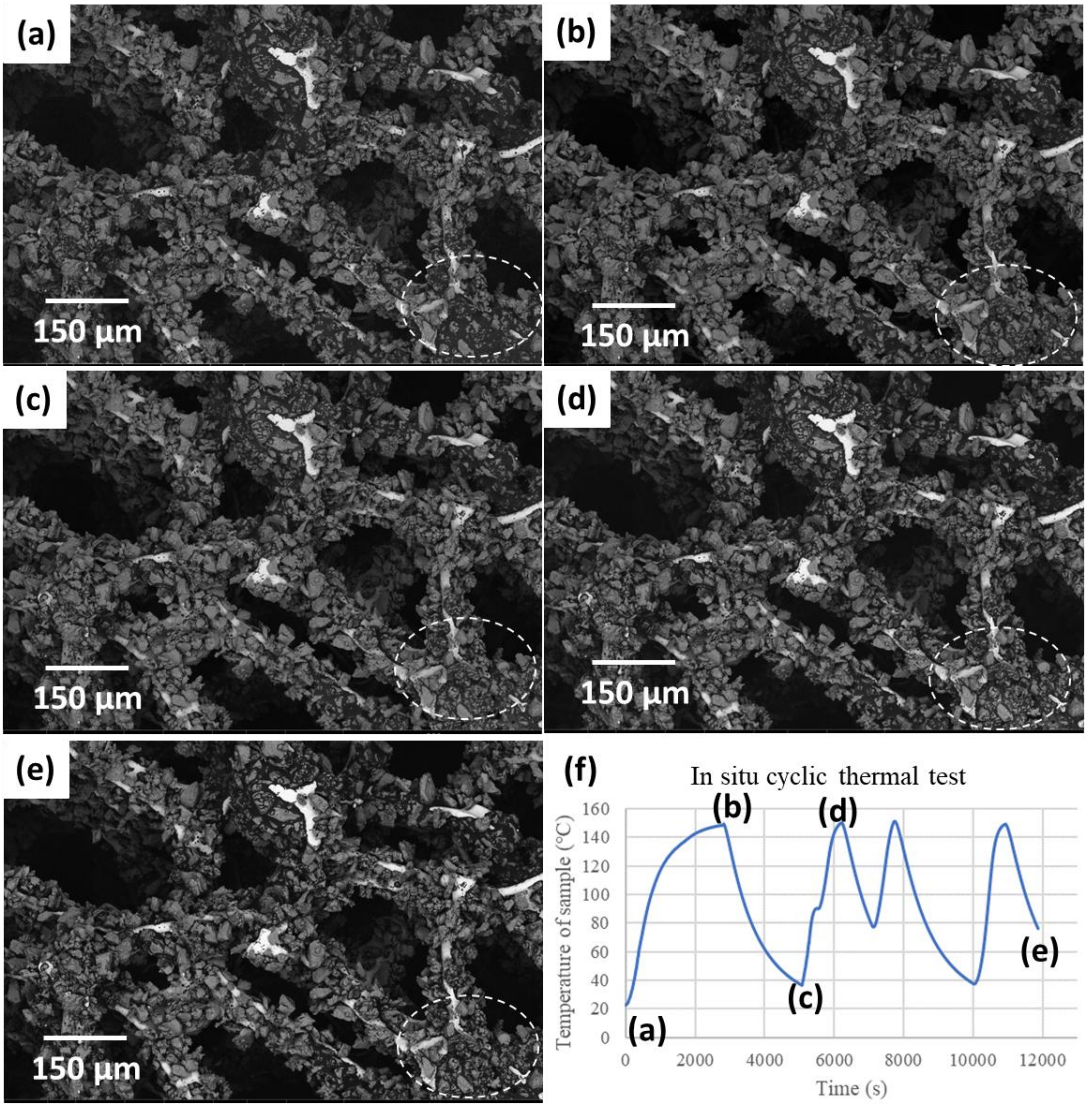

Fig. A.3. BSE images of copper foam-NaCl composite at different states during the in situ cyclic thermal test, where (f) is the sample temperature-time curve, marking the states of the sample corresponding to (a) through (e) during the test.

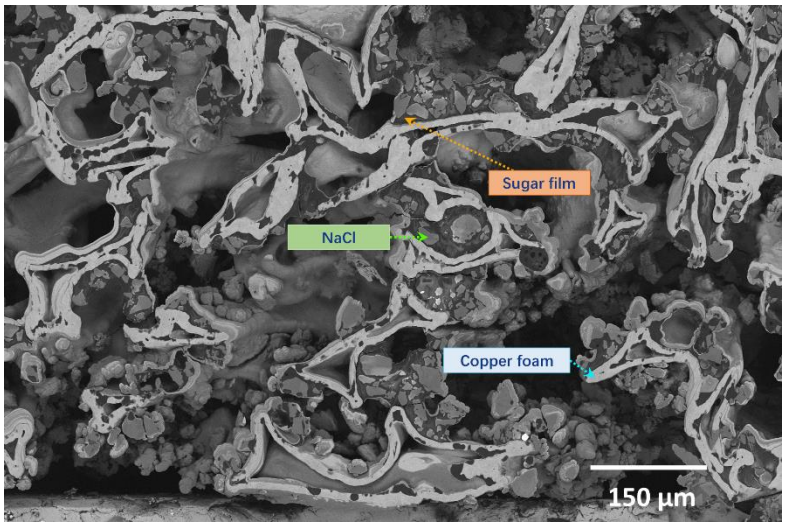

Fig. A.4. BSE image of the cross-section of the copper foam-NaCl composite, with copper foam in white, sugar film in black and NaCl particles in gray.

In situ SEM cyclic thermal test was performed on this sample focusing on the ion-polished cross section. In Fig. A.5, it is clear to observe that with the increase in temperature, the sugar layer continuously expanded and bulged, forming bubble-like structures.

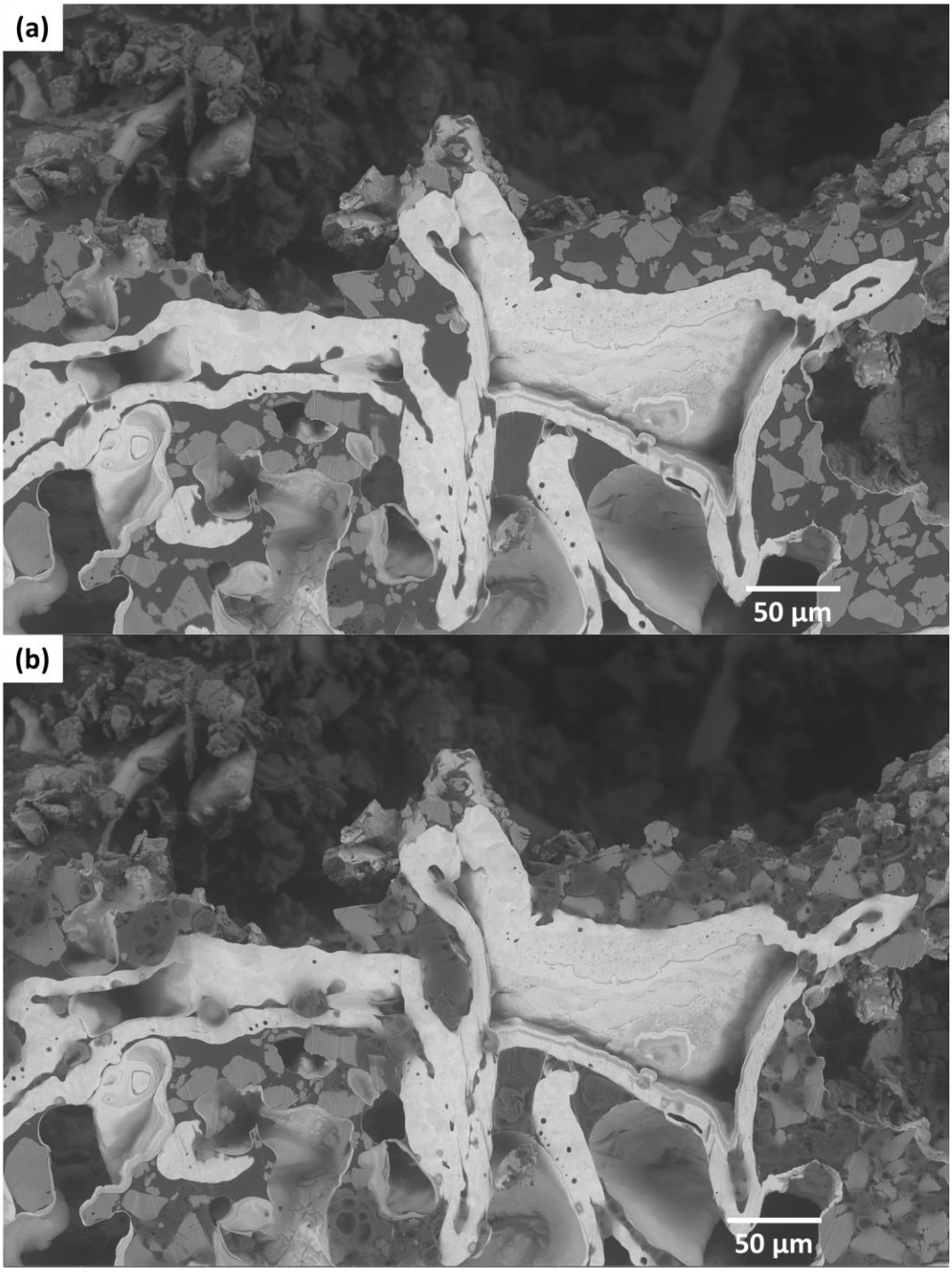

Fig. A.5. BSE images of (a) the initial state of cross section of the composite and (b) the state after heating to 150 ℃ of the same region of interest.

Generally speaking, the structure of composite was stable enough during cyclic thermal tests between the temperature range of 25-150 ℃ by applying the above-

mentioned synthesis method. In the following steps, we tried to apply this synthesis method using hygroscopic salt $CaCl_2$. Composite of nickel foam, sugar layer, and calcium chloride was synthesized and the samples were then subjected to a heating process to observe their thermal stability. In Fig. A.6a, we can see the general structure of the nickel foam-$CaCl_2$ composite with sugar film as binder. The $CaCl_2$ particles were not as evenly distributed as shown in Fig. A.1b, where the salt particles were non-hygroscopic salt NaCl. In addition, it can be clearly seen in Fig. A.6b that the salt particles have already started to hydrated at ambient temperature during the optical microscopy observation. As shown in Fig. A.6c and d, after being heated to 100 ℃, the salt and sugar layer in the composite sample exhibited caramel-colored swollen bubbles, protruding from the pores of the metal foam. While this phenomenon was not observed when using NaCl as the salt. The non-hygroscopic salt NaCl distributed more evenly on the sugar layer and did not hydrate during the experimental process, leading to a better thermal stability. However, for highly hygroscopic salt $CaCl_2$, it was challenging for it to uniformly adhere to the sugar layer during the deposition process. Additionally, during the heating process, continuous hydration reactions occurred, leading to the gradual formation of a solution with varying concentrations of the sugar and salt. This could potentially result in other reactions taking place at high temperatures, leading to the formation of caramel-colored bubbles.

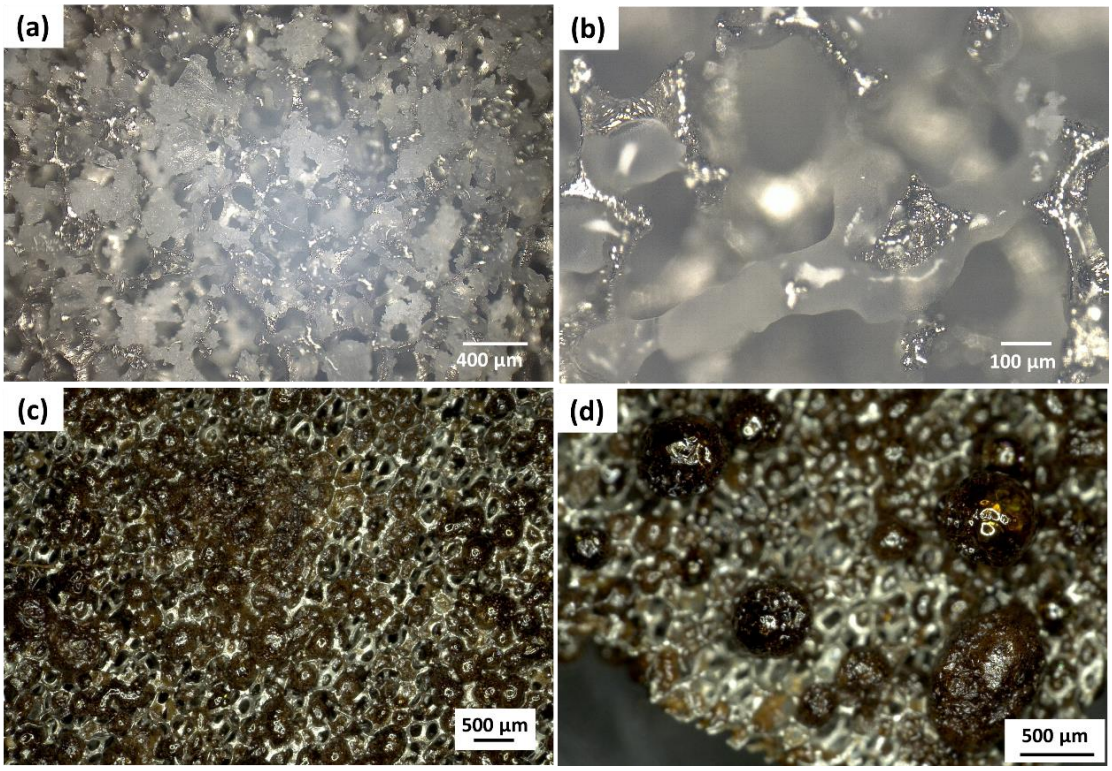

Fig. A.6. Optical microscopy image of (a) nickel foam-$CaCl_2$ composite with sugar film as binder and (b) zooming on one of the struts of the composite. (c) Nickel foam-$CaCl_2$ composite with sugar film as binder after heated to 100 ℃ and (d) zooming on the sample after heated to 100 ℃.

The exact composition of the caramel-colored bubbles was not analyzed. However, the experimental results were sufficient to indicate that the synthesis method described above utilizing the sugar layer as a binder was not suitable for synthesizing composites with highly hygroscopic salt, such as calcium chloride. Therefore, in this study, we developed and employed the synthesis method described in section 3.2.

B. Study of suitable parameters for e-beam lithography

As introduced in section 2.3.2, suitable e-beam settings and appropriate dose are essential for obtaining a clear lithography pattern. A series of doses and different electron beam settings were tested before choosing the most suitable combination.

It is important to note that the actual dose is the product of the set dose and the dose factor. In each lithography process, only one line dose and one area dose can be set. By adjusting different dose factors, it's possible to achieve patterns with varying line thickness, thereby testing the most suitable dose parameters for that specific pattern. The objective is to identify lithography parameters that ensure both accurate and complete patterns while maximizing the thickness of the lines composing the pattern. Thicker lines in the pattern lead to a higher number of pixels constituting each line during imaging at a given resolution, resulting in more reliable DIC results.

For each pattern shown in Fig. 2.22, 3 different dose factors were tested at accelerating voltage of 15 kV and 25 kV, respectively. The set line dose and area dose are presented in Table 2.5. The results are presented in the following figures.

In Fig. B.1, we present the pattern Grids (Fig. 2.22a) realized at accelerating voltage of 15 kV and 25 kV with dose factors of 0.8, 1.0 and 1.2. The results indicate that the dose factor not only affects the thickness of the lines but also has a significant impact on the successful realization of the pattern.

For instance, Fig. B.1a and f presented a relatively successful deposition of the pattern Grids. However, for other e-beam and dose factor settings, the platinum layer that should have been removed completely was not successfully eliminated (Fig. B.1b, c and e). Under an acceleration voltage of 15kV, setting the dose factor to 0.8 can result in the successful generation of the Grids pattern on the sample surface with e-beam lithography. However, under an acceleration voltage of 25kV, setting the dose factor to 1.2 yields clearer Grids patterns as DIC markers.

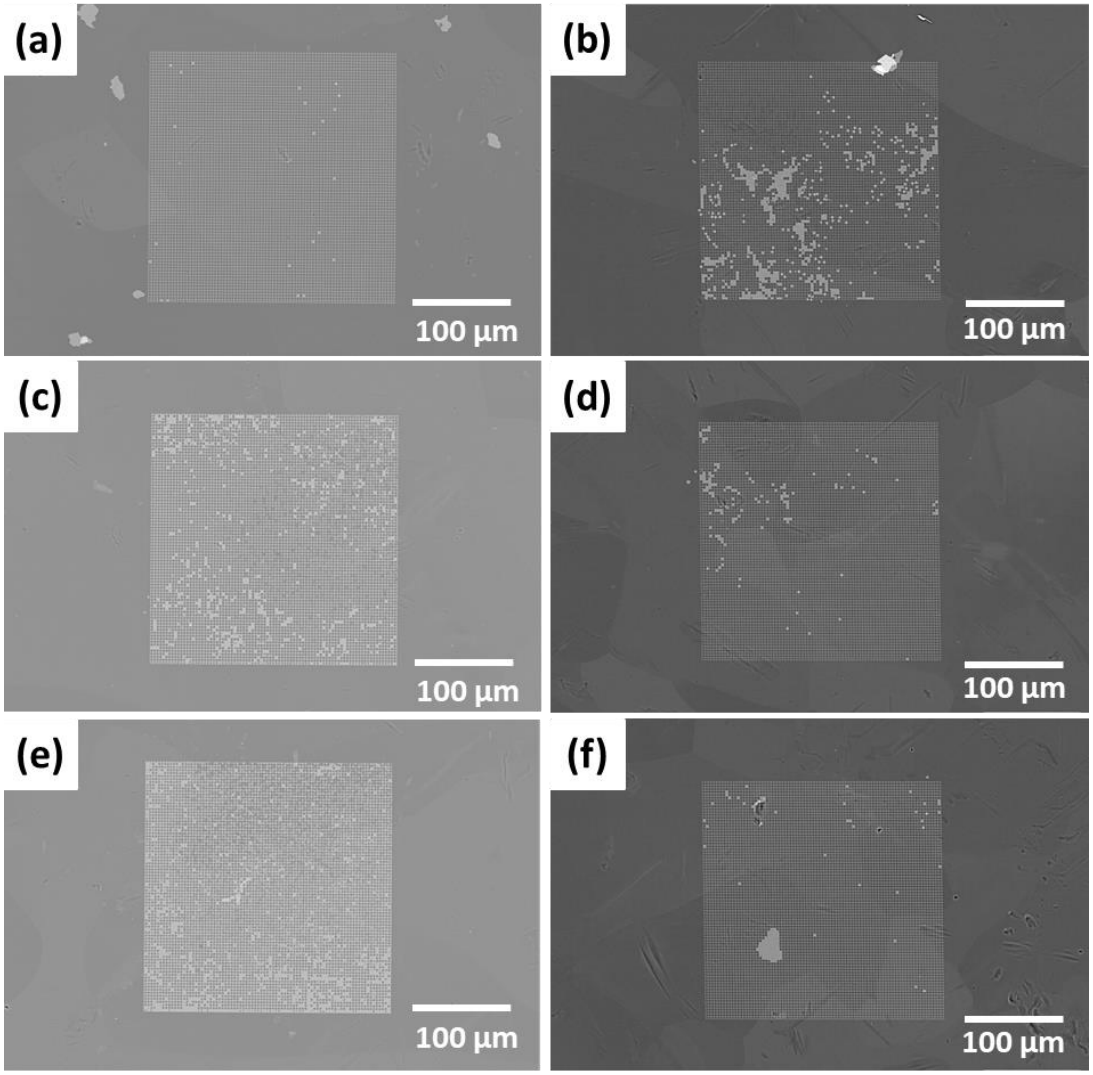

Fig. B.1. BSE images of pattern Grids (Fig. 2.22a) realized at accelerating voltage of 15 kV with dose factors of (a) 0.8, (c) 1.0, (e) 1.2, and at accelerating voltage of 25 kV with dose factors of (b) 0.8, (d) 1.0, (f) 1.2.

In Fig. B.2, zoomed-in views of Grids patterns shown in Fig. B.1a to f are respectively presented. It can be observed that under an acceleration voltage of 15 kV and a dose factor of 0.8, the right angles of the grids can be more fully manifested, whereas using the same acceleration voltage with the other two dose factors can result in rounded corners (Fig. B.2c and e). In general, a higher dose factor tends to result in thicker lines, but it also increases the likelihood of encountering issues with corner rounding. For the case of an acceleration voltage of 25 kV, all three dose factors have preserved right angles. In this scenario, we lean towards selecting the dose factor that leads to thicker lines, which is a dose factor of 1.2.

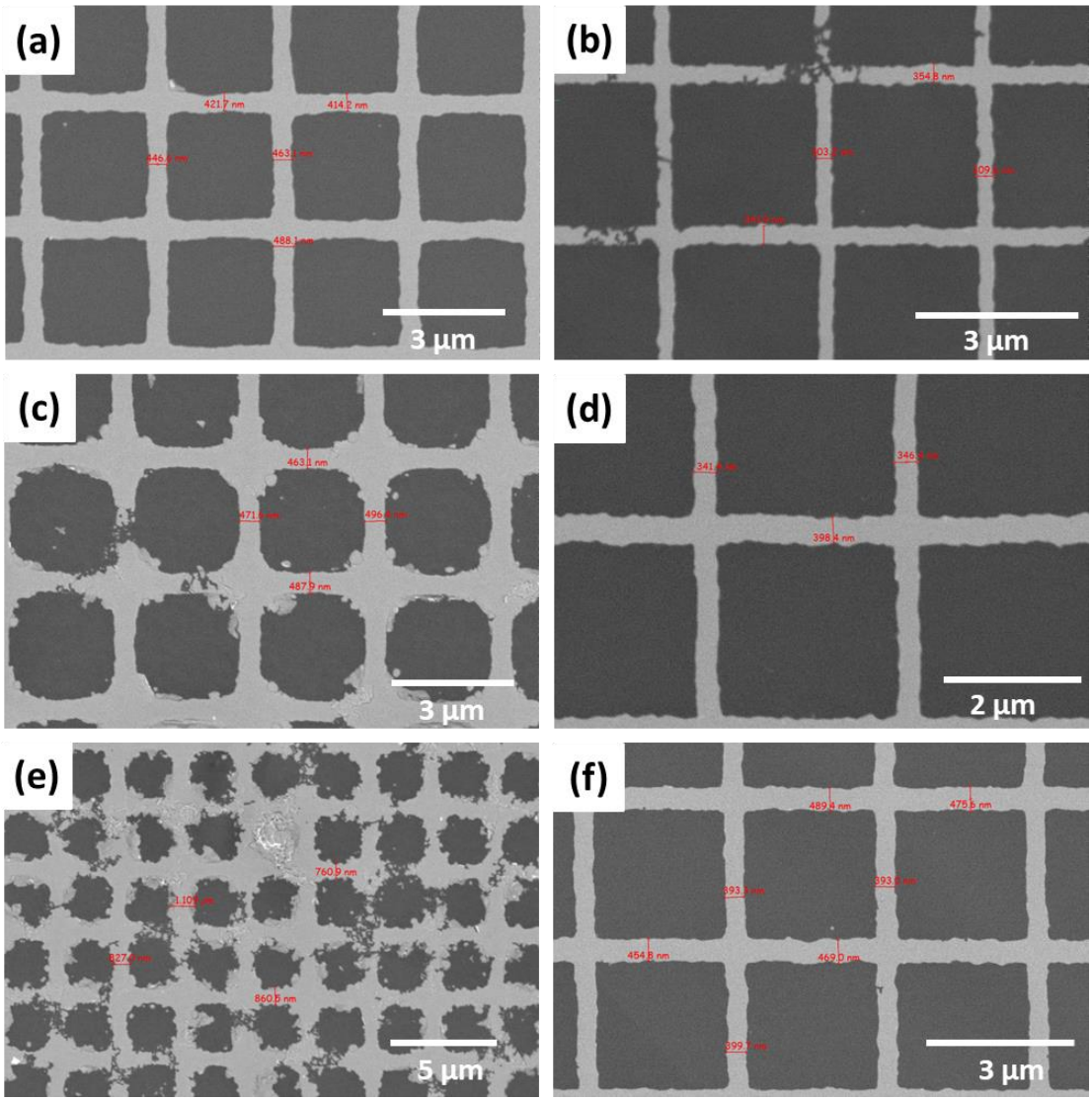

Fig. B.2. BSE images (zoomed-in view) of pattern Grids (Fig. 2.22a) realized at accelerating voltage of 15 kV with dose factors of (a) 0.8, (c) 1.0, (e) 1.2, and at accelerating voltage of 25 kV with dose factors of (b) 0.8, (d) 1.0, (f) 1.2.

In Fig. B.3, we present the pattern Crosses (Fig. 2.22b) realized at accelerating voltage of 15 kV and 25 kV with dose factors of 0.5, 0.7 and 0.9, respectively. From an overall perspective, the implementation of the patterns under these various parameters was successful and clear. Therefore, we examined specific advantages of each parameter set for depositing patterns on the sample surface for DIC by closely examining the details of the localized magnified images of the patterns, as shown in Fig. B.4.

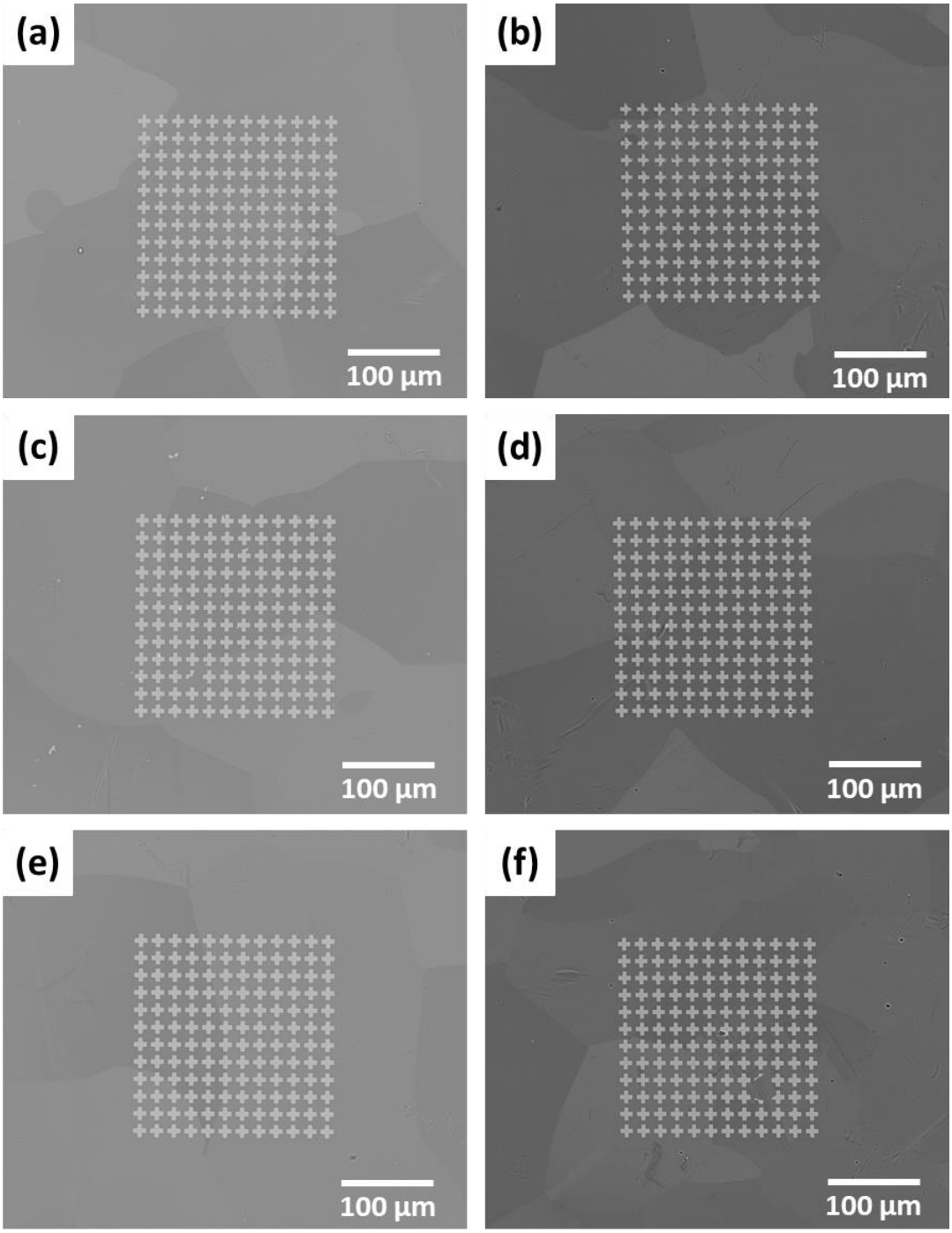

Fig. B.3. BSE images of pattern Crosses (Fig. 2.22b) realized at accelerating voltage of 15 kV with dose factors of (a) 0.5, (c) 0.7, (e) 0.9, and at accelerating voltage of 25 kV with dose factors of (b) 0.5, (d) 0.7, (f) 0.9.

As shown in Fig. B.4, for different combinations of parameters, although the patterns appeared relatively complete overall, there were still significant differences in detail. For example, at an acceleration voltage of 15 kV, with a dose factor of 0.5, the right angles of the cross pattern were clearly visible, and the lines were straighter. With dose factors of 0.7 and 0.9, the right angles tended to become rounded. In the case of an acceleration voltage of 25 kV, all three dose factors effectively presented the right angles of the cross pattern. However, at a dose factor of 0.5, there were micrometer-level defects in the cross pattern. Therefore, for the cross pattern, an acceleration voltage of 15 kV with a dose factor of 0.5, or an acceleration voltage of 25 kV with a dose factor of 0.7 or 0.9, are the more suitable parameters for e-beam lithography.

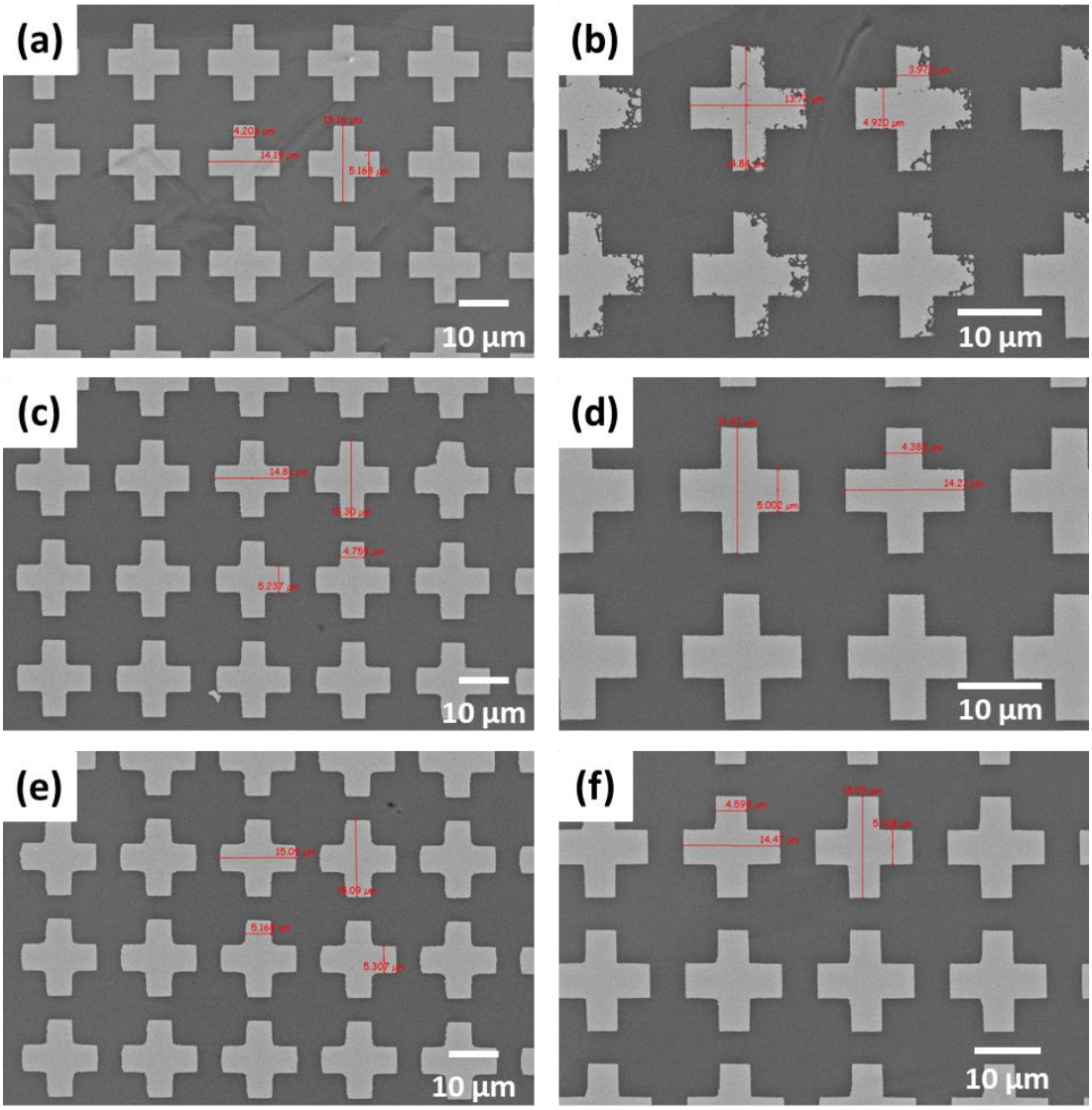

Fig. B.4. BSE images (zoomed-in view) of pattern Crosses (Fig. 2.22b) realized at accelerating voltage of 15 kV with dose factors of (a) 0.5, (c) 0.7, (e) 0.9, and at accelerating voltage of 25 kV with dose factors of (b) 0.5, (d) 0.7, (f) 0.9.

In Fig. B.5, we present the pattern Double-Grids (Fig. 2.22c) realized at accelerating voltage of 15 kV and 25 kV with dose factors of 0.4, 0.5 and 0.6, respectively. It can be observed that under an acceleration voltage of 15 kV, only a dose factor of 0.4 can yield a relatively complete pattern. On the other hand, for an acceleration voltage of 25 kV, all three dose factors can produce relatively complete patterns. Therefore, magnification to examine details is required for further discrimination.

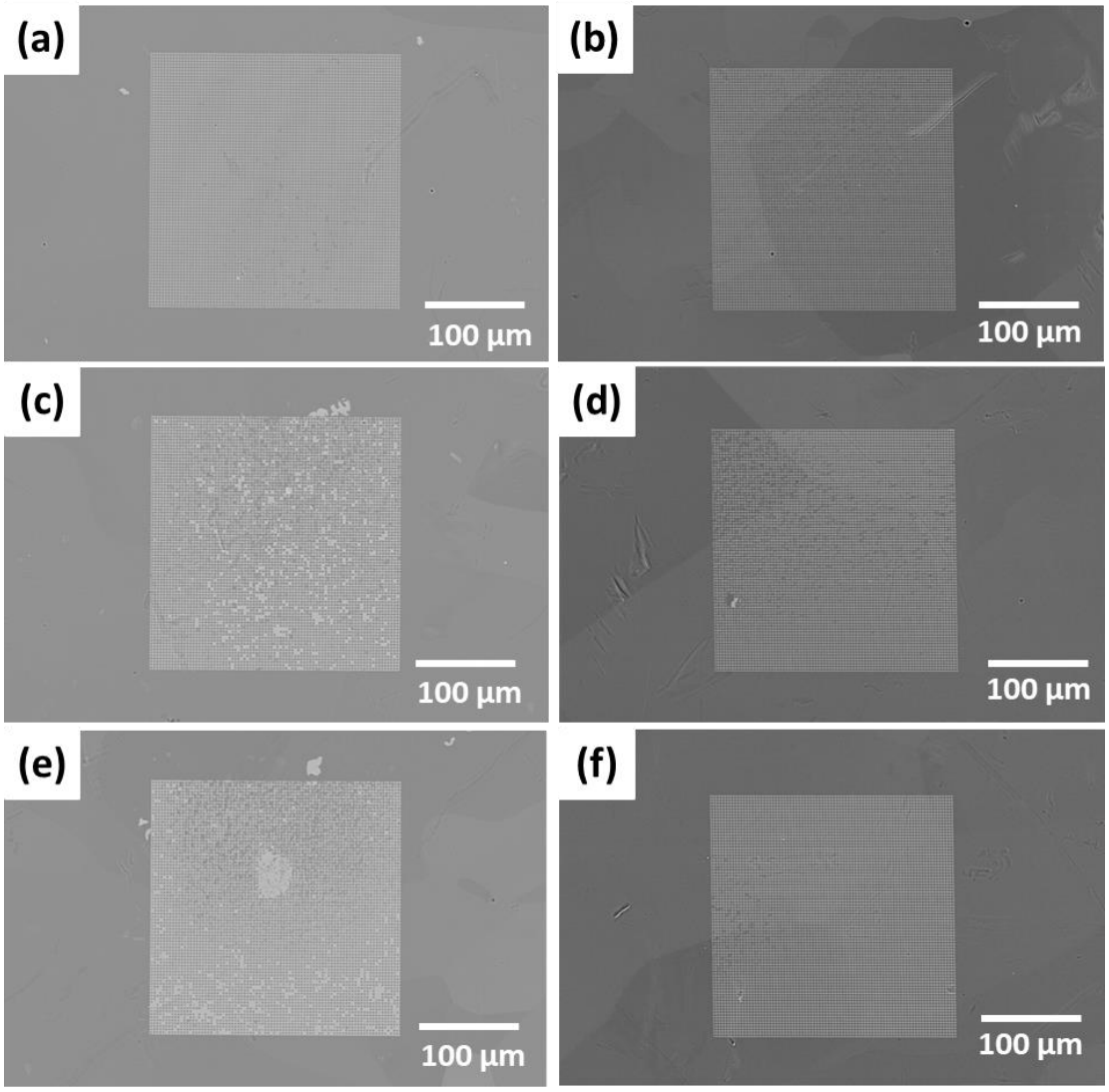

Fig. B.5. BSE images of pattern Double-Grids (Fig. 2.22c) realized at accelerating voltage of 15 kV with dose factors of (a) 0.4, (c) 0.5, (e) 0.6, and at accelerating voltage of 25 kV with dose factors of (b) 0.4, (d) 0.5, (f) 0.6.

As shown in Fig. B.6, at an acceleration voltage of 15 kV and a dose factor of 0.4, the Double-Grids pattern largely realized the intended design concept. However, minor defects were noticeable in the details. For instance, certain platinum layers that should have been removed remained, or there were slight gaps along the lines. These defects became more pronounced as the dose factor increased (such as at 0.5 and 0.6). At an acceleration voltage of 25 kV, all three dose factors relatively comprehensively realized the Double-Grids pattern. The distinction lies in the fact that as the dose factor increased, the lines composing the pattern became progressively thicker. Therefore, for the pattern Double-Grids, an acceleration voltage of 25 kV with a dose factor of 0.6 is more suitable.

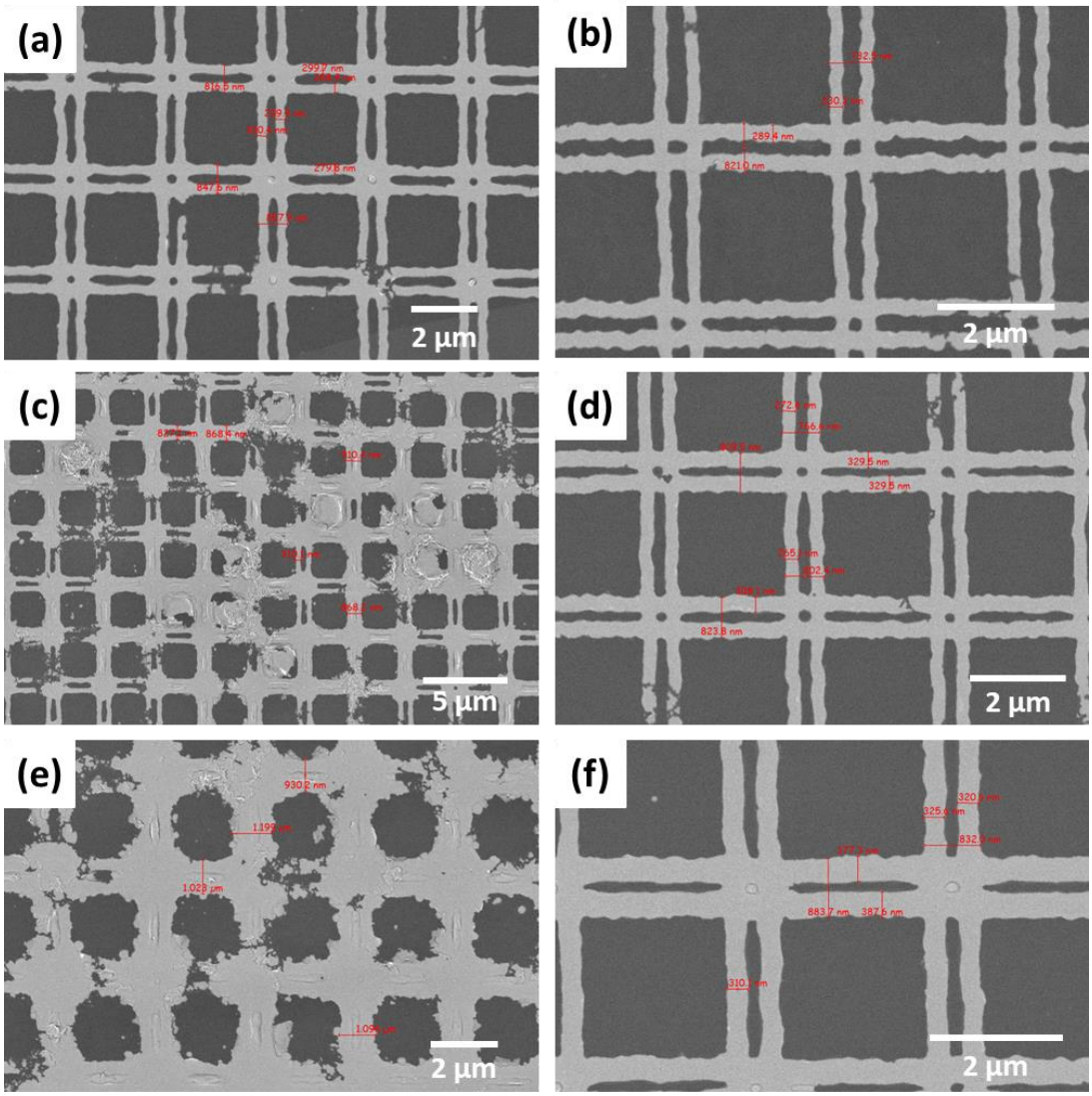

Fig. B.6. BSE images (zoomed-in view) of pattern Double-Grids (Fig. 2.22c) realized at accelerating voltage of 15 kV with dose factors of (a) 0.4, (c) 0.5, (e) 0.6, and at accelerating voltage of 25 kV with dose factors of (b) 0.4, (d) 0.5, (f) 0.6.

In Fig. B.7, we present the pattern Diamonds (Fig. 2.22d) realized at accelerating voltage of 15 kV and 25 kV with dose factors of 1.0, 1.2 and 1.4, respectively. It can be observed that regardless of whether the acceleration voltage is 15 kV or 25 kV, all three dose factors relatively comprehensively realized the Diamonds pattern.

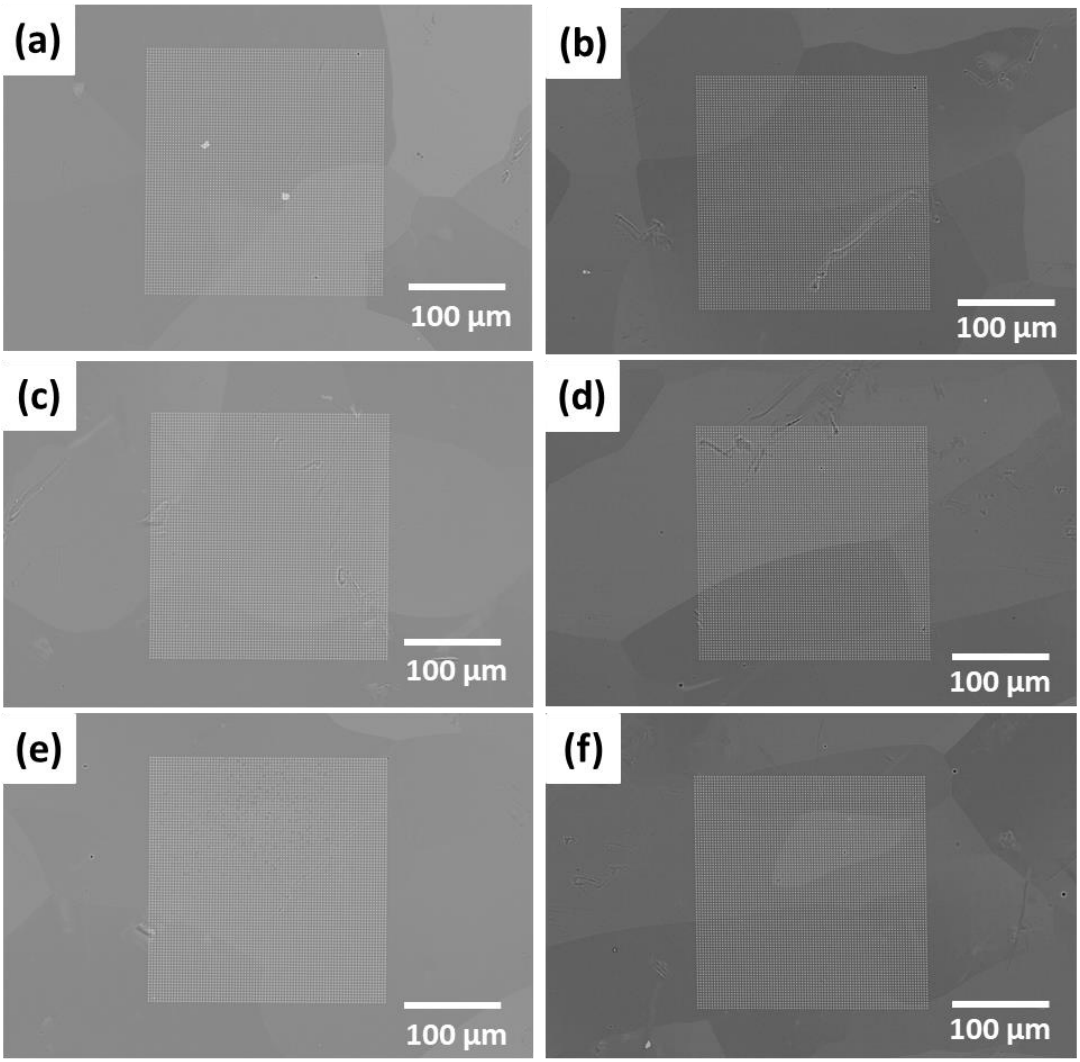

Fig. B.7. BSE images of pattern Diamonds (Fig. 2.22d) realized at accelerating voltage of 15 kV with dose factors of (a) 1.0, (c) 1.2, (e) 1.4, and at accelerating voltage of 25 kV with dose factors of (b) 1.0, (d) 1.2, (f) 1.4.

In Fig. B.8, we can see that at an acceleration voltage of 15 kV, as the dose factor increased, the distinct characteristics of the pattern Diamonds became less pronounced, exhibiting a tendency to gradually transform into a rhombus shape. Under an acceleration voltage of 25 kV, the patterns achieved by all three dose factors were relatively clear, without significant differences. They all met the research requirements.

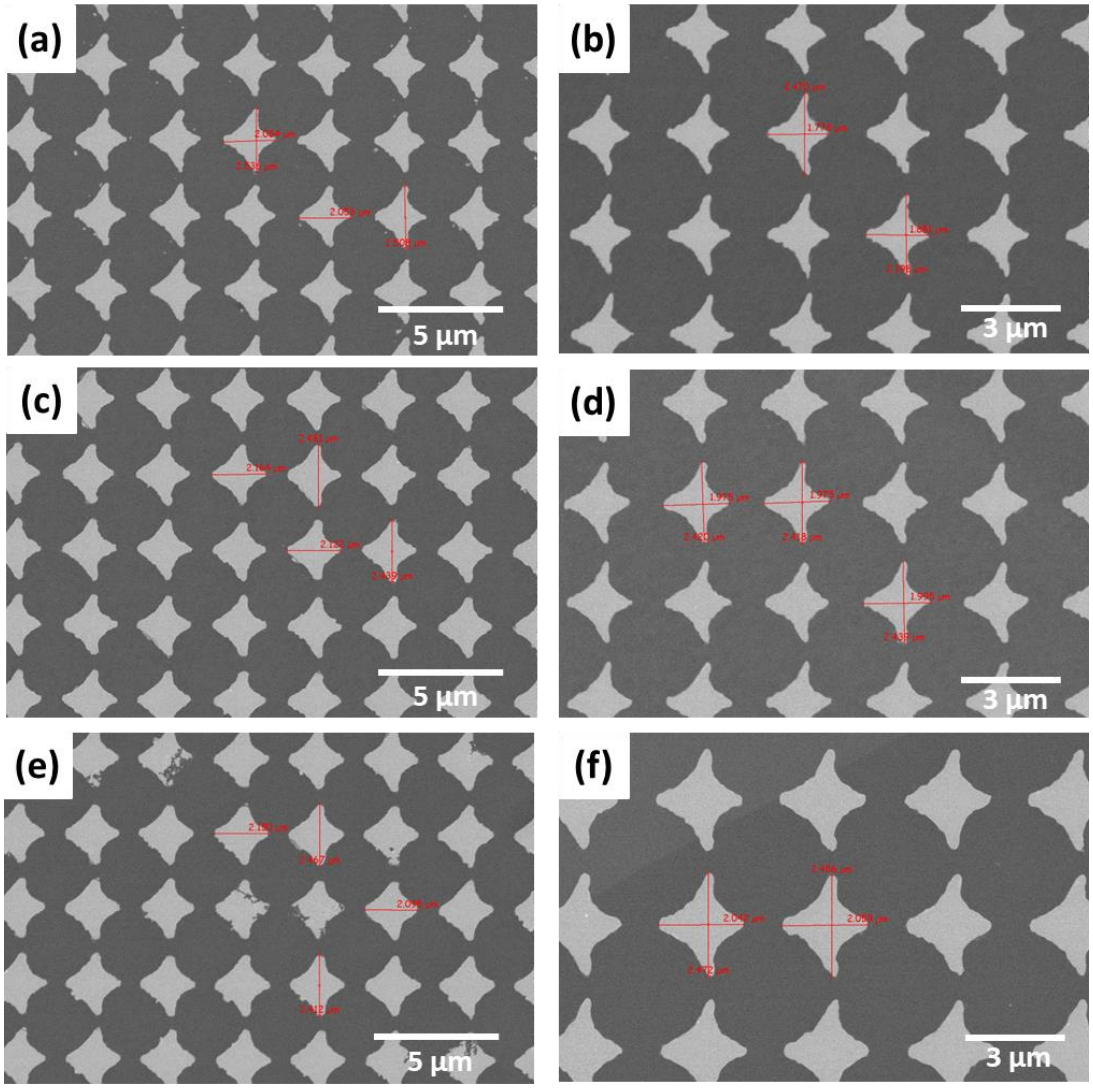

Fig. B.8. BSE images (zoomed-in view) of pattern Diamonds (Fig. 2.22d) realized at accelerating voltage of 15 kV with dose factors of (a) 1.0, (c) 1.2, (e) 1.4, and at accelerating voltage of 25 kV with dose factors of (b) 1.0, (d) 1.2, (f) 1.4.

Due to the microscopic size of each individual marker, Diamonds and Crosses are better suited for computing macroscopic deformation and strain fields. On the other hand, the component line widths of Grids and Double-Grids are within the range of 300-400 nm, making them more suitable for computing microscopic deformations and strain fields. They can be effectively used to study grain boundary sliding by DIC.

ECOLE DOCTORALE

Titre : Composites mousses métalliques-hydrates de sel pour le stockage thermochimique d'énergie

Mots clés : Stockage d'énergie, Réaction thermochimique, Stockage thermique par sorption, Sorbant d'eau sélectif, Chlorure de calcium, Mousse métallique

Résumé : Les systèmes de stockage thermochimique basés sur la réaction d'hydratation/déshydratation entre la vapeur d'eau et les sels hygroscopiques sont considérés comme des systèmes simples, peu coûteux et respectueux de l'environnement. Toutefois, les sels hygroscopiques présentent des inconvénients tels que le gonflement et l'agglomération des particules de sel au cours des cycles, ce qui entraîne progressivement une diminution de la surface de réaction spécifique et de la cinétique du transfert de chaleur et de masse, d'où une performance cyclique et une stabilité médiocres. Pour pallier les limitations mentionnées ci-dessus, nous proposons un composite basé sur une mousse métallique à cellules ouvertes comme matrice hôte, contenant du chlorure de calcium comme sel hygroscopique dispersé dans les pores. Avec une microstructure adaptée évitant l'agglomération des cristallites de sel pendant l'hydratation/ déshydratation, ce composite facilite les transferts de vapeur d'eau et de chaleur et empêche la perte de surface de réaction spécifique, améliorant ainsi les performances du système de stockage d'énergie.

Ce travail se concentre d'abord sur les propriétés mécaniques des mousses métalliques. Le comportement de déformation multi-échelle de différents mousses métalliques a été étudié par des essais de compression réalisés in situ avec observation par microscopie optique avec caméra à haute résolution et MEB. La technique de microtomographie à rayons X a aussi été appliquée. Les images ont été analysées par corrélation d'images numériques 2D et 3D pour le calcul des champs de déplacement et de déformation. Les résultats montrent que pour l'intégrité mécanique, la microstructure de la mousse métallique est plus importante que le métal lui-même. La localisation des déformations est limitée dans les mousses métalliques avec microstructure plus homogène, ce qui empêche l'effondrement complet des pores et préserve ainsi les propriétés de transfert. En revanche, une microstructure de mousse métallique hétérogène entraîne la formation de bandes de localisation importantes, qui peuvent entraver le transfert de vapeur d'eau, ce qui affecte les performances du composite.

Les propriétés thermochimiques des composites sont étudiées par calorimétrie différentielle à balayage. En particulier, les propriétés thermochimiques des composites pendant les cycles d'hydratation et déshydratation sont comparées à celles de poudres de sel. L'évolution des propriétés thermochimiques est analysée par l'observation in situ au cours des cycles d'hydratation/déshydratation dans un MEB environnemental. Il est montré que les composites présentent une amélioration significative en termes de stabilité cyclique et de quantité d'énergie libérée/stockée, par rapport à la poudre de sel en vrac. Les observations in situ MEBE montrent que le gonflement et la déliquescence induisent une redistribution modérée des hydrates de sel dans la mousse métallique. Cependant, la porosité ouverte du composite est préservée. La mousse métallique empêche efficacement l'agglomération des sels et la perte de surface de réaction spécifique, ce qui explique l'amélioration substantielle des propriétés thermochimiques du composite et de sa stabilité cyclique.

En conclusion, le composite mousse métallique-hydrate de sel développé dans notre travail est adapté pour le stockage de l'énergie thermochimique, offrant à la fois des avantages mécaniques et thermochimiques. D'une part, la mousse métallique assure l'intégrité structurelle permettant une manipulation industrielle flexible des unités de stockage thermochimique. D'autre part, la mousse métallique assure la stabilité microstructurale du matériau réactif, préservant une durée de vie économiquement durable. Enfin, les composites ont une faible empreinte environnementale et permettent un recyclage total.

ECOLE DOCTORALE

Title : Metal foam-salt hydrate composites for thermochemical energy storage

Keywords : Energy storage, Thermochemical reaction, Sorption thermal storage, Selective water sorbent, Calcium chloride, Metal foam

Abstract : Thermochemical heat storage (THS) systems based on the hydration/dehydration reaction between water vapor and hygroscopic salts are considered to be a simple, low-cost and environmentally friendly system. However, hygroscopic salts have drawbacks such as swelling and agglomeration of the crystalline salt particles during hydration/dehydration cycles, which progressively leads to decreasing specific reaction surface, and kinetics of heat and mass transfer, thus resulting in efficiency degradation due to poor cyclic performance and stability.

To alleviate the limitations mentioned above, we propose a composite based on open-cell metal foam as host matrix, containing calcium chloride as hygroscopic salt dispersed in the pores. With an adapted microstructure avoiding agglomeration during swelling and shrinking of the salt crystallites related to hydration and dehydration respectively, this composite facilitates the transfers of water vapor and heat and prevents loss of specific reaction surface, thus improving the performance of the THS system.

This thesis work focuses first on the mechanical properties of metal foam. The multiscale deformation behavior of different metal foams was studied by compression tests realized in situ with observation by optical microscopy with high-resolution camera (pixel size of 2.75 μm) and scanning electron microscopy (SEM). Laboratory X-ray microtomography technique was also applied. Images were analyzed by 2D and 3D Digital Image Correlation (DIC) for the computation of displacement fields and strain fields. The results show that concerning the mechanical integrity the microstructure of the metal foam is by far more important than the metal itself. Strain localization is limited in metal foams with a comparatively homogeneous microstructure, precluding complete pore collapse, thus preserving the mass transfer properties. In opposition, highly heterogeneous metal foam microstructure leads to the formation of strong localization bands. This may impede the water vapor transfer, affecting the performance of the designed composite.

The thermochemical properties of the metal foam-salt composites are studied by differential scanning calorimetry (DSC), with respect to the synthesis method and the type of metal foam. In particular, the thermochemical properties of the composites during hydration/dehydration cycles are compared with those of salt hydrate powders of calcium chloride. The evolution of the thermochemical properties is further analyzed, based on in situ observation of the microstructural and morphological evolution during hydration/dehydration cycling in an environmental scanning electron microscope (ESEM). It is demonstrated that the metal foam-salt composites show significant improvement in terms of cyclic stability and quantity of thermal energy released/stored, compared to bulk calcium chloride powder. In situ ESEM observations show that swelling and deliquescence induce moderate redistribution of salt hydrates within the metal foam. However, the open porosity of the composite is essentially preserved. The metal foam efficiently prevents extensive salt agglomeration and loss of specific reaction area, which explains the substantial improvement of the composite's thermochemical properties and their cyclic stability.

In conclusion, the metal foam-salt hydrate composite developed in our work is suitable and promising for thermochemical storage, offering both mechanical and thermochemical advantages. On the one hand, the metallic foam ensures structural integrity allowing for flexible industrial handling of thermochemical storage units. On the other hand, the metal foam ensures the microstructural stability of the reactive material, hence preserving an economically durable life span. At last, the designed composites have a low environmental footprint. The reactive salt hydrates are environmentally friendly. Both the salt hydrate and the metallic foam allow for total recycling.